

Dissertation zur Erlangung des Doktorgrades
der Fakultät für Chemie und Pharmazie
der Ludwig-Maximilians-Universität München

Synthesis and Structural Chemistry of Subvalent Compounds with Complex Anions

Matthias Paul Benedikt Wörsching

aus
Starnberg, Deutschland

2017

Erklärung

Diese Disstertation wurde im Sinne von §7 der Promotionsordnung vom 28. November 2011 von Herrn Dr. Constantin Hoch im Arbeitskreis von Herrn Prof. Dr. Wolfgang Schnick betreut.

Eidesstattliche Versicherung

Diese Dissertation wurde eigenständig und ohne unerlaubte Hilfe erarbeitet.

München,

Matthias Wörsching
.....

Dissertation eingereicht am:	20.02.2017
1. Gutachter:	Prof. Dr. Wolfgang Schnick
2. Gutachter:	Prof. Dr. Oliver Oeckler
Mündliche Prüfung am:	21.03.2017

to my family

Imagination is more
important than knowledge.
Knowledge is limited.
Imagination encircles the world.
– Albert Einstein

This taught me a lesson
but I'm not quite sure
what it is.
– John McEnroe

Mein besonderer Dank gebührt Prof. Dr. Wolfgang Schnick und Prof. Dr. Bettina Lotsch für die Möglichkeit, diese Arbeit am Lehrstuhl für Festkörperchemie anzufertigen.

Prof. Dr. Oliver Oeckler danke ich für das Übernehmen des Koreferats für diese Arbeit.

Prof. Dr. Lena Daumann, Prof. Dr. Wolfgang Beck, Prof. Dr. Konstantin Karaghiosoff und Prof. Dr. Hans-Christian Böttcher danke ich für die Bereitschaft Teil der Prüfungskommission meines Rigorosums zu sein.

Mein ganz besonderer Dank gilt Dr. Constantin Hoch. Ich danke ihm nicht nur für die hervorragende fachliche Betreuung und Themenstellung, sondern auch für die immer motivierende Art und Weise meine Doktorarbeit betreut zu haben. Tino hatte stets ein offenes Ohr für mich, egal wie blödsinnig meine Fragen auch manchmal waren oder wie kompliziert die Thematik sich darstellte. Es war mir ein Fest mit dir zu arbeiten!

Besonders bedanken möchte ich mich auch bei Dr. Frank Tambornino, der mir vor allem zu Beginn meiner Promotion eine große Hilfe war, sowie für das Messen einer immensen Anzahl an Einkristallen. Und natürlich ein großer Dank für die unvergesslichen zweidimensionalen Squash-Matches.

Ebenso danke ich meinen Praktikantinnen und Praktikanten Irina Zaytseva, Bea Fischer, Florian Geiger, Martin Daiger und Sarah Fricke für den großen Beitrag zu dieser Arbeit.

Christian Minke danke ich für die zahlreichen REM- bzw. NMR-Messungen, sowie Dr. Thomas Bräuniger für die Hilfe bei der Auswertung besagter NMR-Messungen. Thomas Miller danke ich für die tolle Zusammenarbeit bei der Betreuung des Pulverdiffraktometers und für die Messung verschiedener Einkristalle am D8. Wolfgang Wünschheim danke ich die Lösung von so einigen Computerproblemen. Roland Eger danke ich für die Unterstützung bei thermoanalytischen Messungen. Mein Dank gilt auch Olga Lorenz für ihre diversen organisatorischen Tätigkeiten.

Besonders bedanken möchte ich mich bei allen meinen ehemaligen und aktuellen Laborkollegen Florian Pucher, Dr. Sebastian Schneider, Dr. Dominik Baumann, Dr. Alexey Marchuk, Dr. Frank Tambornino, Simon Kloß, Eva Bertschler, Philipp Bielec, Sebastian Wendl und Sebastian Vogel für die tolle Zusammenarbeit, die Riesenstimmung im Labor und die zahlreichen gemeinsamen Laborabende.

Ich danke selbstverständlich auch allen Mitgliedern der Arbeitskreise Hoch, Schnick, Johrendt, Lotsch, Oeckler und Bräuniger für die gute Zusammenarbeit.

Bedanken möchte ich mich auch ganz besonders bei allen Mitgliedern des PIC Schafkopfclubs, Ursi Pachmayr, Andi Binek, Tobi Hassler, Philipp Ratza und Stefan Datz für die tolle Zeit während und nach dem Studium. Letzterem danke ich selbstverständlich auch für die vielen Raman-spektroskopischen Messungen.

Außerdem möchte ich mich bei meiner gesamten Stammtisch-Tennismannschaft sowie bei Niklas und Katya bedanken, auch wenn sich durch die gemeinsamen Abende der ein oder andere darauffolgende Arbeitstag etwas unproduktiv gestaltete.

Zuletzt kann ich meinen Eltern und meiner Freundin Ani gar nicht genug danken. Ihr habt mich dahin gebracht, wo ich heute bin.

Contents

1	Introduction	1
1.1	The heavy alkali and alkaline earth metals – a historical overview	1
1.2	Polar metal bonding – Definitions and state of the art	3
1.2.1	The concept of subvalency: First examples and demarcation to related substance classes	5
1.2.2	Suboxides of the heavy alkali metals	6
1.2.3	Subnitrides of the heavy alkaline earth metals	8
1.3	Expansion of the substance class by introducing complex anions – motivation and synthetic approaches	10
1.3.1	Suboxometalates	10
1.3.2	Subnitridometalates	11
1.3.3	Ionic phases with complex anions	11
1.3.4	Organisation of this work	12
1.4	References	13
2	Methods	17
2.1	Glove box	17
2.2	Schlenk technique	17
2.3	Crucible materials	17
2.4	Light microscopy	18
2.5	Powder X-ray diffractometry	18
2.6	Single crystal X-ray diffractometry	18
2.7	Scanning electron microscopy (SEM)	19
2.8	Nuclear magnetic resonance (NMR)	19
2.9	Raman spectroscopy	19
2.10	Inductively coupled plasma analysis (ICP)	20
2.11	Elemental analysis (CHNS)	20
2.12	Band structure calculations	20
2.13	Lattice energy calculations according to the MAPLE concept	20
2.14	References	21
3	Alkali Metal Suboxometalates – Structural Chemistry between Salts and Metals	23
3.1	Introduction	24
3.2	Experimental Section	27
3.2.1	Materials	27
3.2.2	X-ray Diffraction Analysis	27
3.2.3	Differential Thermal Analysis	28
3.2.4	Density Functional Theory Calculations	28
3.3	Results and Discussion	30

3.4	Conclusion	34
3.5	Acknowledgement	35
3.6	References	36
3.7	Supporting Information	38
4	Chemical Twinning of Salt and Metal in the Subnitridometalates	
	Ba₂₃Na₁₁(MN₄)₄ with M = V, Nb, Ta	47
4.1	Introduction, Results, Discussion and Conclusion	48
4.2	Experimental section	53
4.3	Acknowledgement	54
4.4	References	55
4.5	Supporting Information	57
5	CsOH and its lighter homologues – a comparison	65
5.1	Introduction	66
5.2	Results and Discussion	67
	5.2.1 Crystal structure	67
	5.2.2 Raman spectroscopy	71
5.3	Experimental Section	74
	5.3.1 Preparation and crystal structure investigation	74
	5.3.2 Raman spectroscopy	75
5.4	References	76
6	The triple salt Sr₁₄[Ta₄N₁₃][Ta₄N₄]O – a nitridotantalate oxide with 19-fold rocksalt superstructure	79
6.1	Introduction	80
6.2	Experimental section	81
6.3	Results and Discussion	83
6.4	Conclusion	92
6.5	Acknowledgment	93
6.6	References	94
6.7	Supporting Information	97
7	Additional Results	103
7.1	The Barium Nitridoborate 'Ba ₂₃ (BN ₂) ₁₁ (BN ₃) ₃ (N) ₃ '	103
7.2	The Barium Nitridomolybdate/-tantalate 'Ba ₆ [Mo _x Ta _{1-x} N ₄]N _x '	112
7.3	References	118
8	Summary	119
8.1	Alkali metal suboxometalates – structural chemistry between salts and metals	119
8.2	Chemical Twinning of Salt and Metal in the Subnitridometalates Ba ₂₃ Na ₁₁ (MN ₄) ₄ with M = V, Nb, Ta	120
8.3	CsOH and its lighter homologues – a comparison	120
8.4	The triple salt Sr ₁₄ [Ta ₄ N ₁₃][Ta ₄ N ₄]O – a nitridotantalate oxide with 19-fold rocksalt superstructure	121
8.5	The Barium Nitridoborate 'Ba ₂₃ (BN ₂) ₁₁ (BN ₃) ₃ (N) ₃ '	121
8.6	The Barium Nitridomolybdate/-tantalate 'Ba ₆ [Mo _x Ta _{1-x} N ₄]N _x '	121

8.7	Concluding Words	122
9	Outlook	123
9.1	Suboxometalates	123
9.2	Subnitridometalates	124
9.3	Metal-rich ionic compounds via decomposition	126
9.4	References	127
10	Miscellaneous	129
10.1	List of Publications	129
10.2	Contributions to conferences	130
10.3	Deposited crystallographic data	131

1 Introduction

1.1 The heavy alkali and alkaline earth metals – a historical overview

The heavy alkali metals Rubidium and Caesium were discovered in residues of Bad Dürkheim mineral water by Robert Wilhelm Bunsen and Gustav Robert Kirchhoff in 1860 and 1861 respectively.^[1] Using optical spectroscopy – a very uncommon method at this time – Bunsen and Kirchhoff identified different spectral lines and were able to assign them to two new elements naming them Caesium (from latin: *caesius* = sky blue) and Rubidium (from latin: *rubidus* = deep red).^[1] Bunsen and Kirchhoff also succeeded in synthesising elemental Rb, whereas the synthesis of elemental Cs was realised by Carl Setterberg in 1881.^[2] Today, the metals are synthesised in high purity via reduction of the chromate or chloride with Zr or Ca and subsequent distillation in vacuo.^[4] The heavy alkaline earth elements Strontium (named after the scottish town Strontian) and Barium (from greek: *βαρύς* = heavy and the mineral Baryte) were first synthesised via electrolysis by Humphrey Davy in 1808.^[5] Nowadays, high purity Sr and Ba are obtained via reduction of the respective oxides with Al or decomposition of the azides and subsequent distillation, which – due to their relatively high boiling points – requires great expertise and sophisticated equipment.^[6]



Figure 1.1: Images of elemental Rb and Cs in glass ampoules taken through a light microscope.

Physical properties of all four elements resemble each other as expected from their position in the periodic table. They show silver, metallic luster (in the case of Cs golden luster due to relativistic effects as shown in Figures 1.1 and 1.2), have low melting points ($\sim 28\text{ }^{\circ}\text{C}$ to $\sim 769\text{ }^{\circ}\text{C}$), and are very soft (0.2 to 1.5 Mohs hardness). Their most prominent feature is their outstandingly high reactivity. As all reactions within this work exclude water, the deciding physical parameter is not the position in the electrochemical

series, but rather the ionisation energies of all elements. Rb and Cs have the lowest ionisation energies of the stable elements making them the most ignoble metals of the periodic table. Sr and Ba are ranked closely behind. Their high reactivity in combination with their large ionic radius makes them not only strong reducing agents, but leads to a versatile chemistry towards Oxygen and Nitrogen, which is not observable for other elements. Table 1.1 gives an overview of a few selected physical parameters.

Table 1.1: Physical properties of the heavy alkali and alkaline earth metals in comparison to lighter homologues.

	Cs	Rb	Li	Ba	Sr	Be
First Ionisation Energy ^[7] / eV	3.9	4.2	5.4	5.2	5.7	9.3
Electron Affinity ^[7] / eV	-0.47	-0.49	-0.62	+0.48	+1.51	+0.19
Work function according to Michaelson ^[8] / eV	2.14	2.16	2.9	2.7	2.59	4.98
Electronegativity according to Allred-Rochow ^[9]	0.86	0.89	0.97	0.97	0.99	1.47
Hydration Enthalpy ^[7] / kJmol ⁻¹	-264	-293	-519	-1305	-1443	-2494
Melting Point ^[7] / °C	28	39	181	726	771	1285
Boiling Point ^[7] / °C	705	688	1347	1696	1385	2477
Ionic Radius according to Shannon ^[21] / Å	1.67	1.52	0.76	1.35	1.18	0.45

However, the alkali metals strongly differ from the alkaline earth metals with respect to their reaction behaviour towards O and N, respectively. Most exceptionally and counter-intuitively for elements with such low work functions (see Table 1.1)^[8, 11, 12] the chemistry of Cs and Rb towards O is versatile. Depending on the O content oxides (A₂O),^[13] peroxides (A₂O₂),^[14] hyperoxides (AO₂),^[15] mixed peroxide hyperoxides (A₄O₆)^[16] and ozonides (AO₃)^[17, 18] can be obtained on various pathways (with A = Rb, Cs). The formation of a wide range of different suboxides – compounds, which exhibit a deficiency of O in terms of formal oxidation state – is unique to Rb and Cs and will be discussed in the subsequent chapters. For Sr and Ba only the oxides and the peroxides are known as stoichiometric compounds.^[19, 20]

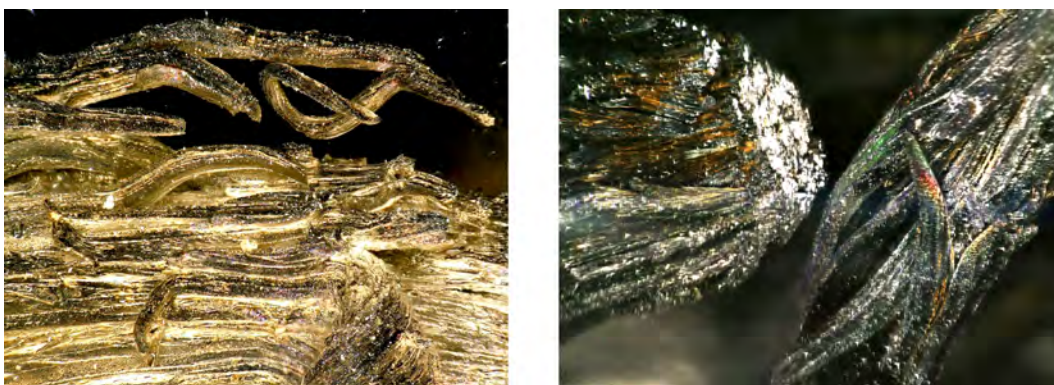


Figure 1.2: Images of elemental Sr and Ba taken through a light microscope.

Considering the reactivity towards N the behaviour of alkali and alkaline earth metals is reversed. Whereas for Cs and Rb only the binary azides are characterised,^[21] for Sr

and Ba a wider range of compounds is known: the diazenides EAN_2 ,^[22] the trinitride Sr_4N_3 ^[23] or the subnitrides EA_2N ^[24] and Ba_3N ^[11] ($EA = Ca, Sr, Ba$). The chemistry of alkaline earth metal subnitrides is of special interest within this work as it seems to show analogies to the one of alkali metal suboxides.

Due to their high reactivity, applications of the heavy alkali and alkaline earth metals are rare. As electrons in Cs suboxides can be excited by IR radiation, they were used in night vision devices until a few years ago. The isotope ^{137}Cs became known to a broader audience after the nuclear accidents in Tschernobyl and Fukushima. Isotopes of Rb and Cs are also used in atomic clocks. Due to their high reactivity and their low gas pressure, Sr and Ba are preferentially used in electrode tubes as getter material. The spectroscopic properties of all four elements, Cs, Rb, Ba and Sr, discovered in the 19th century are still used widely in pyrotechnics.

1.2 Polar metal bonding – Definitions and state of the art

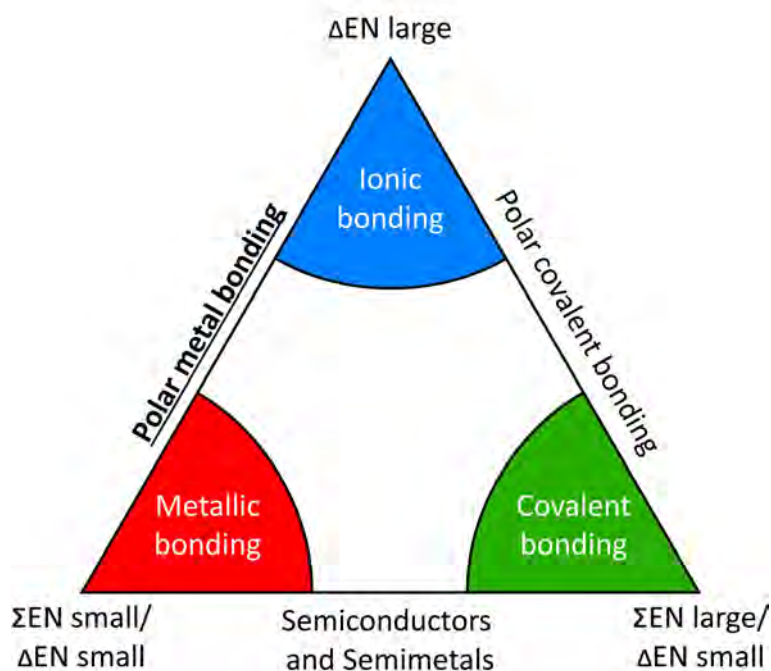


Figure 1.3: van-Arkel-Ketelaar triangle representing the three main chemical bonding types on its vertices.

Figure 1.3 shows an overview of the three main bonding types in chemistry – ionic, metallic, covalent – known as van-Arkel-Ketelaar triangle.^[26,27] It has to be emphasised that the van-Arkel-Ketelaar triangle can only give a conceptual, qualitative idea and by no means aims to quantify chemical bonding within this work. The triangle's edges represent mixtures of the basic bonding types. Mixtures between ionic/covalent (polar

covalent molecules like HCl, CH₄ or H₂O) and metallic/covalent (semiconductors and semimetals like Si, GaAs or AlP) are well-documented in text-book literature, but the transition from metallic to ionic bonding, the polar metallic bonding, is not quite well-defined and often difficult to describe.

Within this work polar metals are understood as compounds whose bonding characteristics represent a mixture of ionic and metallic bonding, in analogy to a polar covalent bonding. In the following section an overview over the main types of intermetallic phases is given within the picture of the van-Arkel-Ketelaar triangle.

Most intermetallic phases are located in the red area of the van-Arkel-Ketelaar triangle (see Figure 1.3), where bonding is predominantly metallic. Well-known examples are the Frank-Kasper phases (e.g. Nb₃Sn, Cr₃Si),^[28,29] Laves phases (e.g. MgCu₂, MgZn₂, MgNi₂)^[30-32] or Hume-Rothery phases (e.g. Cu₅Zn₈, Fe₅Zn₂₁).^[33,34] Their crystal structures can be rationalised with different concepts, evaluating parameters such as packing densities, radius quotients or valence electron concentration. Their typical properties are the consequence of their band structures calculated on the base of the quantum chemical concept of nearly free electrons (NfE).

The green area in Figure 1.3 represents the location of ionic compounds including the Zintl phases. Although Zintl phases are attributed to the intermetallic phases their bonding characteristics are described with the Zintl-Klemm-Busmann concept, applying ionic concepts for an extensive rationalisation of the observed structures.^[35] Classical Zintl phases range from simple compounds (CsSi, K₃Sb, CaGe₂)^[36-38] and more complex compounds (Cs₈Sn₄₄, Ba₅Si₃),^[39,40] to double salts (Cs₁₀[Si₃O₉][Si₄], Cs₁₀[Si₃O₉][Ge₄], Rb₁₄[Si₆O₁₇][Si₄]).^[41] As the Zintl-Klemm-Busmann concept suggests, classical Zintl compounds exhibit macroscopic properties typical for ionic compounds, e.g. a significant band gap, optical transparency, various colours, diamagnetism and solubility in polar solvents. Non-classical Zintl phases, e.g. NaTl,^[42] Li₂₁Si₅^[43] or Li₁₂Si₇,^[44] can conceptionally still be rationalised by ionic concepts, such as the (8-N)-rule. Metallic behaviour in NaTl shows its non-classical character. For Li₂₁Si₅ description becomes rather complicated and from quantum chemical calculations two different types of cluster units result. In the case of Li₁₂Si₇ electron distribution according to the Zintl-Klemm-Busmann concept becomes even more random and the formation of polyanions and cage orbitals emphasise the non-traditional character of Li₁₂Si₇.^[45]

The by far largest part of intermetallic compounds can be attributed to one of the two major attractors in the transition region between metallic and ionic bonding: either the red or the green region in Figure 1.3. The Zintl-Klemm-Busmann concept and the NfE-concept are obviously not sufficient to fully describe the mixture of ionic and metallic bonding. Hoch *et al.* introduced the term 'polar metallic bonding' for the region in between the two attractors,^[46-48] and two different suggestions to synthesise polar metals are provided.

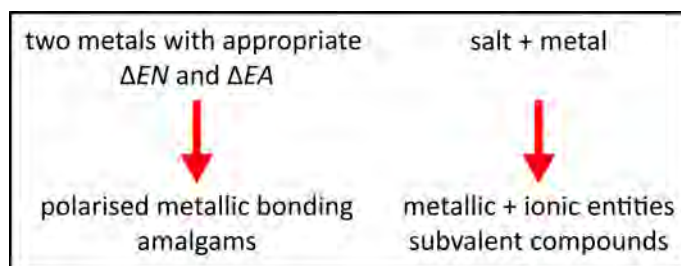


Figure 1.4: The two different synthetic approaches to access polar metals.

The first approach is the synthesis of polar metals from two metallic reactants. The reactants must have a high difference in electronegativity and in addition one of those reactants must have a negative electron affinity in order to achieve partial electron transfer (see Figure 1.4, left). Typical examples are Hg-rich amalgams, e.g. $\text{Na}_{11}\text{Hg}_{52}$,^[46] KHg_6 ,^[48] LiHg_3 ^[49] or $\text{Cs}_2\text{Hg}_{27}$.^[50] The second approach towards polar metals is the synthesis of subvalent compounds which is the main research topic of this work (see Figure 1.4, right). In these compounds anions imply local predominantly ionic bonding and are embedded in a metallic matrix. In the following sections the term 'subvalency' will be defined in more detail within a short literature overview.

1.2.1 The concept of subvalency: First examples and demarcation to related substance classes

As mentioned in the previous chapter, alkali and alkaline earth metals readily react with O/N to form subvalent compounds, respectively, if reaction conditions are chosen appropriately.

The term 'subvalent' emphasises the occurrence of lower formal oxidation states of the metal atoms than commonly found in ionic compounds. They can be described with either fractional oxidation numbers, e.g. $\text{Cs}_{11}\text{O}_3 \equiv 11 \cdot \text{Cs}^{6/11+} + 3 \cdot \text{O}^{2-}$, or by formal use of free electrons, e.g. $\text{Cs}_{11}\text{O}_3 \equiv 11 \cdot \text{Cs}^+ + 3 \cdot \text{O}^{2-} + 5 \cdot e^-$, highlighting the metallic character of subvalent compounds.^[51] Typically, subvalent compounds have a precise stoichiometry (with Cs_{3+x}O representing an exception). They form quasi-molecular cluster entities, which are embedded in a matrix of metal atoms. Within those entities strong ionic interactions are predominant, whereas in between the clusters metallic bonding characteristics prevail, wherefrom the term 'metals with holes' originates.^[11]

Considering subvalent compounds from a structural rather than a bonding point of view one can also use the term 'chemical twin'. Similar to double salts, wherein at least two different anionic or cationic species coexist, at least two structurally independent, chemically different subunits exist in subvalent compounds. In the case of subvalent compounds, one entity is anionic and the other one is metallic, so subvalent compounds will be described as ordered composite structures of salt and metal throughout this work.

Table 1.2 shows an overview of substance classes closely related to subvalent compounds together with demarcation criteria. Historically, some of the Ti oxides were first described as suboxides as they exhibit 'lower than usual' oxidation states and O-centred polyhedra

in ordered crystal structures.^[52–54] However, their structures can not be subdivided into individual, quasi-molecular cluster entities, and are more suitably counted amongst the class of interstitial compounds.

Two further compound classes are the Magnéli phases (or 'Bronzes') and $[M_6X_8]$ -/ $[M_6X_{12}]$ -cluster phases. Magnéli phases represent shear structures in between ReO_3 and NaCl structure types and are oxides of transition metals (mainly Ti, V, Mo and W), occurring in mixed oxidation states.^[55] They have more or less pronounced metallic character and show unusually high electrical conductivity for oxides. The occurring M -centred $[MO_6]$ octahedra are in strong contrast to $[OM_6]$ octahedra in suboxides. $[M_6X_8]$ -/ $[M_6X_{12}]$ -cluster phases, e.g. PbMo_6S_8 ,^[56] also show metallic behaviour in spite of structural ionic subunits. However, the formal oxidation state of Mo is +II, which rules out subvalency.

Also, non-classical Zintl-phases, e.g. NaTl ,^[42] have to be considered. Although they match the first two criteria for subvalent compounds exhibited in Table 1.2, their structures can be elucidated with ionic concepts leading to 'normal' oxidation states. The same holds for Zintl-analogous oxides, e.g. the metallic Ca_3PbO , which can be written as $\text{Ca}_3\text{PbO} \equiv 3 \cdot \text{Ca}^{2+} + \text{Pb}^{4-} + \text{O}^{2-}$.^[57] Here we have double salts rather than chemical twins in the abovementioned sense.

	molecular cluster-entities	local ionic bonding	light element centred polyhedra	ox. number \leq normal valence
Subvalent compounds	✓	✓	✓	✓
Interstitial phases	✗	✗	✓	✓
Magnéli phases and Bronzes	✓	✓	✗	✗
$[M_6X_8]$ -/ $[M_6X_{12}]$ cluster phases	✓	✓	✓ / ✗ ¹	✗
non-classical Zintl phases	✓	✓	✗	✗

Table 1.2: Criteria for the demarcation of subvalent compounds to related phases. ¹Phases with $[M_6]$ octahedra and phases with interstitial atoms occur.

1.2.2 Suboxides of the heavy alkali metals

First reports about suboxides of the heavy alkali metals origin from thermoanalytic investigations at the beginning of the 20th century.^[58] In 1956 the first Cs suboxide, Cs_3O , was characterised crystallographically,^[59] whereas systematic characterisation of further suboxides did not start before the 1970s. As mentioned in the previous section, synthetic approaches for subvalent compounds involve unusually low reaction temperatures for solid state chemistry due to their thermal instability, in the case of suboxides between –120 and 150 °C. Higher temperatures lead to decomposition of the suboxides resulting in ionic compounds (e.g. oxides) and the respective metal. Suboxides fulfil all criteria listed in Table 1.2. They show good electric conductance due to the metallic matrix in which the ionic compartments are embedded. The ionic entities consist of oligomers of face-sharing $[A_6O]$ octahedra. Intercalation of alkali metal atoms between those structural entities emphasises the picture of a chemical twin.

Ionic oligomers occur in two different structural motifs: For Rb suboxides two O-centred octahedra compose doublets with composition $[\text{Rb}_9\text{O}_2]$,^[60] for Cs suboxides triplets with composition $[\text{Cs}_{11}\text{O}_3]$ are formed (see Figure 1.5).^[51] Via insertion of additional Cs or Rb atoms in between the cluster entities a great variety of compounds in addition to the 'parent compounds' Rb_9O_2 and Cs_{11}O_3 was synthesised (e.g. Rb_6O , Cs_4O , Cs_7O , $(\text{Rb}_x\text{Cs}_{1-x})_{11}\text{O}_3$ (with $x = 0.07$ to 0.39), $\text{RbCs}_{11}\text{O}_3$, $\text{Rb}_7\text{Cs}_{11}\text{O}_3$).^[61–66] It is important to note that if Cs and Rb coexist in one compound, Cs always builds up the cluster compartments, whereas additional Rb atoms participate only in the metallic matrix. Insertion of further purely metallic bound alkali metal atoms leads to structural variety. The number of all possible configurations of clusters and metal atoms leading to stable crystalline phases seems to be limited by geometric aspects of packing. The only alkali metal suboxide with a slightly different structural motif is Cs_{3+x}O . Here the condensation degree is increased and $[\text{Cs}_6\text{O}]$ octahedra are connected to infinite one-dimensional chains along the c axis, resulting in an anti- ZrCl_3 -type structure.^[67] Figure 1.5 gives an overview over the different building blocks of suboxides and the resulting structures.

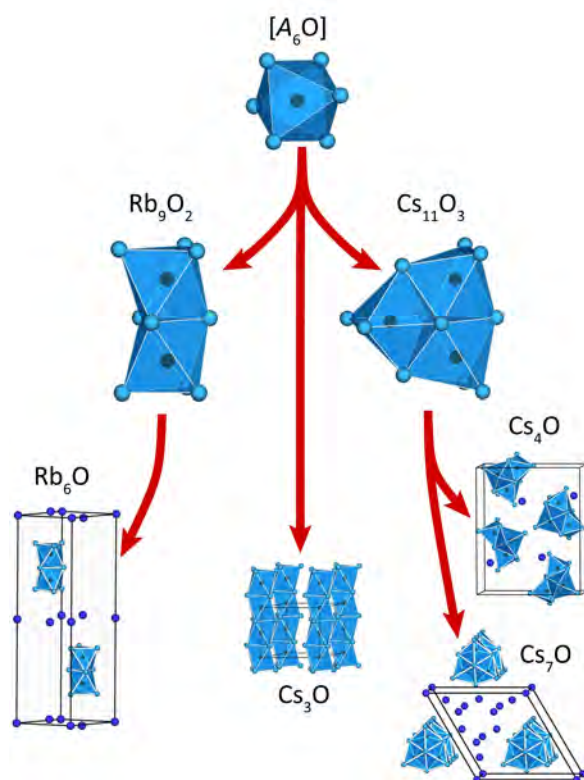


Figure 1.5: Structural entities in the suboxides of the heavy alkali metals and resulting crystal structures. A = Rb, Cs: blue spheres; O: black spheres.

The interplay of two different bonding types in one compound is confirmed by significantly different A – A distances for intercluster and intracluster contacts. Atomic radii for A^0 are about 25 % larger than respective ionic radii of A^+ . As intercluster contacts are mainly of metallic character these distances are enlarged with respect to intracluster contacts. Experimental evidence for this is given by X-ray diffractometry. For A

atoms exhibiting a metallic bonding environment anisotropic displacement parameters appear magnified significantly indicating occupation of the s orbitals. Raman spectroscopy showed the existence of the clusters in the liquid phase corroborating that the cluster concept does not only serve as a topological tool, but that the clusters can be regarded as true chemical entities.

Intracuster bonding in alkali metal suboxides is mainly ionic. The bonding between the cluster entities is dominated by the metallic surface of the cluster and the optionally intercalated metallic atoms. This leads to an overall metallic behaviour of alkali metal suboxides. They show high electric conductivity, metallic luster and very low melting points. Due to their especially low work functions, their reactivity exceeds the one of the elemental alkali metals, leading e.g. to extremely high sensitivity towards air and moisture.^[11]

1.2.3 Subnitrides of the heavy alkaline earth metals

In the 1990s synthesis of subnitrides of the heavy alkaline earth metals was reported. The binary subnitrides Ca_2N , Sr_2N and Ba_2N ^[24] can easily be synthesised from N_2 and the metals at temperatures slightly above their respective melting points ($\sim 830^\circ\text{C}$), the highest reaction temperatures known for synthesis of subvalent compounds. The binary subnitrides crystallise isotypically in the anti- CdCl_2 structure type, wherein $[\text{EA}_6\text{N}]$ octahedra ($\text{EA} = \text{Ca}, \text{Sr}, \text{Ba}$) connect via common edges to infinite sheets (see Figure 1.6, left).

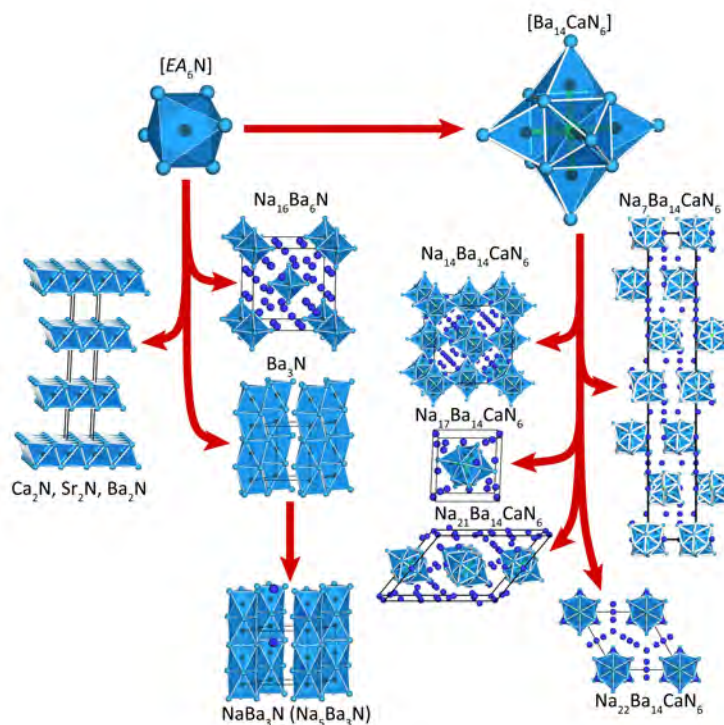


Figure 1.6: Structural entities in the subnitrides of the heavy alkali metals and resulting crystal structures. $\text{EA} = \text{Ca}, \text{Sr}, \text{Ba}$: blue spheres; N : black spheres, centering the blue polyhedra.

All other subnitrides were synthesised at considerably lower temperatures. To achieve reaction conversion at such low temperatures it was often required to add elemental Na as flux agent. With continuous addition of Na, the melting point of the Ba/Na mixture compared to elemental Ba is reduced significantly, and reactivity at low temperatures is increased (see Figure 1.7, right). Incorporation of Na into the products can not always be excluded and is also intended, as the formation of the ternary compounds $\text{Na}_{16}\text{Ba}_6\text{N}$,^[68] NaBa_3N ^[69] and $\text{Na}_5\text{Ba}_3\text{N}$ ^[70] exhibits. By careful thermal treatment of NaBa_3N in vacuo the binary compound Ba_3N could also be obtained.^[11] The dominating motif in all structures are $[\text{Ba}_6\text{N}]$ octahedra with different patterns of condensation. They are embedded in a metallic matrix of Ba and/or Na atoms and thus again corroborate the picture of a chemical twin. The metallic matrix can be varied by insertion of different amounts of Na atoms. As for the suboxides, formation of stable crystalline phases seems to be restricted by geometric aspects of packing. The flexibility of these geometric restrictions is apparently even higher here, as the insertion of various Na amounts and the resulting adjustments of the crystal structure show. However, insertion of larger alkali metal atoms such as K, Rb and Cs has not been observed so far, probably due to their immiscibility with Ba (see phase diagrams K–Ba, Rb–Ba and Cs–Ba).^[71] Exceptions are the binary compounds $E\text{A}_2\text{N}$ and Ba_3N , which are the only subnitrides without intercalated Na. Ba_3N crystallises isotypically to Cs_3O in the anti- ZrCl_3 structure type (see previous section). An overview of the structures of binary and ternary subnitrides is given in Figure 1.6, left.

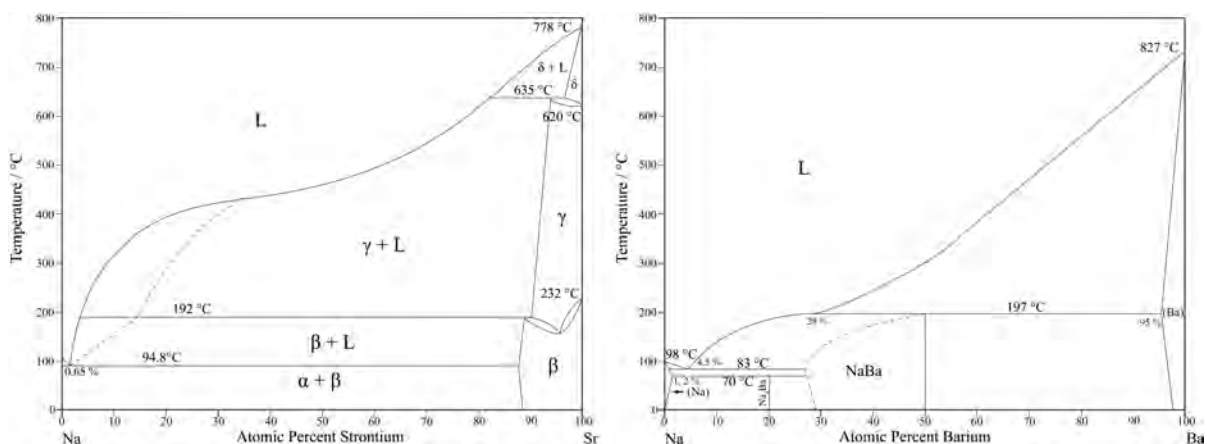


Figure 1.7: Binary phase diagrams of Sr–Na and Ba–Na.^[63]

In contrast to the unobserved insertion of alkali metal atoms other than Na, some quaternary phases with additional Ca atoms have been synthesised. Again, N-centred octahedra are the basic structural motifs but now each N atom is coordinated by one Ca and five Ba atoms. Six of the resulting $[\text{Ba}_5\text{CaN}]$ octahedra connect via sharing faces to stellated clusters with composition $[\text{Ba}_{14}\text{CaN}_6]$ (see Figure 1.6, top right). Here the concept of a 'chemical twin' is corroborated by the observation of variable numbers of inserted Na atoms leading to the formations of $\text{Na}_7\text{Ba}_{14}\text{CaN}_6$,^[72] $\text{Na}_{14}\text{Ba}_{14}\text{CaN}_6$,^[73] $\text{Na}_{17}\text{Ba}_{14}\text{CaN}_6$, $\text{Na}_{21}\text{Ba}_{14}\text{CaN}_6$, and $\text{Na}_{22}\text{Ba}_{14}\text{CaN}_6$.^[74] The structures of quaternary subnitrides are summarised in Figure 1.6, right. Alternatively, one could argue these compounds could rather be addressed as the first subnitridometalates with the complex anion $[\text{CaN}_6]^{16-}$

coordinated by 14 Ba atoms. However, this is a rather formal consideration as an isolated octahedral 'nitridocalcate' anion neither exists in literature nor does it seem to be possible to substitute Ca^{2+} with other cations.

1.3 Expansion of the substance class by introducing complex anions – motivation and synthetic approaches

This work is based on two main synthetic approaches: 1. Synthesis of subvalent compounds containing complex tetrahedral anions with O as the negatively charged species: oxometalate anions, $[\text{MO}_4]^{n-}$. 2. Synthesis of subvalent compounds with complex nitridometalate anions, $[\text{MN}_4]^{n-}$. The first approach builds upon the synthetic procedure used for suboxides. Rb and Cs atoms compose both the cationic and metallic part with complex $[\text{MO}_4]^{n-}$ oxometalate counterions. First examples of this family called 'suboxometalates' were synthesised starting from 2009 by Hoch *et al.*^[75–78]

The second approach uses a reaction pathway similar to the synthesis of subnitrides. Akin to suboxometalates, Sr and Ba (and Na, if used as flux agent) compose both the cationic and metallic parts. Complex tetrahedral nitridometalate anions $[\text{MN}_4]^{n-}$ serve as counterions. Thus, the targeted compounds can be described as subnitridometalates.

Combining the two aforementioned synthetic routes with higher reaction temperatures, compounds with 'normal' ionic bonding characteristics, both oxidic and nitridic, can be obtained. Also thermal decomposition of suboxides leads to metal-rich, ionic metalates, hitherto shown for some exemplary oxometalates.

1.3.1 Suboxometalates

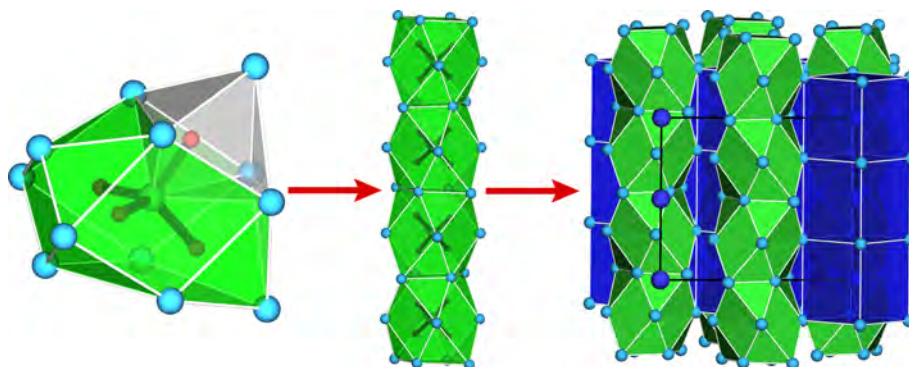


Figure 1.8: Hierarchical organisation of the structure of Cs_9MO_4 . Cs_{ionic} : light blue spheres, $\text{Cs}_{\text{metallic}}$: dark blue spheres, $M^{+\text{III}}$: white, O: red.

In 2009 the first suboxometalates with composition Cs_9MO_4 ($M^{+\text{III}} = \text{Al, Ga, In, Sc, Fe}$) were published.^[75,76] They crystallise isotypically in a unique tetragonal structure type. Synthesis relies on the reaction between elemental Cs, Cs_2O and the respective trivalent metal oxide. Cs and Cs_2O in the correct amounts instantly form a liquid sub-

oxide mixture of dark violet colour. This mixture is highly reactive due to extremely low work functions (e.g. 1.4 eV for Cs_{11}O_3)^[11] and thus offers sufficiently low reaction temperatures for the formation of suboxometalates ($T < 300\text{ }^\circ\text{C}$). The structure of Cs_9MO_4 consists of tetrahedral $[\text{MO}_4]^{5-}$ anions embedded in a metallic substructure. The anions are coordinated by 12 Cs atoms in distorted cuboctahedra, which connect via sharing faces to infinite columns with composition $[\text{Cs}_8\text{MO}_4]$ along the crystallographic c axis of the tetragonal structure. Those one-dimensional cluster entities show ionic bonding in the inside, but metallic bonding on the surface, corroborated by theoretical calculations.^[77] In between the columns one additional Cs atom solely coordinated by other Cs atoms is inserted, leading to the overall sum formula Cs_9MO_4 . Cs–Cs distances within the columnar entities correlate to data for ionic Cs compounds,^[13] whereas Cs–Cs distances between the columns agree with values for Cs metal.^[79] These different Cs–Cs distances, as well as conductivity measurements, theoretical calculations^[77] and Mössbauer spectroscopy^[78] confirm the existence of a chemical twin. The structure is shown in Figure 1.8.

Mixed crystals with Rb also were synthesised, and in analogy to the alkali metal suboxides Rb atoms only substitute Cs on the metallic site.^[76] An incorporation of Rb in the ionic substructure seems to be impossible.

1.3.2 Subnitridometalates

Subnitrides of the heavy alkaline earth metals were synthesised in analogy to the suboxides. Thus, an obvious next step would be the synthesis of subnitridometalates of the heavy alkaline earth metals similar to the suboxometalates depicted in section 1.3.1. Comparing the melting points of Cs ($\sim 28\text{ }^\circ\text{C}$) and Sr/Ba ($\sim 769/\sim 727\text{ }^\circ\text{C}$) it is clearly necessary to use higher reaction temperatures. As for the synthesis of subvalent compounds low reaction temperatures are essential, Na metal could be added to reduce the melting point of the reaction mixture as described in literature.^[11] Appropriate reaction temperatures for Sr–Na and Ba–Na mixtures can be estimated from the respective phase diagrams (see Figure 1.7). Incorporation of Na into the reaction products can not be excluded and might even be auspicious.

To increase reactivity, a mixture of Ba and Ba_2N (Sr and Sr_2N) akin to the Cs/ Cs_2O mixture for suboxometalates is used. A possible pre-formation of subnitridic compounds leads to a reduced work functions and high reactivity.

1.3.3 Ionic phases with complex anions

The ionic substructures of suboxo- and subnitridometalates consist of complex anions. To evaluate these complex anions it is useful to compare them with the respective oxo-/nitridometalate anions (most suitably the *ortho*-oxo-/nitridometalate anion) in ionic compounds in terms of bond length, bond angles and coordination spheres. These ionic compounds can occur as side phases, may be taken from literature or can be synthesised on different ways. Some of them do not only serve as appropriate 'reference materials', but sometimes also exhibit new structural features. For oxidic compounds the oxometalates $\text{Cs}_6\text{In}_2\text{O}_6$,^[80] $\text{Cs}_6\text{Al}_2\text{O}_6$ ^[81] and $\text{Cs}_9[\text{FeO}_4]_2$ are known.^[82] Along with the syntheses

of the first suboxometalates Cs_9MO_4 ($M = \text{Al}, \text{Ga}, \text{In}, \text{Sc}, \text{Fe}$) the compound class of ionic metal-rich oxometalates could be extended by the compounds Cs_4FeO_3 ^[83] and $\text{Cs}_8\text{In}_2\text{O}_7$.^[84] During the synthetic work towards subnitridometalates within this work new ionic compounds could also be synthesised and characterised.

It should thus be shown that research on novel phases with polar metal bonding in the sense of a chemical twin of metal and salt can also enlarge the structural chemistry of ionic metalates.

1.3.4 Organisation of this work

To clarify the organisation of this work, this section gives a short overview of the following Chapters. Chapter 2 gives a brief description of all experimental and analytical methods applied within this dissertation.

Chapters 3, 4, 5 and 6 present peer-reviewed publications and are adopted from the respective journals. Chapters 3 and 4 document in detail synthetic approaches to obtain subvalent compounds, wherein new suboxometalates (Chapter 3) as well as the first subnitridometalates (Chapter 4) could be characterised. Chapter 5 reports about the X-ray diffraction analysis of single crystals of CsOH as an interesting side result. Chapter 6 depicts the investigations on an ionic nitridometalate, exhibiting an extraordinary and peculiar crystal structure.

Chapter 7 consists of the analysis of two further, up to now unpublished compounds obtained within this work, however, to finally elucidate these two structures some more experimental as well as analytical work will be required.

All results are briefly summarised in Chapter 8, a short outlook is given in Chapter 9, on how further synthetic and characterisation approaches related to this work can be accomplished in the future.

1.4 References

- [1] G. Kirchhoff, R. Bunsen, *Ann. Phys.* **1861**, 7, 337–381.
- [2] C. Setterberg, *Justus Liebigs Ann. Chem.* **1881**, 211, 100–116.
- [3] R. Suhrmann, K. Clusius, *Z. Anorg. Allg. Chem.* **1926**, 152, 52–58.
- [4] L. Hackspill, *Helv. Chim. Acta* **1928**, 11, 1003–1026.
- [5] H. Davy, *Philos. T. Roy. Soc.*, **1908**, A98, 333–370.
- [6] Philip S. Danner, *J. Am. Chem. Soc.* **1924**, 46, 2382–2385.
- [7] E. Riedel, C. Janiak, *Anorganische Chemie*, de Gruyter GmbH, Berlin, Germany **2007**, 7, 596–626.
- [8] H. Ibach, H. Lüth, *Festkörperphysik*, Springer-Verlag, Heidelberg, Germany **2009**, 7, 155.
- [9] A. L. Allred, E. G. Rochow, *J. Inorg. Nucl. Chem.* **1958**, 5, 264–268.
- [10] R. D. Shannon, *Acta Crystallogr.* **1976**, A32, 751–767.
- [11] A. Simon, *Coord. Chem. Rev.* **1997**, 163, 253–270.
- [12] D. R. Lide, *CRC Handbook of Chemistry and Physics*, CRC Press, Boca Raton, Florida, US **2008**, 89, 12–114.
- [13] A. Helms, W. Klemm, *Z. Anorg. Allg. Chem.* **1939**, 242, 33–40.
- [14] H. Foepl, *Z. Anorg. Allg. Chem.* **1957**, 291, 12–50.
- [15] A. Helms, *Z. Anorg. Allg. Chem.* **1939**, 241, 97.
- [16] A. Helms, W. Klemm, *Z. Anorg. Allg. Chem.* **1939**, 242, 201–214.
- [17] W. Schnick, M. Jansen, *Angew. Chem. Int. Ed. Engl.* **1985**, 24, 54–55; *Angew. Chem.* **1985**, 97, 48–49.
- [18] W. Assenmacher, M. Jansen, *Z. Kristallogr.* **1991**, 194, 315–318.
- [19] W. Gerlach, *Z. Phys.* **1922**, 9, 184–192.
- [20] J. D. Bernal, E. Djaltova, P. Kasarnowsky, S. Reichstein, A. G. Ward, *Z. Kristallogr. Krist.* **1935**, 92, 344–354 .
- [21] J. A. Joebstl, H. J. Müller, *Z. Kristallogr.* **1965**, 121, 385–391.
- [22] S. B. Schneider, R. Frankovsky, W. Schnick, *Inorg. Chem.* **2012**, 428, 2366–2373.
- [23] Y. Prots, G. Auffermann, M. Tovar, R. Kniep, *Angew. Chem. Int. Ed.* **2002**, 41, 2288–2290; *Angew. Chem.* **2002**, 114, 2392–2394.
- [24] O. Reckeweg, F. J. DiSalvo, *Solid State Sci.* **2002**, 4, 575–884.

- [25] U. Steinbrenner, A. Simon, *Z. Anorg. Allg. Chem.* **1997**, *624*, 228–232.
- [26] A. E. van Arkel, *Molecules and Crystals in: Inorganic Chemistry*, Butterworth, London, UK, **1949**.
- [27] J. A. A. Ketelaar, *Chemical constitution*, Elsevier, Amsterdam, Netherlands, **1958**.
- [28] S. Geller, M. T. Matthias, R. Goldstein, *J. Am. Chem. Soc.* **1955**, *77*, 1502–1504.
- [29] B. Boren, *Ark. Kemi Mineral. Geol.* **1933**, *A11*, 1–28.
- [30] J. B. Friauf, *J. Am. Chem. Soc.* **1929**, *49*, 3107–3114.
- [31] J. B. Friauf, *Phys. Rev.* **1927**, *29*, 34–40.
- [32] H. Witte, F. Laves, *Metallwirtsch., Metallwiss., Metalltechn.* **1935**, *14*, 645–649.
- [33] J. K. Brandon, R. Y. Brizard, P. C. Chieh, R. K. McMillan, W. B. Pearson, *Acta Crystallogr.* **1974**, *30*, 1412–1417.
- [34] G. F. Bastin, F. J. J. van Loo, G. D. Rieck, *Z. Metallk.* **1974**, *65*, 656–660.
- [35] H. Schäfer, B. Eisenmann, W. Müller, *Angew. Chem. Int. Ed. Engl.* **1973**, *12*, 694–712; *Angew. Chem.* **1973**, *85*, 742–760.
- [36] R. Schäfer, W. Klemm, *Z. Anorg. Allg. Chem.* **1961**, *312*, 214–220.
- [37] G. Brauer, E. Zintl, *Z. Phys. Chem.* **1937**, *B37*, 323–352.
- [38] H. J. Wallbaum, *Naturwissenschaften* **1944**, *32*, 76.
- [39] H. G. von Schnering, R. Kroener, M. Baitinger, K. Peters, R. Nesper, Y. Grin, *Z. Kristallogr. – NCS* **2000**, *215*, 205–206.
- [40] K. H. Janzon, H. Schäfer, A. Weiss, *Z. Naturforsch.* **1966**, *B21*, 287–289.
- [41] S. Hoffmann, T. F. Fässler, C. Hoch, C. Röhr, *Angew. Chem. Int. Ed.* **2001**, *40*, 4398–4400; *Angew. Chem.* **2001**, *113*, 4527–4529.
- [42] W. Dullenkopf, E. Zintl, *Z. Phys. Chem.* **1932**, *B16*, 195–205.
- [43] R. Nesper, H. G. von Schnering, *J. Solid State Chem.* **1987**, *70*, 48–57.
- [44] H. G. von Schnering, R. Nesper, J. Curda, K. F. Tebbe, *Angew. Chem. Int. Ed. Engl.* **1980**, *19*, 1033–1034; *Angew. Chem.* **1980**, *12*, 1070.
- [45] S. M. Kauzlarich, *Chemistry, Structure, and Bonding of Zintl Phases and Ions*, VCH Publishers Inc., New York, New York, US, **1996**.
- [46] C. Hoch, A. Simon, *Angew. Chem. Int. Ed.* **2012**, *51*, 3262–3265; *Angew. Chem.* **2012**, *124*, 3316–3319.
- [47] F. Tambornino, J. Sappl, F. Pultar, T. M. Cong, S. Hübner, T. Gifftthaler, C. Hoch, *Inorg. Chem.* **2016**, *55*, 11551–11559.
- [48] F. Tambornino, C. Hoch, *J. Alloys Compd.* **2015**, *618*, 299–304.

- [49] F. Tambornino, Doctoral Thesis, Ludwig-Maximilians-Universität, München **2016**.
- [50] C. Hoch, A. Simon, *Z. Anorg. Allg. Chem.* **2008**, *634*, 853–856.
- [51] A. Simon, E. Westerbeck, *Z. Anorg. Allg. Chem.* **1977**, *428*, 187–198.
- [52] I. Kornilov, V. V. Vavilova, L. E. Fykin, R. P. Ozerov, S. P. Solovev, V. P. Smirnov, *Metallurg. Trans.* **1970**, *1*, 2569–2571.
- [53] B. Holmberg, *Acta Chem. Scand.* **1962**, *16*, 1245–1250.
- [54] S. Yamaguchi, M. Koiwa, M. Hirabayashi, *J. Phys. Chem. Soc. Jpn.* **1966**, *21*, 2096.
- [55] P. Hagenmuller, *Prog. Solid State Chem.* **1971**, *5*, 71–114.
- [56] R. Chevrel, M. Sergent, J. Prigent, *J. Solid State Chem.* **1971**, *3*, 515–519.
- [57] A. Widera, H. Schäfer, *Mat. Res. Bull.* **1980**, *15*, 1805–1809.
- [58] E. Rengade, *Bull. Soc. Chim.* **1909**, *5*, 994.
- [59] K. R. Tsai, P. M. Harris, E. N. Lassetre, *J. Phys. Chem.* **1956**, *60*, 345–347.
- [60] A. Simon, *Z. Anorg. Allg. Chem.* **1977**, *11*, 5–16.
- [61] A. Simon, H. J. Deiseroth, *Rev. Chim. Miner.* **1976**, *13*, 98–112.
- [62] A. Simon, H. J. Deiseroth, E. Westerbeck, B. Hillenkötter, *Z. Anorg. Allg. Chem.* **1976**, *423*, 203–211.
- [63] A. Simon, *Z. Anorg. Allg. Chem.* **1976**, *422*, 208–218.
- [64] A. Simon, H. J. Deiseroth, *Z. Anorg. Allg. Chem.* **1980**, *463*, 14–26.
- [65] H. J. Deiseroth, A. Simon, *Rev. Chim. Miner.* **1983**, *20*, 475–487.
- [66] H. J. Deiseroth, A. Simon, *Inorg. Chem.* **1978**, *17*, 875–879.
- [67] B. Swaroop, S. N. Flengas, *Can. J. Phys.* **1964**, *42*, 1886–1889.
- [68] G. J. Snyder, A. Simon, *Angew. Chem. Int. Ed. Engl.* **1994**, *33*, 689–691; *Angew. Chem.* **1994**, *106*, 713–715.
- [69] P. E. Rauch, A. Simon, *Angew. Chem. Int. Ed. Engl.* **1992**, *31*, 1519–1521; *Angew. Chem.* **1992**, *104*, 1505–1506.
- [70] G. J. Snyder, A. Simon, *J. Am. Chem. Soc.* **1995**, *117*, 1996–1999.
- [71] B. Predel, *Landolt-Börnstein, Zahlenwerte und Funktionen aus Naturwissenschaften und Technik, Neue Serie, Bd. Vb – Phasengleichgewichte, kristallographische und thermodynamische Daten binärer Legierungen, B–Ba ... C–Zr*, Springer Verlag GmbH, Heidelberg, Germany, **2005**.
- [72] G. V. Vajenine, A. Simon, *Eur. J. Inorg. Chem.* **2001**, *5*, 1189–1193.
- [73] U. Steinbrenner, A. Simon, *Angew. Chem. Int. Ed. Engl.* **1996**, *35*, 552–554; *Angew. Chem.* **1996**, *108*, 595–598.

- [74] U. Steinbrenner, A. Simon, *J. Chem. Soc. Faraday T.* **1996**, *92*, 2117–2123.
- [75] C. Hoch, J. Bender, A. Simon, *Angew. Chem. Int. Ed.* **2009**, *48*, 2415–2417; *Angew. Chem.* **2009**, *121*, 2451–2453.
- [76] C. Hoch, J. Bender, A. Wohlfarth, A. Simon, *Z. Anorg. Allg. Chem.* **2010**, *635*, 1777–1782.
- [77] C. Hoch, A. Simon, C. Lee, M.-H. Whangbo, J. Köhler, *Z. Kristallogr.* **2011**, *226*, 553–556.
- [78] C. Hoch, I. Schellenberg, R. Pöttgen, *Z. Naturforsch.* **2011**, *B66*, 441–443.
- [79] C. S. Barrett, *Acta Crystallogr.* **1956**, *9*, 671–677.
- [80] R. Hoppe, G. Wagner, H. Glaum, *Z. Anorg. Allg. Chem.* **1987**, *547*, 188–198.
- [81] R. Hoppe, H. P. Müller, *Solid State Ionics* **1990**, *43*, 23–30.
- [82] G. Frisch, Doctoral Thesis, Albert-Ludwigs-Universität, Freiburg **2006**.
- [83] C. Hoch, *Z. Naturforsch.* **2011**, *B66*, 1248–1249.
- [84] J. Bender, A. Wohlfarth, C. Hoch, *Z. Naturforsch.* **2010**, *B65*, 1416–1426.

2 Methods

2.1 Glove box

Due to high sensitivity of reactants and products towards air and moisture, experimental work was carried out under inert gas atmosphere in an Ar-filled glove box (MBraun MB150, Garching, Germany). Highly sensitive reactants were stored in Schlenk apparatus in the glove box. Partial pressures of O₂ and H₂O were maintained below 1 ppm at all times. The circulating Ar atmosphere was continuously purified by molecular sieve X-13 and BTS catalyst.

2.2 Schlenk technique

Outside of the glove box a full-glass Schlenk-type inert gas apparatus was used in order to work under inert-gas conditions. Vacuum was generated with a rotary vane pump (Vacuubrand GmbH, Wertheim, Germany). If required a N₂-cooled condensation trap was used to protect the vacuum pump from volatile corrosives. Pressure was controlled with a VAP5 Vacuubrand pressure sensor (Vacuubrand GmbH, Wertheim, Germany) with a minimum display output of $1 \cdot 10^{-3}$ mbar. As inert gas Ar was taken from a gas cylinder (purity 4.8, Air Liquide). To remove O₂ and H₂O residues the Ar gas was channeled over columns of silica gel (VWR), molecular sieve (VWR, purum, pore size = 4 Å), KOH (VWR, purum), phosphorus pentoxide (Roth) and heated titanium sponge (operating temperature ~ 760 °C). N₂ (purity 5.0, Air Liquide) was used as reaction gas for educt synthesis. To remove O₂ and H₂O impurities the N₂ gas was channeled over columns of silica gel (VWR), molecular sieve (VWR, purum, pore size = 4 Å), KOH (VWR, purum), phosphorus pentoxide (Roth) and heated BTS catalyst (operating temperature ~ 160 °C).

2.3 Crucible materials

Choice of suitable crucible material was essential in the case of synthetic approaches to subnitridometalates, as all crucible materials took part in the reactions. Glassy carbon, W, Ta, Nb and *h*-BN were used as crucible materials. In case of the former two materials compounds known in literature formed.^[1,2] For the latter three crucible materials new compounds could be synthesised after some synthesis optimisation. Crucibles of *h*-BN were cleaned with boiling ethanol (dried over mole sieve, VWR, purum, pore size: 4 Å) for 1 day to remove boric acid and subsequently dried in vacuo at 300 °C. Nb and Ta crucibles were cleaned with a mixture of concentrated H₂SO₄, concentrated HNO₃ and

HF (40 %) in the ratio 3/1/1 and subsequently dried at 100 °C in a drying oven.

2.4 Light microscopy

For imaging of pure metal samples (see Chapter 1) a Keyence VHX-5000 (Keyence Corporation, Osaka, Japan) was used. For isolation of single crystals a Leica MZ6 light microscope (Leica Camera AG, Wetzlar, Germany) was used.

2.5 Powder X-ray diffractometry

Powder X-ray diffraction (PXRD) was carried out on STOE & Cie. Stadi P diffractometers in parafocussing Debye-Scherrer geometry with either Mo-K $_{\alpha 1}$ ($\lambda = 0.7093 \text{ \AA}$) or Cu-K $_{\alpha 1}$ ($\lambda = 1.5406 \text{ \AA}$) radiation monochromatised with a curved Ge(111) single crystal (STOE & Cie. GmbH, Darmstadt, Germany). Intensity data were collected with a Dectris Mythen 1K Si strip detector. Measured data were evaluated with the software WinXPOW (Stoe & Cie.).^[3] Due to high sensitivity towards air and moisture all samples were sealed in glass capillaries (Hilgenberg GmbH, Malsfeld, Germany, diameter = 0.3 mm). Dried diamond powder was added to control absorption and for preparation of ductile samples. For further analysis of PXRD data the software TOPAS Academic V4.1 was used.^[4,5] Structural models were fitted to the data using the least-squares method of Rietveld.^[6] To describe the peak profiles the fundamental parameters approach was applied and for background fitting a shifted Chebyshev function was used.^[7,8] High-temperature powder X-ray diffraction (HTXRD) experiments were conducted on a STOE & Cie. Stadi P diffractometer with Mo-K $_{\alpha 1}$ ($\lambda = 0.71073 \text{ \AA}$) radiation (monochromatised with a curved Ge(111) single crystal). Intensity data were collected with a fixed-stage imaging plate detector (STOE & Cie.). Structure visualisation was performed with the programme Diamond.^[9] For data comparison International Centre of Diffraction Data (ICSD), ICDD database and Pearson's Crystal Data database were used.^[10-12]

2.6 Single crystal X-ray diffractometry

Due to high sensitivity towards air and moisture all samples were stored under paraffin oil. Beforehand the paraffin oil was degassed and dried with small K pieces. Adequate single crystals were isolated using a Leica MZ6 microscope. The crystals were transferred into glass capillaries (Hilgenberg, Malsfeld, Germany, diameter = 0.2 mm) filled with dry paraffin oil and fixated with a glass fibre. For data collection three diffractometers were used: two STOE IPDS-1 (STOE & Cie. GmbH, Darmstadt, Germany) with Mo-K $_{\alpha}$ ($\lambda = 0.71073 \text{ \AA}$) or Ag-K $_{\alpha}$ ($\lambda = 0.56087 \text{ \AA}$) radiation and imaging plate detector and a Bruker D8-Quest (Bruker Corporation, Billerica, Madison, US) with Mo-K $_{\alpha}$ ($\lambda = 0.71073 \text{ \AA}$) radiation and Goebel mirror optics with a CCD detection system. For IPDS-1 data cell determination, integration and data reduction was performed with the programme X-Area.^[13] For D8-Quest data cell determination, integration, data reduction and semi-empirical absorption correction (SADABS) was performed with the programme

APEX2.^[14] Measurements were conducted by Mr. Philipp Bielec, Dr. Constantin Hoch, Mr. Thomas Miller, Ms. Ursula Pachmayr and Mr. Frank Tambornino.

Determination of space group was evaluated directly from systematic absence conditions and evaluation of the E value statistics. Structure solution was carried out with SHELXS-97 using direct methods, structure refinement with SHELXL-97 using full-matrix least-squares refinement.^[15] The programme PLATON was used for plotting electron density maps, symmetry check, semi-empirical or analytic absorption corrections, the structure tidy tool and calculation of packing density.^[17] Structure visualisation was performed with the programme Diamond.^[9]

2.7 Scanning electron microscopy (SEM)

SEM was conducted on two different microscopes, a JEOL JSM-6500F (JEOL Ltd., Akishima, Japan) and an FEI Dualbeam Helios Nanolab G3 UC (FEI Company, Hillsboro, Oregon, US). Energy-dispersive X-ray spectroscopy (EDX) was performed to determine elemental composition of the materials using the respective detectors, an X-ray detector type 7418 (Oxford Instruments, Abingdon, U. K.) or an X-Max 80 SDD detector (Oxford Instruments, Abingdon, U. K.). Samples were placed on adhesive conducting carbon foil mounted on a metal carrier. Electrically insulating materials were sputtered with carbon to prevent static effects. Measurements were conducted by Mr. Christian Minke.

2.8 Nuclear magnetic resonance (NMR)

Solid state ^1H -NMR experiments with magic angle spinning (MAS) technique were performed with a 500 MHz Bruker DSX 500 Avance Spectrometer (Bruker Corporation, Billerica, Madison, US) operating at a magnetic field strength of 11.7 T. A rotor with 2.5 mm diameter was used for all measurements. Measurements were conducted by Mr. Christian Minke.

2.9 Raman spectroscopy

To record Raman spectra, a He-Ne laser with a 1 mm focus in a confocal Raman microscope (LabRSM HG UV/Vis, Horiba Jobin Ivon GmbH, München) combined with an Olympus BX 41 microscope (Olympus, Shinjuku, Japan) and equipped with a CCD detector was focussed on the samples. Bulk samples were generally sealed in glass capillaries. Single crystals were sealed in glass capillaries (Hilgenberg, Malsfeld, Germany, diameter = 0.2 mm) under dry paraffin oil. Measurements were conducted by Mr. Stefan Datz.

2.10 Inductively coupled plasma analysis (ICP)

Elemental analysis via ICP was performed on an ICP-OES Varian Vista RL (Varian Inc., Palo Alto, CA, US). Measurements were conducted by Ms. Jaroslava Obel.

2.11 Elemental analysis (CHNS)

Elemental analysis for C, H and N were performed with the elemental analyzer systems Vario EL and Vario Micro (Elementar Analysensysteme GmbH, Langenselbold, Germany). Measurements were conducted by Ms. Susanne Sauerer and Mr. Robert Eicher.

2.12 Band structure calculations

DFT calculations of the electronic band structure were performed with the program package WIEN2000 employing the full-potential linearised augmented plane wave (FP-LAPW) method. The exchange and correlation functional of Perdew, Burke and Ernzerhof with generalised gradient approximation (GGA) was applied.^[17,18] All band structure calculations were performed by Mr. Frank Tambornino.

2.13 Lattice energy calculations according to the MAPLE concept

Lattice energy calculations (MAPLE: Madelung part of lattice energy) were performed to prove the electrostatic consistency of crystal structures. Exclusively electrostatic interactions in an ionic crystal were taken into account, depending on the charge, interatomic distances, coordination spheres and ionic radii (according to Shannon)^[19] of the constituting ions. Effective coordination numbers were calculated with the CHARDI concept.^[20-23]

2.14 References

- [1] O. Seeger, M. Hofmann, J. Z. Straehle, *Z. Anorg. Allg. Chem.* **1994**, 620, 2008–2013.
- [2] U. Berger, W. Schnick, *J. Alloy Compd.* **1994**, 206, 179–184.
- [3] STOE & Cie. GmbH, WinXPOW Version 2.09, **2007**.
- [4] A. A. Coelho, J. Evans, I. Evans, A. Kern, S. Parsons, *Powder Diffr.* **2011**, 26, 22–25.
- [5] A. A. Coelho, TOPAS-Academic, Version 4.1, Coelho Software, Brisbane (Australia), **2007**.
- [6] H. M. Rietveld, *J. Appl. Crystallogr.* **1969**, 2, 65–71.
- [7] R. W. Cheary, A. A. Coelho, *J. Appl. Crystallogr.* **1992**, 25, 109–121.
- [8] R. W. Cheary, A. A. Coelho, J. P. Kline, *J. Res. Natl. Inst. Stand. Technol.* **2007**, 109, 1–25.
- [9] Crystal Impact GbR., Diamond Version 3.2g, Bonn (Germany), **1997–2011**.
- [10] P. Hewat, Inorganic Crystal Structure Database, Karlsruhe (Germany), **2003–2012**.
- [11] STOE & Cie. GmbH, WinXPOW Search Version 2.9.3, Darmstadt (Germany), **2007**.
- [12] P. Villars, K. Cenzual, Pearson’s Crystal Data – Crystal Structure Database for Inorganic Compounds, Materials Park, Ohio (US), **2009–2010**.
- [13] STOE & Cie. GmbH, X-Area Version 1.39, Darmstadt (Germany), **2006**.
- [14] Bruker, APEX2 Version 11, Billerica, Madison (US), **2014**.
- [15] G. M. Sheldrick, *Acta Crystallogr.* **2008**, A64, 112–122.
- [16] A. L. Spek, *Acta Crystallogr.* **2009**, D65, 148–155.
- [17] P. Blaha, K. Schwarz, G. K. H. Madsen, D. Kvasnicka, J. Luitz, WIEN2k, An Augmented Plane Wave and Local Orbitals Programme for Calculating Crystal Properties, Technical University of Vienna (Austria), **2006**.
- [18] J. P. Perdew, K. Burke, M. Ernzerhof, *Phys. Rev. Lett.* **1996**, 77, 3865–3868.
- [19] R. D. Shannon, *Acta Crystallogr.* **1976**, A32, 751–767.
- [20] R. Hoppe, *Angew. Chem. Int. Ed. Engl.* **1966**, 5, 95–106; *Angew. Chem.* **1966**, 78, 52–63.
- [21] R. Hoppe, *Angew. Chem. Int. Ed. Engl.* **1970**, 9, 25–34; *Angew. Chem.* **1970**, 82, 7–16.
- [22] K. Köllisch, Doctoral Thesis, Ludwig-Maximilians Universität, **2001**.

- [23] Hübenthal, MAPLE, Programm zur Berechnung des Madelunganteils der Gitterenergie Version 4, University of Gießen (Germany), **1993**.

3 Alkali Metal Suboxometalates – Structural Chemistry between Salts and Metals

Matthias Wörsching, Constantin Hoch

published in: *Inorg. Chem.* **2015**, *54*, 7058–7064. DOI:10.1021/acs.inorgchem.5b01060

Reprinted (adapted) with permission from Inorganic Chemistry. Copyright 2015 American Chemical Society.

Abstract

The crystal structures of new, cesium-poor alkali metal suboxometalates $\text{Cs}_{10}\text{MO}_5$ ($\text{M} = \text{Al, Ga, Fe}$) show both metallic and ionic bonding following the formal description $(\text{Cs}^+)_{10}(\text{MO}_4^{5-})(\text{O}^{2-}) \cdot 3\text{e}^-$. Comparable to the cesium-rich suboxometalates Cs_9MO_4 ($\text{M} = \text{Al, Ga, In, Fe, Sc}$) with ionic subdivision $(\text{Cs}^+)_9(\text{MO}_4^{5-}) \cdot 4\text{e}^-$, they contain an oxometalate anion $[\text{M}^{\text{III}}\text{O}_4]^{5-}$ embedded in a metallic matrix of cesium atoms. Column-like building units form with prevalent ionic bonding inside and metallic bonding on the outer surface. In the cesium-rich suboxometalates Cs_9MO_4 additional cesium atoms with no contact to any anion are inserted between columns of the formal composition $[\text{Cs}_8\text{MO}_4]$. In the cesium-poor suboxometalates $\text{Cs}_{10}\text{MO}_5$ the same columns are extended by face-sharing $[\text{Cs}_6\text{O}]$ units, and no additional cesium atoms are present. The terms "cesium-rich" and "cesium-poor" here refer to the Cs:O ratio. The new suboxometalates $\text{Cs}_{10}\text{MO}_5$ crystallize in two modifications with new structure types. The orthorhombic modification adopts a structure with four formula units per unit cell in space group *Pnmm* with $a = 11.158(3)$ Å, $b = 23.693(15)$ Å and $c = 12.229(3)$ Å for $\text{Cs}_{10}\text{AlO}_5$. The monoclinic modification crystallizes with eight formula units per unit cell in space group *C2/c* and eight formula units per unit cell with $a = 21.195(3)$ Å, $b = 12.480(1)$ Å, $c = 24.120(4)$ Å and $\beta = 98.06(1)^\circ$ for $\text{Cs}_{10}\text{AlO}_5$. Limits to phase formation are given by the restriction that M atoms must be trivalent and by geometric size restrictions for the insertion of $[\text{Cs}_6\text{O}]$ blocks in $\text{Cs}_{10}\text{MO}_5$. All suboxometalate structures show similar structural details and form mixed crystal series with statistical occupation for the M elements following the patterns $\text{Cs}_9(\text{M}_x^1\text{M}_{1-x}^2)\text{O}_4$ and $\text{Cs}_{10}(\text{M}_x^1\text{M}_{1-x}^2)\text{O}_5$. The suboxometalates are a new example of ordered intergrowth of ionic and metallic structure elements, allowing for the combination of properties related with both ionic and metallic materials.

3.1 Introduction

In intermetallic compounds from metals with a high electronegativity difference, the metallic bond gets polarized. The extreme case is known as Zintl compounds, where the electron transfer can be assumed to be complete, resulting in ion formation. Less polar metal–metal bonding normally results in overall metallic behavior, but with high specific resistivity and nonlinear temperature dependence, sometimes described by the term "bad metal behavior".^[1] This kind of polar metallic bonding has interesting consequences for both properties and crystal structures.

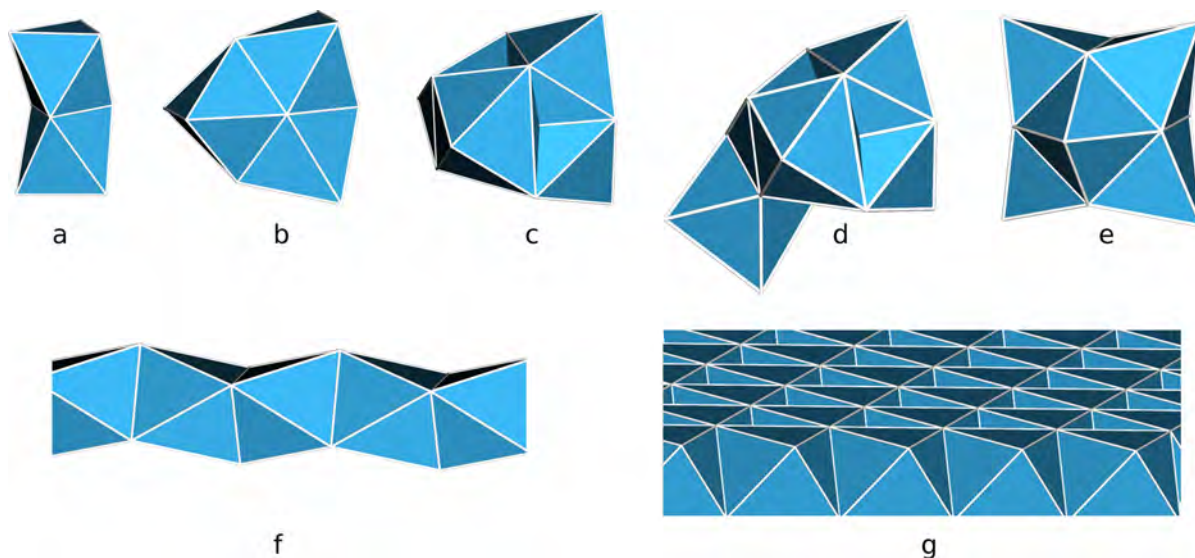


Figure 3.1: Clusters as structural building units in suboxides, subnitrides, and suboxometalates, based on connected octahedra: (a) two octahedra in Rb_9O_2 ; (b) three octahedra in Cs_{11}O_3 ; (c) four octahedra in Cs_9MO_4 ; (d) five octahedra in $\text{Cs}_{10}\text{MO}_5$; (f) infinite chain of octahedra in Ba_3N and Cs_3O ; (g) infinite sheet of octahedra in Cs_2O .

Model substances for the study of polar metal–metal bonding can principally be accessed by two different synthetic routes. First, two metallic educts with considerable electronegativity differences can react to form a product with more or less electron transfer from the electropositive to the electronegative partner.^[2] Second, an ionic and a metallic educt can react to form a product still containing both basic bonding situations. This second synthetic strategy can lead to interesting crystal structures and a combination of properties of both salts and metals. The cesium suboxometalates we present here are excellent examples for products of this second approach.

In 2009 we reported the preparation, structures and properties of cesium suboxometalates Cs_9MO_4 ($\text{M} = \text{Al}, \text{Ga}, \text{Fe}, \text{Sc}, \text{In}$).^[3] They were obtained from reactions of oxides, i.e. M_2O_3 and Cs_2O , with metallic cesium at temperatures of about 300 °C. As all suboxometalates Cs_9MO_4 crystallize isotypically, mixed crystal series with different trivalent metals M can be prepared.^[3] In their crystal structures, compartments with ionic bonding and compartments with metallic bonding alternate in an ordered pattern. This structural motif has previously been described extensively for the alkali metal suboxides and

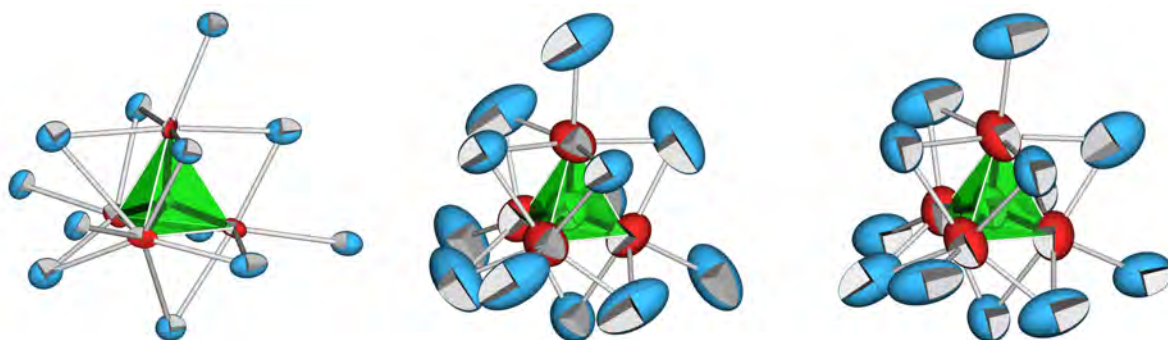


Figure 3.2: Juxtaposition of $[\text{GaO}_4]^{5-}$ oxometalate anions in (left) Rb_5GaO_4 ,^[7] in (center) Cs_9GaO_4 , and (right) $\text{Cs}_{10}\text{GaO}_5$, together with their respective coordination by alkali metal cations. The topological analogy is evident. Blue spheres, alkali metal atoms; red spheres, oxygen atoms; green spheres, gallium atoms; green tetrahedra, $[\text{GaO}_4]^{5-}$ anions. All ellipsoids are drawn at a probability level of 90 %.

alkaline-earth metal subnitrides.^[4,5] In those compounds the anionic part is constituted from monoatomic oxide (O^{2-}) or nitride (N^{3-}) anions, whereas in the suboxometalates the anionic part is built from complex oxometalate anions $[\text{M}^{\text{III}}\text{O}_4]^{5-}$. This leads to a higher variety of possible anions by alternation of M.

The alkali metal suboxides and the alkaline-earth metal subnitrides are built from discrete cluster entities. The structures of rubidium suboxides are based on dimers of face-sharing oxide-centered octahedra $[\text{Rb}_9\text{O}_2]$ and those of cesium suboxides on trimers $[\text{Cs}_{11}\text{O}_3]$. These clusters are closely packed in the crystal structures of Rb_9O_2 and Cs_{11}O_3 . In suboxides with higher metal content, a number of additional metallic alkali metal atoms are intercalated. Akin to the alkali metal suboxides, the crystal structure common to all of the cesium suboxometalates Cs_9MO_4 is built from polyhedral cluster entities. Where the small oxide (or nitride) anions in alkali metal suboxides (or alkaline-earth metal subnitrides) are coordinated octahedrally by cesium (or barium), the bigger tetrahedral oxometalate anions $[\text{MO}_4]^{5-}$ in the cesium suboxometalates are coordinated by 12 cesium atoms in a distorted cuboctahedron $[\text{Cs}_{12}\text{MO}_4]$. This cuboctahedron is the result of the octahedral coordination of each of the four oxygen atoms of the $[\text{MO}_4]^{5-}$ anion by five cesium and one M atom. The $[\text{Cs}_{12}\text{MO}_4]$ cuboctahedra are condensed by sharing of common faces to form columns $\frac{1}{\infty}[\text{Cs}_8\text{MO}_4]$ as building blocks corresponding to the cluster entities in suboxides and subnitrides. Metallic cesium atoms are intercalated between these columns, creating the metallic substructure. A compilation of building units in suboxides, subnitrides, and suboxometalates based on their description as oligomers of face-sharing octahedra is shown in Figure 3.1.

The ionic sublattice is by no means different from "normal", purely ionic oxometalates, as strongly supported by density functional theory (DFT) calculations.^[3] The $[\text{MO}_4]^{5-}$ anion behaves as a quasi-molecular entity and shows no significant electronic contribution from the 12 coordinating Cs atoms. $[\text{A}_{12}\text{MO}_4]$ entities (A = alkali metal) of distorted cuboctahedral shape are very common in the structural chemistry of orthometalates, and all of the geometric details in the anionic part of the suboxometalates are very similar to those of anions in comparable ionic oxometalates (see Figure 3.2).

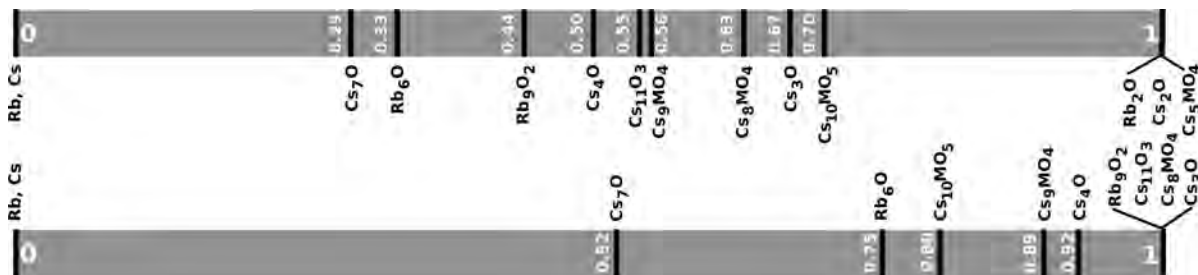


Figure 3.3: Comparison of alkali metal suboxides and suboxometalates with respect to their alkali metal contents. Upper scale: arrangement of the compounds following the mean formal oxidation number of the alkali metal atom (given in white). Lower scale: arrangement following the quotient number alkali metal atoms in cluster units per total number of alkali metal atoms in the compound (given in white).

The additional cesium atom in $\text{Cs}_9\text{MO}_4 = [\text{Cs}_8\text{MO}_4]\cdot\text{Cs}$ is coordinated by eight further cesium atoms in the shape of a slightly compressed $[\text{Cs}_8\text{Cs}]$ cube with Cs–Cs distances between 528.1 and 531.9 pm, reminiscent of the body-centered cubic packing in elemental cesium with comparable Cs–Cs distances of 525 pm.^[3,6] It has no direct contact to the oxometalate anion. The likeness of the local surrounding of both the oxometalate anion and the cesium atom in the suboxometalates Cs_9MO_4 to those in the ionic structures on the one hand and metallic cesium on the other hand emphasizes the character of an intergrowth structure with two independent sublattices. However, the two sublattices influence each other slightly: The isolated cesium atom shows higher s electron density than Cs^0 because of the compressed cubic environment and consequently must be addressed as partially negatively charged $\text{Cs}^{\delta-}$.^[3]

Cs_9MO_4 can be formally divided into two sublattices according to $[\text{Cs}_8\text{MO}_4]\cdot\text{Cs}$, as can many of the alkali metal suboxides ($\text{Rb}_6\text{O} = \text{Rb}_9\text{O}_2 \cdot 3 \text{Rb}$, $\text{Cs}_4\text{O} = [\text{Cs}_{11}\text{O}_3] \cdot \text{Cs}$, $\text{Cs}_7\text{O} = [\text{Cs}_{11}\text{O}_3] \cdot 10 \text{Cs}$).^[4] Following this analogy, the more cesium-poor suboxometalate Cs_8MO_4 can be postulated (paralleling Cs_{11}O_3) as well as more cesium-rich suboxometalates, $[\text{Cs}_8\text{MO}_4]\cdot n \text{Cs}$. The introduced terms "cesium-poor" and "cesium-rich" refer to the Cs:O ratio in the respective empirical formulas. "Cesium-rich" means a high Cs:O ratio, leading to a higher number of metallic cesium atoms in the compound according to the formal division of the sum formulas as above. The comparison of suboxides and suboxometalates with respect to the variable amount of metallic alkali metal is given in Figure 3.3. The upper scale emphasizes the overall electron count in the respective phases, and the lower scale emphasizes structural similarities between them.

Following the similarities between the building principles of alkali metal suboxides and subnitrides on the one hand and cesium suboxometalates on the other hand, we found it worthwhile to extend the structural plethora of suboxides by preparing new suboxometalates with both higher and lower cesium contents than Cs_9MO_4 . We have synthesized and characterized a family of new cesium-poor suboxometalates with composition $\text{Cs}_{10}\text{MO}_5$ ($M = \text{Al}, \text{Ga}, \text{Fe}$). Here we show that their crystal structures indeed follow the above-mentioned structural building principles but at the same time broaden the spectrum of compounds of the suboxometalates by unexpected novel combinations of known building units.

3.2 Experimental Section

3.2.1 Materials

As starting materials, the commercially available oxides Al_2O_3 (Alfa Aesar, 99.99 %), Fe_2O_3 (Merck, 99 %), and Ga_2O_3 (Sigma-Aldrich, 99.99%) were employed and dried under dynamic vacuum at 300–400 °C prior to use.

Cs_2O was prepared following a modified version of the pathway reported by Brauer.^[8] About 10 g of cesium metal was reacted with a stoichiometric amount of oxygen calculated for Cs_3O under vigorous stirring with initial cooling, and then heating of the reaction vessel. The oxygen was generated by thermal decomposition of HgO at 600 °C.^[9] At the end of the reaction a black compound, Cs_3O , was formed. The reaction progress could be easily monitored by observing the melting point of the reaction product via the binary phase diagram Cs–O. Subsequently, the reaction mixture was heated to 160 °C under vacuum to remove excess cesium by distillation, resulting in the formation of Cs_2O with its orange color. The purity was controlled by powder X-ray diffraction (see the Supporting Information).

The suboxometalates $\text{Cs}_{10}\text{MO}_5$ were synthesized from mixtures of Cs, M_2O_3 and Cs_2O in the ratio 6:1:7. All operations were performed under an argon atmosphere. The reaction mixture was weighed in a tantalum crucible cleaned priorly with a mixture of concentrated H_2SO_4 , HNO_3 , and HF. To prevent distillation of cesium, the crucibles were placed in steel autoclaves positioned in quartz tubes under argon and placed in a tube furnace. The samples were heated to 250–320 °C for 5 h and then rapidly cooled to room temperature by turning off the furnace. Crystals of the suboxometalates $\text{Cs}_{10}\text{MO}_5$ were always accompanied by the cesium-rich suboxometalates Cs_9MO_4 and liquid cesium suboxide mixtures.

3.2.2 X-ray Diffraction Analysis

Single crystals were selected under dry paraffin oil with the aid of a stereo microscope and sealed in glass capillaries filled with dry paraffin oil. Single crystal X-ray data were collected at room temperature on an IPDS-1 single-crystal diffractometer (STOE & Cie. GmbH, Darmstadt, Germany) equipped with an imaging plate detector and graphite-monochromatized $\text{MoK}\alpha$ or $\text{AgK}\alpha$ radiation. Absorption corrections were performed by numerical methods on the basis of indexed crystal faces or by semiempirical methods on the basis of data redundancy.^[10–12] Structure solution was carried out with direct methods^[13] and structure refinement with least-squares methods.^[13]

Excess liquid cesium suboxide required the samples to be mixed with dried diamond powder for use in powder X-ray diffraction experiments. The samples were sealed in glass capillaries. Measurements were executed at 298 K on a Stadi P system (STOE & Cie. GmbH, Darmstadt, Germany) with $\text{Mo-K}\alpha 1$ radiation and the para-focusing Debye-Scherrer geometry (Ge(111) monochromator, Si as an external standard). For data handling and processing, the implemented software WINXPOW was employed,^[14] and for Rietveld refinement, the software TOPAS was applied.^[15]

Details on data collection, lattice parameters, and structure refinement are compiled in Table 6.2, while fractional atomic coordinates, isotropic thermal displacement parameters, anisotropic thermal displacement parameters and relevant interatomic distances and angles are compiled in the Supporting Information. Further information on data collection and structural details can be obtained by requesting the respective crystal information files (CIFs) from Fachinformationszentrum Karlsruhe, D-76344 Eggenstein-Leopoldshafen, Germany (e-mail:crysdata@fiz-karlsruhe.de) upon quoting the depository numbers CSD-429344 ($\text{Cs}_{10}\text{AlO}_5$, monoclinic modification), CSD-429345 ($\text{Cs}_{10}\text{AlO}_5$, orthorhombic modification), CSD-429355 ($\text{Cs}_{10}\text{GaO}_5$), CSD-429356 ($\text{Cs}_{10}(\text{Al}/\text{Ga})\text{O}_5$) and CSD-429358 ($\text{Cs}_{10}(\text{Al}/\text{Fe})\text{O}_5$), the names of the authors, and the citation of the paper.

3.2.3 Differential Thermal Analysis

Differential thermal analysis was performed with a differential calorimeter (self-constructed, Max-Planck-Institut für Festkörperforschung, Stuttgart, Germany). Measurements were conducted in sealed tantalum crucibles. The heating rate was $3 \text{ K} \cdot \text{min}^{-1}$, and the cooling rate was $1 \text{ K} \cdot \text{min}^{-1}$. Potassium nitrate was used as a reference (phase transformation at 401 K, melting point at 610 K). Data were exported with the device-specific software and evaluated with ORIGIN.^[16]

3.2.4 Density Functional Theory Calculations

DFT calculations on the relative stabilities of the two modifications of $\text{Cs}_{10}\text{AlO}_5$ were performed with VASP using the generalized gradient approximation (GGA) and the Perdew-Burke-Ernzerhof (PBE) functional with 500 eV and PW cutoff. For the orthorhombic and monoclinic modification, $2 \times 1 \times 2$ and for $1 \times 2 \times 1$ matrices were applied, respectively.

Table 3.1: Crystallographic Data and Details on Structure Solution and Refinement of Cs₁₀MO₅ in the Orthorhombic and the Monoclinic modification. Numbers in Parentheses Are Standard Deviations in Units of the Last Digits.

	Cs ₁₀ AlO ₅	Cs ₁₀ Al _{0.15} Fe _{0.85} O ₅	Cs ₁₀ Al _{0.32} Ga _{0.68} O ₅	Cs ₁₀ AlO ₅	Cs ₁₀ GaO ₅
crystal system		– orthorhombic –		– monoclinic –	
space group		– <i>Pnmm</i> (No. 58) –		– <i>C2/c</i> (No. 15) –	
lattice parameters /Å /°	<i>a</i> = 11.158(3) <i>b</i> = 23.693(15) <i>c</i> = 12.229(3)	<i>a</i> = 11.227(2) <i>b</i> = 23.742(9) <i>c</i> = 12.371(2)	<i>a</i> = 11.1799(2) <i>b</i> = 23.6590(5) <i>c</i> = 12.2957(2)	<i>a</i> = 21.195(12) <i>b</i> = 12.480(4) <i>c</i> = 24.12(3) β = 98.06(12)	<i>a</i> = 21.3877(17) <i>b</i> = 12.4608(11) <i>c</i> = 24.064(2) β = 98.558(6) 6341.8(9)
volume /10 ⁶ Å ³	3233(2)	3297.5(15)	3252.28(10)	– 8 –	– 8 –
<i>Z</i>		– 4 –			
measured density /g · cm ⁻³	2.950	2.943	2.992	3.020	3.076
diffractometer		– STOE IPDS-I, MoK α radiation, graphite monochromator, room temperature –			
absorption coefficient /mm ⁻¹	11.159	11.281	11.628	11.421	12.181
θ -range /°	1.87–20.00	2.45–25.00	1.72–25.00	2.02–25.62	1.90–25.00
index range	–10 ≤ <i>h</i> ≤ 10 –22 ≤ <i>k</i> ≤ 22 –11 ≤ <i>l</i> ≤ 11	–13 ≤ <i>h</i> ≤ 13 –28 ≤ <i>h</i> ≤ 28 –13 ≤ <i>h</i> ≤ 14	–13 ≤ <i>h</i> ≤ 13 28 ≤ <i>k</i> ≤ 28 –14 ≤ <i>l</i> ≤ 14	–25 ≤ <i>h</i> ≤ 25 –15 ≤ <i>k</i> ≤ 15 –29 ≤ <i>l</i> ≤ 29	–25 ≤ <i>h</i> ≤ 24 –14 ≤ <i>k</i> ≤ 14 –28 ≤ <i>l</i> ≤ 28
no. of measured reflns	10666	17337	34069	25888	27001
no. of independent reflns	1583	3025	3014	5903	5443
no. of independent reflns with $I \geq 2\sigma(I)$	831	1041	2429	2097	2636
R_{int}	0.1139	0.11707	0.0697	0.1899	0.2020
R_{σ}	0.1037	0.1389	0.0246	0.1704	0.1321
$F(000)$	2412	2457	2461	4824	4968
corrections		– semiempirical –		– Lorentz, polarization, absorption –	
absorption correction					
structure solution		– direct methods ^[13] –			
structure refinement		– full matrix least-squares on F^2 [13] –			
no. of least-squares parameters	84	86	85	146	146
GOF on F^2	0.693	0.743	1.280	0.790	1.132
R values (for reflns with $I \geq 2\sigma(I)$)	$R1 = 0.0316$ $wR2 = 0.0562$	$R1 = 0.0556$ $wR2 = 0.1325$	$R1 = 0.0423$ $wR2 = 0.1540$	$R1 = 0.0783$ $wR2 = 0.1667$	$R1 = 0.1273$ $wR2 = 0.3252$
R values (all data)	$R1 = 0.0751$ $wR2 = 0.0603$	$R1 = 0.1495$ $wR2 = 0.1537$	$R1 = 0.0616$ $wR2 = 0.1715$	$R1 = 0.1854$ $wR2 = 0.1899$	$R1 = 0.2414$ $wR2 = 0.3730$
Residual electron density /e ⁻ · 10 ⁻⁶ pm ⁻³	0.587 / –0.734	1.366 / –0.884	1.164 / –1.619	1.129 / –1.263	2.460 / –2.156

3.3 Results and Discussion

The crystal structures of both the cesium-rich suboxometalates Cs_9MO_4 and the cesium-poor suboxometalates $\text{Cs}_{10}\text{MO}_5$ with $M = \text{Al}, \text{Ga}, \text{Fe}$ can be constructed by packing of columnar units as shown in Figure 3.4. Subdividing the crystal structures into smaller building blocks is a common picture in solid state chemistry, even in cases where these building blocks are merely figurative and do not refer to chemically separated entities that could, e.g., be extracted from the structure by a solvent. In many solid-state structures the bonding forces between the building units are as strong as they are within them, and the definition of such subunits is arbitrary and justified only by a better topological understanding of the complete structure. In the alkali metal suboxometalates, however, the columnar subunits can effectively be addressed as chemically independent entities, and the assumption of columnar clusters formed in the respective melts may be applicable.

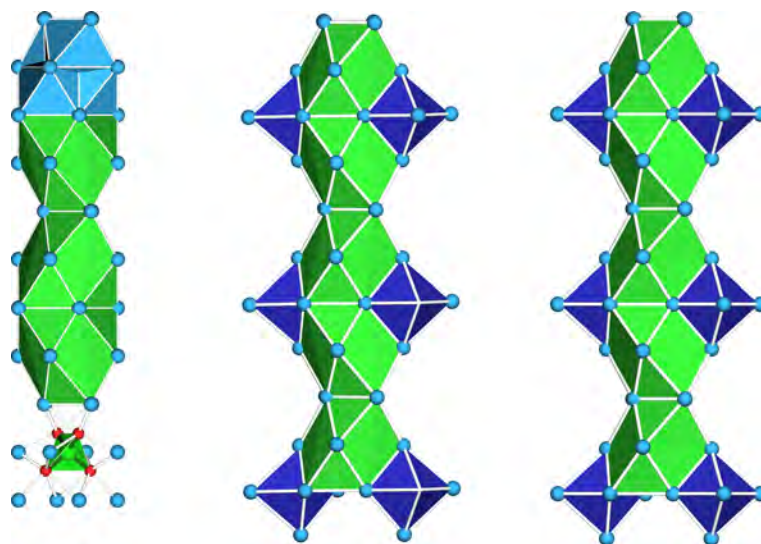


Figure 3.4: Comparison of the columnar building units in (left) Cs_9AlO_4 , (center) $\text{Cs}_{10}\text{AlO}_5$, monoclinic modification, and (right) $\text{Cs}_{10}\text{AlO}_5$, orthorhombic modification. On the left, three ways of presentation as used in Figure 3.1 and Figure 3.2 have been combined for clarification. The topological equivalency of the two columns in the two modifications of $\text{Cs}_{10}\text{AlO}_5$ and their close relation to the column in Cs_9AlO_4 is obvious. The blue octahedra are centered with oxide anions, and the green distorted cuboctahedra with oxoaluminate anions $[\text{AlO}_4]^{5-}$. Cs, blue; Al, green; O, red.

The $[\text{Cs}_{10}\text{MO}_5]$ columns present in the cesium-poor suboxometalates $\text{Cs}_{10}\text{MO}_5$ can be derived from the $[\text{Cs}_8\text{MO}_4]$ columns in the cesium-rich suboxometalates Cs_9MO_4 by inserting additional $[\text{Cs}_6\text{O}]$ octahedra via face-sharing. These octahedra show similar features as the ones constituting the various cluster units in the binary alkali metal suboxides. The Cs–O distances range from 565 to 578 pm in the suboxides and from 579 to 585 pm in the suboxometalates (see Table 3.2 and the Supporting Information). As a results of the strong Coulomb repulsions between the oxide ions centering the $[\text{Cs}_6\text{O}]$ octahedra and the adjacent $[\text{MO}_4]^{5-}$ oxometalate anions, the oxide anions are shifted considerably from the centers of the $[\text{Cs}_6\text{O}]$ octahedra (see Figure 3.6, left). The same situation is found in the $[\text{Cs}_{11}\text{O}_3]$ triple octahedra in the cesium suboxides.

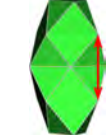
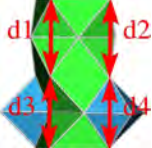
	Cs₇O [4] 563.4 (3x) 565.8 (6x)	Cs₄O [4] 564.4 (3x) 566.2 (6x)	Cs₁₁O₃ [17] 566.6 (1x) 568.6 (1x) 562.4 (1x) 570.6 (1x) 572.9 (1x) 558.5 (1x) 572.0 (1x) 570.9 (1x) 569.4 (1x)	Cs₃O [18] 578.0 (3x)	Cs₂O [19] 572.5 (3x)
	$\varnothing_{\text{Cs}_7\text{O}} = 565.0$	$\varnothing_{\text{Cs}_4\text{O}} = 565.6$	$\varnothing_{\text{Cs}_{11}\text{O}_3} = 568.0$ $\varnothing_{\text{overall}} = \mathbf{567.8}$	$\varnothing_{\text{Cs}_3\text{O}} = 578.0$	$\varnothing_{\text{Cs}_2\text{O}} = 572.5$
	Cs₉AlO₄ 621.0	Cs₉GaO₄ 624.4	Cs₉FeO₄ 628.7	Cs₉ScO₄ 639.6	Cs₉InO₄ 645.0
	$\varnothing_{\text{overall}} = \mathbf{631.7}$				
	Cs₁₀AlO₅ (orthorhombic) d1: 620.6 d2: 643.5 d3: 602.3 d4: 579.4	Cs₁₀AlO₅ (monoclinic) 619.2 644.5 610.7 585.4	Cs₁₀GaO₅ (monoclinic) 627.6 655.7 612.9 584.8	Cs₁₀(Al/Ga)O₅ (orthorhombic) 623.5 649.2 606.0 580.4	Cs₁₀(Al/Fe)O₅ (orthorhombic) 626.9 655.1 610.2 582.0
	$\varnothing_{\text{d4}} = \mathbf{582.4}$				

Table 3.2: Apical Cs–Cs Distances [pm] in [Cs₆O] Octahedra from Cesium Suboxides and Cesium Oxide and Averaged Values in Comparison with Empty Voids in Suboxometalates Cs₉MO₄ and the Unoccupied Interstices d1, d2 and d3 and Occupied Interstices (d4, bold numbers) in the Suboxometalates Cs₁₀MO₅. \varnothing Indicates the Arithmetic Average.

The comparison of the [Cs₈MO₄] columns from the suboxometalates Cs₉MO₄ with the [Cs₁₀MO₅] columns shows that the insertion of [Cs₆O] units, sharing common faces with only a quarter of all available interstices in the [Cs₈MO₄] unit, leads to a distortion of the columns and lower symmetry. In the [Cs₈MO₄] columns, all four topologically suitable positions for the insertion of [Cs₆O] groups are symmetrically equivalent. The M atom at the center of the distorted cuboctahedron has point symmetry $42m$. In Cs₁₀MO₅, only one of the possible positions is occupied in both the monoclinic and the orthorhombic modification. The M atoms only have point symmetry 1 (monoclinic structures) or 2 (orthorhombic structures). The distortion of the columns is necessary to account for the preferential apical Cs–Cs distance in a [Cs₆O] octahedron, which can be derived from a comparison of all binary cesium–oxygen compounds (see Table 3.2). The undistorted [Cs₈MO₄] column has longer Cs–Cs distances in the possible positions, so the insertion of a shorter octahedron leads to alternating Cs–Cs distances along the [Cs₁₀MO₅] column. This geometric criterion provides an explanation of why the variety of M in Cs₉MO₄ is higher (M = Al, Ga, Fe, Sc, or In and mixed crystals thereof) than in Cs₁₀MO₅ (M = Al, Ga, or Fe and mixed crystals thereof). It was shown that the increasing ionic radius of M in going from Al³⁺ to In³⁺ influences only the length of the [Cs₈MO₄] column but not its diameter,^[3] and therefore the distortion of the Cs–Cs distances necessary to accommodate the insertion of a [Cs₆O] octahedron is smaller and feasible only for smaller M = Al, Ga, or Fe. The interstices are so large in Cs₉InO₄ and Cs₉ScO₄ that the distortion becomes unfavourable (see Figure 3.5) and no cesium-poor suboxoindate or suboxoscandate is formed. The limit distance in Cs₉MO₄ suboxometalates lies around 630 pm for the apical Cs–Cs distance in the column. Below this value, the distortion towards the optimal value of 567.8 pm still is possible. Parallel to the decrease of one of the four distances, d4 in Table 3.2, an increase in one of the other distances, d2 in Table

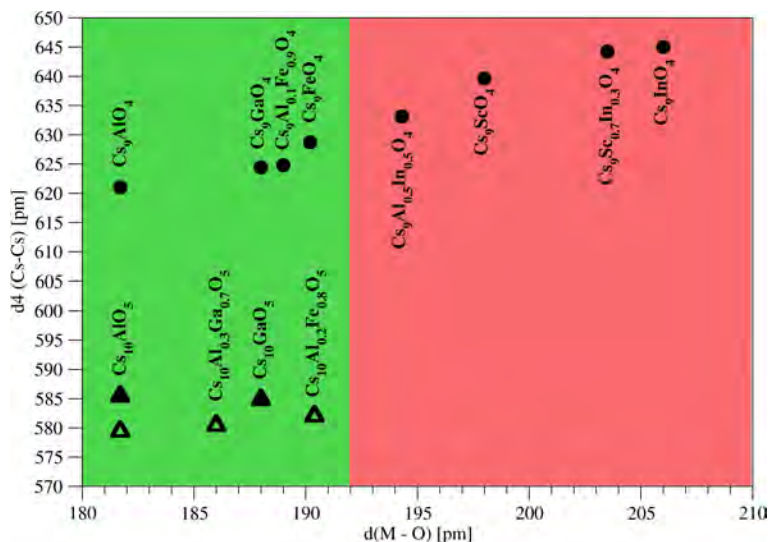


Figure 3.5: Dependence of the apical Cs–Cs distance d_4 (see table 3.2) on the increasing size of the $[\text{MO}_4]^{5-}$ anion in suboxometalates. For $M = \text{Al}, \text{Ga}$, or Fe , the distances are suitable for insertion of $[\text{Cs}_6\text{O}]$, while for $M = \text{Sc}$ or In , the distances are too large. Circles: suboxometalates Cs_9MO_4 ; open triangles, suboxometalates $\text{Cs}_{10}\text{MO}_5$ (orthorhombic modification), filled triangles, suboxometalates $\text{Cs}_{10}\text{MO}_5$ (monoclinic modification).

3.2, has to occur, constituting the geometrical limit for the Cs-poor suboxometalates.

The cesium suboxometalates $\text{Cs}_{10}\text{MO}_5$ crystallize in two modifications. The representatives of the two crystal structures are strictly isotypic for different M metals. Consequently, mixed crystals $\text{Cs}_{10}\text{Al}_x\text{Ga}_{1-x}\text{O}_5$ and $\text{Cs}_{10}\text{Al}_x\text{Fe}_{1-x}\text{O}_5$ can be prepared in which no ordering of the different metals occurs. This finding is consistent with the mixed-crystal behavior of the suboxometalates Cs_9MO_4 . In contrast to these, the substitution of cesium by rubidium was never found for the suboxometalates $\text{Cs}_{10}\text{MO}_5$. This can be understood because in $\text{Cs}_{9-x}\text{Rb}_x\text{MO}_4$, only the purely metallic Cs position is substituted, whereas in $\text{Cs}_{10}\text{MO}_5$ no such purely metallic position is present.

The crystal structures of the two modifications are shown in Figure 3.6. Both modifications are built from the same columnlike motifs with composition $[\text{Cs}_{10}\text{MO}_5]$, built from $[\text{Cs}_8\text{MO}_4]$ columns as found in the cesium-rich suboxometalates Cs_9MO_4 , but with additional $[\text{Cs}_6\text{O}]$ octahedra condensed via common faces (see Figure 3.4). Arranging the $[\text{Cs}_{10}\text{MO}_5]$ columns differently leads to the two modifications: either a parallel arrangement (orthorhombic modification) or a skew arrangement (monoclinic modification).

Comparison of the two modifications shows high similarity in geometric details of the $[\text{Cs}_{10}\text{MO}_5]$ columns (see the Supporting Material) and, as a consequence, similar unit cell volumes. For example, the orthorhombic modification of $\text{Cs}_{10}\text{AlO}_5$ has a unit cell volume of $3233(3) \text{ \AA}^3$ and $Z = 4$, whereas its monoclinic modification has a unit cell volume of $6318(9) \text{ \AA}^3$ and $Z = 8$. The orthorhombic modification thus has a volume per formula unit that is about 2% higher than that of the monoclinic modification, and the density of the orthorhombic modification ($2.950 \text{ g}\cdot\text{cm}^{-3}$) is slightly lower than the one of the monoclinic modification with $3.020 \text{ g}\cdot\text{cm}^{-3}$. Because of these very small differences, it can be estimated that the difference in thermodynamic stabilities of the

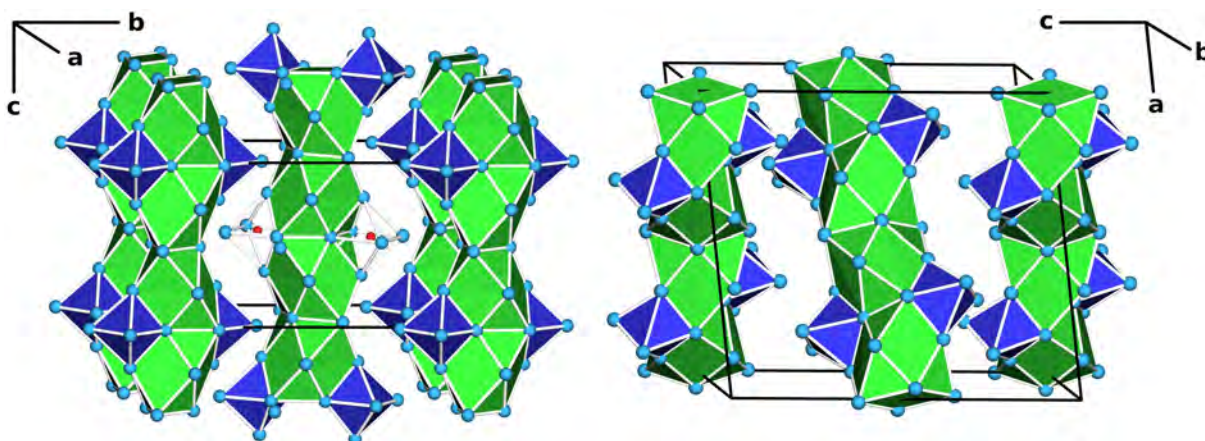


Figure 3.6: Crystal structures of the two modifications of $\text{Cs}_{10}\text{MO}_5$: (left) orthorhombic modification, space group $Pnnm$; (right) monoclinic modification, space group $C2/c$. In the left picture, two $[\text{Cs}_6\text{O}]$ octahedra are drawn transparent to show the shift of the oxide anions from the center of the octahedron. Cs atoms, blue; M atoms, surrounded by green polyhedra; O atoms, red.

two modifications also is only marginal. In our experiments it remained unclear which parameter determines whether the orthorhombic or the monoclinic modification can be obtained; however, it was normally observed that in a given sample, single-crystal specimens belonged to only one of the two modifications.

Thermoanalytic investigations show the difficulty in deliberately synthesizing one of the two modifications of the new suboxometalates as a phase-pure samples. A 7:6:1 mixture of cesium oxide, cesium metal and Al_2O_3 , fitting for the synthesis of $\text{Cs}_{10}\text{AlO}_5$, was heated to $400\text{ }^\circ\text{C}$, cooled to room temperature, and again heated to $400\text{ }^\circ\text{C}$ and cooled to room temperature (see Figure 3.7). The first heating curve of the pristine reaction mixture shows three endothermic and two weak and broad exothermic signals. At about $50\text{ }^\circ\text{C}$, a cesium-rich suboxidic component spontaneously formed from Cs and Cs_2O melts, in accordance with the Cs–O phase diagram.^[17] At ca. $150\text{ }^\circ\text{C}$, two adjacent signals show further melting processes of more oxygen-rich suboxidic species. At ca. 270 and $320\text{ }^\circ\text{C}$ two exothermic reactions occur, one belonging to the formation of Cs_9AlO_4 and the other to the formation of $\text{Cs}_{10}\text{AlO}_5$. As slow cooling of reaction mixtures from $350\text{ }^\circ\text{C}$ always yields phase-pure samples of Cs_9AlO_4 and rapid cooling yields mixtures of Cs_9AlO_4 and $\text{Cs}_{10}\text{AlO}_5$ (see the Supporting Information), the higher reaction signal belongs to the formation of Cs_9AlO_4 by consumption of $\text{Cs}_{10}\text{AlO}_5$. The cooling curve shows two signals at ca. 155 and $160\text{ }^\circ\text{C}$ belonging to the solidification of residual suboxidic species and a third signal at ca. $175\text{ }^\circ\text{C}$ belonging to the crystallization of Cs_9AlO_4 . The second heating consequently shows no reaction signals and shifted endothermic effects belonging to the melting of the suboxide species, as the composition of the reaction mixture has been shifted toward more cesium-poor suboxides by the formation of Cs_9AlO_4 . The effects of the first cooling process can be reproduced in the second cooling. It seems clear that the formation of Cs_9AlO_4 renders the phase-pure synthesis of either modification of $\text{Cs}_{10}\text{AlO}_5$ difficult. The formation of the more cesium-poor suboxometalate and its decomposition to the more cesium-rich suboxometalate plus cesium suboxides occur at very closely neighboring temperatures.

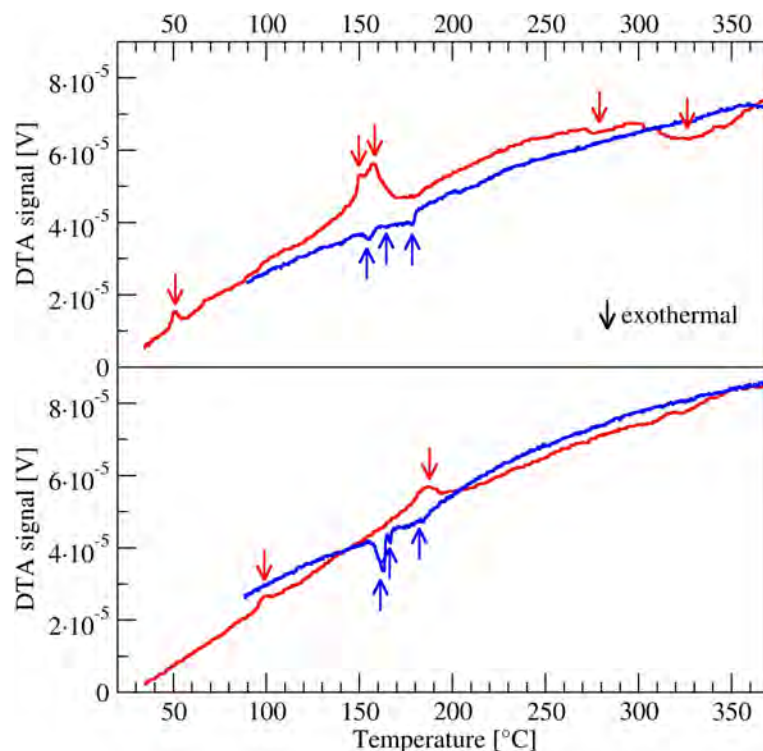


Figure 3.7: Differential thermal analysis of reaction mixtures for $\text{Cs}_{10}\text{AlO}_5$: (top) heating and cooling curves for a pristine mixture of Cs_2O , Cs , and Al_2O_3 in proportions 7 : 6 : 1; (bottom) second heating and cooling curves for the same sample.

DFT calculations on the basis of the single-crystal structure models showed that the electronic contributions of the two modifications differed only by $1.1 \text{ kJ}\cdot\text{mol}^{-1}$, with the orthorhombic modification being slightly thermodynamically preferred. However, the calculations of the relative energies are based on the electronic structures only. Following a concept based on information theory, the respective complexities of the two modifications can be quantified.^[20] The difference is again very small with 256 bits for the orthorhombic and 224 bits for the monoclinic modification.

3.4 Conclusion

The structural chemistry of cesium suboxometalates shows the chance to twin ionic and metallic substructures in ordered crystals. This leads to the mixing of typical physical properties common to both systems. Future work may show the extent to which this route leads to systems with interesting combinations such as e.g. high electric and low thermal conductivity, multiferroic properties, further reduction of the metallic sublattice toward ordered quantum dots, and others. At the moment, this chemistry is constrained to alkali metal-rich systems showing high reactivity toward ambient conditions. However, combinations containing even larger anionic sublattices such as Keggin ions and polyoxometalates combined with substitution of the highly reactive alkali metals by other metals can help to find ways toward more stable compounds suitable for application purposes.

3.5 Acknowledgement

The authors thank Kristina Ritter, Jasmin Dums, Patrick Hirschle, Irina Zaytseva and Claudia Lenk for the sample preparations. Roland Eger at MPI FKF, Stuttgart, Germany, is gratefully acknowledged for help in the thermoanalytic investigations. The DFT calculations kindly were provided by Prof. Dr. R. Dronskowski and his group at RWTH Aachen, Germany.

3.6 References

- [1] Gunnarsson, O.; Calandra, M.; Han, J. E. *Rev. Mod. Phys.* **2003**, *75*, 1085–1099.
- [2] (a) Hoch, C.; Simon, A. *Angew. Chem.* **2012**, *124*, 3316–3319. (b) Hoch, C.; Simon, A. *Angew. Chem., Int. Ed.* **2012**, *51*, 3262–3265. (c) Tambornino, F.; Hoch, C. *J. Alloys Compd.* **2015**, *618*, 299–304. (d) Tambornino, F.; Hoch, C. *Z. Anorg. Allg. Chem.* **2015**, *641*, 537–542
- [3] (a) Hoch, C.; Bender, J.; Simon, A. *Angew. Chem.* **2009**, *121*, 2451–2453. (b) Hoch, C.; Bender, J.; Simon, A. *Angew. Chem., Int. Ed.* **2009**, *48*, 2415–2417. (c) Hoch, C.; Bender, J.; Wohlfahrt, A.; Simon, A. *Z. Anorg. Allg. Chem.* **2009**, *635*, 1777–1782. (d) Hoch, C.; Simon, A.; Lee, C.; Whangbo, M. H.; Köhler, J. *Z. Kristallogr.* **2011**, *226*, 553–556. (e) Hoch, C. *Z. Naturforsch.* **2011**, *66b*, 1248–1254.
- [4] (a) Simon, A.; Deiseroth, H. J. *Rev. Chim. Miner.* **1976**, *13*, 98–112. (b) Simon, A.; Deiseroth, H. J.; Westerbeck, E.; Hillenkötter, B. *Z. Anorg. Allg. Chem.* **1976**, *423*, 203–211. (c) Simon, A. *Z. Anorg. Allg. Chem.* **1976**, *422*, 208–218.
- [5] (a) Rauch, P. E.; Simon, A. *Angew. Chem.* **1992**, *104*, 1505–1506. (b) Rauch, P. E.; Simon, A. *Angew. Chem., Int. Ed. Engl.* **1992**, *31*, 1519–1521. (c) Snyder, G. F.; Simon, A. *Angew. Chem.* **1994**, *106*, 713–715. (d) Snyder, G. F.; Simon, A. *Angew. Chem., Int. Ed. Engl.* **1994**, *33*, 689–691. (e) Snyder, G. J.; Simon, A. *J. Am. Chem. Soc.* **1995**, *117*, 1996–1999.
- [6] Barrett, C. S. *J. Chem. Phys.* **1971**, *54*, 2768–2770.
- [7] Bender, J.; Wohlfarth, A.; Hoch, C. *Z. Naturforsch.* **2010**, *65b*, 1416–1426.
- [8] Brauer, G. *Handbuch der Präparativen Anorganischen Chemie*, 2nd ed.; Ferdinand Enke Verlag: Stuttgart, Germany, **1962**; Vol. 1, p 978.
- [9] Simon, A. *Z. Anorg. Allg. Chem.* **1973**, *395*, 301–319.
- [10] *X-Area*, version 1.39; Stoe & Cie.: Darmstadt, Germany, **2006**.
- [11] *X-Shape*, version 2.07; Stoe & Cie.: Darmstadt, Germany, **2005**.
- [12] *X-Red*, version 1.31; Stoe & Cie.: Darmstadt, Germany, **2005**.
- [13] Sheldrick, G. M. *Acta Crystallogr.*, **2008**, *A64*, 112–122.
- [14] *Winxpow*, version 2.09; Stoe & Cie.: Darmstadt, Germany, **2005**.
- [15] Coelho, A. A.; Evans, J.; Evans, I.; Kern, A.; Parsons, S. *Powder Diffr.*, **2011**, *26*, 22–25.
- [16] *Origin*, version 6.1; OriginLab: Northampton, MA, **1991–2000**.
- [17] Simon, A.; Westerbeck, E. *Z. Anorg. Allg. Chem.* **1977**, *428*, 187–198.
- [18] Tsai, K. R.; Harris, P. M.; Lassetre, E. N. *J. Phys. Chem.* **1956**, *60*, 345–347.

- [19] Helms, A.; Klemm, W. *Z. Anorg. Allg. Chem.* **1939**, *242*, 33–40.
- [20] Krivovichev, S. *Acta Crystallogr.* **2012**, *A68*, 393–398.

3.7 Supporting Information

Table S4.1: Fractional atomic coordinates for Cs₁₀MO₅ in monoclinic and orthorhombic modifications as result from single crystal X-ray structure refinement. All standard deviations are given in parentheses in units of the last digit.

Monoclinic										
	Cs(1)			Cs(2)			Cs(3)			
	x	y	z	x	y	z	x	y	z	
Cs ₁₀ AlO ₅	0.00708(8)	0.04895(18)	0.14247(7)	0.04497(6)	0.12101(12)	0.51744(6)	0.06960(8)	0.32554(15)	0.07868(8)	
Cs ₁₀ GaO ₅	0.01002(6)	0.04349(12)	0.14577(5)	0.04454(4)	0.11943(8)	0.51671(4)	0.07156(6)	0.32338(10)	0.08065(6)	
	Cs(4)			Cs(5)			Cs(6)			
	x	y	z	x	y	z	x	y	z	
Cs ₁₀ AlO ₅	0.10989(14)	0.4247(3)	0.30080(16)	0.18064(7)	0.07113(16)	0.41815(9)	0.19683(7)	0.00306(16)	0.62264(8)	
Cs ₁₀ GaO ₅	0.11117(9)	0.43032(18)	0.29861(9)	0.17955(6)	0.06722(10)	0.41571(6)	0.19851(5)	0.00327(11)	0.62261(5)	
	Cs(7)			Cs(8)			Cs(9)			
	x	y	z	x	y	z	x	y	z	
Cs ₁₀ AlO ₅	0.25522(6)	0.26864(12)	0.07477(6)	0.30864(16)	0.1890(4)	0.24790(12)	0.33454(6)	0.02104(12)	0.03590(8)	
Cs ₁₀ GaO ₅	0.25627(4)	0.26634(8)	0.07492(4)	0.30791(11)	0.1922(2)	0.24762(8)	0.33483(5)	0.01982(8)	0.03573(5)	
	Cs(10)			M(1)			O(1)			
	x	y	z	x	y	z	x	y	z	
Cs ₁₀ AlO ₅	0.43545(7)	0.23389(15)	0.12449(7)	0.3776(2)	0.3749(5)	0.0012(3)	0.0842(5)	0.1034(11)	0.0611(6)	
Cs ₁₀ GaO ₅	0.43516(5)	0.23098(10)	0.12499(5)	0.37724(6)	0.37614(12)	0.00080(7)	0.0826(4)	0.0995(8)	0.0635(4)	
	O(2)			O(3)			O(4)			
	x	y	z	x	y	z	x	y	z	
Cs ₁₀ AlO ₅	0.2025(6)	0.0699(12)	0.0093(6)	0.3721(6)	0.2366(12)	0.0124(6)	0.4222(5)	0.4380(12)	0.0614(6)	
Cs ₁₀ GaO ₅	0.2038(4)	0.0659(7)	0.0092(4)	0.3697(4)	0.2301(7)	0.0114(4)	0.4253(4)	0.4414(7)	0.0635(4)	
	O(5)									
	x	y	z							
Cs ₁₀ AlO ₅	0.3255(7)	0.0958(15)	0.1513(6)							
Cs ₁₀ GaO ₅	0.3257(5)	0.0955(9)	0.1534(5)							
Orthorhombic										
	Cs(1)			Cs(2)			Cs(3)			
	x	y	z	x	y	z	x	y	z	
Cs ₁₀ AlO ₅	0.09725(10)	0.14260(3)	0.23701(10)	0.20569(8)	0.45575(5)	0.25375(10)	0.0741(2)	0.27614(6)	0	
Cs ₁₀ (Al/Fe)O ₅	0.09890(18)	0.14347(6)	0.23526(10)	0.20558(14)	0.45587(8)	0.25339(12)	0.0841(4)	0.27716(12)	0	
Cs ₁₀ (Al/Ga)O ₅	0.09803(6)	0.14323(2)	0.23594(4)	0.20559(4)	0.45552(3)	0.25357(5)	0.07822(16)	0.27676(4)	0	
	Cs(4)			Cs(5)			Cs(6)			
	x	y	z	x	y	z	x	y	z	
Cs ₁₀ AlO ₅	0.12511(13)	0.86783(5)	0	0.13940(11)	0.03830(5)	0	0.22757(12)	0.57032(7)	0	
Cs ₁₀ (Al/Fe)O ₅	0.1252(2)	0.86384(8)	0	0.13776(19)	0.03861(8)	0	0.2215(2)	0.57207(12)	0	
Cs ₁₀ (Al/Ga)O ₅	0.12519(7)	0.86613(3)	0	0.13880(6)	0.03853(3)	0	0.22524(7)	0.57113(4)	0	
	Cs(7)			Cs(8)			M			
	x	y	z	x	y	z	x	y	z	
Cs ₁₀ AlO ₅	0.37215(17)	0.17794(8)	0	0.42935(11)	0.43193(5)	0	0	0	0.2535(6)	
Cs ₁₀ (Al/Fe)O ₅	0.3751(3)	0.17613(16)	0	0.4310(2)	0.43193(9)	0	0	0	0.2533(3)	
Cs ₁₀ (Al/Ga)O ₅	0.37333(10)	0.17714(6)	0	0.43053(6)	0.43184(3)	0	0	0	0.25363(9)	
	O(1)			O(2)			O(3)			
	x	y	z	x	y	z	x	y	z	
Cs ₁₀ AlO ₅	0.1168(6)	0.0276(3)	0.3383(7)	0.4375(6)	0.4458(3)	0.3295(7)	0.1307(11)	0.1696(5)	0	
Cs ₁₀ (Al/Fe)O ₅	0.1212(12)	0.0305(5)	0.3438(8)	0.4337(13)	0.4417(5)	0.3349(8)	0.134(2)	0.1671(9)	0	
Cs ₁₀ (Al/Ga)O ₅	0.1201(4)	0.0291(2)	0.3422(3)	0.4359(4)	0.44375(19)	0.3332(3)	0.1351(8)	0.1682(3)	0	
	occ. M ¹ /M ²									
	x	y	z							
Cs ₁₀ (Al/Fe)O ₅	0.15(2)/0.85(2)									
Cs ₁₀ (Al/Ga)O ₅	0.288(7)/0.712(7)									

Table S4.2: Coefficients of the anisotropic displacement parameter U_{ij} for $\text{Cs}_{10}\text{AlO}_5$ (monoclinic, upper lines) and $\text{Cs}_{10}\text{GaO}_5$ (lower lines) and equivalent isotropic displacement parameter U_{eq} in \AA^2 . Standard deviations in units of the last digit are given in parentheses. U_{ij} is defined as $U_{ij} = \exp\{-2\pi^2[U_{11}(\text{ha}^*)^2 + \dots + 2U_{21}\text{hka}^*\text{b}^*]\}$, and U_{eq} is 1/3 of the trace of the anisotropic tensor.

Atom	U_{11}	U_{22}	U_{33}	U_{23}	U_{13}	U_{12}	U_{eq}
Cs(1)	0.1063(12)	0.182(2)	0.0711(11)	-0.0279(11)	0.0266(9)	-0.0695(13)	0.1185(8)
	0.0985(8)	0.1515(12)	0.0638(7)	-0.0204(7)	0.0214(6)	-0.0566(8)	0.1036(5)
Cs(2)	0.0552(7)	0.0845(10)	0.0906(10)	-0.0016(8)	0.0097(7)	0.0131(7)	0.0768(4)
	0.0562(5)	0.0701(6)	0.0851(7)	-0.0007(5)	0.0105(5)	0.0121(5)	0.0705(3)
Cs(3)	0.0956(11)	0.1037(13)	0.1402(16)	-0.0358(11)	0.0482(11)	-0.0243(10)	0.1102(7)
	0.0940(8)	0.0907(8)	0.1330(11)	-0.0369(8)	0.0485(8)	-0.0186(7)	0.1027(4)
Cs(4)	0.162(2)	0.278(4)	0.220(3)	-0.130(3)	-0.041(2)	0.004(2)	0.2264(17)
	0.1415(14)	0.1849(18)	0.1850(19)	-0.0862(15)	-0.0217(13)	-0.0127(13)	0.1751(9)
Cs(5)	0.0786(10)	0.1155(14)	0.1491(17)	0.0495(12)	0.0361(10)	0.0200(10)	0.1125(7)
	0.0838(8)	0.0971(9)	0.1383(12)	0.0471(8)	0.0359(7)	0.0169(7)	0.1044(5)
Cs(6)	0.0732(9)	0.1349(15)	0.1054(13)	-0.0467(11)	-0.0076(8)	0.0315(10)	0.1064(6)
	0.0713(7)	0.1149(10)	0.1032(9)	-0.0426(7)	-0.0041(6)	0.0266(6)	0.0982(4)
Cs(7)	0.0585(7)	0.0878(10)	0.0764(9)	-0.0016(8)	0.0095(6)	-0.0189(7)	0.0742(4)
	0.0563(5)	0.0707(6)	0.0738(7)	-0.0014(5)	0.0105(4)	-0.0135(4)	0.0668(3)
Cs(8)	0.228(3)	0.324(5)	0.117(2)	-0.050(2)	0.043(2)	-0.067(3)	0.2210(16)
	0.205(2)	0.240(2)	0.1057(13)	-0.0365(14)	0.0351(13)	-0.0273(18)	0.1822(9)
Cs(9)	0.0638(8)	0.0780(10)	0.1306(14)	0.0123(10)	0.0080(8)	0.0001(8)	0.0913(5)
	0.0643(6)	0.0625(6)	0.1225(10)	0.0092(6)	0.0110(6)	0.0015(5)	0.0833(4)
Cs(10)	0.0717(9)	0.1341(15)	0.1005(13)	0.0331(11)	-0.0164(8)	-0.0303(10)	0.1048(6)
	0.0691(6)	0.1109(9)	0.0972(9)	0.0289(7)	-0.0119(6)	-0.0255(6)	0.0949(4)
Al(1)	0.036(3)	0.064(4)	0.078(4)	-0.003(3)	0.005(3)	-0.013(3)	0.0596(15)
Ga(1)	0.0432(8)	0.0577(9)	0.0649(10)	-0.0006(8)	0.0103(7)	-0.0153(7)	0.0550(4)
O(1)	0.048(7)	0.086(10)	0.094(10)	-0.015(8)	0.025(7)	-0.025(7)	0.074(4)
	0.053(5)	0.084(7)	0.078(7)	-0.002(6)	0.017(5)	-0.024(5)	0.071(3)
O(2)	0.048(7)	0.097(11)	0.100(11)	0.000(9)	-0.006(7)	-0.015(7)	0.084(4)
	0.048(5)	0.063(6)	0.096(8)	0.005(5)	0.007(5)	-0.011(4)	0.069(3)
O(3)	0.062(8)	0.101(11)	0.078(10)	0.016(8)	0.024(7)	-0.006(8)	0.079(4)
	0.057(5)	0.057(6)	0.088(7)	0.000(5)	0.010(5)	-0.016(5)	0.067(3)
O(4)	0.043(7)	0.101(11)	0.085(10)	0.002(8)	0.006(6)	-0.019(7)	0.077(4)
	0.046(5)	0.070(6)	0.074(7)	-0.004(5)	0.012(4)	-0.014(4)	0.063(2)
O(5)	0.080(9)	0.175(17)	0.049(9)	0.010(10)	-0.006(7)	-0.013(10)	0.103(6)
	0.094(8)	0.100(9)	0.076(8)	0.028(6)	0.008(6)	-0.013(6)	0.091(3)

Table S4.3: Coefficients of the anisotropic displacement parameter U_{ij} for $\text{Cs}_{10}\text{AlO}_5$ (orthorhombic, upper lines), $\text{Cs}_{10}(\text{Al}/\text{Ga})\text{O}_5$ (center lines) and $\text{Cs}_{10}(\text{Al}/\text{Fe})\text{O}_5$ (lower lines) and equivalent isotropic displacement parameter U_{eq} in \AA^2 . Standard deviations in units of the last digit are given in parentheses. U_{ij} is defined as $U_{ij} = \exp\{-2\pi^2[U_{11}(\text{ha}^*)^2 + \dots + 2U_{21}\text{hka}^*\text{b}^*]\}$, and U_{eq} is 1/3 of the trace of the anisotropic tensor.

Atom	U_{11}	U_{22}	U_{33}	U_{23}	U_{13}	U_{12}	U_{eq}
Cs(1)	0.1330(8)	0.0857(6)	0.0732(9)	-0.0074(5)	-0.0023(8)	-0.0213(6)	0.0973(4)
	0.1281(9)	0.0728(5)	0.0609(5)	-0.0080(4)	-0.0027(5)	-0.0212(5)	0.09061(19)
	0.1511(16)	0.0937(10)	0.0678(7)	-0.0083(7)	-0.0009(9)	-0.0208(10)	0.1042(6)
Cs(2)	0.0635(5)	0.1550(9)	0.0887(10)	0.0001(9)	-0.0034(5)	-0.0192(6)	0.1024(4)
	0.0580(5)	0.1446(10)	0.0742(6)	0.0019(5)	-0.0040(4)	-0.0206(5)	0.0955(2)
	0.0823(12)	0.1720(16)	0.0772(9)	0.0016(10)	-0.0040(7)	-0.0204(11)	0.1105(6)
Cs(3)	0.231(3)	0.0752(11)	0.224(3)	0	0	0.0029(13)	0.1770(11)
	0.218(2)	0.0614(8)	0.225(3)	0	0	0.0018(11)	0.1725(6)
	0.254(5)	0.0830(18)	0.234(4)	0	0	-0.002(2)	0.1903(17)
Cs(4)	0.0924(10)	0.0815(9)	0.0849(12)	0	0	0.0201(8)	0.0863(5)
	0.0838(8)	0.0692(6)	0.0725(7)	0	0	0.0222(6)	0.0788(2)
	0.112(2)	0.0897(14)	0.0772(11)	0	0	0.0216(13)	0.0931(7)
Cs(5)	0.0650(8)	0.0811(8)	0.0615(10)	0	0	-0.0002(7)	0.0692(4)
	0.0582(6)	0.0644(6)	0.0487(5)	0	0	-0.0005(4)	0.06068(17)
	0.0873(15)	0.0847(13)	0.0532(8)	0	0	0.0015(11)	0.0751(6)
Cs(6)	0.0731(9)	0.1502(13)	0.0768(13)	0	0	0.0395(9)	0.1000(5)
	0.0675(7)	0.1426(12)	0.0626(7)	0	0	0.0427(7)	0.0946(3)
	0.105(2)	0.179(3)	0.0655(12)	0	0	0.0504(17)	0.1165(9)
Cs(7)	0.1066(14)	0.1585(16)	0.187(2)	0	0	-0.0353(13)	0.1507(8)
	0.0993(12)	0.1463(16)	0.171(2)	0	0	-0.0367(11)	0.1443(4)
	0.123(3)	0.179(3)	0.175(3)	0	0	-0.035(2)	0.1588(12)
Cs(8)	0.0729(8)	0.0884(9)	0.0633(11)	0	0	-0.0038(7)	0.0749(4)
	0.0683(6)	0.0750(7)	0.0489(5)	0	0	-0.0021(5)	0.06748(19)
	0.0955(17)	0.0999(14)	0.0529(9)	0	0	0.0000(11)	0.0828(6)
Al(1)	0.058(3)	0.081(4)	0.056(5)	0	0	-0.003(3)	0.0651(15)
Al/Ga(1)	0.0456(12)	0.0613(13)	0.0313(10)	0	0	-0.0018(9)	0.0505(5)
Al/Fe(1)	0.071(3)	0.080(3)	0.0367(19)	0	0	-0.002(2)	0.0626(17)
O(1)	0.056(5)	0.101(6)	0.062(7)	-0.005(5)	-0.010(4)	-0.014(4)	0.073(3)
	0.058(4)	0.086(5)	0.045(4)	-0.001(4)	-0.002(3)	-0.011(4)	0.0659(12)
	0.073(10)	0.103(10)	0.053(6)	-0.016(6)	-0.012(6)	-0.013(8)	0.077(4)
O(2)	0.077(5)	0.073(6)	0.049(7)	-0.001(4)	0.008(4)	-0.009(4)	0.066(2)
	0.065(4)	0.062(4)	0.047(4)	-0.001(3)	0.002(3)	-0.008(3)	0.0606(11)
	0.103(11)	0.099(10)	0.046(6)	0.011(6)	-0.001(6)	-0.008(8)	0.083(4)
O(3)	0.087(9)	0.096(9)	0.069(11)	0	0	-0.018(8)	0.084(4)
	0.120(11)	0.062(7)	0.072(8)	0	0	-0.014(7)	0.084(2)
	0.14(2)	0.118(16)	0.039(8)	0	0	-0.033(15)	0.101(7)

Table S4.4: Selected interatomic distances in pm in the monoclinic crystal structure of Cs₁₀AlO₅. Standard deviations in units of the last digit are given in parentheses.

Atoms		Distance	Atoms		Distance	Atoms		Distance							
Cs(1)	-	O(1)	280.9(12)	O(3)	318.1(13)	O(1)	-	O(1)	182.4(16)						
		O(4)	282.7(13)		Cs(7)			361.3(5)	Al	182.4(16)					
		Cs(2)	386.3(4)		Cs(9)			370.1(3)	Cs(1)	280.8(14)					
		Cs(2)	396.5(6)		Cs(6)			384.2(3)	Cs(3)	282.8(14)					
		Cs(5)	405.1(4)		Cs(10)			386.4(4)	Cs(6)	294.5(12)					
		Cs(3)	407.6(3)		Cs(5)			400.8(3)	Cs(2)	306.6(14)					
		Cs(6)	416.7(3)		Cs(3)			401.2(3)	Cs(2)	311.1(12)					
Cs(2)	-	Cs(10)	421.5(3)	Cs(9)	402.6(4)	O(2)	-	Al	181.7(14)						
		O(4)	303.4(12)	Cs(8)	428.7(6)			Cs(5)	280.4(15)						
		O(1)	306.6(13)	O(5)	267.3(16)			Cs(9)	284.8(13)						
		O(1)	311.0(13)	Cs(4)	397.6(6)			Cs(6)	290.0(15)						
		O(4)	311.2(14)	Cs(7)	428.7(6)			Cs(7)	306.6(15)						
		Cs(2)	360.8(3)	Cs(6)	429.0(6)			Cs(7)	308.0(15)						
		Cs(1)	386.3(4)	Cs(10)	431.8(6)			O(3)	-	Al	175.3(16)				
		Cs(1)	396.4(6)	O(2)	284.8(13)					Cs(3)	277.8(15)				
		Cs(3)	402.6(4)	O(3)	288.4(15)					Cs(10)	284.5(14)				
		Cs(5)	404.0(5)	O(5)	296.7(16)					Cs(9)	288.4(15)				
		Cs(6)	408.4(5)	Cs(7)	370.1(3)					Cs(7)	309.9(15)				
		Cs(10)	412.5(5)	Cs(6)	383.4(5)					Cs(7)	318.1(13)				
		Cs(3)	-	O(3)	277.7(14)					Cs(10)	386.2(4)	O(4)	-	Al	179.9(15)
				O(1)	282.8(14)					Cs(7)	402.6(4)			Cs(1)	282.7(13)
Cs(7)	401.2(3)			Cs(3)	412.4(5)	Cs(5)	283.8(13)								
Cs(2)	402.6(4)			Cs(4)	412.9(7)	Cs(10)	296.0(15)								
Cs(1)	407.6(3)			Cs(8)	-	O(5)	367.3(16)			Cs(2)	303.5(13)				
Cs(9)	412.4(5)					Cs(4)	397.6(6)			Cs(2)	311.3(15)				
O(5)	270.7(17)					Cs(7)	428.7(6)			O(5)	267.3(16)				
Cs(8)	397.6(6)					Cs(6)	429.0(6)			Cs(4)	270.7(17)				
Cs(9)	412.5(2)					Cs(10)	431.8(6)	Cs(9)	296.7(16)						
Cs(6)	434.6(5)					Cs(9)	-	O(2)	284.8(13)	Cs(6)	298.5(16)				
Cs(10)	442.1(5)	O(3)	288.4(15)					Cs(10)	304.0(17)						
Cs(4)	495.0(7)	O(5)	296.7(16)					Cs(7)	308.4(17)						
Cs(4)	-	O(2)	280.4(15)					Cs(7)	370.1(3)	O(5)	-	Cs(8)	267.3(16)		
		O(4)	283.8(13)					Cs(6)	383.4(5)			Cs(4)	270.7(17)		
		Cs(7)	400.8(3)	Cs(10)	386.2(4)			Cs(9)	296.7(16)						
		Cs(2)	404.0(5)	Cs(7)	402.6(4)			Cs(6)	298.5(16)						
		Cs(1)	405.1(4)	Cs(3)	412.4(5)			Cs(10)	304.0(17)						
		Cs(9)	417.5(6)	Cs(4)	412.9(7)			Cs(7)	308.4(17)						
		Cs(5)	417.5(6)	Cs(5)	417.5(6)			Cs(10)	-			O(3)	284.5(14)		
Cs(5)	-	O(2)	290.0(15)	O(4)	296.0(15)	O(5)	304.0(17)								
		O(1)	294.5(12)	O(5)	304.0(17)	Cs(9)	386.2(4)								
		O(5)	298.5(16)	Cs(9)	386.2(4)	Cs(7)	386.4(4)								
		Cs(9)	383.4(5)	Cs(7)	386.4(4)	Cs(2)	412.5(5)								
		Cs(7)	384.2(3)	Cs(2)	412.5(5)	Cs(1)	421.5(3)								
		Cs(2)	408.4(5)	Cs(8)	431.8(6)	Cs(8)	431.8(6)								
		Cs(1)	416.7(3)	Cs(1)	421.5(3)	Cs(4)	442.1(5)								
		Cs(8)	429.9(6)	Cs(4)	442.1(5)	Cs(7)	-			O(3)	175.3(16)				
		Cs(4)	434.6(5)	O(3)	175.3(16)					O(4)	179.9(15)				
		O(2)	306.6(15)	O(4)	179.9(15)					O(2)	181.7(14)				
		O(2)	308.0(15)	O(2)	181.7(14)										
		Cs(6)	-	O(1)	294.5(12)										
				O(5)	298.5(16)										
				Cs(9)	383.4(5)										
Cs(7)	384.2(3)														
Cs(7)	-	Cs(2)	408.4(5)												
		Cs(1)	416.7(3)												
		Cs(8)	429.9(6)												
		Cs(4)	434.6(5)												
		O(2)	306.6(15)												
		O(2)	308.0(15)												
		O(5)	308.4(17)												
		O(3)	309.9(15)												

Table S4.5: Selected interatomic distances in pm in the monoclinic crystal structure of Cs₁₀GaO₅. Standard deviations in units of the last digit are given in parentheses.

Atoms		Distance	Atoms		Distance	Atoms		Distance		
Cs(1)	-	O(1)	277.5(9)	O(3)	314.2(8)	O(1)	-	O(1)	189.7(10)	
		O(4)	278.7(9)		Cs(7)			358.55(14)	Ga	189.7(10)
		Cs(2)	387.48(16)		Cs(9)			371.97(15)	Cs(1)	277.5(10)
		Cs(2)	401.19(17)		Cs(6)			384.88(17)	Cs(3)	286.9(10)
		Cs(5)	410.9(2)		Cs(10)			385.75(14)	Cs(6)	296.3(9)
		Cs(3)	415.2(2)		Cs(5)			403.01(17)	Cs(2)	304.5(10)
		Cs(6)	418.73(18)		Cs(3)			403.32(17)	Cs(2)	309.6(8)
Cs(2)	-	Cs(10)	425.53(18)	Cs(9)	406.99(14)	O(2)	-	Ga	186.2(9)	
		O(4)	303.1(9)	Cs(8)	422.7(2)	Cs(5)		278.7(9)		
		O(1)	304.6(9)	O(5)	264.3(12)	Cs(9)		283.7(9)		
		O(1)	309.6(9)	Cs(4)	396.2(3)	Cs(6)		287.3(10)		
		O(4)	308.6(9)	Cs(7)	422.7(2)	Cs(7)		309.9(9)		
		Cs(2)	359.0(2)	Cs(6)	429.4(3)	Cs(7)		312.8(10)		
		Cs(1)	387.48(17)	Cs(10)	431.8(3)	O(3)		-	Ga	187.0(9)
Cs(3)	-	Cs(1)	401.19(17)	O(2)	284.8(13)	Cs(3)	277.9(10)			
		Cs(3)	406.15(16)	O(3)	288.4(15)	Cs(9)	283.9(9)			
		Cs(5)	408.51(16)	O(5)	296.7(16)	Cs(10)	287.0(9)			
		Cs(6)	411.43(15)	Cs(7)	370.1(3)	Cs(7)	308.1(10)			
		Cs(10)	419.02(15)	Cs(6)	383.4(5)	Cs(7)	314.2(8)			
		O(3)	277.8(10)	Cs(10)	386.2(4)	O(4)	-	Ga	187.9(9)	
		O(1)	286.8(10)	Cs(7)	402.6(4)	Cs(1)	278.6(9)			
Cs(4)	-	Cs(7)	403.32(16)	Cs(3)	412.4(5)	Cs(5)	284.9(9)			
		Cs(2)	406.15(16)	Cs(4)	412.9(7)	Cs(10)	302.8(9)			
		Cs(1)	407.6(3)	O(5)	367.3(16)	Cs(2)	303.1(9)			
		Cs(9)	416.53(18)	Cs(4)	397.6(6)	Cs(2)	308.6(9)			
		O(5)	270.7(17)	Cs(7)	428.7(6)	O(5)	-	Cs(8)	264.3(12)	
		Cs(8)	397.6(6)	Cs(6)	429.0(6)	Cs(4)	265.0(11)			
		Cs(9)	412.5(2)	Cs(10)	431.8(6)	Cs(6)	298.1(11)			
Cs(5)	-	Cs(6)	430.3(2)	O(2)	283.7(9)	Cs(9)	301.1(12)			
		Cs(10)	438.8(3)	O(3)	283.9(9)	Cs(10)	305.4(11)			
		Cs(4)	497.0(3)	O(5)	301.1(12)	Cs(7)	309.1(11)			
		O(2)	278.7(9)	Cs(7)	371.97(15)					
		O(4)	284.9(9)	Cs(6)	383.45(17)					
		Cs(7)	403.01(17)	Cs(10)	386.04(16)					
		Cs(2)	408.50(18)	Cs(7)	406.99(14)					
Cs(6)	-	Cs(1)	410.94(18)	Cs(4)	412.5(2)					
		Cs(9)	420.12(17)	Cs(3)	416.53(19)					
		O(2)	287.3(10)	Cs(5)	420.12(17)					
		O(1)	296.3(9)	O(3)	287.0(9)					
		O(5)	298.1(11)	O(4)	302.8(9)					
		Cs(9)	383.45(17)	O(5)	305.4(11)					
		Cs(7)	384.88(17)	Cs(7)	385.75(14)					
Cs(7)	-	Cs(2)	411.44(14)	Cs(9)	386.04(16)					
		Cs(1)	418.73(18)	Cs(2)	419.02(16)					
		Cs(8)	429.4(2)	Cs(1)	425.5(2)					
		Cs(4)	430.3(2)	Cs(8)	431.8(3)					
		O(3)	308.1(10)	Cs(4)	438.8(3)					
		O(5)	309.1(11)	O(2)	186.2(9)					
		O(2)	309.9(9)	O(3)	187.0(9)					
Cs(7)	-	O(2)	312.8(10)	O(4)	187.9(9)					

Table S4.6: Selected interatomic distances in pm in the orthorhombic crystal structure of Cs₁₀AlO₅. Standard deviations in units of the last digit are given in parentheses.

Atoms		Distance	Atoms		Distance	Atoms		Distance			
Cs(1)	-	O(2)	286.8(7)	Cs(5)	-	O(2)	309.3(8)	Al	-	O(2)	177.9(9)
		O(3)	299.2(3)			O(3)	311.2(12)			O(1)	178.9(9)
		O(1)	300.1(7)			O(2)	314.4(8)			O(1)	178.9(9)
		Cs(4)	382.33(15)			Cs(4)	369.55(19)			Cs(6)	282.0(8)
		Cs(5)	383.79(13)			Cs(1)	383.79(13)			Cs(2)	284.4(7)
		Cs(8)	411.97(14)			Cs(2)	398.52(14)			Cs(1)	300.1(7)
		Cs(6)	413.49(15)			Cs(4)	404.21(18)			Cs(8)	303.4(7)
		Cs(3)	429.87(15)			Cs(7)	420.6(2)			Cs(8)	305.2(8)
Cs(2)	-	O(2)	275.74(7)	Cs(6)	-	O(1)	282.0(8)	O(2)	-	Al	177.9(9)
		O(1)	284.4(7)			O(1)	282.0(8)			Cs(2)	275.7(7)
		Cs(5)	398.52(14)			Cs(8)	382.83(19)			Cs(1)	286.8(7)
		Cs(8)	402.19(14)			Cs(8)	397.7(2)			Cs(4)	287.2(8)
		Cs(4)	411.98(15)			Cs(2)	413.02(17)			Cs(5)	309.3(8)
Cs(3)	-	O(3)	260.2(11)	Cs(7)	-	O(3)	270.1(12)	O(3)	-	Cs(3)	260.2(12)
		Cs(7)	405.9(3)			Cs(3)	405.9(3)			Cs(7)	270.1(12)
		Cs(4)	407.1(2)			Cs(5)	420.6(2)			Cs(4)	298.9(12)
		Cs(1)	429.87(1)			Cs(1)	430.23(18)			Cs(1)	299.2(3)
Cs(4)	-	O(2)	287.2(8)	Cs(8)	-	O(1)	303.4(8)			Cs(5)	311.2(12)
		O(3)	298.9(12)			O(1)	305.2(8)				
		Cs(5)	369.55(15)			Cs(6)	382.83(19)				
		Cs(1)	382.33(15)								

Table S4.7: Selected interatomic distances in pm in the orthorhombic crystal structure of Cs₁₀Al/FeO₅. Standard deviations in units of the last digit are given in parentheses.

Atoms		Distance	Atoms		Distance	Atoms		Distance			
Cs(1)	-	O(2)	287.7(13)	Cs(5)	-	O(3)	306(2)	Al/Fe	-	O(1)	190.2(12)
		O(3)	298.3(5)			O(2)	309.8(13)			O(2)	191.3(12)
		O(1)	301.2(12)			O(2)	317.8(11)			Al/Fe	190.2(12)
		Cs(4)	384.2(2)			Cs(4)	375.0(3)			Cs(6)	279.3(12)
		Cs(5)	385.15(19)			Cs(1)	385.15(19)			Cs(2)	289.1(12)
		Cs(8)	417.5(2)			Cs(2)	402.7(2)			Cs(8)	300.9(12)
		Cs(6)	419.6(2)			Cs(4)	415.8(3)			Cs(1)	301.2(12)
		Cs(3)	430.8(3)			Cs(7)	421.5(4)			Cs(8)	309.1(11)
Cs(2)	-	O(2)	276.8(14)	Cs(6)	-	O(1)	279.3(12)	O(2)	-	Al/Fe	191.3(12)
		O(1)	289.1(12)			Cs(8)	389.6(3)			Cs(2)	276.8(14)
		Cs(5)	402.7(2)			Cs(8)	407.7(4)			Cs(4)	283.1(11)
		Cs(8)	406.0(2)			Cs(2)	417.7(3)			Cs(1)	287.7(13)
		Cs(6)	417.7(3)			Cs(1)	419.6(2)			Cs(5)	309.8(13)
Cs(3)	-	O(3)	268(2)	Cs(7)	-	O(3)	271(2)	O(3)	-	Cs(3)	268(2)
		Cs(7)	405.1(5)			Cs(3)	405.1(5)			Cs(7)	271(2)
		Cs(4)	409.2(4)			Cs(5)	421.5(4)			Cs(1)	298.3(5)
		Cs(1)	430.8(3)			Cs(1)	431.4(3)			Cs(4)	300(2)
Cs(4)	-	O(2)	283.1(11)	Cs(8)	-	O(1)	300.9(12)			Cs(5)	306(2)
		O(3)	300(2)			O(1)	309.1(11)				
		Cs(5)	375.0(3)			Cs(6)	389.6(3)				
		Cs(1)	384.2(2)								

Table S4.8: Selected interatomic distances in pm in the orthorhombic crystal structure of Cs₁₀Al/GaO₅. Standard deviations in units of the last digit are given in parentheses.

Atoms		Distance	Atoms		Distance	Atoms		Distance				
Cs(1)	-	O(2)	287.1(5)	Cs(5)	-	O(3)	306.8(7)	Al/Ga	-	O(2)	185.1(4)	
		O(3)	298.95(19)			O(2)	308.7(4)			O(1)	186.1(4)	
		O(1)	301.0(5)			O(2)	315.2(4)			Al/Ga	186.1(4)	
		Cs(4)	383.31(8)			Cs(4)	371.46(10)			Cs(6)	278.3(4)	
	Cs(2)	-	Cs(5)	384.19(7)	Cs(6)	-	Cs(1)	384.19(7)	Cs(2)	-	Cs(2)	286.6(5)
			Cs(8)	414.76(7)			Cs(2)	400.81(8)			Cs(1)	301.0(5)
			Cs(6)	416.60(8)			Cs(4)	408.16(10)			Cs(8)	301.8(4)
			Cs(3)	429.48(9)			Cs(7)	419.87(15)			Cs(8)	306.3(4)
Cs(3)		-	Cs(7)	430.5(1)	Cs(7)	-	O(1)	278.3(4)	O(2)	-	Al/Ga	185.1(4)
			Cs(8)	414.76(7)			Cs(8)	384.91(10)			Cs(2)	276.9(4)
			Cs(6)	415.34(9)			Cs(8)	401.59(11)			Cs(4)	283.6(4)
			Cs(4)	415.13(8)			Cs(2)	415.34(9)			Cs(1)	287.1(5)
	Cs(4)	-	O(3)	264.6(7)	Cs(7)	-	Cs(1)	416.60(8)	O(3)	-	Cs(5)	308.7(4)
			Cs(7)	405.5(2)			O(3)	267.2(9)			Cs(5)	315.2(4)
			Cs(4)	407.43(15)			Cs(3)	405.5(2)			Cs(3)	264.6(7)
			Cs(1)	429.48(9)			Cs(5)	419.87(15)			Cs(7)	267.2(9)
Cs(4)		-	O(2)	283.6(4)	Cs(8)	-	Cs(1)	430.5(1)	Cs(1)	-	Cs(1)	298.95(19)
			O(3)	302.1(9)			O(1)	301.8(4)			Cs(4)	302.1(9)
			Cs(5)	371.46(10)			O(1)	306.3(4)			Cs(5)	306.8(7)
			Cs(1)	383.31(8)			Cs(6)	384.91(10)				

Table S4.9: Selected angles in ° in the monoclinic crystal structures of Cs₁₀AlO₅ (left) and Cs₁₀AlO₅ (right). Standard deviations in units of the last digit are given in parentheses.

Atoms		Angle	Atoms		Angle
O(3)	- Al - O(4)	110.2(7)	O(3)	- Ga - O(4)	111.8(4)
O(3)	- Al - O(2)	108.3(7)	O(3)	- Ga - O(2)	107.9(4)
O(3)	- Al - O(1)	108.7(7)	O(3)	- Ga - O(1)	109.2(4)
O(4)	- Al - O(2)	108.8(6)	O(4)	- Ga - O(2)	108.5(4)
O(4)	- Al - O(1)	110.9(7)	O(4)	- Ga - O(1)	108.6(4)
O(2)	- Al - O(1)	110.1(6)	O(2)	- Ga - O(1)	110.8(4)
Cs(8)	- O(5) - Cs(9)	171.4(6)	Cs(8)	- O(5) - Cs(9)	169.7(5)
Cs(4)	- O(5) - Cs(7)	168.6(7)	Cs(4)	- O(5) - Cs(7)	168.4(5)
Cs(6)	- O(5) - Cs(10)	152.6(6)	Cs(6)	- O(5) - Cs(10)	151.5(4)

Table S4.10: Selected angles in ° in the orthorhombic crystal structures of Cs₁₀AlO₅ (left), Cs₁₀Al/FeO₅ (centre) and Cs₁₀Al/GaO₅ (right). Standard deviations in units of the last digit are given in parentheses.

Atoms		Angle	Atoms		Angle	Atoms		Angle
O(1)	- Al - O(1)	109.2(3)	O(1)	- Al/Fe - O(1)	108.1(5)	O(1)	- Al/Ga - O(1)	108.36(19)
O(1)	- Al - O(2)	108.0(3)	O(1)	- Al/Fe - O(2)	109.5(5)	O(1)	- Al/Ga - O(2)	108.92(18)
O(1)	- Al - O(2)	110.6(3)	O(1)	- Al/Fe - O(2)	109.6(5)	O(1)	- Al/Ga - O(2)	110.54(18)
O(2)	- Al - O(2)	110.4(3)	O(2)	- Al/Fe - O(2)	110.6(5)	O(2)	- Al/Ga - O(2)	109.53(19)
Cs(3)	- O(3) - Cs(5)	167.7(5)	Cs(3)	- Al/Fe - Cs(5)	168.7(9)	Cs(3)	- O(3) - Cs(5)	166.9(3)
Cs(4)	- O(3) - Cs(7)	166.9(5)	Cs(4)	- Al/Fe - Cs(7)	170.3(9)	Cs(4)	- O(3) - Cs(7)	168.9(4)
Cs(1)	- O(3) - Cs(1)	151.3(3)	Cs(1)	- Al/Fe - Cs(1)	153.4(3)	Cs(1)	- O(3) - Cs(1)	152.06(13)

Table S4.11: Crystallographic data and specifications to Rietveld refinement of Cs₂O.

phase	Cs ₂ O
formula mass	281.81
crystal system / space group	$R\bar{3}m$
lattice parameters	$a = 4.2513 \text{ \AA}$ $c = 18.968 \text{ \AA}$
cell volume	296.89 \AA^3
Z	3
X-ray density [gcm^{-3}]	4.7286
linear absorption coefficient [cm^{-1}]	200.01
radiation	Mo-K α_1 ($\lambda = 70.930 \text{ pm}$)
monochromator	Ge(111)
diffractometer	Stoe StadiP
detector	linear PSD
2θ -range [$^\circ$]	3–45
temperature [K]	298
data points	4200
number of observed reflections	69
number of parameters	34
constraints	0
software	TOPAS Academic 4.1
structure refinement	Rietveld-method
profile function	fundamental parameters model
background function	shifted Chebychev
R_p	4.482
R_{wp}	6.438
R_{exp}	5.424
R_{Bragg}	0.8880
χ^2	1.187

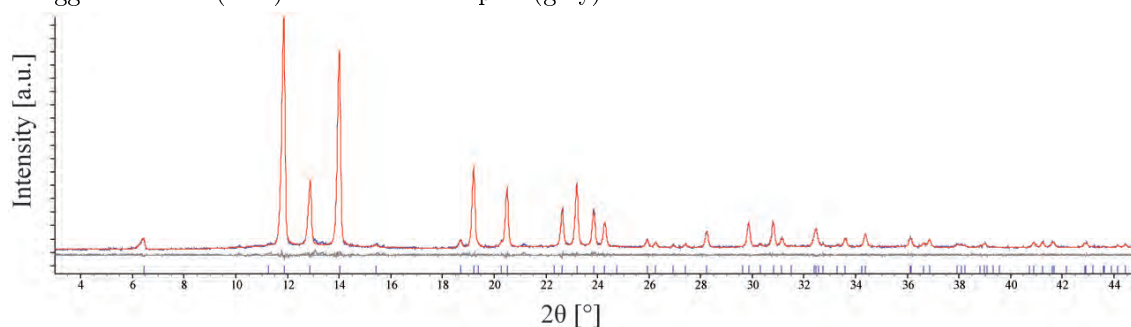
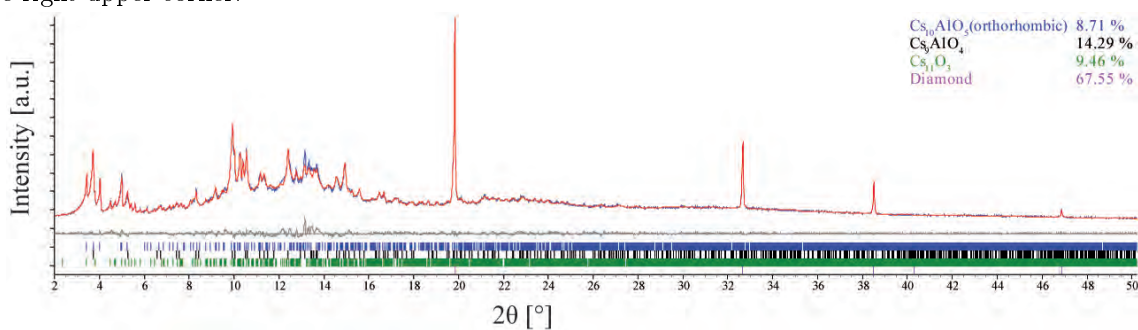
Figure S4.1: Observed (blue line) and calculated (red line) powder diffraction pattern of Cs₂O as well as Bragg reflections (blue) and differential plot (grey).

Table S4.12: Crystallographic data and specifications to Rietveld refinement of the three phase sample of $\text{Cs}_{10}\text{AlO}_5$, Cs_9AlO_4 and Cs_{11}O_3 . Diamond powder was added for powder preparation purposes to allow proper grinding.

phase	$\text{Cs}_{10}\text{AlO}_5$	Cs_9AlO_4	Cs_{11}O_3	diamond
formula mass	1436.08	1287.17	1510.01	12.01
crystal system / space group	<i>Pnmm</i>	<i>I4/mcm</i>	<i>P2₁/c</i>	<i>Fd$\bar{3}m$</i>
lattice parameters	$a = 11.152(2) \text{ \AA}$ $b = 23.736(5) \text{ \AA}$ $c = 12.217(3) \text{ \AA}$	$a = 15.4780(13) \text{ \AA}$ $c = 12.3863(16) \text{ \AA}$	$a = 17.610(2) \text{ \AA}$ $b = 9.2309(10) \text{ \AA}$ $c = 24.057(3) \text{ \AA}$ $\beta = 100.22(12)^\circ$	$a = 3.5675(7) \text{ \AA}$
cell volume	$3233.8(12) \text{ \AA}^3$	$2967.3(6) \text{ \AA}^3$	$3848.3(9) \text{ \AA}^3$	$45.40(24) \text{ \AA}^3$
Z	4	4	4	1
X-ray density [gcm^{-3}]	2.9496(11)	2.8811(6)	2.606(6)	3.51407(19)
linear absorption coefficient [cm^{-1}]	122.7(4)	120.38(3)	113.06(3)	2.19989(12)
radiation		- Mo-K α_1 ($\lambda = 70.930 \text{ pm}$) -		
monochromator		- Ge(111) -		
diffractometer		- Stoe StadiP -		
detector		- MYTHEN 1K -		
2θ -range [$^\circ$]		- 3-45 -		
temperature [K]		- 298 -		
data points		- 4200 -		
number of observed reflections		- 69 -		
number of parameters		- 34 -		
constraints		- 0 -		
software		- TOPAS Academic 4.1 -		
structure refinement		- Rietveld method -		
profile function		- fundamental parameters model -		
background function		- shifted Chebychev -		
R_p		- 4.482 -		
R_{wp}		- 6.438 -		
R_{exp}		- 5.424 -		
R_{Bragg}	1.287	1.399	1.631	0.2905
χ^2		- 1.187 -		

Figure S4.2: Observed (blue line) and calculated (red line) powder diffraction pattern of $\text{Cs}_{10}\text{AlO}_5$, Cs_9AlO_4 and Cs_{11}O_3 as well as Bragg reflections (blue for $\text{Cs}_{10}\text{AlO}_5$, black for Cs_9AlO_4 and green for Cs_{11}O_3) and differential plot (grey). Respective weight percentages of the different phases are given in the right upper corner.



4 Chemical Twinning of Salt and Metal in the Subnitridometalates

$\text{Ba}_{23}\text{Na}_{11}(\text{MN}_4)_4$ with $\text{M} = \text{V}, \text{Nb}, \text{Ta}$

Matthias Wörsching, Frank Tambornino, Stefan Datz, Constantin Hoch

published in: *Angew. Chem. Int. Ed.* **2016**, *55*, 10868–10871.
DOI: 10.1002/anie.201605113

published in: *Angew. Chem.* **2016**, *128*, 11026–11030. DOI: 10.1002/anie.201605113

Reprinted (adapted) with permission from Angewandte Chemie. Copyright 2016 John Wiley and Sons.

Abstract

The subnitridometalates $\text{Ba}_{23}\text{Na}_{11}(\text{MN}_4)_4$ ($\text{M} = \text{V}, \text{Nb}, \text{Ta}$) crystallize in a new structure type, which shows ionic ortho-nitridometalate anions and motifs from simple (inter)-metallic packings: Na-centered $[\text{Na}_8]$ cubes as cutouts of the bcc structure of elemental Na and Na-centered $[\text{Ba}_{10}\text{Na}_2]$ icosahedra as found in Laves phases, for example. Single-crystal and powder X-ray diffraction studies in combination with quantum-chemical calculations of the electronic structure and Raman spectroscopy support the characterization of the subnitridometalates as “chemical twins”. They consist of independent building units with locally prevalent ionic or metallic bonding in an overall metallic compound.

4.1 Introduction, Results, Discussion and Conclusion

In recent years, several ternary alkali-metal suboxometalates with the composition A_9MO_4 ($A = Rb, Cs$; $M = Al, Ga, Fe, Sc, In$)^[1] and $Cs_{10}MO_5$ ($M = Al, Ga, Fe$)^[2] have been described. The chemical bonding in these subvalent compounds can be described as ordered intergrowth of low-dimensional ionic structural compartments in a metallic matrix, as first established for alkali-metal suboxides.^[3] The intergrowth can be seen as a special case of ordered heterostructures, namely as a chemical twin. The suboxometalates expanded the structural chemistry of the suboxides by replacing monoatomic oxide anions with complex *ortho*-oxometalate anions. Alkaline-earth subnitridometalates now expand the chemistry of binary subnitrides, for example, Ba_2N or Ba_3N ,^[4] to structures with complex *ortho*-nitridooxometalate anions. All three subnitridometalates $Ba_{23}Na_{11}(MN_4)_4$ ($M = V, Nb, Ta$) crystallise isotypically in the tetragonal crystal system with the space group $P4_2/n$.^[7] The crystal structure contains three distinct building blocks: *ortho*-nitridometalate anions $[MN_4]^{7-}$, centered $[Na@Na_8]$ cubes, and centered $[Na@Ba_{10}Na_2]$ icosahedra (Figure 4.1). The tetrahedral $[MN_4]^{7-}$ anions show geometric details that are in good agreement with those of known ionic nitridometalates (Table 6.2). The M–N bond is only weakly influenced by the metallic surrounding in the subnitridometalates and was investigated by Raman spectroscopy on single-crystal samples of $Ba_{23}Na_{11}(VN_4)_4$, $Ba_{23}Na_{11}(NbN_4)_4$ and $Ba_{23}Na_{11}(Ta_4N_4)_4$ (Figure 4.3). In each case, we observed a single broad signal with a maximum at low wave numbers between 102 cm^{-1} and 106 cm^{-1} . As literature data for Raman frequencies of $[MN_4]^{7-}$ are unavailable, a single-crystal of $Ba_5(NbN_4)_4N_x$ was analyzed under similar conditions as a reference.^[9] Its spectrum shows two signals at 102 cm^{-1} and 125 cm^{-1} corresponding to two of the four Raman-active vibration modes of the tetrahedral $[NbN_4]^{7-}$ species. A regular MX_4 tetrahedron is expected to show one A_1 , one E , and two F_2 vibration modes. We could assign the two signals to the A_1 (stretching vibrations only) and the E mode (deformation vibrations only). The much weaker F_2 modes could not be detected due to high background noise. For $Ba_{23}Na_{11}(MN_4)_4$, broad signals were observed extending over a range from 85 cm^{-1} to 140 cm^{-1} with asymmetric broadening to higher wavenumbers. These signals cover the range expected for the four vibration modes of tetrahedral $[MN_4]^{7-}$ anions, and the loss of resolution with respect to the spectrum of $Ba_5(NbN_4)_4N_x$ may be attributed to the metallic behavior and resulting optical phonons. Similar observations were made for intermetallic compounds, such as $MgCu_2$ -type Laves phases.^[10]

The ionic nitridometalate anions $[MN_4]^{7-}$ are coordinated by augmented triangular prisms (Johnson polyhedron J_{49})^[11] of seven Ba atoms (Ba2 to Ba7, see the Supporting Information, Tables S5.2–S5.4). The four crystallographically independent N atoms are located on two triangular and two square faces of the Johnson polyhedron (Figure 4.1 a). The augmented trigonal prisms are connected to tetramers through common edges. This results in two sets of Ba atoms, namely terminal ones (Ba2, Ba3, and Ba4) and connecting ones (Ba5, Ba6, and Ba7; the latter being centred in the tetramer of augmented trigonal prisms), correlating with two sets of slightly different anisotropic thermal displacement parameters for the Ba atoms (see Tables S5 to S7). Bonding within the $[Ba_7MN_4]$ prisms is prevalently ionic, as the Ba–N distances agree with those in the respective ionic compounds Ba_2VN_3 , Ba_2NbN_3 and $Ba_2Ta_4N_3$ (Table 6.2).

These ionic blocks are twinned with a metallic substructure consisting of two distinct

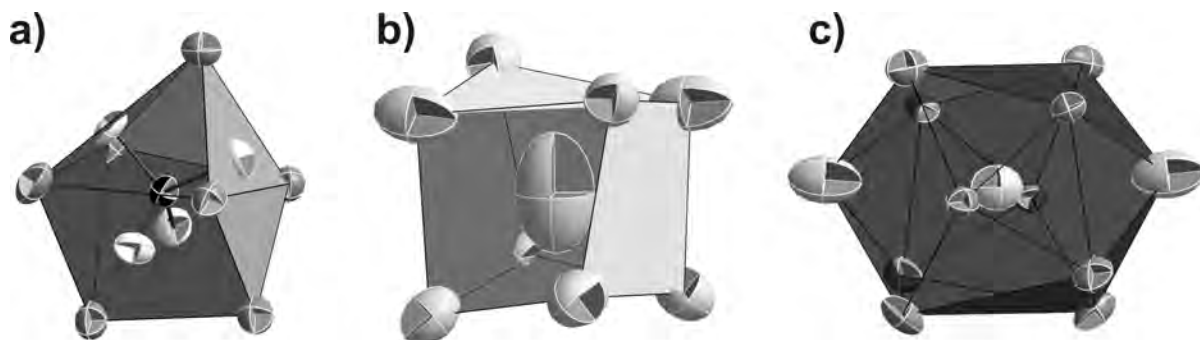
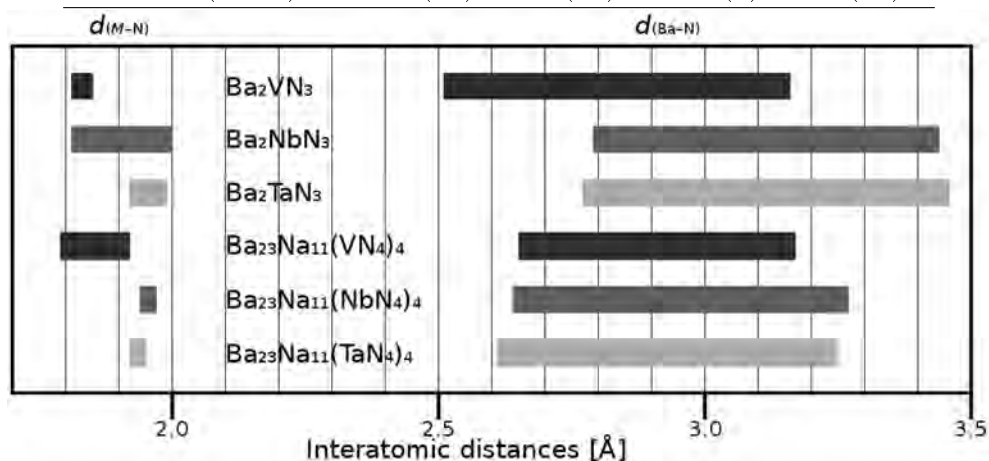


Figure 4.1: Coordination polyhedra in $\text{Ba}_{23}\text{Na}_{11}(\text{MN}_4)_4$. a) $[\text{Ba}_7\text{MN}_4]$ augmented triangular prism; b) distorted $[\text{Na}_8]\text{Na}$ cube; c) distorted $[\text{Ba}_{10}\text{Na}_2]\text{Na}$ icosahedron; M (M = V, Nb, Ta): black, Ba: dark grey; Na: light grey; N: white. Ellipsoids are drawn at 90 % probability level.

Table 4.1: Selected geometric details of ionic nitridometalates from literature and the new subnitridometalates.

Compound	$d_{(\text{M}-\text{N})}$ [\AA]	$d_{(\text{Ba}-\text{N})}$ [\AA]
Ba_2VN_3 ^[8]	1.81(4)–1.854(8)	2.51(4)–3.162(18)
Ba_2NbN_3 ^[8]	1.876(13)–2.000(10)	2.792(12)–3.435(12)
Ba_2Ta_3 ^[8]	1.921(13)–1.989(9)	2.772(13)–3.461(18)
$\text{Ba}_{23}\text{Na}_{11}(\text{VN}_4)_4$	1.788(16)–1.822(17)	2.652–3.174(16)
$\text{Ba}_{23}\text{Na}_{11}(\text{NbN}_4)_4$	1.940(7)–1.969(7)	2.640(7)–3.270(7)
$\text{Ba}_{23}\text{Na}_{11}(\text{Ta}_4)_4$	1.926(10)–1.950(10)	2.611(8)–3.250(10)



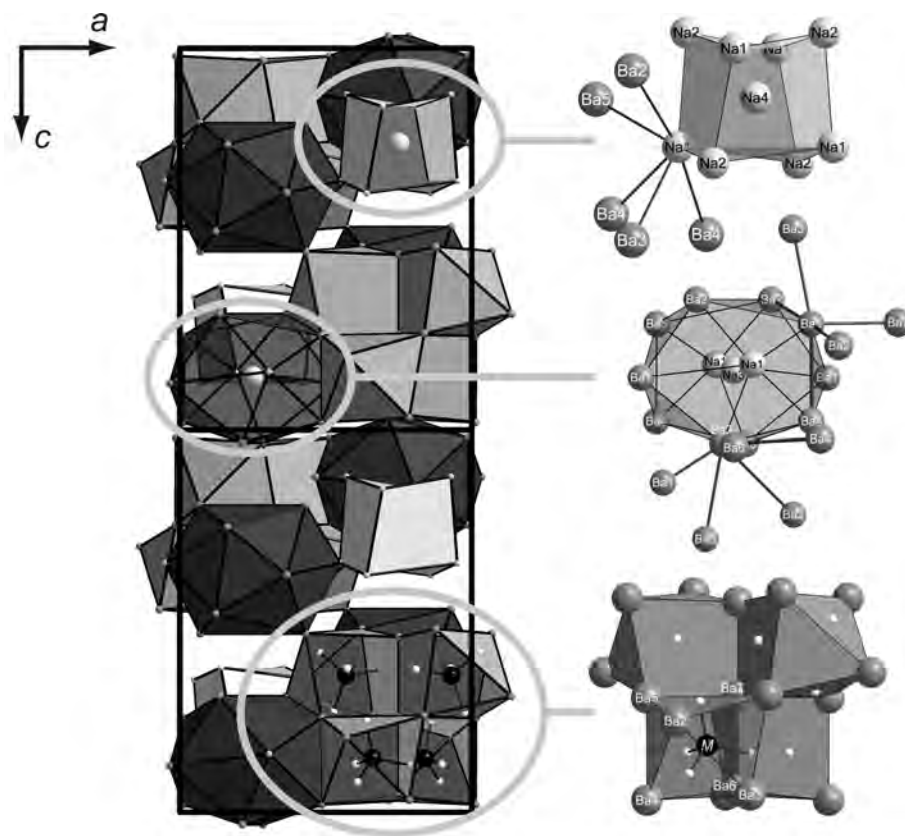


Figure 4.2: Crystal structure of $\text{Ba}_{23}\text{Na}_{11}(\text{MN}_4)_4$ along the crystallographic b -axis. Augmented triangular prisms: dark grey; distorted cubes: light grey; distorted icosahedra: black.

motifs that are best described as cutouts from well-known simple metallic structure types.

The first motif is a distorted centered $[\text{Na}@\text{Na}_8]$ cube of sodium atoms (Na2 and Na4) coordinated to the central Na1 atom (Figure 4.1 b). This arrangement strongly resembles the bcc structure of elemental sodium. The distortion of the cube leads to two sets of Na–Na distances: Na2 has is further away from the central Na1 atom ($3.875(6) \text{ \AA}$) than Na4 ($3.509(8) \text{ \AA}$). The average of 3.692 \AA is only about 1 % larger than the Na–Na distance in metallic Na (3.656 \AA).^[12] Na4 connects the sodium cube with the second metallic structural motif, resulting in the considerable distortion of the cube. Analysis of the interatomic distances (see Tables S5.8 to S5.10), combined with the large anisotropic thermal displacement parameter of Na1 (Figure 4.1 b and Tables S5 to S7) corroborates the metallic character for Na1 or even suggests a $\text{Na}^{\delta-}$ atom. This situation would be comparable to the Cs atom in Cs_9MO_4 , which is only in contact with other Cs atoms.^[1] The second metallic structural motif is a $[\text{Na}@\text{Ba}_{10}\text{Na}_2]$ icosahedron with Na3 at the center (Figure 4.1 c). Na3 is coordinated by two Na1 atoms and by atoms Ba1 to Ba5. Ba1 does not participate in the $[\text{Ba}_7\text{MN}_4]$ prisms, while the $[\text{Ba}_7\text{MN}_4]$ prisms and $[\text{Na}@\text{Ba}_{10}\text{Na}_2]$ icosahedra are connected by Ba3 through common vertices, and by Ba2, Ba4 and Ba5 through common edges (Figure 4.2). In contrast to Laves phases, for example, BaNa_2 , the icosahedral coordination consists of ten Ba and two Na atoms (6 Ba and 6 Na atoms in BaNa_2), leading to significantly larger Na–Na distances (Na1–Na3:

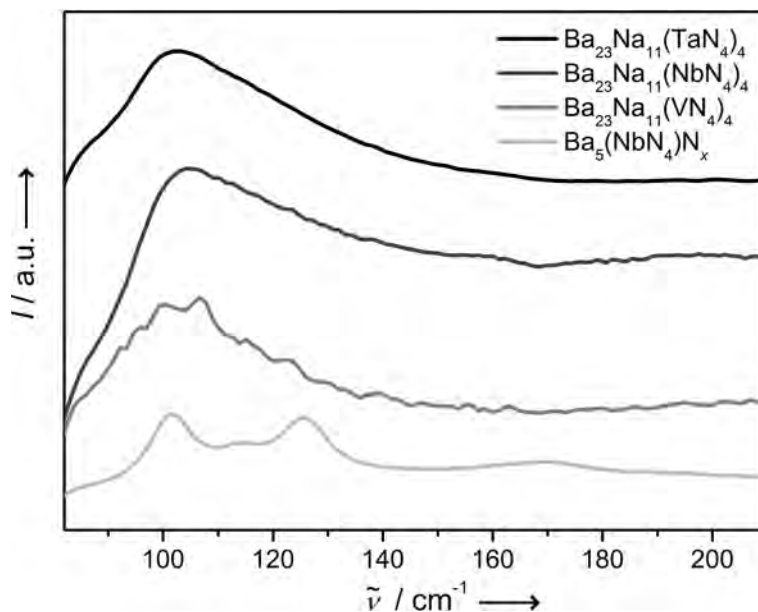


Figure 4.3: Raman spectra of $\text{Ba}_{23}\text{Na}_{11}(\text{TaN}_4)_4$ (black), $\text{Ba}_{23}\text{Na}_{11}(\text{NbN}_4)_4$ (dark grey), $\text{Ba}_{23}\text{Na}_{11}(\text{VN}_4)_4$ (medium grey) and $\text{Ba}_5(\text{NbN}_4)_x$ (light grey).

4.387(9) Å in $\text{Ba}_{23}\text{Na}_{11}(\text{MN}_4)_4$ compared to 3.72 Å in BaNa_2). Apparently, the higher number of Ba atoms in the $[\text{Na}@\text{Ba}_{10}\text{Na}_2]$ icosahedron prevents the formation of closer Na–Na contacts as found for the icosahedral $[\text{Na}@\text{Ba}_6\text{Na}_6]$ coordination in BaNa_2 , and Na–Na distances are forced to adopt values that are close to typical Ba–Na distances (see Tables S8 to S11). The average Ba–Na distance in the $[\text{Na}@\text{Ba}_{10}\text{Na}_2]$ icosahedra amounts to 4.311 Å (ca. 1 % larger than 4.27 Å in BaNa_2).^[6] The icosahedral void may thus be filled with larger metal atoms such as K, Rb, or Cs. The crystal structure of the barium sodium subnitridometalates is built from the abovementioned structural motifs by sharing common atoms: One Na atom of the $[\text{Na}@\text{Na}_8]$ cube is also an apical atom of the $[\text{Na}@\text{Ba}_{10}\text{Na}_2]$ icosahedron, and terminal Ba atoms of the ionic $[\text{Ba}_7\text{MN}_4]$ prisms participate in the icosahedron as well. There is a clear distinction between the Ba atoms belonging only to the ionic substructure in the sense of closer distances to the neighboring atoms (suggesting Ba^{2+} cations) and those Ba atoms in the partially metallic structures with longer distances to their respective neighbors, pointing towards metallic behavior. This diversification of atoms of one and the same element owing to different bonding modes is known from alkali-metal suboxides and subnitrides of earth-alkaline metals and alkali metals.^[1,3,4]

The calculated electronic structure of $\text{Ba}_{23}\text{Na}_{11}(\text{Ta}_4\text{N}_4)_4$ emphasizes the picture of independent building units with either metallic or ionic character, resulting in overall metallic behavior and a "chemical twin". The total density of states and selected partial densities are shown in Figure 4.4. The total density of states (DOS) shows no band gap at the Fermi level, hence $\text{Ba}_{23}\text{Na}_{11}(\text{Ta}_4\text{N}_4)_4$ is a metal. The sharp bands between about -4 and -2 eV were attributed to the anionic $[\text{Ta}_4\text{N}_4]^{7-}$ part. These bands with low dispersion resemble the band structure representation of an MO scheme for the quasi-molecular tetrahedral anion, and only few interactions with adjacent Ba atoms could be observed. The Ba atoms have different surroundings, most of them being part of metallic

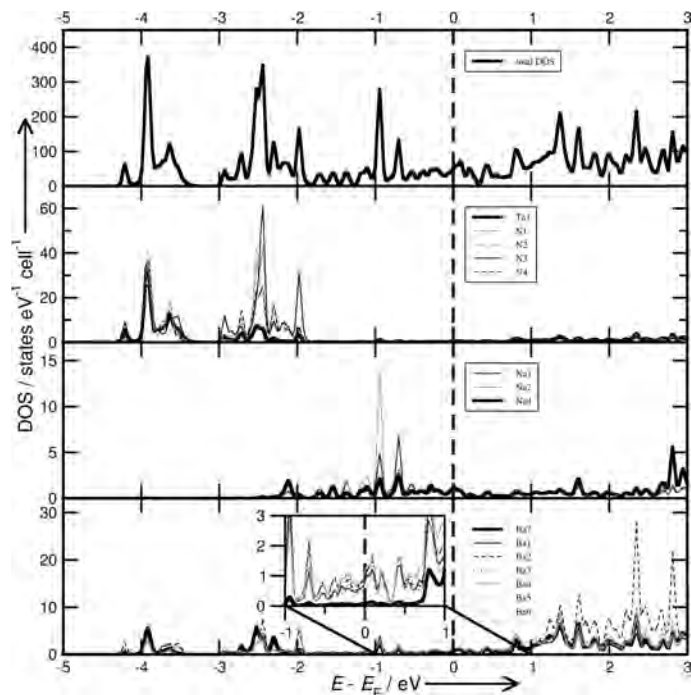


Figure 4.4: Density of states calculated for $\text{Ba}_{23}\text{Na}_{11}(\text{TaN}_4)_4$. Top: total DOS, one below: partial DOS for the atoms of the TaN_4 anions, two below: partial DOS for the Na atoms of the metallic $[\text{Na}@\text{Na}_8]$ cube, bottom: partial DOS of all Ba atoms. Inset: magnified view of the region close to E_F .

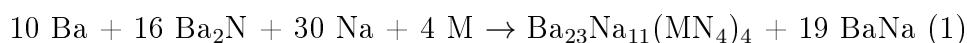
$[\text{Na}@\text{Ba}_{10}\text{Na}_2]$ icosahedra and at the same time coordinating the nitridotantalate anions. These Ba atoms show low but significant electron density at the Fermi level and contribute to the metallic behavior. Only Ba7, the center of the tetrameric $[\text{Ba}_{19}(\text{TaN}_4)_4]$ unit (Figure 4.4), is different. It is not in contact with metallic parts of the structure and shows no electron density at the Fermi level, corresponding to a real Ba^{2+} cation. The Ba states show mixing with the $[\text{TaN}_4]^{7-}$ states but almost no interaction with the states of the $[\text{Na}@\text{Na}_8]$ cubes. These cubes consist of metallic Na atoms as they all show considerable and similar electron densities at the Fermi level, supporting the presence of Na^0 atoms rather than for Na^+ cations. Thus the well-segmented total DOS can be deconvoluted into the contributions of the three different building units, emphasizing the picture of chemical twinning.

In conclusion, with the series of barium sodium subnitridometalates of V, Nb and Ta, we have presented a new class of subvalent compounds with tetrahedral nitridometalate anions. There is, however, no reason for subnitridometalates to be limited to these metals. Further expansions of this structure class seem promising on different ways. Transition metals with radii and valence electron concentrations similar to those of V, Nb and Ta as well as pentavalent main-group elements such as As, Sb, Bi or even P could be incorporated into the anionic sublattice. Various mixed crystal series from the isotypic compounds should be viable, comparable to the suboxometalates.^[1,2] Modifications of the metallic sublattice should also be feasible. Akin to alkaline-earth metal subnitrides and alkali metal suboxides, the content of metallicly bound alkali-metal atoms may be increased or reduced. The voids within the Ba/Na icosahedron seem large enough to incorporate metal atoms such as K, Rb or Cs, or perhaps also alkaline-earth met-

als. This opens new possibilities to unite ionic and metallic aspects and properties in one material, and to change them independently as the different sublattices show only marginal interaction.

4.2 Experimental section

The subnitridometalates were synthesised by reaction of Ba₂N (made from the elements, purity confirmed by Rietveld refinement with the software TOPAS Academic4,^[13] see Figure S2), Ba (distilled, 99.95 %, SMT Metalle Wimmer, Weinburg, Austria), M (M = V, Nb, Ta; powder, 99.5 %, Alfa Aesar, Karlsruhe, Germany or Merck, Darmstadt, Germany), and Na (distilled, MPI für Festkörperforschung Stuttgart, Germany) at 500 °C in argon atmosphere. Typical sample amounts were 1.5 g with a molar ratio Ba₂N/Ba/M/Na = 8:5:2:15. Employing tantalum crucibles led to the partial occupation of the vanadium positions in Ba₂₃Na₁₁(VN₄)₄ with 7.0(5) % Ta, as shown by single-crystal structure refinement. The formation temperature of the subnitridometalates is low with respect to the melting temperatures of Ba (729 °C) and Ba₂N (> 900 °C, according to temperature-dependent powder diffractometry, see Figure S5.1). Higher temperatures led to the formation of simple ionic nitridometalates and to reaction of the starting material mixture with the crucible materials. The necessarily low reaction temperatures could be realized with the help of a Ba/Na flux. Appropriate reaction temperatures and respective Ba/Na ratios were taken from the phase diagram of the binary system Ba–Na.^[5] As a consequence, reaction products were always accompanied by BaNa^[6] as observed in the Rietveld refinements (see Figures S5.3 to S5.5) according to the Equation (1):



Syntheses leading to phase-pure products would require higher nitride contents in the starting material mixture. As a barium nitride Ba₃N₂ is unknown and sodium nitride Na₃N is not available in larger quantities, Ta₃N₅ would be the only feasible possibility; however, V₃N₅ and Nb₃N₅ are unknown. Employment of azides such as Ba(N₃)₂ or NaN₃ is rather unpromising as the evolving nitrogen would be not reactive at the low temperatures. At the moment, we are trying to establish alternative synthetic routes leading to lower amounts of or no accompanying phases; however, the difficulty consists of the necessity for low reaction temperatures for the formation of subnitridic phases while the temperature for complete reaction of the starting material mixture increases with the nitridic content.

A general problem that is encountered when Ba-rich compounds are synthesized from metallic Ba is possible hydride formation. To discern whether particular hydrides are incorporated or not is of especially high importance when compounds receive attention owing to electronically non-precise formal charge distributions. A quite obvious hint for the absence of hydridic species is the observation that in all experiments, the subnitride phases were the major components and not minor byproducts. Further evidence was obtained by solid-state ¹H NMR spectroscopy (see Figure S5.6). Quantitative hydride incorporation in the subnitridometalates would lead to sharp and significant signals even in stationary spectra, at chemical shifts of about –6 to –8 ppm.^[15] The observed broad

and weak signal around 0 ppm is most probably caused by traces of hydrolysis products of the delicate samples or by traces of humidity in the NMR rotor walls.

For single-crystal structure analysis,^[7] suitable specimens were isolated under dry paraffin oil, sealed in oil-filled glass capillaries, and checked for crystal quality on the respective diffractometer systems (see Table S5.1).

The DFT calculations of the electronic band structure were performed with the program package WIEN2000, employing the full-potential linearized augmented plane wave (FP-LAPW) method. The exchange and correlation functional of Perdew, Burke, and Ernzerhof with generalised gradient approximation (GGA) was applied. The Muffin-Tin radii were set to $2.5 a_0$ for Ba and Na, to $1.97 a_0$ for Ta and to $1.61 a_0$ for N. The number of basis functions was determined by the value of $r_{\text{mt}} k_{\text{max}} = 7$ with k_{max} as the largest k vector. The separation energy was set to -6 Ry. 18 k points in the Brillouin zone (3 thereof in the irreducible Brillouin zone) were calculated in a $3 \times 3 \times 2$ Monkhorst-Pack grid.^[16]

For Raman spectroscopic analysis, a He-Ne laser with a 1 mm focus in a confocal Raman microscope (LabRSM HG UV/Vis, Horiba Jobin Ivon GmbH, München, combined with an Olympus BX 41 microscope) equipped with a CCD detector was focused on $\text{Ba}_{23}\text{Na}_{11}(\text{MN}_4)_4$ single crystals in capillaries filled with dry paraffin oil. For comparison, a $\text{Ba}_5(\text{NbN}_4)_4\text{N}_x$ single crystal was measured under identical conditions.

4.3 Acknowledgement

We thank Prof. Dr. Wolfgang Schnick for generous financial support and outstanding resources, Prof. Dr. Thomas Bein for access to the Raman spectrometer, and Martin Daiger for sample preparation. We are particularly grateful to Christian Minke and Dr. Thomas Bräuniger for NMR spectroscopic measurements.

4.4 References

- [1] C. Hoch, J. Bender, A. Simon, *Angew. Chem. Int. Ed.* **2009**, *48*, 2415; *Angew. Chem.* **2009**, *121*, 2451; b) C. Hoch, J. Bender, A. Wohlfarth, A. Simon, *Z. Anorg. Allg. Chem.* **2009**, *635*, 1777; c) C. Hoch, I. Schellenberg, R. Pöttgen, *Z. Naturforsch. B* **2011**, *66*, 441.
- [2] M. Wörsching, C. Hoch, *Inorg. Chem.* **2015**, *54*, 7058.
- [3] a) K.-R. Tsai, P. M. Harris, E. N. Lassette, *J. Phys. Chem.* **1956**, *60*, 345; b) A. Simon, H.-J. Deiseroth, E. Westerbeck, B. Hillenkötter, *Z. Anorg. Allg. Chem.* **1976**, *423*, 203; c) A. Simon, E. Westerbeck, *Z. Anorg. Allg. Chem.* **1977**, *428*, 187; d) A. Simon, *Z. Anorg. Allg. Chem.* **1977**, *481*, 5.
- [4] a) U. Steinbrenner, A. Simon, *Z. Anorg. Allg. Chem.* **1998**, *624*, 228; b) O. Reckweg, F. J. DiSalvo, *Solid State Sci.* **2002**, *4*, 575.
- [5] A. D. Pelton, *Bull. Alloy Phase Diagr.* **1985**, *6*, 26.
- [6] a) G. J. Snyder, A. Simon, *J. Chem. Soc. Dalton Trans.* **1994**, *7*, 1159; b) G. J. Snyder, A. Simon, *Z. Naturforsch. B* **1993**, *49*, 189.
- [7] a) $\text{Ba}_{23}\text{Na}_{11}(\text{VN}_4)_4$: $T = 293$ K; tetragonal, space group $P4_2/n$ (No. 86), $a = 14.131(17)$ Å, $c = 18.537(2)$ Å, $V = 3703.0(9)$ Å³, $Z = 2$, $\rho = 3.476$ gcm⁻³; diffractometer: Bruker D8-Quest ($\text{MoK}\alpha$ radiation, Göbel mirror); $2\theta_{\text{max}} = 50.00^\circ$; 29461 observed intensities, 3217 unique; Lorentz, polarization, and semi-empirical absorption correction;^[14] least-squares refinement on I (all atoms anisotropic) with SHELXL97;^[14] 125 free variables, R values ($I \geq 2\sigma(I)$: $R1 = 0.0823$, $wR2 = 0.1259$; min./max. residual electron density: $-2.461/+2.303$ e⁻ Å⁻³; b) $\text{Ba}_{23}\text{Na}_{11}(\text{NbN}_4)_4$: $T = 293$ K; tetragonal, space group $P4_2/n$ (No. 86), $a = 14.3724(9)$ Å, $c = 18.8431(5)$ Å, $V = 3892.3(4)$ Å³, $Z = 2$, $\rho = 3.419$ gcm⁻³; diffractometer: STOE IPDS-1 ($\text{MoK}\alpha$ radiation, graphite monochromator); $\mu(\text{MoK}\alpha) = 12.047$ mm⁻¹; $2\theta_{\text{max}} = 55.00^\circ$; 39074 observed intensities, 4479 unique; Lorentz, polarization, and numerical absorption correction;^[14] least-squares refinement on I (all atoms anisotropic) with SHELXL97;^[14] 123 free variables, R values ($I \geq 2\sigma(I)$: $R1 = 0.0373$, $wR2 = 0.0653$; min./max. residual electron density: $-1.359/+1.375$ e⁻ Å⁻³; c) $\text{Ba}_{23}\text{Na}_{11}(\text{Ta}_4\text{N}_4)_4$: $T = 293$ K; tetragonal, space group $P4_2/n$ (No. 86), $a = 14.3603(12)$ Å, $c = 18.7552(17)$ Å, $V = 3867.7(6)$ Å³, $Z = 2$, $\rho = 3.744$ gcm⁻³; diffractometer: STOE IPDS-1 ($\text{MoK}\alpha$ radiation, graphite monochromator); $\mu(\text{MoK}\alpha) = 17.186$ mm⁻¹; $2\theta_{\text{max}} = 55.00^\circ$; 38628 observed intensities, 4447 unique; Lorentz, polarization, and semi-empirical absorption correction;^[14] least-squares refinement on I (all atoms anisotropic) with SHELXL97;^[14] 123 free variables, R values ($I \geq 2\sigma(I)$: $R1 = 0.0387$, $wR2 = 0.0590$; min./max. residual electron density: $-1.007/+1.719$ e⁻ Å⁻³; d) further details on crystal-structure investigations may be obtained from the Fachinformationszentrum Karlsruhe, 76344 Eggenstein-Leopoldshafen, Germany (fax: (+49)7247-808-666; email: crysdata@fiz-karlsruhe.de) on quoting the depository numbers CSD-431345 ($\text{Ba}_{23}\text{Na}_{11}(\text{VN}_4)_4$), CSD-431343 ($\text{Ba}_{23}\text{Na}_{11}(\text{NbN}_4)_4$) and CSD-431344 ($\text{Ba}_{23}\text{Na}_{11}(\text{Ta}_4\text{N}_4)_4$).

- [8] a) D. H. Gregory, M. G. Barker, P. P. Edwards, D. J. N. Siddons, *Inorg. Chem.* **1995**, *34*, 3912; b) O. Seeger, M. Hofmann, J. Strähle, *Z. Anorg. Allg. Chem.* **1994**, *620*, 2008; c) F. K.-J. Helmlinger, P. Höhn, R. Kniep, *Z. Naturforsch. B* **1993**, *48*, 1015.
- [9] O. Reckeweg, C. Lind, A. Simon, F. DiSalvo, *J. Alloys Compd.* **2004**, *384*, 98.
- [10] a) J. Weidlein, U. Müller, D. Dehnicke, *Schwingungsspektroskopie – eine Einführung*, Georg Thieme, Stuttgart, **1988**, p.135; b) H. Ibach, H. Lüth, *Festkörperphysik*, Springer, Heidelberg, **2008**, 105; c) J. Su, C. Zhu, *Mater. Res. Bull.* **2003**, *38*, 2025; d) L.-S. Hsu, M. A. Tischler, *Phys. Status Solidi B* **1999**, *214*, 419.
- [11] N. W. Johnson, *Can. J. Math.* **1966**, *18*, 169.
- [12] a) P. E. Rauch, A. Simon, *Angew. Chem. Int. Ed. Engl.* **1992**, *31*, 1519; *Angew. Chem.* **1992**, *104*, 1505; b) R. Berliner, O. Fajen, H. G. Smith, R. L. Hitterman, *Phys. Rev. B* **1989**, *40*, 12086.
- [13] A. A. Coelho, TOPAS-Academic, Version 4.1, Coelho Software, Brisbane (Australia), **2007**.
- [14] a) STOE & Cie GmbH, X-Area, Version 1.39, Darmstadt (Germany), **2006**; b) Bruker, Apex2, Version 11, Billerica, Madison (US), **2014**; c) G. M. Sheldrick, *Acta Crystallogr. Sect. A* **2008**, *64*, 112; d) E. Parthé, L. M. Gelato, *Acta Crystallogr. Sect. A* **1984**, *40*, 169; e) L. M. Gelato, E. Parthé, *J. Appl. Crystallogr.* **1987**, *20*, 139.
- [15] M. Wendorff, H. Scherer, C. Röhr, *Z. Anorg. Allg. Chem.* **2010**, *636*, 1038.
- [16] a) P. Blaha, K. Schwarz, G. K. H. Madsen, D. Kvasnicka, J. Luitz, WIEN2k, An Augmented Plane Wave and Local Orbitals Programme for Calculating Crystal Properties, Technical University of Vienna (Austria), **2006**; b) J. P. Perdew, K. Burke, M. Ernzerhof, *Phys. Rev. Lett.* **1996**, *77*, 3865.

4.5 Supporting Information

Table of contents

- Table S5.1: Crystallographic data and details on data collection and refinement for $\text{Ba}_{23}\text{Na}_{11}(\text{MN}_4)_4$.
- Table S5.2: Fractional atomic coordinates, equivalent isotropic thermal displacement parameters and site occupancies for $\text{Ba}_{23}\text{Na}_{11}(\text{VN}_4)_4$.
- Table S4.3: Fractional atomic coordinates, equivalent isotropic thermal displacement parameters and site occupancies for $\text{Ba}_{23}\text{Na}_{11}(\text{NbN}_4)_4$.
- Table S5.4: Fractional atomic coordinates, equivalent isotropic thermal displacement parameters and site occupancies for $\text{Ba}_{23}\text{Na}_{11}(\text{Ta}_4\text{N}_4)_4$.
- Table S5.5: Anisotropic displacement parameters in $\text{Ba}_{23}\text{Na}_{11}(\text{VN}_4)_4$.
- Table S5.6: Anisotropic displacement parameters in $\text{Ba}_{23}\text{Na}_{11}(\text{NbN}_4)_4$.
- Table S5.7: Anisotropic displacement parameters in $\text{Ba}_{23}\text{Na}_{11}(\text{Ta}_4\text{N}_4)_4$.
- Table S5.8: Selected interatomic distances / Å for $\text{Ba}_{23}\text{Na}_{11}(\text{VN}_4)_4$.
- Table S5.9: Selected interatomic distances / Å for $\text{Ba}_{23}\text{Na}_{11}(\text{NbN}_4)_4$.
- Table S5.10: Selected interatomic distances / Å for $\text{Ba}_{23}\text{Na}_{11}(\text{Ta}_4\text{N}_4)_4$.
- Table S5.11: Selected interatomic angles / ° for $\text{Ba}_{23}\text{Na}_{11}(\text{MN}_4)_4$.
- Figure S5.1: Temperature-dependent XRD of Ba_2N .
- Figure S5.2: Rietveld refinement of Ba_2N .
- Figure S5.3: Rietveld refinement of $\text{Ba}_{23}\text{Na}_{11}(\text{Ta}_4\text{N}_4)_4$.
- Figure S5.4: Rietveld refinement of $\text{Ba}_{23}\text{Na}_{11}(\text{NbN}_4)_4$.
- Figure S5.5: Rietveld refinement of $\text{Ba}_{23}\text{Na}_{11}(\text{VN}_4)_4$.
- Figure S5.6: Solid state ^1H NMR spectrum of $\text{Ba}_{23}\text{Na}_{11}(\text{VN}_4)_4$.

Table S5.1: Crystallographic information for Ba₂₃Na₁₁(MN₄)₄.

formula	Ba ₂₃ Na ₁₁ (VN ₄) ₄	Ba ₂₃ Na ₁₁ (NbN ₄) ₄	Ba ₂₃ Na ₁₁ (Ta ₄) ₄
crystal system		– tetragonal –	
space group		– P ₄ ₂ /n (no. 86) –	
lattice parameters / Å	a = 14.134(2) c = 18.536(2)	a = 14.3724(9) c = 18.8431(14)	a = 14.3603(12) c = 18.7552(17)
cell volume / Å ³	3703.0(9)	3892.3(4)	3867.7(6)
Z	2	2	2
calculated density / g/cm ⁻³	3.476	3.419	3.744
corrections		– Lorentz, polarisation, absorption –	
absorption coefficient / μ/mm ⁻¹	12.927	12.047	17.186
absorption method	Multiscan (Apex2)	ABST (PLATON)	MULABS (PLATON)
diffractometer / radiation	D8-Quest / Mo-K _α (λ = 0.71073 Å)	– Stoe IPDS 1 / Mo-K _α (λ = 0.71073 Å) –	
temperature / K		– 293(2) –	
F(000)	3254	3370	3626
θ-range / °	1.81-24.99	2.83-27.50	2.84-27.49
index range	-16 ≤ h ≤ 16 -16 ≤ k ≤ 16 -22 ≤ l ≤ 22	-18 ≤ h ≤ 18 -18 ≤ k ≤ 18 -24 ≤ l ≤ 24	-18 ≤ h ≤ 18 -18 ≤ k ≤ 18 -24 ≤ l ≤ 24
total no. of reflections	29461	39074	38628
independent reflections	3217	4479	4447
independent reflections with I ≥ 2(I)	2336	3071	2716
structure solution		– direct method –	
structure refinement		– full-matrix least-squares on F ² –	
refined parameters	125	123	123
Goof on F ²	1.202	0.856	0.790
R ₁ (for reflns with I ≥ 2(I)), R1 (all data)	0.0823, 0.1259	0.0373, 0.0743	0.0387, 0.0971
wR ₂ (for reflns with I ≥ 2(I)), wR2 (all data)	0.1583, 0.1844	0.0653, 0.0731	0.0491, 0.0590
R _{int} , R _σ	0.1205, 0.0666	0.1506, 0.0784	0.1218, 0.0978
residual electron density / e · Å ⁻³	-2.461/2.303	-1.359/1.375	-1.007/1.719

Table S5.2: Fractional atomic coordinates, isotropic thermal displacement parameters and site occupancies for Ba₂₃Na₁₁(VN₄)₄.

Atom	Wyckoff Symbol	x	y	z	U _{eq} / Å ²	Occupancy
V1	8g	0.3388(17)	0.07235(17)	0.1422(13)	0.0195(10)	0.930(5)
Ta1	8g	0.3388(17)	0.07235(17)	0.1422(13)	0.0195(10)	0.070(5)
Ba1	8g	0.03392(8)	0.13497(8)	0.12175(6)	0.0270(3)	1
Ba2	8g	0.07151(10)	0.62961(9)	0.19338(7)	0.0408(4)	1
Ba3	8g	0.28116(9)	0.56217(10)	0.03059(7)	0.0413(4)	1
Ba4	8g	0.51065(9)	0.11939(9)	0.02477(7)	0.0377(4)	1
Ba5	8g	0.51035(8)	0.16339(8)	0.24790(6)	0.0256(3)	1
Ba6	4f	1/4	1/4	0.04172(9)	0.0255(4)	1
Ba7	2a	1/4	1/4	1/4	0.0250(5)	1
Na1	8g	0.0553(16)	0.198(1)	0.6578(8)	0.133(7)	1
Na2	8g	0.3595(7)	0.0668(8)	0.6195(6)	0.058(3)	1
Na3	4e	3/4	1/4	0.1395(7)	0.054(4)	1
Na4	2b	1/4	1/4	3/4	0.236(3)	1
N1	8g	0.0343(10)	0.1438(11)	0.2646(8)	0.023(3)	1
N2	8g	0.1051(10)	0.3129(10)	0.1281(8)	0.024(3)	1
N3	8g	0.1112(10)	0.516(1)	0.0816(9)	0.028(4)	1
N4	8g	0.2140(11)	0.0803(11)	0.1234(8)	0.026(3)	1

Table S5.3: Fractional atomic coordinates, isotropic thermal displacement parameters and site occupancies for Ba₂₃Na₁₁(NbN₄)₄.

Atom	Wyckoff Symbol	x	y	z	U _{eq} / Å ²	Occupancy
Nb1	8g	0.33951(5)	0.06920(5)	0.14184(4)	0.02119(14)	1
Ba1	8g	0.03368(4)	0.13406(4)	0.12167(3)	0.02659(11)	1
Ba2	8g	0.06944(5)	0.63604(4)	0.19612(3)	0.04145(16)	1
Ba3	8g	0.28536(4)	0.56985(5)	0.03195(3)	0.04220(16)	1
Ba4	8g	0.51313(4)	0.12283(5)	0.02024(3)	0.03823(15)	1
Ba5	8g	0.51438(4)	0.16283(4)	0.24704(3)	0.02677(12)	1
Ba6	4f	1/4	1/4	0.04075(4)	0.02804(16)	1
Ba7	2a	1/4	1/4	1/4	0.0308(2)	1
Na1	8g	0.0495(6)	0.1942(5)	0.6526(3)	0.089(2)	1
Na2	8g	0.3598(4)	0.0713(4)	0.6208(3)	0.0631(13)	1
Na3	4e	3/4	1/4	0.1383(3)	0.0526(16)	1
Na4	2b	1/4	1/4	3/4	0.172(10)	1
N1	8g	0.0261(6)	0.1405(6)	0.2616(4)	0.0316(16)	1
N2	8g	0.1023(5)	0.3086(5)	0.1258(4)	0.0291(16)	1
N3	8g	0.1082(6)	0.5242(6)	0.0791(4)	0.0311(17)	1
N4	8g	0.2069(5)	0.0730(6)	0.1228(4)	0.0305(16)	1

Table S5.4: Fractional atomic coordinates, isotropic thermal displacement parameters and site occupancies for Ba₂₃Na₁₁(Ta₂N₄)₄.

Atom	Wyckoff Symbol	x	y	z	U _{eq} / Å ²	Occupancy
Ta1	8g	0.33950(3)	0.06868(3)	0.14162(2)	0.02366(10)	1
Ba1	8g	0.03382(5)	0.13469(5)	0.12185(3)	0.03055(15)	1
Ba2	8g	0.07006(7)	0.63710(6)	0.19620(4)	0.0466(2)	1
Ba3	8g	0.28603(6)	0.56993(7)	0.03125(4)	0.0481(2)	1
Ba4	8g	0.51379(6)	0.12281(6)	0.02008(4)	0.0427(2)	1
Ba5	8g	0.51468(5)	0.16232(5)	0.24710(4)	0.03042(16)	1
Ba6	4f	1/4	1/4	0.04042(5)	0.0313(2)	1
Ba7	2a	1/4	1/4	1/4	0.0324(3)	1
Na1	8g	0.0495(7)	0.1943(6)	0.6522(4)	0.105(3)	1
Na2	8g	0.3605(5)	0.0718(5)	0.6201(3)	0.0716(19)	1
Na3	4e	3/4	1/4	0.1374(4)	0.054(2)	1
Na4	2b	1/4	1/4	3/4	0.169(10)	1
N1	8g	0.0270(7)	0.1410(8)	0.2609(4)	0.038(2)	1
N2	8g	0.1030(7)	0.3099(7)	0.1265(5)	0.031(2)	1
N3	8g	0.1094(7)	0.5250(7)	0.0794(5)	0.035(2)	1
N4	8g	0.2068(6)	0.0736(7)	0.1217(5)	0.035(2)	1

Table S5.5: Anisotropic displacement parameters occurring in Ba₂₃Na₁₁(VN₄)₄.

Atom	U ₁₁ / Å ²	U ₂₂ / Å ²	U ₃₃ / Å ²	U ₂₃ / Å ²	U ₁₃ / Å ²	U ₁₂ / Å ²
V1	0.0179(15)	0.0208(16)	0.0198(16)	-0.0031(10)	0.0021(9)	0.0003(9)
Ta1	0.0179(15)	0.0208(16)	0.0198(16)	-0.0031(10)	0.0021(9)	0.0003(9)
Ba1	0.0249(6)	0.0291(7)	0.0270(6)	-0.0008(5)	-0.0018(5)	-0.0013(4)
Ba2	0.0516(9)	0.0315(7)	0.0393(8)	-0.0017(6)	-0.0043(6)	0.0143(6)
Ba3	0.0322(8)	0.0469(8)	0.0447(9)	0.0223(6)	0.0036(6)	-0.0014(5)
Ba4	0.0372(8)	0.0367(8)	0.0392(8)	-0.0097(6)	0.0160(6)	0.0007(5)
Ba5	0.0233(6)	0.0276(7)	0.0260(7)	-0.0029(4)	-0.0012(4)	0.0023(4)
Ba6	0.0239(9)	0.0304(9)	0.0223(8)	0	U ₂₃	0.0011(6)
Ba7	0.0257(8)	U ₁₁	0.0236(12)	0	U ₂₃	U ₂₃
Na1	0.25(2)	0.068(9)	0.080(9)	-0.011(8)	0.049(12)	-0.021(11)
Na2	0.052(6)	0.066(7)	0.057(6)	0.012(5)	-0.008(5)	-0.005(5)
Na3	0.043(8)	0.064(9)	0.054(9)	0	U ₂₃	0.002(6)
Na4	0.18(3)	U ₁₁	0.35(10)	0	U ₂₃	U ₂₃
N1	0.019(8)	0.029(9)	0.022(8)	-0.002(6)	0.007(6)	0.003(6)
N2	0.029(9)	0.017(8)	0.024(8)	0.006(6)	-0.003(6)	0.001(6)
N3	0.019(8)	0.024(9)	0.043(10)	0.006(7)	-0.017(7)	0.005(6)
N4	0.027(9)	0.026(8)	0.025(8)	0.000(7)	0.002(7)	0.003(6)

Table S5.6: Anisotropic displacement parameters occurring in $\text{Ba}_{23}\text{Na}_{11}(\text{NbN}_4)_4$.

Atom	$U_{11} / \text{\AA}^2$	$U_{22} / \text{\AA}^2$	$U_{33} / \text{\AA}^2$	$U_{23} / \text{\AA}^2$	$U_{13} / \text{\AA}^2$	$U_{12} / \text{\AA}^2$
Nb1	0.0233(3)	0.0221(4)	0.0182(3)	-0.0026(3)	0.0018(3)	0.0014(3)
Ba1	0.0267(3)	0.0290(3)	0.0241(2)	-0.0005(2)	-0.0023(2)	-0.0008(2)
Ba2	0.0544(4)	0.0340(3)	0.0360(3)	-0.0027(3)	-0.0039(3)	0.0148(3)
Ba3	0.0362(3)	0.0491(4)	0.0414(3)	0.0204(3)	0.0018(3)	-0.0033(3)
Ba4	0.0411(3)	0.0389(3)	0.0347(3)	-0.0091(3)	0.0145(3)	0.0028(3)
Ba5	0.0260(3)	0.0300(3)	0.0244(2)	-0.0029(2)	-0.0002(2)	0.0014(2)
Ba6	0.0290(4)	0.0340(4)	0.0212(3)	0	U_{23}	0.0027(3)
Ba7	0.0325(4)	U_{11}	0.0275(5)	0	U_{23}	U_{23}
Na1	0.136(6)	0.068(4)	0.063(3)	-0.006(3)	-0.006(4)	-0.018(4)
Na2	0.059(3)	0.068(3)	0.062(3)	0.016(3)	-0.005(3)	-0.005(3)
Na3	0.033(3)	0.073(5)	0.052(4)	0	U_{23}	-0.004(3)
Na4	0.118(10)	U_{11}	0.28(3)	0	U_{23}	U_{23}
N1	0.032(4)	0.040(4)	0.023(3)	0.003(3)	-0.006(3)	-0.002(3)
N2	0.033(4)	0.020(3)	0.034(4)	0.000(3)	0.004(3)	0.001(3)
N3	0.034(4)	0.033(4)	0.027(4)	0.010(3)	-0.010(3)	0.010(3)
N4	0.023(4)	0.038(4)	0.031(4)	0.002(4)	0.003(3)	0.003(3)

Table S5.7: Anisotropic displacement parameters occurring in $\text{Ba}_{23}\text{Na}_{11}(\text{Ta}_4\text{N}_4)_4$.

Atom	$U_{11} / \text{\AA}^2$	$U_{22} / \text{\AA}^2$	$U_{33} / \text{\AA}^2$	$U_{23} / \text{\AA}^2$	$U_{13} / \text{\AA}^2$	$U_{12} / \text{\AA}^2$
Ta1	0.0249(3)	0.0253(3)	0.02074(17)	-0.0036(2)	0.0017(2)	0.0016(2)
Ba1	0.0305(4)	0.0338(4)	0.0274(3)	-0.0007(39)	-0.0015(3)	-0.0016(3)
Ba2	0.0611(6)	0.0374(5)	0.0412(4)	-0.00300(4)	-0.0047(4)	0.0154(4)
Ba3	0.0403(5)	0.0567(6)	0.0475(5)	0.0240(4)	0.0018(4)	-0.0032(4)
Ba4	0.0448(5)	0.0442(5)	0.0391(4)	-0.0106(4)	0.0155(4)	0.0025(4)
Ba5	0.0289(4)	0.0339(4)	0.0285(3)	-0.0032(3)	-0.0009(3)	0.0019(3)
Ba6	0.0318(6)	0.0379(6)	0.0242(4)	0	U_{23}	0.0030(5)
Ba7	0.0344(5)	U_{11}	0.0285(7)	0	U_{23}	U_{23}
Na1	0.155(9)	0.082(6)	0.077(5)	-0.006(4)	0.022(5)	-0.025(5)
Na2	0.061(4)	0.080(5)	0.074(4)	0.019(4)	-0.006(3)	0.000(4)
Na3	0.030(4)	0.072(6)	0.061(5)	0	U_{23}	-0.007(4)
Na4	0.132(13)	U_{11}	0.24(3)	0	U_{23}	U_{23}
N1	0.042(6)	0.054(7)	0.018(4)	0.005(5)	0.001(4)	-0.008(5)
N2	0.031(5)	0.031(5)	0.032(5)	0.005(4)	0.000(4)	0.000(4)
N3	0.043(6)	0.035(6)	0.028(5)	0.015(4)	-0.012(4)	0.002(5)
N4	0.024(5)	0.048(7)	0.034(5)	0.002(5)	0.000(4)	0.012(4)

Table S5.8: List of selected interatomic distances / \AA for $\text{Ba}_{23}\text{Na}_{11}(\text{VN}_4)_4$.

V1/Ta1-N4	1.801(16)	Ba2-Ba3	4.3352(19)	Ba5-Ba4	4.1824(18)
V1/Ta1-N3	1.823(15)	Ba2-Na1	4.01(2)	Ba5-Ba3	4.2427(18)
V1/Ta1-N2	1.825(14)	Ba2-Na2	4.032(11)	Ba5-Ba2	4.2503(18)
V1/Ta1-N1	1.826(15)	Ba2-Na1	4.094(16)	Ba5-Na3	4.124(6)
V1/Ta1-Ba2	3.264(3)	Ba2-Na3	4.342(9)	Ba5-Na1	4.402(18)
V1/Ta1-Ba3	3.282(3)	Ba3-Ba4	4.0405(19)	Ba6-Ba1	3.7645(14)
V1/Ta1-Ba4	3.329(3)	Ba3-Ba1	4.1774(18)	Ba6-Ba7	3.8607(17)
V1/Ta1-Ba6	3.369(3)	Ba3-Ba5	4.2437(18)	Ba6-Ba4	4.1326(14)
V1/Ta1-Ba5	3.373(3)	Ba3-Ba2	4.3352(19)	Ba6-Na2	4.246(11)
V1/Ta1-Ba5	3.414(3)	Ba3-Na1	4.041(16)	Ba7-Ba6	3.8607(17)
V1/Ta1-Ba7	3.445(2)	Ba3-Na3	4.145(10)	Ba7-Ba5	4.1326(14)
Ba1-Ba5	3.6613(16)	Ba4-Ba4	3.5105(19)	Ba7-Ba1	4.1979(12)
Ba1-Ba5	3.7392(14)	Ba4-Ba1	3.9601(18)	Na1-Na4	3.32(2)
Ba1-Ba6	3.7655(16)	Ba4-Ba3	4.0405(19)	Na1-Na2	3.606(19)
Ba1-Ba4	3.9601(18)	Ba4-Ba6	4.1326(14)	Na1-Na2	4.210(19)
Ba1-Ba3	4.1774(18)	Ba4-Ba2	4.1366(19)	Na1-Na3	4.39(2)
Ba1-Ba7	4.1979(12)	Ba4-Ba5	4.1824(18)	Na2-Na1	3.606(19)
Ba1-Ba2	4.2396(18)	Ba4-Na1	4.381(18)	Na2-Na4	3.867(11)
Ba1-Na2	4.146(11)	Ba4-Na3	4.402(6)	Na2-Na1	4.210(19)
Ba1-Na3	4.3423(16)	Ba4-Na2	4.457(11)	Na3-Na1	4.390(15)
Ba2-Ba4	4.1366(19)	Ba5-Ba1	3.6613(16)	Na4-Na1	3.32(2)
Ba2-Ba1	4.2296(17)	Ba5-Ba1	3.7392(16)	Na4-Na2	3.867(11)
Ba2-Ba5	4.3352(19)	Ba5-Ba7	3.8783(12)		

Table S5.9: List of selected interatomic distances / Å for Ba₂₃Na₁₁(NbN₄)₄.

Nb1-N4	1.940(7)	Ba2-Ba3	4.4839(9)	Ba5-Ba4	4.3121(9)
Nb1-N3	1.940(8)	Ba2-Na2	4.056(6)	Ba5-Ba3	4.3050(9)
Nb1-N1	1.943(8)	Ba2-Na1	4.072(8)	Ba5-Ba2	4.3602(9)
Nb1-N2	1.969(7)	Ba2-Na1	4.123(7)	Ba5-Na3	4.152(6)
Nb1-Ba2	3.3852(10)	Ba2-Na3	4.376(4)	Ba5-Na1	4.377(8)
Nb1-Ba3	3.3915(10)	Ba3-Ba4	4.1055(9)	Ba6-Ba1	3.8429(7)
Nb1-Ba6	3.4693(9)	Ba3-Ba1	4.2675(9)	Ba6-Ba7	3.9429(8)
Nb1-Ba5	3.4723(9)	Ba3-Ba5	4.3050(9)	Ba6-Ba4	4.2181(6)
Nb1-Ba4	3.4743(9)	Ba3-Ba2	4.4839(9)	Ba6-Na2	4.284(6)
Nb1-Ba5	3.5036(9)	Ba3-Na1	4.093(6)	Ba7-Ba6	3.9429(8)
Nb1-Ba7	3.5442(7)	Ba3-Na3	4.118(6)	Ba7-Ba5	4.0014(6)
Ba1-Ba5	3.77573(8)	Ba4-Ba4	3.6318(10)	Ba7-Ba1	4.2767(6)
Ba1-Ba5	3.8183(8)	Ba4-Ba1	4.0391(9)	Na1-Na4	3.509(8)
Ba1-Ba6	3.8429(7)	Ba4-Ba3	4.1055(9)	Na1-Na2	3.663(9)
Ba1-Ba4	4.0391(9)	Ba4-Ba2	4.1608(9)	Na1-Na2	4.351(8)
Ba1-Ba3	4.2675(9)	Ba4-Ba6	4.2181(6)	Na1-Na3	4.387(9)
Ba1-Ba7	4.2767(6)	Ba4-Ba5	4.3121(9)	Na2-Na1	3.663(9)
Ba1-Ba2	4.3129(9)	Ba4-Na1	4.374(7)	Na2-Na4	3.875(6)
Ba1-Na2	4.221(6)	Ba4-Na3	4.459(3)	Na2-Na1	4.351(8)
Ba1-Na3	4.4157(7)	Ba4-Na2	4.487(6)	Na3-Na1	4.387(7)
Ba2-Ba4	4.1608(9)	Ba5-Ba1	3.7573(8)	Na4-Na1	3.509(8)
Ba2-Ba1	4.3129(8)	Ba5-Ba1	3.8183(8)	Na4-Na2	3.875(6)
Ba2-Ba5	4.3602(9)	Ba5-Ba7	4.0014(6)		

Table S5.10: List of selected interatomic distances / Å for Ba₂₃Na₁₁(Ta₄N₄)₄.

Ta1-N3	1.926(10)	Ba2-Ba3	4.4855(12)	Ba5-Ba4	4.2955(11)
Ta1-N4	1.943(9)	Ba2-Na2	4.059(7)	Ba5-Ba3	4.2966(11)
Ta1-N1	1.944(8)	Ba2-Na1	4.083(10)	Ba5-Ba2	4.3578(12)
Ta1-N2	1.950(10)	Ba2-Na1	4.110(8)	Ba5-Na3	4.152(4)
Ta1-Ba2	3.3863(10)	Ba2-Na3	4.364(5)	Ba5-Na1	4.367(9)
Ta1-Ba3	3.3906(10)	Ba3-Ba4	4.0972(13)	Ba6-Ba1	3.8356(8)
Ta1-Ba6	3.4690(7)	Ba3-Ba1	4.2678(12)	Ba6-Ba7	3.9307(10)
Ta1-Ba5	3.4714(9)	Ba3-Ba5	4.2966(11)	Ba6-Ba4	4.2227(9)
Ta1-Ba4	3.4734(9)	Ba3-Ba2	4.4855(12)	Ba6-Na2	4.258(7)
Ta1-Ba5	3.5018(9)	Ba3-Na1	4.064(8)	Ba7-Ba6	3.9307(10)
Ta1-Ba7	3.5445(5)	Ba3-Na3	4.118(6)	Ba7-Ba5	4.0044(8)
Ba1-Ba5	3.7480(10)	Ba4-Ba4	3.6284(12)	Ba7-Ba1	4.2610(7)
Ba1-Ba5	3.8080(10)	Ba4-Ba1	4.0296(11)	Na1-Na4	3.506(9)
Ba1-Ba6	3.8356(8)	Ba4-Ba3	4.0972(13)	Na1-Na2	3.649(11)
Ba1-Ba4	4.0296(11)	Ba4-Ba2	4.1412(11)	Na1-Na2	4.354(9)
Ba1-Ba7	4.2610(7)	Ba4-Ba6	4.2227(9)	Na1-Na3	4.384(10)
Ba1-Ba3	4.2678(12)	Ba4-Ba5	4.2955(11)	Na2-Na1	3.649(11)
Ba1-Ba2	4.3048(11)	Ba4-Na1	4.357(9)	Na2-Na4	3.873(7)
Ba1-Na2	4.220(7)	Ba4-Na3	4.437(4)	Na2-Na1	4.354(10)
Ba1-Na3	4.4089(9)	Ba4-Na2	4.480(7)	Na3-Na1	4.384(9)
Ba2-Ba4	4.1412(11)	Ba5-Ba1	3.7480(10)	Na4-Na1	3.506(8)
Ba2-Ba1	4.3048(11)	Ba5-Ba1	3.8080(10)	Na4-Na2	3.873(7)
Ba2-Ba5	4.3578(12)	Ba5-Ba7	4.0044(8)		

Table S5.11: List of relevant bond angles / ° for Ba₂₃Na₁₁(MN₄)₄.

N-V-N		N-Nb-N		N-Ta-N	
N4-V1-N3	107.6(7)	N4-Nb1-N3	106.7(3)	N3-Ta1-N4	106.4(4)
N3-V1-N1	109.2(7)	N3-Nb1-N1	107.0(3)	N3-Ta1-N1	107.5(4)
N4-V1-N1	109.5(7)	N4-Nb1-N1	109.1(3)	N4-Ta1-N1	109.5(4)
N1-V1-N2	109.8(7)	N3-Nb1-N2	111.0(3)	N1-Ta1-N2	110.5(4)
N4-V1-N2	110.0(7)	N4-Nb1-N2	111.3(3)	N4-Ta1-N2	110.8(4)
N3-V1-N2	110.6(6)	N1-Nb1-N2	111.4(3)	N3-Ta1-N2	112.0(4)

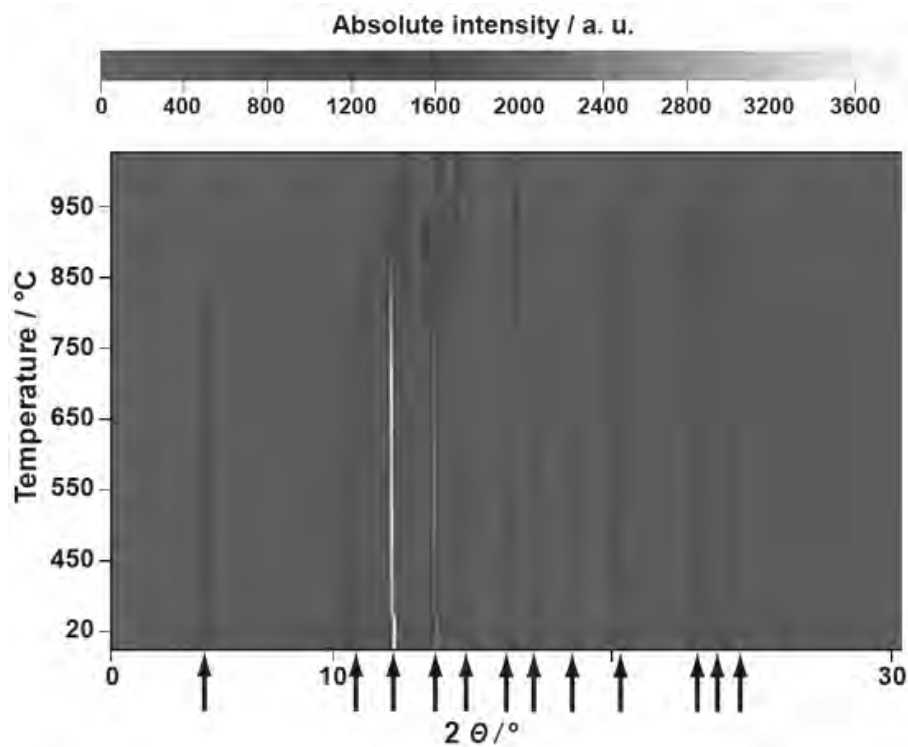


Figure S5.1: Temperature dependent XRD of Ba_2N to verify melting/decomposition above 900 °C. Most prominent peaks corresponding to the phase Ba_2N are marked with arrows.

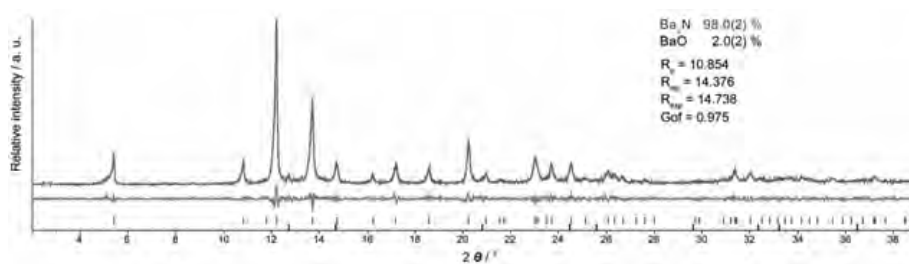


Figure S5.2: Rietveld refinement of Ba_2N . Mass percentages of individual phases with standard deviations and relevant figures of merit are shown. Ba_2N : grey; BaO : black.

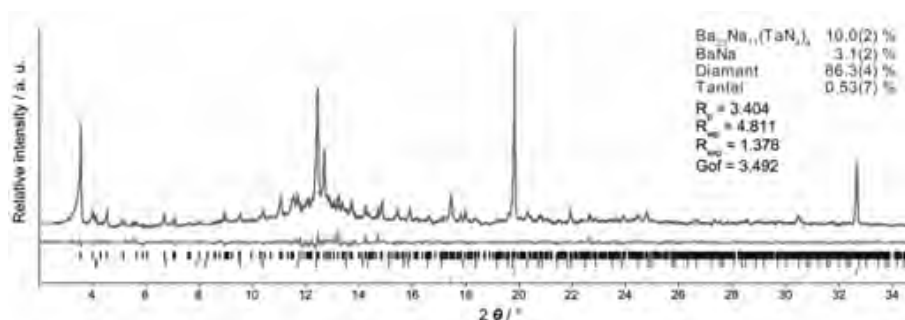


Figure S5.3: Rietveld refinement for Ba₂₃Na₁₁(Ta₄N₄)₄. Mass percentages of individual phases with standard deviations and relevant figures of merit are shown. Ba₂₃Na₁₁(Ta₄N₄)₄: black tick marks; BaNa: dark grey; diamant: medium grey; Ta: light grey. Diamond powder was added due to high ductility of the sample and as internal standard.

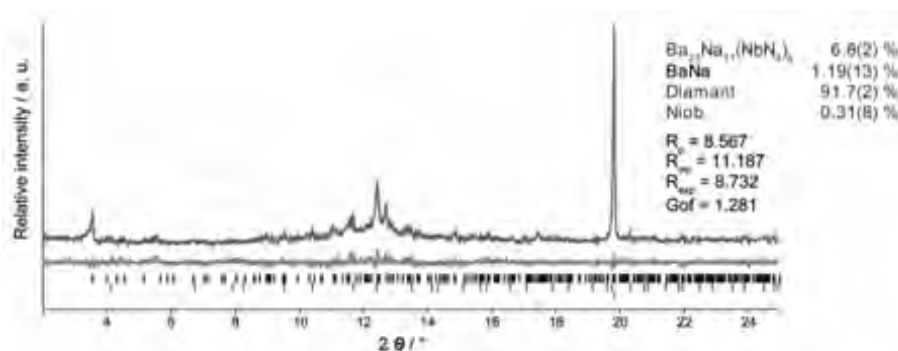


Figure S5.4: Rietveld refinement for Ba₂₃Na₁₁(Nb₄N₄)₄. Mass percentages of individual phases with standard deviations and relevant figures of merit are shown. Ba₂₃Na₁₁(Nb₄N₄)₄: black tick marks; BaNa: dark grey; diamant: medium grey; Ta: light grey. Diamond powder was added due to high ductility of the sample and as internal standard.

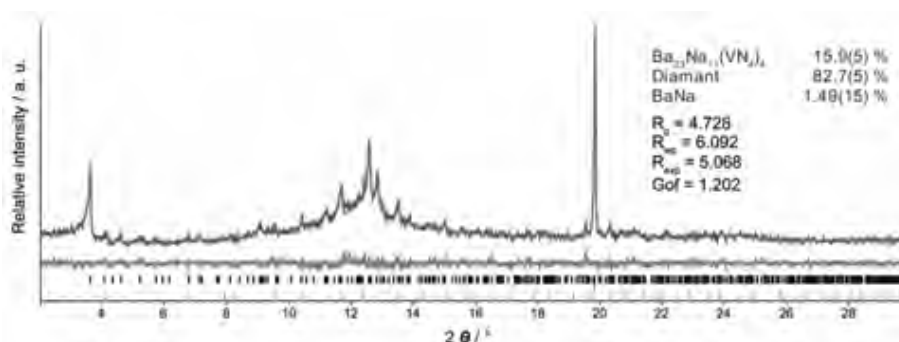


Figure S5.5: Rietveld refinement for Ba₂₃Na₁₁(V₄N₄)₄. Mass percentages of individual phases with standard deviations and relevant figures of merit are shown. Ba₂₃Na₁₁(V₄N₄)₄: black tick marks; BaNa: dark grey; diamant: medium grey; Ta: light grey. Diamond powder was added due to high ductility of the sample and as internal standard.

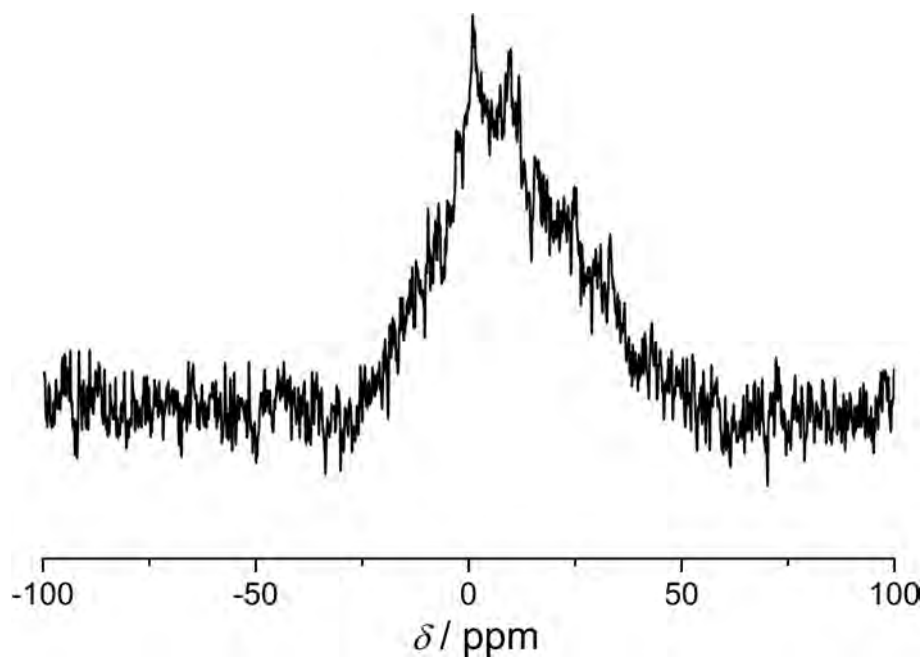


Figure S5.5: Solid state ^1H -NMR spectrum of $\text{Ba}_{23}\text{Na}_{11}(\text{VN}_4)_4$. The broad signal with low significance has a maximum in the range of 0 to +10 ppm. For hydridic species a sharp signal in the range of -6 to -8 ppm would be expected. The observed signal rather is caused by minor amounts of hydrolysis products or by traces of moisture in the rotor walls. The powdered sample was filled in a 4 mm zirconia rotor with KelF inlay. The spectrum was registered in a T1 saturation experiment on a Bruker Avance III WB device 400 MHz with a 4 mm sample head at a rotational frequency of 10 kHz, a relaxation delay of 32 s and an acquisition time of 0.012 s.

5 CsOH and its lighter homologues – a comparison

Matthias Wörsching, Constantin Hoch

published in: *Z. Naturforsch.* **2014**, *69b*, 1229–1236. DOI: 10.5560/ZNB.2014-4163

Reprinted (adapted) with permission from Zeitschrift für Naturforschung. Copyright 2014 De Gruyter Verlag.

Abstract

Cesium hydroxide, CsOH, was for the first time characterised on the basis of single-crystal data. The structure is isotypic to the one of the room-temperature modification of NaOH and can be derived from the NaCl structure type allowing the comparison of all alkali metal hydroxide structures. Raman spectroscopic investigations show the hydroxide anion to behave almost as a free ion as in the gas phase. The X-ray investigations indicate possible H atom positions.

5.1 Introduction

Among the most important chemical compounds for laboratory, industrial and household application count the alkali metal hydroxides. Their application ranges from the production of paints and varnishes, household cleaners, glasses, aluminium and paper to mercerisation of cotton and food production. However, the structural elucidation of these simple compounds remained elusive for a long time. The highly hygroscopic and CO₂-absorbant substances require sophisticated preparation methods. If not handled under strict exclusion of atmosphere, the hydroxides form numerous hydrates (see Table 5.1) or carbonates. Moreover, the hydroxides tend to crystallise poorly from solution or melts and form numerous modifications between room temperature and the respective melting points. Most of the former crystal structure descriptions therefore were based on powder data, and structural details remained elusive.

Table 5.1: Alkali metal hydroxides and their hydrates.

Li	Na	K	Rb	Cs
LiOH ^[1–3]	NaOH ^[9–14]	KOH ^[9,13]	RbOH ^[9,13]	CsOH ^[29–36]
LiOH · H ₂ O ^[4–8]	NaOH · H ₂ O ^[15–17]	KOH · H ₂ O ^[25,26]	RbOH · H ₂ O ^[26]	CsOH · H ₂ O ^[37,38]
		KOH · 2 H ₂ O ^[27]	RbOH · 2 H ₂ O ^[28]	CsOH · 2 H ₂ O ^[39]
				CsOH · 3 H ₂ O ^[39]
	NaOH · 3.5 H ₂ O ^[17,18]			
	NaOH · 4 H ₂ O ^[17,19–22]	KOH · 4 H ₂ O ^[27]		
	NaOH · 7 H ₂ O ^[18,23,24]			

Several ways for the preparation of CsOH have been published,^[29–36] all of them requiring high preparative skills and elaborated equipment. During our investigations on suboxometallates of the heavy alkali metals^[40–43] we found a new and simple method for the preparation of single-crystalline samples of CsOH. This method does not yield large amounts of the phase-pure substance but is suitable for the growth of large single crystal with high quality. It may be adapted for the lighter alkali metals and also for the preparation of deuterated samples.

The first crystal structure description of CsOH^[36] attracted the attention because of the especially weakly coordinated OH[−] anion. Compared to the vibrational frequency of the hydroxide anion in the gas phase (3555.6 cm^{−1}^[54]), ν_{OH} can be shifted either to higher or lower frequencies in solid hydroxides, depending on the sort and strength of *M*–O interactions. Covalent contributions to the *M*–O bond as e.g. in transition metal hydroxides and also OH[−] ··· *X* hydrogen bonding account for a decrease of ν_{OH} . An increase of ν_{OH} correlates with a decreasing *M*–O distance in the predominantly ionic alkali hydroxides.^[58] Occurrence of additional hydrogen bonding between hydroxide anions and hydrate water molecules render the estimation of trends for the shift of ν_{OH} very difficult.

Table 5.2: O–H stretching mode frequencies in alkali metal hydroxides (cm^{-1}).

	Infrarot	Raman	Lit.
LiOH	3678	3664	[44–48]
NaOH	3637	3633	[49]
KOH	3600		[50–52]
CsOH		3589	this work
		3586	[53]
Gas phase		3556	[54–57]

5.2 Results and Discussion

5.2.1 Crystal structure

CsOH crystallises isotypically to the room temperature modification of NaOH in the CrB (or as well anti-TII) structure type.^[59–62] Details on data collection, crystallographic data, structure solution and refinement are given in Table 6.2. Standardised atomic coordinates^[63] and isotropic displacement parameters are compiled in Table 5.4, the anisotropic displacement parameters and selected interatomic distances and angles can be found in Tables 5.5 and 5.6, respectively.

Table 5.3: Crystallographic data and selected details on the data collection, structure solution and refinement of CsOH.

Crystal system	orthorhombic
Space group	<i>Cmcm</i> , (no. 63)
Lattice parameters, Å	<i>a</i> 4.3414(15) <i>b</i> 11.959(6) <i>c</i> 4.5036(14)
Volume, Å ³	233.82(16)
<i>Z</i>	4
Calculated density, gcm ⁻³	4.23
Diffractometer	Stoe IPDS-I, MoK _α radiation graphite-monochromatized
Data collection temperature	295 K
Absorption coefficient, mm ⁻¹	15.4
Data range ϑ , deg	5.00-27.50
Index range	$-5 \leq h \leq 5$, $-15 \leq k \leq 15$, $-5 \leq l \leq 5$
No. of observed reflections	1888
No. of independent reflections	164
No. of independent reflections with ($I > 2 \sigma(I)$)	150
$F(000)$, e ⁻	252
Corrections	Absorption (analytical) ^[66,67]
Structure solution	direct methods ^[3]
Structure refinement	least squares on F^2 ^[3,69]
No. of l. s. parameters	9
Goof on F^2	1.208
$R1/wR2$ (for reflections with $I > 2 \sigma(I)$)	0.0385 / 0.0850
$R1/wR2$ (all data)	0.0411 / 0.0859
Residual electron density (max. / min.), e ⁻ ·Å ⁻³	1.82 / -1.12
ICSD depository number	CSD-426540

Table 5.4: Standardised fractional atomic coordinates^[63] and equivalent isotropic displacement parameters for CsOH. All atoms occupy crystallographic sites with Wyckoff-No. 4c and point symmetry $m2m$. Standard deviations in units of the last digit are given in parentheses.

Atom	x	y	z	U_{eq} (\AA^2)
Cs1	0	0.35977(10)	$\frac{1}{4}$	0.0526(5)
O1	0	0.1118(13)	$\frac{1}{4}$	0.068(4)

Table 5.5: Anisotropic displacement parameters U_{ij} for CsOH (\AA^2). Standard deviations in units of the last digit are given in parentheses. $U_{12} = U_{13} = U_{23} = 0$ for all atoms.

Atom	U_{11}	U_{22}	U_{33}
Cs1	0.0445(6)	0.0650(8)	0.0482(8)
O1	0.058(9)	0.086(10)	0.059(9)

Table 5.6: Selected interatomic distances (\AA), angles (deg) and their respective frequencies for CsOH. Standard deviations in units of the last digit are given in parentheses. Only interatomic distances below 4.5 \AA were taken into account.

Atoms	Distance	Atoms	Angle
Cs1–O1	2.965(15)	Cs1–O1–Cs1	83.8(3)
	3.1461(18)		87.25(6)
	3.714(12)		91.41(7)
Cs1–Cs1	4.040(25)	O1–Cs1–O1	167.6(6)
	4.0836(19)		60.6(3)
	4.3414(15)		71.5(3)
O1–O1	3.50(2)		87.25(6)
			91.41(7)
			96.2(3)
			108.4(2)
			144.2(1)
			167.6(6)

All cesium atoms occupy one single crystallographic position with Wyckoff no. 4c and site symmetry $m2m$. Also the oxygen atoms occupy a 4c position. The Cs atoms are coordinated by O atoms in a square pyramid with Cs–O distances ranging from 296.5(15) to 315.2(3) pm. The Cs atom is shifted slightly from the centre of the square base towards the barycentre of the pyramid. The coordination sphere of Cs is completed by two O atoms with longer distances of 374(2) pm (see Fig. 5.1 and Table 5.6).

The square pyramids $[\text{Cs}_5\text{O}]$ are linked to sheets perpendicular to the crystallographic

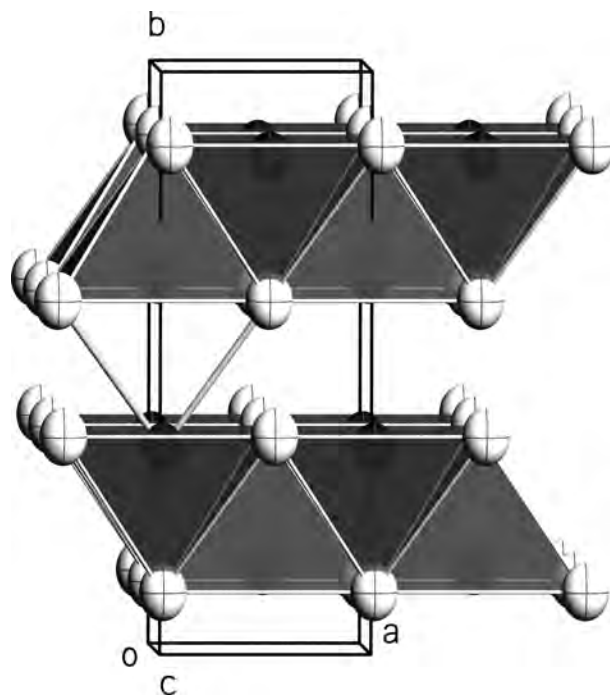


Figure 5.1: The crystal structure of CsOH. All displacement ellipsoids are drawn on a probability level of 90 %. Dark ellipsoids: Cs atoms, bright ellipsoids: O atoms. The additional contacts to O atoms in the neighbouring layer were drawn for the Cs atom in the lower left as light grey bonds.

b axis via common edges. The additional contacts of Cs and O atoms belonging to adjacent sheets renders the CsOH structure to a 3D arrangement with no pronounced layer compound character, in contrast to Cs₂O (anti-CdCl₂ structure).^[64]

From the single-crystal data, no H atoms could be refined. However, a close analysis of the electron density in the difference Fourier map reveals two sharp maxima with about 0.5 electrons each and distances of 0.96 Å to the neighbouring O atom. These maxima can be assigned to the H atom positions and are in good agreement with the positions of D atoms obtained by neutron diffraction on CsOD samples,^[65] see Fig. 5.2.

The crystal structures of the anhydrous alkali metal hydroxides can be derived from simple structure types when the H atom positions are neglected (see Fig. 5.3 and 5.4).

LiOH crystallises in an anti-PbO structure with square nets of Li⁺ cations capped alternately above and below the net plane by OH⁻ anions (tetragonal, space group *P4/nmm*).^[1-3] The structure can be derived from the CaF₂ structure type by removing one layer of F atoms. A structure with NaCl-type arrangement (cubic, space group *Fm $\bar{3}$ m*) is common to the high-temperature modifications of NaOH,^[12] KOH and RbOH.^[23] At room temperature, NaOH and CsOH crystallise in an orthorhombic structure^[23] (space group *Cmcm*) which can be derived from the NaCl structure type by cutting out blocks and shifting them with respect to each other about $a_{\text{NaCl}}/4$. Shifting about $a_{\text{NaCl}}/2$ leads to a monoclinic structure type (space group *P2₁/m*) adopted by NaOH between 513 and 566 K and by KOH and RbOH at room temperature.^[26,27] A fourth structure (space group *Pbcm*) can be derived from the NiAs structure type by slight distortions of all coordination polyhedra. It is adopted by a high-pressure mod-

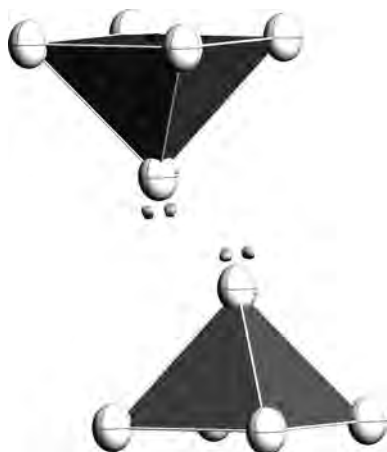


Figure 5.2: The two maxima in the difference Fourier electron density map correspond to the H atom positions. The Fourier map was included in the structure drawing at a height of $0.3 \text{ e}^- \cdot \text{\AA}^{-3}$.^[70]

ification of NaOH^[71] and NaOD at ambient pressure.^[72] This can be rationalised in analogy to the pressure-homologue rule,^[73] however, H is not substituted by its higher homologue but by its higher isotope.

5.2.2 Raman spectroscopy

The Raman spectrum of CsOH was recorded on the very same crystal used for the single-crystal X-ray analysis. It was sealed in a glass capillary filled with dry paraffin oil. The resulting spectrum thus contains contributions from C–H stretching and bending modes in the range of 1000 and 1500 and around 3000 cm^{-1} in addition to the characteristic O–H stretching mode of CsOH at 3589 cm^{-1} (see Fig. 5.5). It is very close to the one reported for powder samples of CsOH^[53] and also to the one reported for the OH[−] ion in the gas phase,^[54] see Table 5.2.

The crystal structures of the alkali metal hydroxides are a textbook example for the formal derivation of low-symmetric hettotype structures from simple and high-symmetric aristotype structures. The symmetry reduction can be explained by the chemical reason of distorting the respective structures by introducing a non-spherical hydroxide anion and thus distorting the local Coulomb potential. At high temperatures, the OH[−] anion begins to rotate as a quasi-free particle, and the distortion is suppressed.

According to vibration-spectroscopical investigations, the OH[−] anion in CsOH shows a behaviour only influenced by the M–O contacts, and the O–H stretching mode occurs at a frequency very close to the one of hydroxide anions in the gas phase.

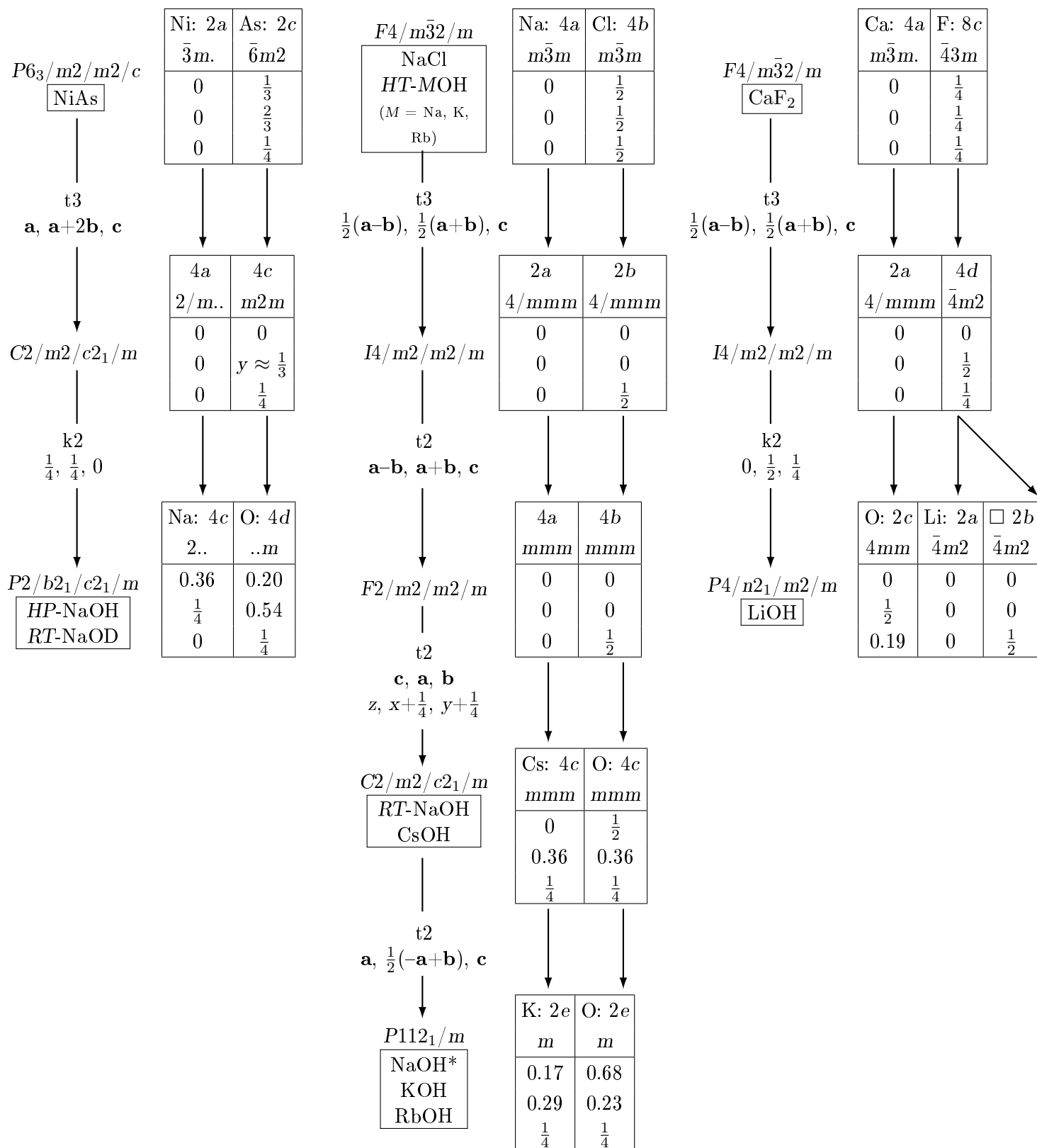


Figure 5.3: Bärnighausen tree explaining the symmetric relations between the alkali metal hydroxides and their respective aristotypes. *NaOH in space group $P2_1/m$ is stable between 513 and 566 K.

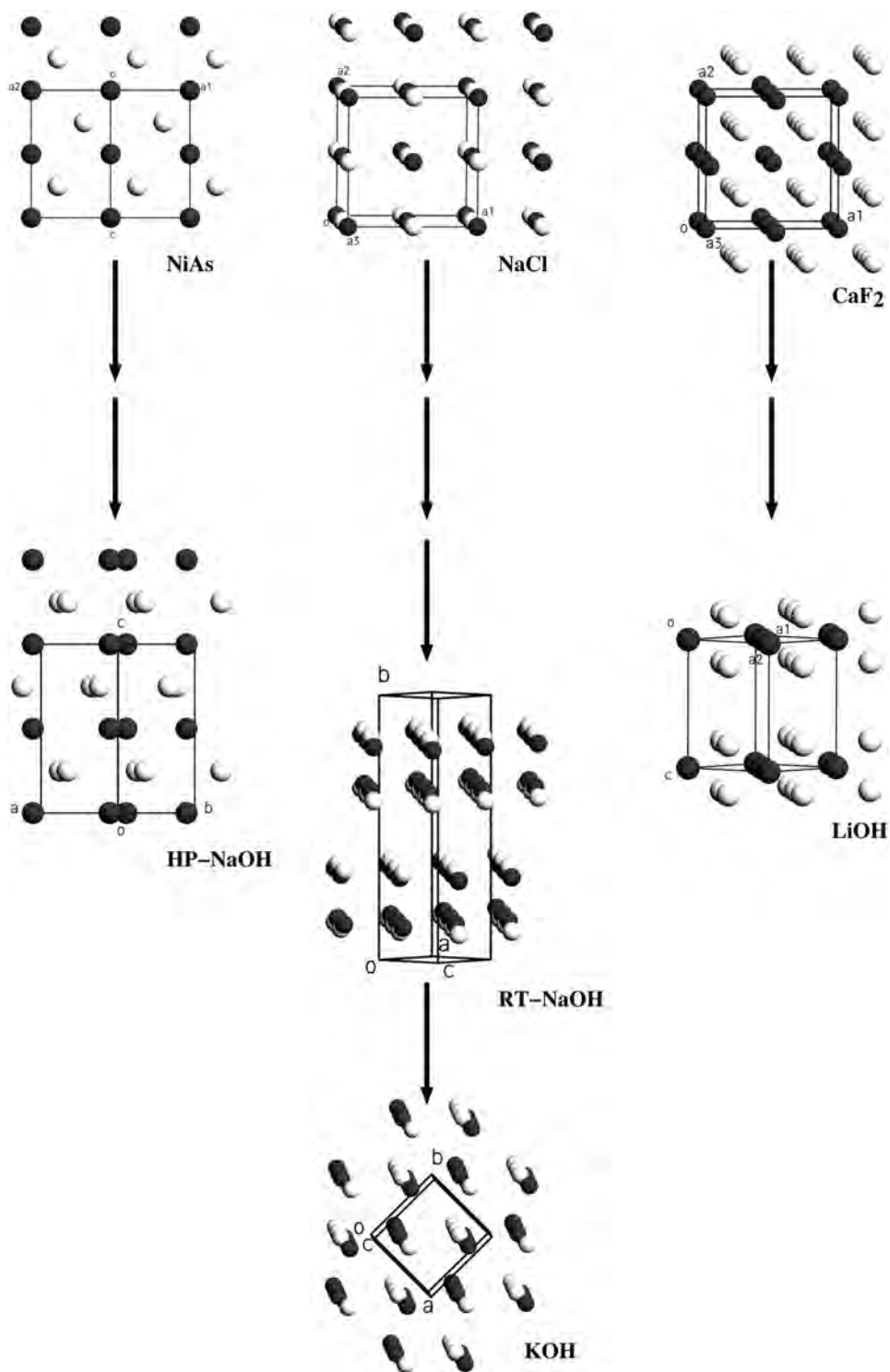


Figure 5.4: Structural relations between alkali metal hydroxides and their aristotypes. The respective unit cells of the structures from Fig. 5.3 are drawn in projections which allow a direct comparison.

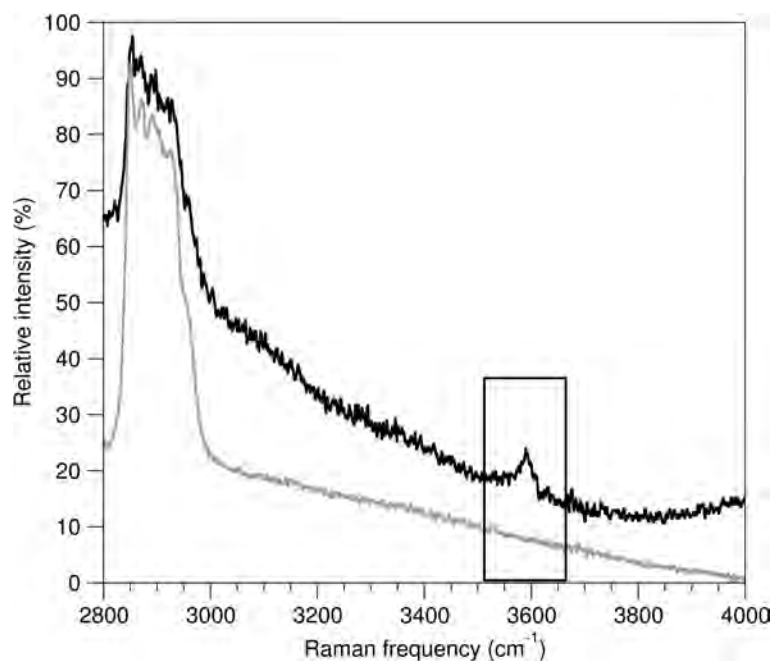


Figure 5.5: Raman spectrum of a CsOH single crystal (black) and of a glass capillary filled with dry paraffin oil (gray). The signal in the box belongs to the characteristic O–H stretching mode of CsOH.

5.3 Experimental Section

5.3.1 Preparation and crystal structure investigation

Single crystals of CsOH were obtained by covering small portions of Cs metal in a petri dish inside an argon-filled glove box with thoroughly dried paraffin oil and subsequently exposing the petri dish to air. After three days, CsOH single crystals had formed on the surface of the excess Cs metal by slow diffusion of air through the paraffin oil barrier. When all Cs metal is consumed, hydrates and finally the carbonate are formed. CsOH crystallises in brittle, transparent irregularly shaped blocks and is very hygroscopic.

Single crystals suitable for X-ray investigations were selected under a binocular with polarisation filter and sealed in paraffin-filled glass capillaries with an inner diameter of 0.2 mm. They were centred on the one-circle goniometer of a diffractometer system IPDS1 (Stoe & Cie., Darmstadt, Germany) equipped with an imaging plate detector and graphite-monochromatised MoK_{α} radiation. The data of the accessible part of one Ewald sphere were collected and subsequently corrected for Lorentz, polarisation and absorption effects.^[66,67] The orthorhombic metric, the extinction conditions (hkl : $h+k = 2n$ and $h0l$: $l = 2n$) and the statistics on $E^2 - 1$ indicated space group $Cmcm$. Structure solution^[3] revealed all Cs and O atoms which were subsequently refined applying anisotropic displacement parameters.^[3] Further details on the structure investigation may be obtained from Fachinformationszentrum Karlsruhe, D-76344 Eggenstein-Leopoldshafen, Germany (Fax: (+49)6247-808-666, e-mail: crysdata@fiz-karlsruhe.de), on quoting the deposition number CSD-426540.

5.3.2 Raman spectroscopy

A He-Ne laser with a 1 mm focus in a confocal Raman microscope (LabRSM HG UV/Vis, Horiba Jobin Ivon GmbH, München, combined with an Olympus BX 41 microscope) equipped with a CCD detector was focussed on the capillary filled with paraffin oil and the CsOH single crystal. For the identification of the paraffin oil absorption bands, an identical spectrum was recorded at a position of the capillary where no CsOH crystal was in the focus.

Acknowledgement

We thank Stefan Niedermayer and Stefan Datz from the group of Prof. Dr. Thomas Bein at Ludwig-Maximilians-Universität München for the registration of the Raman spectra and Frank Tambornino for the collection of the single-crystal data.

5.4 References

- [1] T. Ernst, *Z. Phys. Chem.* **1933**, *B20*, 65–88.
- [2] H. Dachs, *Z. Kristallogr.* **1959**, *112*, 60–67.
- [3] S. L. Mair, *Acta Crystallogr.* **1978**, *A34*, 542–547.
- [4] R. Pepinsky, *Z. Kristallogr.* **1940**, *102*, 119–140.
- [5] H. Rabaud, R. Gay, *Bull. Soc. Franc. Min. Cristallogr.* **1957**, *80*, 166–180.
- [6] N. W. Alcock, *Acta Crystallogr.* **1971**, *B27*, 1682–1683.
- [7] K. Hermansson, J. O. Thomas, *Acta Crystallogr.* **1982**, *B38*, 2555–2563.
- [8] L. Ojamajee, K. Hermansson, C. Pisani, M. Causa, C. Roetti, *Acta Crystallogr.* **1994**, *B50*, 268–279.
- [9] T. Ernst, *Angew. Chem.* **1948**, *60*, 77.
- [10] W. J. Smothers, R. F. Kruh, J. K. Carlton, Y. Chiang, *J. Appl. Chem.* **1954**, *4*, 268–273.
- [11] H. Stehr, *Z. Kristallogr.* **1967**, *125*, 332–359.
- [12] H. J. Bleif, H. Dachs, *Acta Crystallogr.* **1982**, *A38*, 470–476.
- [13] H. Jacobs, J. Kockelhorn, T. Tacke, *Z. Anorg. Allg. Chem.* **1985**, *531*, 119–124.
- [14] H. P. Beck, G. Lederer, *J. Chem. Phys.* **1993**, *98*, 7289–7294.
- [15] J. A. Wunderlich, *Acta Crystallogr.* **1957**, *10*, 462–463.
- [16] H. Jacobs, U. Metzner, *Z. Anorg. Allg. Chem.* **1991**, *597*, 97–106.
- [17] J. R. Rustad, A. R. Felmy, K. M. Rosso, E. J. Bylaska, *Am. Mineral.* **2003**, *88*, 436–449.
- [18] D. Mootz, H. Rütter, R. Wiskemann, *Z. Anorg. Allg. Chem.* **1994**, *620*, 1509–1513.
- [19] P. W. Hemily, *Compt. Rend.* **1952**, *234*, 2085–2087.
- [20] P. W. Hemily, *Acta Crystallogr.* **1957**, *10*, 37–44.
- [21] G. Beurskens, G. A. Jeffrey, *J. Chem. Phys.* **1964**, *41*, 924–929.
- [22] D. Mootz, R. Seidel, *Z. Anorg. Allg. Chem.* **1990**, *582*, 162–168.
- [23] P. W. Hemily, *Compt. Rend.* **1953**, *236*, 1579–1581.
- [24] J. A. Wunderlich, *Bull. Soc. Min. Cristallogr.* **1958**, *81*, 287–314.
- [25] J. Clastre, *Cah. Phys.* **1956**, *74*, 24–25.
- [26] H. Jacobs, T. Tacke, J. Kockelkorn, *Z. Anorg. Allg. Chem.* **1984**, *516*, 67–78.

- [27] H. Rütter, D. Mootz, *Z. Anorg. Allg. Chem.* **1991**, 601, 73–82.
- [28] H. Jacobs, A. Schardey, *Z. Anorg. Allg. Chem.* **1988**, 656, 34–40.
- [29] G. Kirchhoff, R. Bunsen, *Pogg. Ann.* **1861**, 113, 364.
- [30] D. Forcrand, *Compt. Rend.* **1906**, 142, 1254.
- [31] G. v. Hevesy, *Z. Phys. Chem.* **1910**, 73, 667.
- [32] E. Barnes, *J. Chem. Soc.* **1931**, 1931, 2605–2620.
- [33] P. Touzain, *Compt. Rend.* **1974**, C279, 41–42.
- [34] R. Hoppe, *J. Solid State Chem.* **1979**, 27, 99.
- [35] R. Hoppe, *Angew. Chem. Int. Ed. Engl.* **1980**, 19, 110–125.
- [36] H. Jacobs, B. Harbrecht, *Z. Naturforsch.* **1981**, 36b, 270–271.
- [37] H. Jacobs, B. Harbrecht, P. Müller, W. Bronger, *Z. Anorg. Allg. Chem.* **1982**, 491, 154–162.
- [38] R. Cerny, V. Favre Nicolin, B. Bertheville, *Acta Crystallogr.* **2002**, C58, i31–i32.
- [39] D. Mootz, H. Rütter, *Z. Anorg. Allg. Chem.* **1992**, 608, 123–130.
- [40] C. Hoch, J. Bender, A. Simon, *Angew. Chem. Int. Ed.* **2009**, 48, 2451–2453.
- [41] C. Hoch, J. Bender, A. Wohlfarth, A. Simon, *Z. Anorg. Allg. Chem.* **2009**, 635, 1777–1782.
- [42] J. Bender, A. Wohlfarth, C. Hoch, *Z. Naturforsch.* **2010**, 65b, 1416–1426.
- [43] C. Hoch, *Z. Naturforsch.* **2011**, 66b, 1248–1254.
- [44] L. H. Jones, *J. Chem. Phys.* **1954**, 22, 217–219.
- [45] K. A. Wickersheim, *J. Chem. Phys.* **1959**, 31, 863–869.
- [46] R. M. Hexter, *J. Chem. Phys.* **1961**, 34, 941–947.
- [47] R. A. Buchanan, E. L. King, H. H. Caspers, *J. Chem. Phys.* **1962**, 36, 2665–2675.
- [48] R. A. Buchanan, H. H. Caspers, H. R. Marlin, *J. Chem. Phys.* **1964**, 40, 1125–1127.
- [49] W. R. Busing, *J. Chem. Phys.* **1955**, 23, 933–936.
- [50] J. A. Ibers, J. Kumamoto, R. G. Snyder, *J. Chem. Phys.* **1960**, 33, 1164–1170.
- [51] J. A. Ibers, J. Kumamoto, R. G. Snyder, *J. Chem. Phys.* **1960**, 33, 1171–1177.
- [52] R. A. Buchanan, *J. Chem. Phys.* **1959**, 31, 870–874.
- [53] H. D. Lutz, J. Henning, H. Jacobs, B. Mach, *J. Mol. Struct.* **1986**, 145, 277–285.
- [54] J. C. Owrutsky, N. H. Rosenbaum, L. M. Tack, R. J. Saykally, *J. Chem. Phys.* **1986**, 84, 5308–5313.

- [55] Y. I. Ryskin, G. P. Stavitskaya, *Opt. Spektrosc.* **1981**, *50*, 398–400.
- [56] H. D. Lutz, W. Eckers, H. Haeuseler, *J. Mol. Struct.* **1982**, *80*, 221–224.
- [57] H. J. Werner, P. Rosmus, E. A. Reinsch, *J. Chem. Phys.* **1983**, *79*, 905–916.
- [58] K. Beckenkamp, H. D. Lutz, *J. Mol. Struct.* **1992**, *270*, 393–405.
- [59] R. Kiessling, *Acta Chem. Scand.* **1949**, *3*, 595–602.
- [60] S. Okada, T. Atoda, I. Higashi, *J. Solid State Chem.* **1987**, *68*, 61–67.
- [61] L. Helmholtz, *Z. Kristallogr.* **1936**, *95*, 129–137.
- [62] D. Becker, H. P. Beck, *Z. Kristallogr.* **2004**, *219*, 348–358.
- [63] L. M. Gelato, E. Parthé, *J. Appl. Crystallogr.* **1987**, *20*, 139–143.
- [64] K. R. Tsai, P. M. Harris, E. N. Lassette, *Z. Anorg. Allg. Chem.* **1939**, *242*, 33–40.
- [65] H. Jacobs, B. Mach, B. Harbrecht, H. D. Lutz, J. Henning, *Z. Anorg. Allg. Chem.* **1987**, *544*, 55–73.
- [66] X-RED, Data Reduction for STADIP and IPDS, Version 1.31, **2005**, Stoe & Cie., Darmstadt, Germany.
- [67] X-SHAPE, Crystal Optimization for Numerical Absorption Correction Version 2.07, **2005**, Stoe & Cie., Darmstadt, Germany.
- [68] G. M. Sheldrick, *Acta Crystallogr.* **2008**, *A64*, 112–122.
- [69] V. Petříček, M. Dušek, L. Palatinus, *Z. Kristallogr.* **2014**, *229*, 345–352.
- [70] L. W. Finger, M. Kroeker, B. H. Toby, *J. Appl. Crystallogr.* **2007**, *40*, 188–192.
- [71] H. P. Beck, G. Lederer, *Angew. Chem. Int. Ed. Engl.* **1993**, *32*, 292–293.
- [72] J. S. Loveday, W. G. Marshall, R. J. Nelmes, S. Klotz, G. Hamel, J. M. Besson, *J. Phys. Cond. Matt.* **1996**, *8*, 597–604.
- [73] W. Kleber, *Kristall und Technik* **1967**, *2*, 13–14.

6 The triple salt $\text{Sr}_{14}[\text{Ta}_4\text{N}_{13}][\text{TaN}_4]\text{O}$ – a nitridotantalate oxide with 19-fold rocksalt superstructure

Matthias Wörsching, Martin Daiger, Constantin Hoch

published in: *Inorg. Chem.* **2017**, DOI: 10.1021/acs.inorgchem.6b03053

Reprinted (adapted) with permission from Inorganic Chemistry. Copyright 2015 American Chemical Society.

Abstract

A new structure motif in nitridometalate chemistry is the *tetracatena*-nitridotantalate anion $[\text{Ta}_4\text{N}_{13}]^{19-}$. It occurs in the crystal structure of the triple salt $\text{Sr}_{14}[\text{Ta}_4\text{N}_{13}][\text{TaN}_4]\text{O}$ (monoclinic, space group $P2_1/c$ with $a = 15.062(2)$ Å, $b = 7.2484(6)$ Å, $c = 24.266(3)$ Å and $\beta = 97.280(10)^\circ$) together with *ortho*-tantalate and isolated oxide anions. Synthesis followed a new approach with employment of Sr surplus and reductive conditions aimed at the preparation of subvalent compounds. The new structure type was established on the basis of single crystal X-ray diffraction data and also Rietveld refinement. It is a complex superstructure of the rocksalt structure type with Ta and Sr atoms forming the fcc packing and N and O atoms occupying 18/19 of the octahedral voids. We discuss structure and stability of the triple salt with respect to other known nitridometalates and the use of this triple salt for preparative access toward new metal-rich compounds in this field.

6.1 Introduction

Tetrahedral anions as building blocks of crystal structures are a very common motif in structural inorganic chemistry. Among this large family of crystalline compounds silicates are the most extensively investigated representatives. They show the highest number of structural examples with respect to condensation degree and variability. Although in oxidosilicates the $[\text{SiO}_4]$ entities are connected only by sharing common corners, roughly 4000 crystal structures belonging to about 1160 different structure types are known.^[1] From all imaginable configurations and condensation grades some few cases are especially common. *Phyllo*-silicates often show a honeycomb-like layer type derived from *zweier* single chains. Three- and six-membered rings are much more often found in *cyclo*-silicates than four-membered or larger rings. In *soro*-silicates the disilicate anion is by far the most abundant one. The already huge structural variability is in principle further increased in nitridosilicates, as $[\text{SiN}_4]$ entities can be connected not only by sharing common corners but also edges. Furthermore, at one corner up to four tetrahedra can join together.^[2-4] Also here, the plethora of imaginable structures is not fully expressed in the known crystal structures as some configurations show a higher stability defined not only by the anionic sublattice but also by its coordination with the respective cations. There are only few examples for a linear four-membered anionic chain, e.g. the *tetracatena*-silicate anions in $\text{Na}_4\text{Sc}_2[\text{Si}_4\text{O}_{13}]$ ^[5] or $\text{Ba}_2\text{Nd}_2[\text{Si}_4\text{O}_{13}]$,^[6] and no nitridic species of this kind are known so far, see Table 6.1.

Table 6.1: Overview over reported compounds containing *ortho*- and *catena*-anions, and further anionic species.

Compound	Anions	Conformation
$\text{Na}_4\text{Sc}_2[\text{Si}_4\text{O}_{13}]$ ^[5]	<i>tetracatena</i> -silicate	zig-zag
$\text{Ba}_2\text{Nd}_2[\text{Si}_4\text{O}_{13}]$ ^[6]	<i>tetracatena</i> -silicate	zig-zag
$\text{Ag}_{18}[\text{Si}_4\text{O}_{13}][\text{SiO}_4]_2$ ^[8]	<i>tetracatena</i> -silicate, <i>ortho</i> -silicate	zig-zag
$\text{La}_6[\text{Si}_4\text{O}_{13}][\text{SiO}_4]_2$ ^[9]	<i>tetracatena</i> -silicate, <i>ortho</i> -silicate	horseshoe
$\text{Pb}_{21}[\text{Si}_7\text{O}_{22}]_2[\text{Si}_4\text{O}_{13}]$ ^[10]	heptameric silicate unit, <i>tetracatena</i> -silicate	branched zig-zag
$\text{Al}_2[\text{SiO}_4](\text{F}/\text{OH})_2$	<i>ortho</i> -silicate, fluoride, hydroxide	–
$\text{Al}_2[\text{SiO}_4]\text{O}$	<i>ortho</i> -silicate, oxide	–
$\text{Cs}_{10}[\text{GeO}_4]_2\text{O}$ ^[12]	<i>ortho</i> -germanate, oxide	–
$\text{Li}_{16}[\text{Ta}_4\text{N}_4]_2\text{O}$ ^[13]	<i>ortho</i> -nitridotantalate, oxide	–
$\text{Ba}_9\text{N}[\text{N}_3][\text{Ta}_4\text{N}_4]_2$ ^[14]	<i>ortho</i> -nitridotantalate, azide, nitride	–
$\text{Li}_3\text{Sr}_2[\text{Ta}_4\text{N}_4]$ ^[15]	<i>ortho</i> -nitridotantalate	–
$\text{Li}_7[\text{Ta}_4\text{N}_4]$ ^[16]	<i>ortho</i> -nitridotantalate	–
$\text{Sr}_2[\text{Ta}_4\text{N}_3]$ ^[17]	<i>ino</i> -nitridotantalate	<i>zweier</i> single chain
$\text{Ba}_2[\text{Ta}_4\text{N}_3]$ ^[18]	<i>ino</i> -nitridotantalate	<i>zweier</i> single chain
$\text{Ba}_2\text{Cl}_2[\text{Ta}_4\text{N}_3]$ ^[19]	<i>ino</i> -nitridotantalate, chloride	<i>zweier</i> single chain

The coexistence of two different, spatially separated silicate anions in the fashion of a double salt named *sub-silicate* according to silicate nomenclature^[7] also is quite rare. The combination of a *tetracatena*-anion together with a second anionic unit therefore may be anticipated as a very improbable structural motif. However, some examples for the coexistence of *ortho*- and *tetracatena*-anions are known, but only for the two synthetic silicates $\text{Ag}_{18}[\text{Si}_4\text{O}_{13}][\text{SiO}_4]_2$,^[8] $\text{La}_6[\text{Si}_4\text{O}_{13}][\text{SiO}_4]_2$,^[9] and with the crystal structure of $\text{Pb}_{21}[\text{Si}_7\text{O}_{22}]_2[\text{Si}_4\text{O}_{13}]$ ^[10] there exists one example for a *sub-catena*-silicate with two *catena*-anions of different lengths. There are two conformations for the linear *catena*-anion. In most cases the zig-zag or *trans*-configuration is observed, only in $\text{La}_6[\text{Si}_4\text{O}_{13}][\text{SiO}_4]_2$ the anion has a horseshoe or *cis*-configuration.

Mixing a silicate anion with a small nonsilicatic anion as e.g. oxide is less uncommon. There are *sub-silicates* in which isolated, small additional anions stabilise the lattice in terms of Pauling's second rule for ionic crystals:^[11] in structures with small and highly charged anions combined with rather large and low-charged cations the insertion of a single oxide, hydroxide or fluoride ion can provide the amount of Coulombic energy necessary to form a stable lattice. This lattice stabilisation through additional oxide anions is well documented in literature, e.g. for the minerals topaz, $\text{Al}_2[\text{SiO}_4](\text{F}/\text{OH})_2$, sillimanite, kyanite and andalusite (all modifications of $\text{Al}_2[\text{SiO}_4]\text{O}$) or for the synthetic $\text{Cs}_{10}[\text{GeO}_4]_2\text{O}$,^[12] whereas the corresponding simple aluminium *ortho*-silicate and cesium *ortho*-germanate are unknown so far.

All nitridotantalates known so far either exhibit isolated $[\text{Ta}_4\text{N}_4]^{7-}$ anions as in e.g. $\text{Ba}_9\text{N}[\text{N}_3][\text{Ta}_4\text{N}_4]_2$,^[14] $\text{Li}_3\text{Sr}_2[\text{Ta}_4\text{N}_4]$,^[15] $\text{Li}_7[\text{Ta}_4\text{N}_4]$ ^[16] and $\text{Li}_{16}[\text{Ta}_4\text{N}_4]_2\text{O}$,^[13] or infinite chains of corner-sharing $[\text{Ta}_4\text{N}_4]$ tetrahedra as in e.g. $\text{Sr}_2[\text{Ta}_4\text{N}_3]$,^[17] $\text{Ba}_2[\text{Ta}_4\text{N}_3]$ ^[18] and $\text{Ba}_2\text{Cl}_2[\text{Ta}_4\text{N}_3]$.^[19] In this work we show a crystal structure combining three aspects, the combination of which must be seen as an unexpected and rare case. $\text{Sr}_{14}[\text{Ta}_4\text{N}_{13}][\text{Ta}_4\text{N}_4]\text{O}$ is a nitridometalate presenting the first examples for *tetracatena*-nitridotantalate anions, combined with additional *ortho*-nitridotantalate and isolated oxide anions in a triple salt. Due to the unexpected and very unusual condensation degree in $\text{Sr}_{14}[\text{Ta}_4\text{N}_{13}][\text{Ta}_4\text{N}_4]\text{O}$ the question of thermodynamic stability arises with regard to decomposition of the triple salt into the three quasi-binary phases and also the 'comproportionation' of the *tetracatena*- and the *ortho*-nitridotantalate anion into one with intermediate chain length. Taking this into account it is important to emphasise that the reaction of Sr_2N and Sr with elemental tantalum in a sodium flux actually was aimed at the synthesis of a different metastable compound class, the so-called subnitridometalates, as has been done in previous work.^[19]

6.2 Experimental section

Starting materials

Sr_2N was prepared by reaction of Sr (distilled, 99.95 %, SMT Metalle Wimmer, Weinburg, Austria) in N_2 flow at 830 °C. Tantalum was used as reaction vessel material. Nitrogen gas was dried and purified by passing over columns of KOH, silica gel, molecular sieve, P_4O_{10} and BTS catalyst prior to reaction.

Synthesis of $\text{Sr}_{14}[\text{Ta}_4\text{N}_{13}][\text{TaN}_4]\text{O}$

Prismatic single crystals of $\text{Sr}_{14}[\text{Ta}_4\text{N}_{13}][\text{TaN}_4]\text{O}$ were obtained by reaction of 127.2 mg (1.452 mmol) Sr (distilled, 99.95 %, SMT Metalle Wimmer, Weinburg, Austria), 104.9 mg (0.605 mmol) Ta (powder, 99.5 %, Merck, Darmstadt, Germany) and 439.0 mg (2.320 mmol) Sr_2N at 900 °C in a Na flux (100.1 mg; 4.354 mmol) in sealed tantalum crucibles. Sr_2N was observed in the product mixture as a side phase. Due to the high sensitivity of reactants and products towards air and moisture all handling was carried out under argon atmosphere using either glove boxes or Schlenk technique. Na excess was removed after the reaction by distillation. Traces of oxygen were probably introduced during arc-welding of the tantalum crucible. The composition of $\text{Sr}_{14}[\text{Ta}_4\text{N}_{13}][\text{TaN}_4]\text{O}$ as the main phase was confirmed by EDX analysis (see Table S6.5 and Figure S6.2 in the Supporting Information), which shows the expected Sr/Ta ratio, the absence of Na in the bulk sample and the simultaneous (yet not quantifiable) presence of O and N and Sr_2N as the minority phase.

Powder X-ray diffraction

Powder X-ray diffraction experiments were performed to verify purity of all starting materials on a STOE Stadi P powder diffractometer system (Stoe & Cie. GmbH, Darmstadt, Germany) in Debye-Scherrer geometry with Ge(111)-monochromatised $\text{Cu}_{\text{K}\alpha 1}$ radiation ($\lambda = 1.5405 \text{ \AA}$) and a Mythen 1K detector system (Dectris Ltd., Baden-Daettwil, Switzerland). The reaction product was also analysed by powder diffractometry applying $\text{Cu}_{\text{K}\alpha 1}$ radiation, despite the high absorption coefficient of the product in this radiation. As Sr shows strong anomalous dispersion in $\text{Mo}_{\text{K}\alpha}$ radiation the powder diffraction results were taken as complementary confirmation of the structure model derived from the single crystal studies. Rietveld refinement was performed with the software TOPAS Academic 4 using the fundamental parameter approach.^[21] The results are given in Figure S6.1 and Table S6.3 in the Supporting Information.

Single crystal X-ray diffraction

Single crystal X-ray diffraction patterns were recorded with a D8 Quest diffraction system (Bruker AXS GmbH, Karlsruhe, Germany) equipped with a PHOTON 100 CMOS Detector in $\text{Mo}_{\text{K}\alpha}$ radiation ($\lambda = 0.71073 \text{ \AA}$, Göbel mirror optics). Due to the high sensitivity of the samples towards air and moisture all single crystals were prepared under dry paraffin oil and sealed in oil-filled glass capillaries. Crystallographic details are given in Tables 6.2 and 6.3, and in Tables S6.1, S6.2 and S6.4 in the Supporting Information.

Lattice Energy Calculations According to the MAPLE Concept

Lattice energy calculations (MAPLE: Madelung part of the lattice energy) were performed to prove the electrostatic consistency of the crystal structure.^[22, 23] Exclusively electrostatic interactions in an ionic crystal were taken into account, depending on the charge, distance and coordination spheres of the constituting ions. The results of the calculations are presented in Table 6.3.

6.3 Results and Discussion

Crystal structure

$\text{Sr}_{14}[\text{Ta}_4\text{N}_4][\text{Ta}_4\text{N}_{13}]\text{O}$ crystallises in the monoclinic system with space group $P2_1/c$ in a new structure type. The crystals are black and form platelets. After structure solution with direct methods the crystal structure was refined to satisfying R values (see Table 6.2) in full-matrix least-squares cycles. All heavy atom positions were taken from structure solution, the positions of N and O atoms were assigned from the difference Fourier map. The criteria for assignment of the difference electron density maxima to either N or O atoms are addressed below.

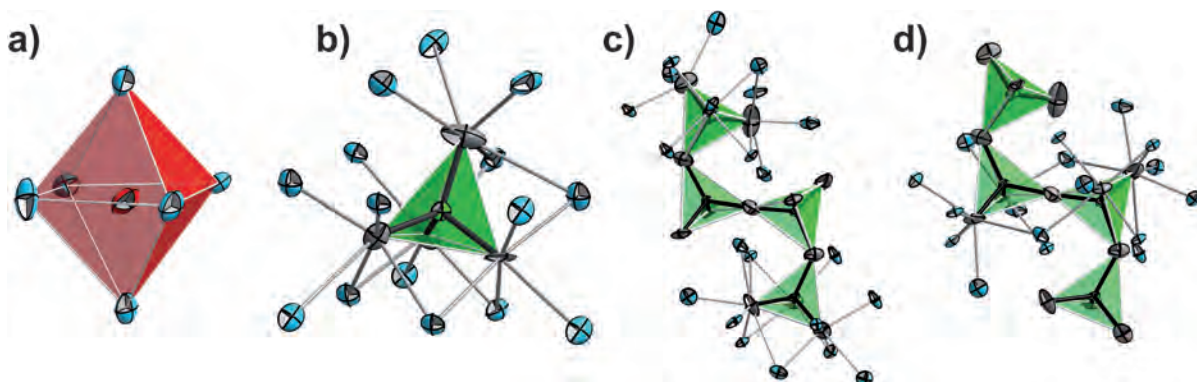


Figure 6.1: The three different anions in $\text{Sr}_{14}\text{Ta}_5\text{N}_{17}\text{O}$. a: Octahedrally coordinated oxide anion; b: *ortho*-nitridotantalate anion; c and d: *catena*-tetranitridotantalate anion. Coordination of N atoms is plotted (c: N atoms of the two terminal nitridotantalate units, d: N atoms of the two internal nitridotantalate units). Sr atoms: blue, Ta atoms: green, N atoms: grey, O atoms: red. Thermal ellipsoids for all atoms are drawn at a 99% probability level.

Due to high Sr content and resulting high anomalous dispersion effects in Mo radiation, much work has been put into absorption correction. However, relatively high residual electron densities could not fully be suppressed. In addition to the single crystal diffraction experiments in Mo radiation, powder diffractograms were recorded in $\text{Cu}_{K\alpha 1}$ radiation and Rietveld refinement supports the single crystal structure model. The location of the highest residual electron density peaks indicate termination effects of both Ta and Sr (peak distances 0.41 Å to 1.13 Å from the heavy atom positions). All atoms were refined with anisotropic treatment of the thermal displacement parameters. For detailed information on crystallographic data see Tables 6.2 and 6.3 and Tables S6.1, S6.2 and S6.4 in the Supporting Information. Further details on the structure investigations are available from the Fachinformationszentrum Karlsruhe, D-76344 Eggenstein Leopoldshafen, Germany (fax:(+ 49)-7247-808-666; e-mail:crysdata@fiz-karlsruhe.de) on quoting the depository number CSD-432368.

The crystal structure of $\text{Sr}_{14}[\text{Ta}_4\text{N}_{13}][\text{Ta}_4\text{N}_4]\text{O}$ (see Figure 6.6) shows three different anionic structural motifs embedded in a matrix of Sr^{2+} cations. Ta₃ constitutes the centre of an isolated, tetrahedral *ortho*-nitridotantalate anion, $[\text{Ta}_4\text{N}_4]^{7-}$ (see Figure 6.1b). All four N atoms are crystallographically independent (see Table 6.3), as all atoms occupy the general position. Thus, the $[\text{Ta}_4\text{N}_4]^{7-}$ anion does not have a point symmetry higher than 1. The deviation from ideal T_d symmetry is considerable. Bond angles (see Ta-

Table 6.2: Crystallographic data and selected detail about data collection, structure solution and refinement of $\text{Sr}_{14}\text{Ta}_5\text{N}_{17}\text{O}$

Crystal system	monoclinic
Space group	$P2_1/c$ (No. 14)
Lattice parameters / \AA / $^\circ$	a 15.062(2) b 7.2484(6) c 24.226(3) β 97.280(10)
Volume / \AA^3	2623.6(5)
Z	4
Calculated density / $\text{g} \cdot \text{cm}^{-3}$	6.040
Diffractometer	D8-Quest, MoK_α radiation Göbel mirror
Data collection temperature /K	295(2)
Absorption coefficient / mm^{-1}	48.97
Data range ϑ / $^\circ$	2.31–30.00
Index range	$-21 \leq h \leq 21$, $-9 \leq k \leq 10$, $-34 \leq l \leq 34$
No. of observed reflections	61592
No. of independent reflections	7653
No. of independent reflections with $(I \geq 2\sigma(I))$	5734
$F(000)$	4096
Corrections	absorption (multi-scan) ^[2]
Structure solution	direct methods ^[3]
Structure refinement	full-matrix least squares on F^2 ^[3]
No. of l. s. parameters	334
G_{ooF} on F^2	1.004
$R_{\text{int}} / R_\sigma$	0.0682 / 0.0453
R values (for reflections with $I \geq 2\sigma(I)$)	$R_1 = 0.0320$, $wR_2 = 0.0529$
R values (all data)	$R_1 = 0.0580$, $wR_2 = 0.0571$
Residual electron density / $\text{e}^- \cdot \text{\AA}^{-3}$	2.989 / -2.760
ICSD depository number	CSD-432368

Table 6.3: Standardised fractional atomic coordinates^[26] and equivalent isotropic displacement parameters for Sr₁₄Ta₅N₁₇O. All atoms occupy crystallographic sites with Wyckoff number 4e. Standard deviations of the last digits are given in parentheses. Partial MAPLE values for each atom are given in the last column.

Atom	x	y	z	$U_{\text{eq}} / \text{\AA}^2$	Partial MAPLE values / kJmol ⁻¹
Ta1	0.05337(2)	0.32974(3)	0.402560(10)	0.00292(6)	12475
Ta2	0.12915(2)	0.15035(3)	0.145957(10)	0.003860(6)	12343
Ta3	0.30975(2)	0.66285(3)	0.009710(10)	0.00348(6)	12182
Ta4	0.40552(2)	0.14017(3)	0.314019(10)	0.00426(6)	12387
Ta5	0.76476(2)	0.31944(3)	0.232080(10)	0.00324(6)	12871
Sr1	0.00757(5)	0.02126(8)	0.24067(2)	0.00877(14)	2160
Sr2	0.06393(4)	0.86965(8)	0.37733(2)	0.00601(13)	1992
Sr3	0.11727(5)	0.61414(8)	0.51757(2)	0.00756(13)	1812
Sr4	0.11827(4)	0.40907(8)	0.01893(2)	0.00577(13)	1905
Sr5	0.14827(5)	0.63789(8)	0.14694(2)	0.00885(14)	1942
Sr6	0.20820(5)	0.34812(8)	0.27008(2)	0.00798(13)	2202
Sr7	0.25543(4)	0.11617(8)	0.40237(2)	0.00724(13)	1770
Sr8	0.31363(4)	0.13309(8)	0.03324(2)	0.00808(13)	1811
Sr9	0.35597(5)	0.41036(9)	0.15488(3)	0.00994(14)	1848
Sr10	0.47889(4)	0.37516(8)	0.43222(2)	0.00748(13)	2051
Sr11	0.52124(4)	0.38246(8)	0.06837(2)	0.00631(13)	1952
Sr12	0.56041(5)	0.10732(9)	0.20679(3)	0.01155(14)	1796
Sr13	0.65178(5)	0.40792(9)	0.33938(3)	0.01201(15)	2016
Sr14	0.74262(4)	0.09827(8)	0.10596(2)	0.00622(13)	1869
N1	0.0125(4)	0.6440(7)	0.0083(12)	0.0083(12)	4575
N2	0.0220(4)	0.0581(7)	0.0947(2)	0.0107(12)	4580
N3	0.0763(4)	0.2272(8)	0.3315(2)	0.0140(13)	4571
N4	0.0823(4)	0.3450(7)	0.1867(2)	0.0079(12)	5260
N5	0.1434(4)	0.6985(2)	0.3014(2)	0.0095(12)	4681
N6	0.1648(4)	0.3585(7)	0.4512(2)	0.0081(11)	4487
N7	0.1786(4)	0.5208(7)	0.7063(2)	0.0108(12)	4619
N8	0.2160(4)	0.2481(9)	0.1036(2)	0.0185(14)	5410
N9	0.2588(4)	0.07350(8)	0.0772(2)	0.0161(13)	5718
N10	0.2877(4)	0.6331(7)	0.2270(2)	0.0064(11)	4822
N11	0.3462(4)	0.3410(7)	0.3494(2)	0.0061(11)	4388
N12	0.3751(4)	0.0714(7)	0.4970(2)	0.0076(11)	4665
N13	0.4085(5)	0.1976(9)	0.2376(2)	0.0249(16)	4644
N14	0.5212(4)	0.1356(7)	0.3575(2)	0.0147(13)	4361
N15	0.6181(4)	0.1394(7)	0.0182(2)	0.0080(12)	4556
N16	0.6672(4)	0.4055(7)	0.1724(2)	0.0104(12)	4306
N17	0.8002(4)	0.3486(7)	0.0430(2)	0.0073(11)	4298
O1	0.4448(3)	0.1274(6)	0.1106(2)	0.0195(12)	1668

^a Typical partial MAPLE values in (oxo-)nitridosilicates / kJmol⁻¹: Sr: 1500–2100; N: 4300–6200; O: 2000–2800.^[4]

^b Calculated MAPLE values for Sr₂TaN₃ as reference material / kJmol⁻¹: Ta: 12903; Sr: 1850, 1916; N: 4637, 4516, 5334, 5454.

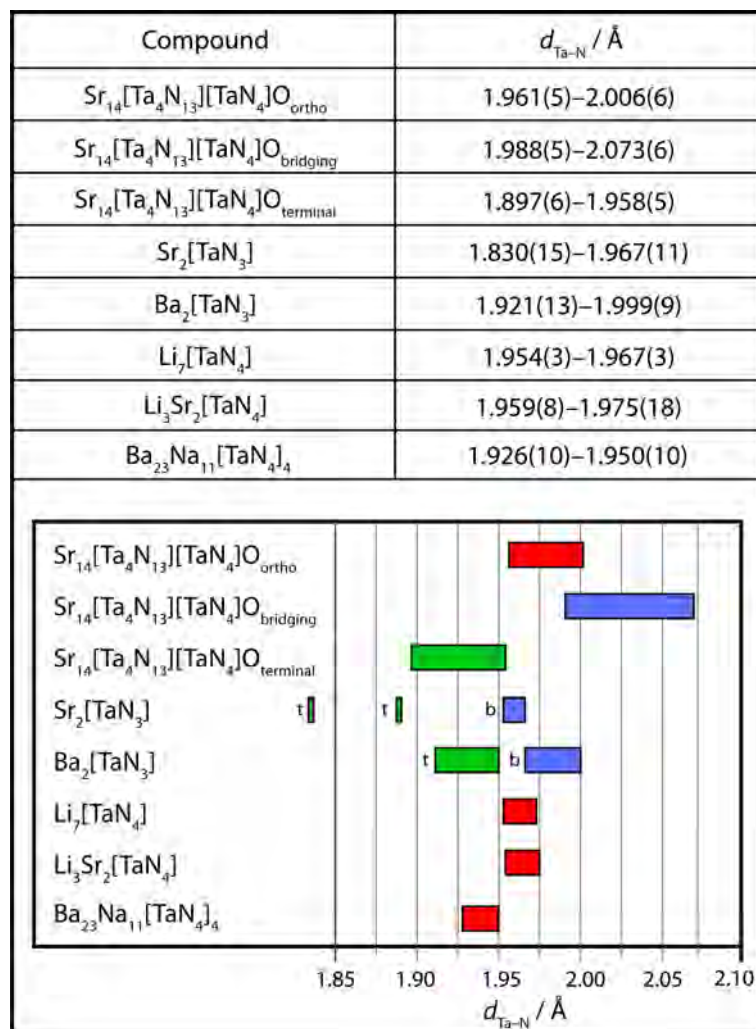


Figure 6.2: Tabular and graphical representation of Ta–N distances in $\text{Sr}_{14}[\text{Ta}_4\text{N}_{13}][\text{TaN}_4]\text{O}$ classified in three different groups due to their type of motif. Literature data for known *ortho*- and *ino*-nitridotantalate compounds is given for comparison. t = terminal; b = bridging.^[15–19]

ble S6.4 in the Supporting Information) range from 99.7(2) to 127.3(3)°. The interatomic Ta–N distances vary between 1.961(5) and 2.006(6) Å (see Table S6.2 in the Supporting Information and Figure 6.2) and are very well in agreement with those found in comparable crystal structures.^[14,15,19] The strong distortion of the [Ta₄N₄]⁷⁻ tetrahedron may be attributed to the coordination needs of the N atoms versus Ta and Sr cations. All N atoms have a sixfold coordination by one Ta and five Sr atoms (see Table 6.3 and Figure 6.1b), arranged in distorted octahedra. A large range of Sr–N distances (2.535(6) to 3.243(6) Å) is also found in e.g. Li₃Sr₂TaN₄ (Sr–N distances: 2.602(13) to 2.941(8) Å). Here it leads to different electrostatic environments for the four individual N atoms and to a distortion of the [Ta₄N₄]⁷⁻ anion. Partial MAPLE values for Ta and N atoms correlate to the energy range documented in literature as well as with the values calculated for Sr₂TaN₃ as a reference, respectively (see Table 6.3 and footnotes therein). Considering the second coordination sphere of Ta3 by Sr²⁺ cations a strongly distorted cuboctahedron results, as is the case in the majority of compounds with tetrahedral *ortho*-metalate anions.

The second nitridometalate anion in Sr₁₄[Ta₄N₁₃][Ta₄N₄]O is a linear *catena*-tetranitridotantalate anion, [Ta₄N₁₃]¹⁹⁻, in *trans*-configuration. It consists of four crystallographically independent Ta atoms (Ta1, Ta2, Ta4, Ta5 in Table 6.3) each tetrahedrally coordinated by altogether 13 N atoms. The individual tetrahedral units are connected via common vertices forming a *vierer* chain. As mentioned above, *catena*-tetranitridotantalate anions have hitherto not been documented in literature. Analogous structural entities are known from silicate chemistry: in e.g. Ag₁₀[Si₄O₁₃]^[8] the *catena*-tetrasilicate anions occur in a *trans* or zigzag conformation, whereas in e.g. La₆[Si₄O₁₃][SiO₄]₂^[9] a *cis* or horseshoe conformation can be found. The zigzag conformation is also present in the crystal structure of Sr₁₄[Ta₄N₁₃][Ta₄N₄]O, and following the law of Clark and Morley^[27] this should be the more favourable conformation. In accordance with the few literature examples for *catena*-nitridotantalate anions^[17,18] two different sets of interatomic Ta–N distances occur (see Figure 6.2 and Table S6.2 in the Supporting Information). Terminal N atoms have shorter bonds (1.897(6) to 1.958(5) Å) and bridging N atoms have longer ones (1.988(5) to 2.073(5) Å). In direct comparison, the interatomic Ta–N distances in the *ortho*-nitridotantalate anion have intermediate values. For Sr₂[Ta₃N₃]^[17] one extremely short Ta–N contact of 1.830(15) Å is reported, not matching the pattern of all other reference values. The reason thereof is not clear. As in the *ortho*-nitridotantalate anion deviation of the tetrahedral units from ideal T_d point symmetry is considerable. For the terminal [Ta₄N₄] entities around Ta1 and Ta4 the interatomic angles range from 101.8(2) to 120.5(2)° and hence deviate slightly less from true tetrahedral geometry than the internal [Ta₄N₄] units around Ta2 and Ta5 showing angles of 100.9(2) to 124.0° (see Table S6.4 in the Supporting Information). Figures 6.1c and d show the coordination of N atoms by Sr²⁺ cations. For enhanced clarity the coordination of the two terminal nitridotantalate subunits around Ta1 and Ta4 are shown in Figures 6.1c, and in Figure 6.1d the coordination of the two inner nitridotantalate subunits around Ta2 and Ta5 is displayed. As in the *ortho*-nitridotantalate anion around Ta3, the N atoms aim at octahedral coordination by five Sr and one Ta atoms, however coordination numbers now vary between five (N7, N14 and N17) and seven (N3 and N8). All calculated partial MAPLE values are in good agreement with literature data and values of the respective reference compound (see Table 6.3 and footnotes therein).

The third anionic species completing the 'triple salt' is an O^{2-} anion, only coordinated by 6 Sr^{2+} cations (Sr8 to Sr13) constituting a slightly distorted octahedron (see Figure 6.1a). Sr–O distances range from 2.457(6) to 2.741(6) Å and correspond well to literature data (e.g. 2.562(5) Å in SrO).^[28] Traces of oxygen were probably introduced during arc-welding of the tantalum crucible. As mentioned above, the insertion of isolated O^{2-} anions into metalate structures is well-documented in literature^[12,13] and provide an additional Coulombic interaction in structures with otherwise too low lattice energies in terms of Pauling's second rule for ionic crystals. Comparison of Sr–O with Sr–N distances shows Sr–O distances to be expectedly shorter. Shortest contacts between Sr and O add up to 2.457 Å compared to 2.514 Å between Sr and N. It is not easy to discern O from N atoms only on the basis of single crystal structure data, especially when high anomalous dispersion is present. In addition to the difference in interatomic distances and to the charge balance achieved only in the case of oxide anions, their presence was further assigned to this crystallographic position on the basis of lattice energy calculations with MAPLE. The partial MAPLE value for the O^{2-} anion is slightly lower than those generally documented for silicate compounds.^[4] Much lower energies have been observed in oxonitridosilicates ($\sim 1200 \text{ kJmol}^{-1}$).^[29] Literature data for N atoms, however, suggest much higher energies.^[4] The partial MAPLE value strongly corroborates the existence of one O^{2-} anion on this crystallographic site, and analogous calculations with N^{3-} give very different and unreasonable results.

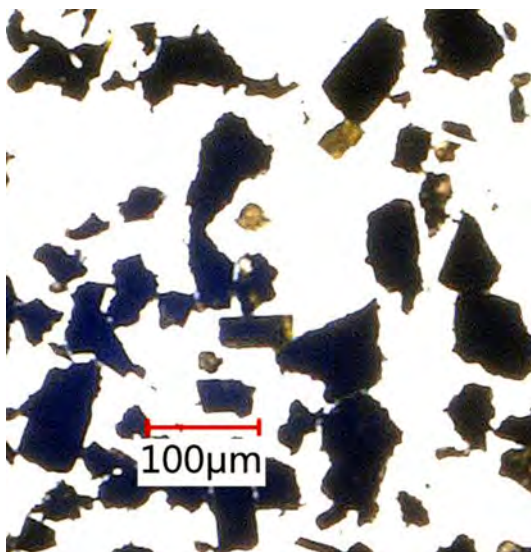


Figure 6.3: Photograph in transmitted light of a sample of $Sr_{14}[Ta_4N_{13}][TaN_4]O$. Thin crystals show transparency and yellow colour.

The reaction product contains the metallic subnitride Sr_2N as a minority phase (see Table S6.5 and Figure S6.2 in the Supporting Information) and therefore no conductance or susceptibility measurements could be performed in order to prove $Sr_{14}[Ta_4N_{13}][TaN_4]O$ to be a purely ionic, electron-precise valence compound. As the synthesis was performed with a large metal surplus under reducing conditions and indeed was intended to the formation of a subvalent nitridometalate, it may not be clear on the first glance why we regard this compound to be electron-precise. There are several independent characteristics favouring strongly this view: (1) The crystals of $Sr_{14}[Ta_4N_{13}][TaN_4]O$ are very brittle

and not ductile as known suboxo- and subnitridometalates. (2) The crystal structure of $\text{Sr}_{14}[\text{Ta}_4\text{N}_{13}][\text{Ta}_4\text{N}_4]\text{O}$ shows only typical ionic building units. Subvalent compounds all show metal-metal contacts. (3) Interatomic distances point clearly to Ta(V) rather than Ta(III). (4) Interatomic distances to Sr clearly point to Sr^{2+} rather than Sr^0 . The large difference between the atomic radius of Sr and the ionic radius of Sr^{2+} can be used as indicative for subvalent crystal structures. (5) Thin fragments of crystals of $\text{Sr}_{14}[\text{Ta}_4\text{N}_{13}][\text{Ta}_4\text{N}_4]\text{O}$, which appears black as a bulk material, show optical transparency and yellow colour in transmitted light (see Figure 6.3), indicating a rather large band gap in the optical range, as could be expected for an ionic nitridotantalate.

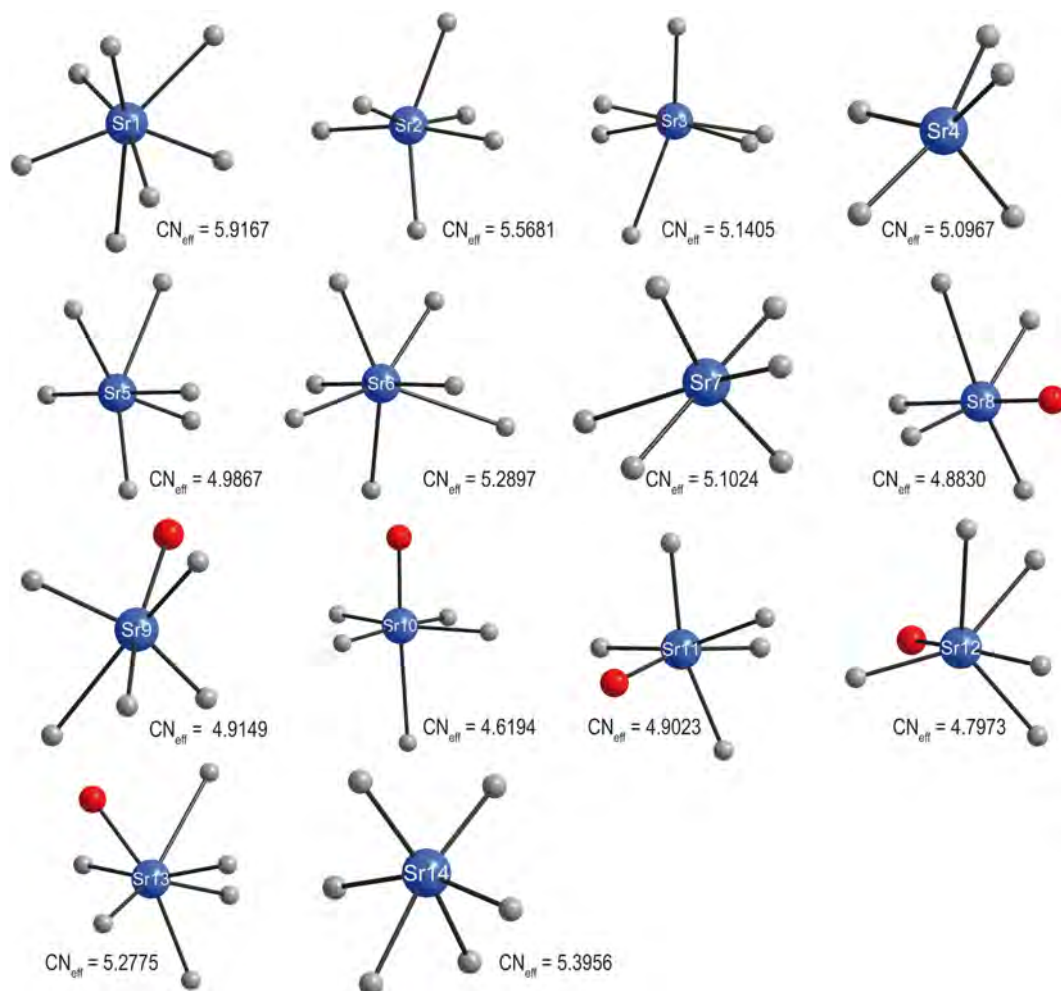


Figure 6.4: Coordination of the 14 crystallographically independent Sr atoms in $\text{Sr}_{14}[\text{Ta}_4\text{N}_{13}][\text{Ta}_4\text{N}_4]\text{O}$. Sr atoms: blue spheres, N atoms: grey spheres, O atoms: red spheres. Effective coordination numbers (ECoN) were calculated with MAPLE (CHARDI concept).

The coordination of the 14 crystallographically independent Sr^{2+} cations by N and O atoms is shown in Figure 6.4. As in many other ionic Sr-N and Sr-O compounds the coordination numbers vary from 5 to 7, however, these values are to be considered with care as the coordination spheres around Sr are not well defined: no clear cut-offs in Sr-N(O) distances can be observed. We have calculated effective coordination numbers of Sr using MAPLE (CHARDI concept) and the results are given in Figure 6.4. Sr-

N(O) distances range from 2.457(6) Å to 3.578(5) Å, well in agreement for comparable literature values.^[30,31] As the coordination spheres are poorly defined, the partial contributions of longer Sr–N contacts to an individual coordination sphere had to be taken into consideration in the calculation of partial MAPLE values, which agree quite well with literature data (see Table 6.3).

Packing analysis

The crystal structure of Sr₁₄[Ta₄N₁₃][TaN₄]O can be rationalised by considering the packing of the heavy atoms. Sr together with Ta atoms are arranged in a distorted *fcc* superstructure, see Figure 6.5. The stacking direction of the hexagonal layers is approximately $[-1\ 0\ 5]$ with respect to the monoclinic unit cell. In this direction, nine layers are present in one translational period, leading to the packing pattern ABCA'B'C'A''B''C''. Along the second stacking direction shown in Figure 6.5 also nine layers are arranged along an approximate $[2\ 0\ 3]$ direction. The orientation of the basic *fcc* unit cell with respect to the actual monoclinic unit cell is also shown in Figure 6.5.

The directions of the lattice vectors of the pseudocubic unit cell are connected with the monoclinic lattice by the matrix $\begin{pmatrix} -1/2 & 2/3 & 1/2 \\ -1/2 & -2/3 & 1/2 \\ 2/3 & 0 & 3/4 \end{pmatrix}$. The lattice parameter and the volume of the pseudocubic cell are $a_{\text{cub}} = 5.14(8)$ Å and $V_{\text{cub}} = 135(5)$ Å³. With a volume of 2623.6(5) Å³ the monoclinic cell is 19 times larger, in accordance with both monoclinic and pseudocubic unit cells having $Z = 4$. The nitride and oxide anions occupy octahedral voids within the *fcc* arrangement of cations. The *catena*-tetranitridotantalate anion has a zigzag conformation, resulting from the ordering pattern of Sr and Ta atoms in the *fcc* packing, see Figure 6.6. Two Ta atoms belong to one of the hexagonal layers, and the other two to an adjacent layer. The chemical formula $\underbrace{\text{Sr}_{14}\text{Ta}_5}_{\text{fcc}} \underbrace{\text{N}_{17}\text{O}}_{\text{oct.voids}}$ shows that in this

NaCl-type topology every 19th octahedral void must be vacant. The ordering patterns of Ta and Sr atoms, of O and N anions and the ordering of the vacancies give the reason for the complicated and low-symmetric 19-fold superstructure of the underlying NaCl-type topology. With $Z = 4$ and the given composition, a total of 76 sphere-packing cations and 72 void-filling anions is present in the unit cell, accounting for 4 empty octahedral voids. Their position is shown in Figure 6.5. The two layers c and a'' show rows of voids left empty, leading to considerable relaxation of the atomic positions in direct vicinity. These are the terminal N atoms of the *catena*-nitridotantalate units, which by this relaxation allow for a less distorted tetrahedral coordination for Ta than in the case of the *ortho*-nitridotantalate units.

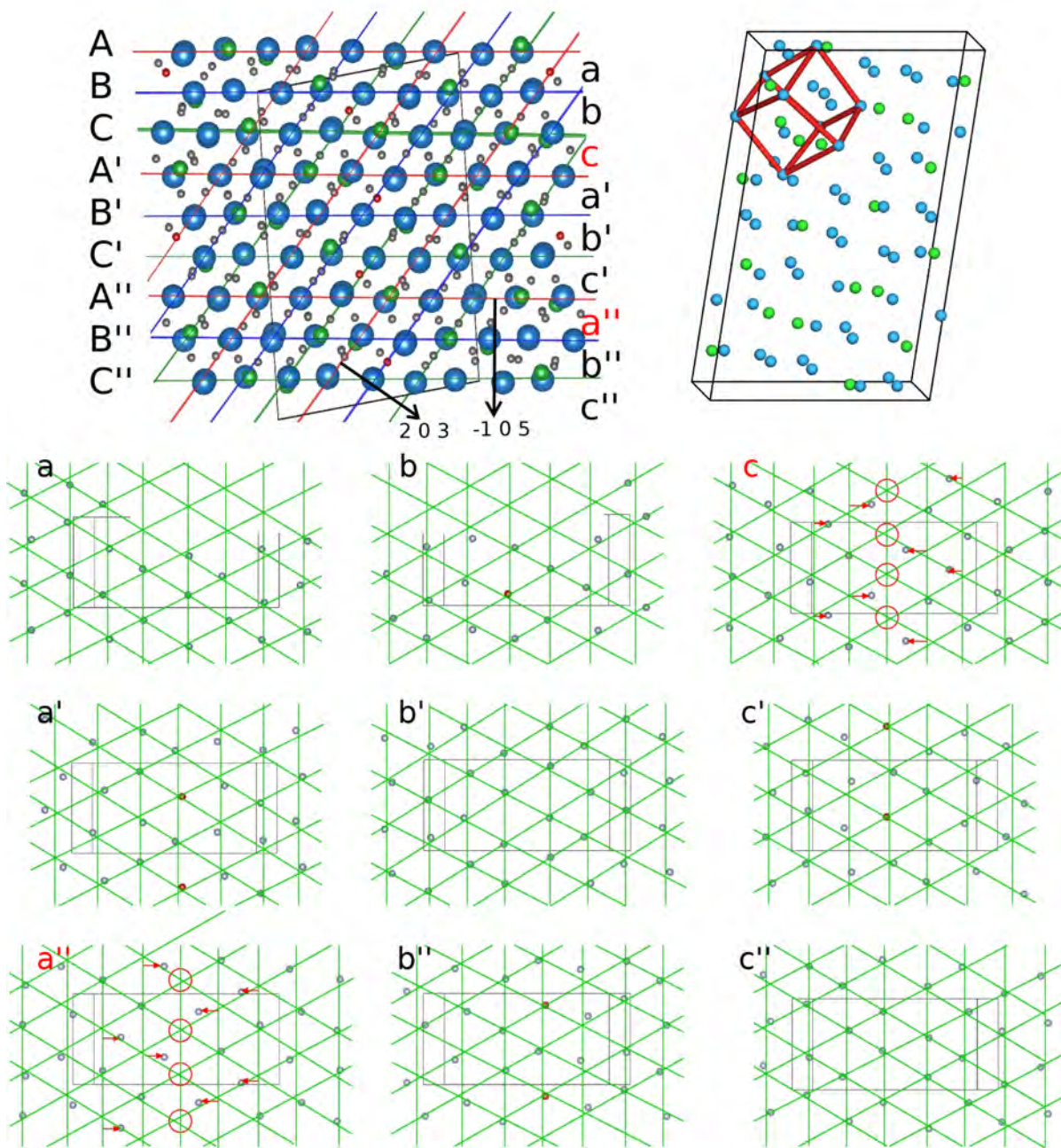


Figure 6.5: Crystal structure of $\text{Sr}_{14}[\text{Ta}_4\text{N}_{13}][\text{TaN}_4]\text{O}$. Upper left: view along the b axis of the monoclinic unit cell. Sr atoms (blue spheres) and Ta atoms (green spheres) form a slightly distorted fcc packing. One unit cell comprises three stacking sequences ABC along both of the two given stacking directions. The orientation of the basic fcc unit cell is shown on the upper right. N atoms (grey spheres) and O atoms (red spheres) are situated in the octahedral gaps. Projections on the individual octahedral layers abc are shown below, together with lines of best fit as optical guidance. The octahedral layers c and a'' given in red contain the voids (red circles) and show considerable displacement of the adjacent atoms from their ideal positions (red arrows).

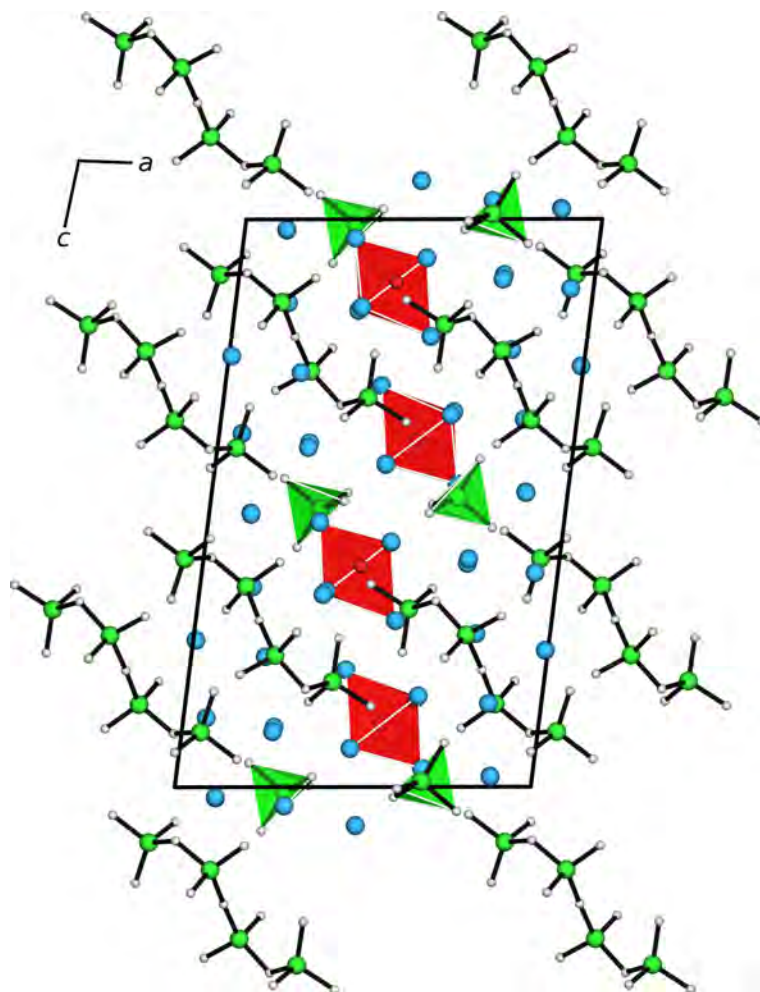


Figure 6.6: Crystal structure of $\text{Sr}_{14}[\text{Ta}_4\text{N}_{13}][\text{TaN}_4]\text{O}$. The coordination of O atoms (red spheres) is depicted as red octahedra, the *ortho*-nitridotantalate anions are drawn as green tetrahedra, the *tetracatena*-nitridotantalate anions are drawn as ball-and-stick pattern (Ta: green, N: grey and Sr: blue spheres).

The considerable deviation from ideal T_d symmetry of the nitridotantalate units is a direct consequence of the underlying NaCl-type packing. The occupation of octahedral voids by N (and O) atoms in a packing of Sr and Ta atoms cannot lead to a regular tetrahedral coordination of Ta, and a rearrangement of the atomic positions has to follow both the requirements of the NaCl-type lattice as well as the formation of a tetrahedral anionic moiety with fitting cationic coordination pattern and lowest possible distortions.

6.4 Conclusion

We present synthesis and crystal structure of the nitridotantalate oxide $\text{Sr}_{14}[\text{Ta}_4\text{N}_{13}][\text{TaN}_4]\text{O}$. Its crystal structure exhibits finitely condensed *catena*-tetranitridotantalate anions $[\text{Ta}_4\text{N}_{13}]^{19-}$, as well as isolated *ortho*-nitridotantalate $[\text{TaN}_4]^{7-}$ and isolated oxide anions, O^{2-} . The successful synthesis of $\text{Sr}_{14}[\text{Ta}_4\text{N}_{13}][\text{TaN}_4]\text{O}$ and its unique structural motifs shows synthesis of further new nitridometalates (or nitridometalate oxides) with tetrahedrally coordinated transition metals to be auspicious.

We employed a new synthetic approach with reductive conditions and a Sr surplus. An analogous approach previously proved successful for the synthesis of metal-rich alkali metal oxidometalates with low connectivity in the anionic substructures.^[32–35] The unusual variation of the degree of condensation within the anionic part of one compound further broadens the conceivable structural variations. Our synthetic approach based on the application of reducing conditions with surplus elemental alkali or earth alkaline metal combined with relatively low temperatures can yield metal-rich compounds in two ways. As we have shown previously, subvalent compounds, e.g. subnitridometalates, can be prepared.^[19] Here we could show that the formation of ionic structures with unusually small, highly charged anions can also be observed. The triple salt itself can be the starting point for the synthesis of the quasi-binary metal-rich nitridotantalates due to its probable thermodynamic instability towards decomposition. *Ortho*-salts often are difficult to obtain by standard synthetic procedures, as is known for e.g. cesium *ortho*-silicate (hitherto unknown), cesium disilicate or cesium *cyclo*-trisilicate (both reaction products of SiO₂ with elemental Cs).^[33] The limits given by Pauling’s second rule for ionic compounds can be stretched to their limits by this unusual synthetic approach.

The formation of a ‘triple salt’ may seem unusual and the question arises whether it is thermodynamically stable with regard to decomposition into the quasi-binary compounds. These would in this case be SrO, Sr₇[TaN₄]₂ and Sr₁₉[Ta₄N₁₃]₂, the latter two being unknown so far. The thermodynamic stability can be estimated by lattice energy calculations in the case that all respective structures are known. Here we can only guess that the NaCl-type topology in Sr₁₄[Ta₄N₁₃][TaN₄]O provides lattice energy high enough to favour the formation of the triple salt over the quasi-binary compounds. As SrO has a very high lattice energy, the ones for the hypothetical Sr *ortho*-nitridotantalate and the also hypothetical Sr *tetracatena*-nitridotantalate may therefore be very low, perhaps even too low for the formation of a stable structure. Whether the quasi-binary structures are stable enough to be yielded via thermolysis of the triple salt has yet to be examined.

6.5 Acknowledgment

The authors would like to thank Prof. Dr. W. Schnick, Department Chemie, LMU München, for his generous and longstanding support. We also thank Christian Minke for recording EDX spectra.

6.6 References

- [1] Villars, P.; Cenzual, K. *Pearson's Crystal Data: Crystal Structure Database for Inorganic Compounds*, Release 2016/17, ASM International, Materials Park, Ohio, USA.
- [2] Huppertz, H.; Schnick, W. BaYbSi₄N₇ – Unexpected Structural Possibilities in Nitridosilicates. *Angew. Chem. Int. Ed.* **1996**, *35*, 1983–1984.
- [3] Huppertz, H.; Schnick, W. Edge-sharing SiN₄ Tetrahedra in the Highly Condensed Nitridosilicate BaSi₇N₁₀. *Chem. – Eur. J.* **1997**, *3*, 249–252.
- [4] Zeuner, M.; Pagano, S.; Schnick, W. Nitridosilicates and Oxonitridosilicates: From Ceramic Materials to Structural and Functional Diversity. *Angew. Chem. Int. Ed.* **2011**, *50*, 7754–7775.
- [5] Maximov, B. A.; Melnikov, O. K.; Zhdanova, T. A.; Ilyukhin, V. V.; Belov, N. V. Crystal structure of Na₄Sc₂Si₄O₁₃. *Dokl. Akad. Nauk SSSR* **1980**, *251*, 98–102.
- [6] Tamazyan, R. A.; Malinovskii, Y. A. Crystal structure of Nd₂Ba₂Si₄O₁₃. *Dokl. Akad. Nauk SSSR* **1985**, *285*, 124–128.
- [7] Liebau, F. *Structural Chemistry of Silicates – Structure, Bonding, and Classification*, Springer Verlag, Berlin, Germany, 1985.
- [8] Heidebrecht, K.; Jansen, M. Ag₁₈(SiO₄)₂(Si₄O₁₃), das erste Silbersilicat mit gemischten Anionen. *Z. Anorg. Allg. Chem.* **1991**, *597*, 79–86.
- [9] Müller-Bunz, H.; Schleid, T. La₂Si₂O₇ im I-Typ: gemäß La₆(Si₄O₁₃)(SiO₄)₂ kein echtes Lanthandisilicat. *Z. Anorg. Allg. Chem.* **2002**, *628*, 564–569.
- [10] Siidral, O. I.; Zenko, D. S.; Krivovichev, S. V. Structural complexity of lead silicates: Crystal structure of Pb₂₁[Si₇O₂₂]₂[Si₄O₁₃] and its comparison to hyttsjoeite. *Am. Mineral.* **2014**, *99*, 817–823.
- [11] Pauling, L. The principles determining the structure of complex ionic crystals. *J. Am. Chem. Soc.* **1929**, *51*, 1010–1026.
- [12] Hoch, C.; Röhr, C. Neue Oxogermanate(IV) der schweren Alkalimetalle: Synthesen

- und Kristallstrukturen. *Z. Naturforsch.* **2001**, *B56*, 1245–1256.
- [13] Wachsmann, C.; Brokamp, T.; Jacobs, H. Darstellung und Struktur eines neuen Nitridoxides mit Lithium und Tantal: $\text{Li}_6\text{Ta}_2\text{N}_8\text{O}$. *J. Alloys Compd.* **1992**, *185*, 109–119.
- [14] Höhn, P.; Kniep, R.; Maier, J. A $\text{Ba}_9\text{N}(\text{N}_3)(\text{Ta}_4\text{N}_4)_2$: Nitridotantalate(V) with Nitride and Azide Ions. *Angew. Chem. Int. Ed. Engl.* **1993**, *32*, 1350–1352.
- [15] Chen, X.-Z.; Ward, D. L.; Eick, H. A. Synthesis and structure of two new quaternary nitrides: $\text{Li}_3\text{Sr}_2\text{MN}_4$ ($\text{M} = \text{Nb}, \text{Ta}$). *J. Solid State Chem.* **1997**, *130*, 1–8.
- [16] Wachsmann, C.; Jacobs, H. Darstellung und Struktur des Lithiumnitridotantalats(V) $\text{Li}_7\text{Ta}_4\text{N}_4$. *J. Alloys Compd.* **1992**, *190*, 113–116.
- [17] Bowman, A.; Gregory, D. H. Synthesis and characterisation of the ternary nitride, $\text{Sr}_2\text{Ta}_2\text{N}_3$. *J. Alloys Compd.* **2003**, *348*, 80–87.
- [18] Helmlinger, F. K. J.; Hoehn, P.; Kniep, R. $\text{Ba}_2(\text{Ta}_2\text{N}_3)$ und $\text{Sr}_2(\text{Ta}_2\text{N}_3)$: Isotype Nitridotantalate(V) mit Tetraederketten $[\text{Ta}_2\text{N}_2\text{N}_2]^{4-}$. *Z. Naturforsch.* **1993**, *B48*, 1015–1018.
- [19] Blaschkowski, B.; Duerr, O.; Reckeweg, O.; Schleid, T. Crystal growth and structure of the barium chloride nitrido-tantalate(V) $\text{Ba}_3\text{Cl}_2\text{Ta}_2\text{N}_3$. *Z. Anorg. Allg. Chem.* **2015**, *641*, 1515–1520.
- [20] Wörsching, M.; Tambornino, F.; Datz, S.; Hoch, C. Chemical Twinning of Salt and Metal in the Subnitridometalates $\text{Ba}_{23}\text{Na}_{11}(\text{MN}_4)_4$ with $\text{M} = \text{V}, \text{Nb}, \text{Ta}$. *Angew. Chem. Int. Ed.* **2016**, *55*, 10868–10871.
- [21] TOPAS-Academic, Version 4.1, Coelho Software, Brisbane, Australia, 2007.
- [22] Hoppe, R. The Coordination Number – an “Inorganic Chameleon”. *Angew. Chem. Int. Ed. Engl.* **1970**, *9*, 25–34.
- [23] Hoppe, R. Madelung Constants. *Angew. Chem. Int. Ed. Engl.* **1966**, *5*, 95–106.
- [24] Apex2 Version 11, Bruker AXS Inc., Madison, Wisconsin, USA, 2014.
- [25] Sheldrick, G. M. A short history of SHELX. *Acta Crystallogr.* **2008**, *A64*, 112–122.

- [26] Gelato, L. M.; Parthé, E. STRUCTURE TIDY – a computer program to standardize crystal structure data. *J. Appl. Cryst.* **1987**, *20*, 139–143.
- [27] Clark, G. M.; Morley, R. Inorganic pyro-compounds $M_a[(X_2O_7)_b]$. *Chem. Soc. Rev.* **1976**, *5*, 269–295.
- [28] Gerlach, W. Die Gitterstruktur der Erdalkalioxyde. *Z. Phys.* **1922**, *9*, 184–192.
- [29] Köllisch, K. Neue Beiträge zur Strukturchemie der Sione und Sialone. PhD Thesis, University of Munich, 2001.
- [30] Hoehn, P.; Kniep, R. Crystal structure of tristrontium (tetranitridomolybdate(VI)), $Sr_3(MoN_4)$. *Z. Kristallogr. – NCS* **2000**, *215*, 325–326.
- [31] O’Meara, P. M.; Barker, M. G.; Blake, A. J.; Cooke, P. A.; Gregory, D. H. Synthesis and crystal structure of a new strontium nitridomolybdate oxide, $Sr_4(MoN_4)O$. *J. Chem. Soc., Dalton Trans.* **2000**, *2000*, 633–638.
- [32] Hoch, C.; Röhr, C. Rubidium stannate(IV), Rb_4SnO_4 . *Acta Crystallogr.* **2000**, *C56*, 136–137.
- [33] Hoch, C.; Röhr, C. Alkalimetall-Oxosilicate $A_6[Si_3O_9]$ und $A_6[Si_2O_7]$ ($A = Rb, Cs$): Darstellung und Kristallstruktur. *Z. Naturforsch.* **2001**, *B56*, 423–430.
- [34] Bender, J.; Wohlfarth, A.; Hoch, C. Crystal structures of new alkali metal-rich oxometallates: rubidium aluminate tetrahydroxide, $Rb_9(AlO_4)(OH)_4$, rubidium orthogallate, Rb_5GaO_4 , cesium bis-chromate(IV) oxide, $Cs_{10}(CrO_4)_2O$ and cesium diindate, $Cs_8In_2O_7$. *Z. Naturforsch.* **2010**, *B65*, 1416–1426.
- [35] Hoch, C. The New Oxometallates $Cs_4[FeO_3]$, $Cs_4[ZnO_3]$ and $Cs_3[BO_3]$ with Trigonal Planar Anions – Decomposition Products of Alkalimetal Suboxometallates. *Z. Naturforsch.* **2011**, *B66*, 1248–1254.

6.7 Supporting Information

Table of contents

- Table S6.1 Anisotropic displacement parameters U_{ij} for $\text{Sr}_{14}[\text{Ta}_4\text{N}_{13}][\text{TaN}_4]\text{O}$
- Table S6.2 Selected interatomic distances for $\text{Sr}_{14}[\text{Ta}_4\text{N}_{13}][\text{TaN}_4]\text{O}$
- Figure S6.1 Rietveld refinement of $\text{Sr}_{14}[\text{Ta}_4\text{N}_{13}][\text{TaN}_4]\text{O}$
- Table S6.3 Crystallographic data and specifications to Rietveld refinement of $\text{Sr}_{14}[\text{Ta}_4\text{N}_{13}][\text{TaN}_4]\text{O}$
- Table S6.4 Selected interatomic angles for $\text{Sr}_{14}[\text{Ta}_4\text{N}_{13}][\text{TaN}_4]\text{O}$
- Table S6.5 Results of EDX analysis on the bulk sample
- Figure S6.2 Electron micrograph of the EDX sample region and one exemplary EDX scan

Table S6.1: Anisotropic displacement parameters U_{ij} for $\text{Sr}_{14}[\text{Ta}_4\text{N}_{13}][\text{TaN}_4]\text{O}$ in \AA^2 . Standard deviations in units of the last digits are given in parentheses.

Atom	U_{11}	U_{22}	U_{33}	U_{23}	U_{13}	U_{12}
Ta1	0.00096(14)	0.00443(12)	0.00340(11)	0.00028(9)	0.00040(10)	-0.00046(10)
Ta2	0.00242(14)	0.00480(12)	0.00366(12)	0.00051(9)	0.00064(10)	0.00045(10)
Ta3	0.00151(14)	0.00492(12)	0.00398(12)	-0.00007(9)	0.00024(10)	-0.00051(10)
Ta4	0.00251(14)	0.00549(13)	0.00500(12)	0.00035(9)	0.00099(10)	0.00083(11)
Ta5	0.00231(14)	0.00450(12)	0.00291(12)	-0.00039(9)	0.00030(10)	-0.00041(10)
Sr1	0.0081(4)	0.0103(3)	0.0086(3)	0.0012(2)	0.0039(3)	-0.0014(3)
Sr2	0.0028(3)	0.0079(3)	0.0069(3)	-0.0012(2)	-0.0013(2)	0.0000(2)
Sr3	0.0071(3)	0.0066(3)	0.0100(3)	-0.0030(2)	0.0055(3)	-0.0018(3)
Sr4	0.0050(3)	0.0069(3)	0.0054(3)	-0.0004(2)	0.0008(2)	0.0012(3)
Sr5	0.0074(4)	0.0115(3)	0.0066(3)	0.0026(2)	-0.0032(3)	-0.0038(3)
Sr6	0.0062(3)	0.0093(3)	0.0071(3)	0.0016(2)	-0.0041(2)	-0.0014(3)
Sr7	0.0058(3)	0.0071(3)	0.0096(3)	0.0016(2)	0.0041(3)	0.0003(3)
Sr8	0.0069(4)	0.0073(3)	0.0101(3)	-0.0004(2)	0.0011(3)	0.0008(3)
Sr9	0.0069(4)	0.0122(3)	0.0113(3)	-0.0030(2)	0.0034(3)	-0.0033(3)
Sr10	0.0047(3)	0.0092(3)	0.0079(3)	-0.0014(2)	-0.0018(2)	0.0008(3)
Sr11	0.0050(3)	0.0070(3)	0.0076(3)	-0.0007(2)	0.0033(2)	0.0009(2)
Sr12	0.0049(3)	0.0144(3)	0.0153(3)	-0.0054(3)	0.0012(3)	-0.0015(3)
Sr13	0.0120(4)	0.0154(3)	0.0091(3)	-0.0015(2)	0.0037(3)	0.0066(3)
Sr14	0.0060(3)	0.0071(3)	0.0055(3)	0.0007(2)	0.0003(2)	-0.0015(3)
N1	0.006(3)	0.006(3)	0.011(3)	-0.002(2)	0.003(2)	0.002(2)
N2	0.005(3)	0.012(3)	0.014(3)	-0.002(2)	0.000(2)	0.004(2)
N3	0.016(4)	0.017(3)	0.011(3)	-0.002(2)	0.010(3)	0.001(3)
N4	0.007(3)	0.009(3)	0.008(3)	-0.005(2)	0.001(2)	0.003(2)
N5	0.004(3)	0.015(3)	0.010(3)	-0.004(2)	0.002(2)	-0.003(2)
N6	0.004(3)	0.007(3)	0.014(3)	-0.001(2)	0.005(2)	-0.001(2)
N7	0.009(3)	0.010(3)	0.013(3)	-0.001(2)	0.001(2)	0.003(2)
N8	0.004(3)	0.039(4)	0.012(3)	0.005(3)	0.000(3)	-0.006(3)
N9	0.009(4)	0.030(3)	0.009(3)	-0.003(2)	0.001(2)	0.004(3)
N10	0.004(3)	0.010(3)	0.006(3)	0.000(2)	0.003(2)	0.001(2)
N11	0.001(3)	0.008(3)	0.009(3)	-0.001(2)	0.000(2)	0.000(2)
N12	0.005(3)	0.007(3)	0.011(3)	-0.002(2)	0.003(2)	-0.002(2)
N13	0.020(4)	0.036(4)	0.018(3)	0.011(3)	0.005(3)	0.013(3)
N14	0.013(4)	0.014(3)	0.017(3)	-0.001(2)	0.000(3)	0.003(3)
N15	0.009(3)	0.012(3)	0.005(3)	0.000(2)	0.006(2)	-0.002(2)
N16	0.012(3)	0.008(3)	0.012(3)	0.003(2)	0.004(2)	0.005(2)
N17	0.005(3)	0.007(3)	0.009(3)	-0.003(2)	0.000(2)	0.003(2)
O1	0.017(3)	0.019(3)	0.022(3)	-0.002(2)	0.002(2)	0.001(2)

Table S6.2: Selected interatomic distances between N/O and respective cations for $\text{Sr}_{14}[\text{Ta}_4\text{N}_{13}][\text{Ta}_4\text{N}_4]\text{O}$ in Å. Standard deviations of the last digits are given in parentheses.

Atoms	distance	Atoms	distance	Atoms	distance	Atoms	distance	Atoms	distance
Ta1-N1	1.938(6)	N9-Sr13	2.602(6)	N17-Sr4	2.708(6)	N11-Sr12	2.838(6)	N8-Sr8	2.534(6)
Ta1-N6	1.940(5)	N9-Sr5	2.612(7)	N1-Sr4	2.622(5)	N13-Sr9	2.570(7)	N8-Sr9	2.592(6)
Ta1-N3	1.944(5)	N9-Sr3	2.657(7)	N1-Sr4	2.635(6)	N13-Sr12	2.579(8)	N8-Sr4	2.636(6)
Ta1-N2	2.016(6)	N9-Sr8	3.221(7)	N1-Sr3	2.669(6)	N13-Sr13	2.877(7)	N8-Sr5	3.220(7)
Ta2-N8	1.897(6)	N9-Sr9	3.243(6)	N1-Sr5	2.716(5)	N13-Sr12	3.271(7)	N8-Sr13	3.360(7)
Ta2-N4	1.905(5)	N9-Sr4	3.361(7)	N1-Sr2	2.811(5)	N13-Sr6	3.394(8)	N8-Sr3	3.560(6)
Ta2-N7	1.988(5)	N12-Sr8	2.535(6)	N3-Sr1	2.751(5)	N14-Sr9	2.514(6)	N10-Sr12	2.628(5)
Ta2-N2	2.018(5)	N12-Sr11	2.641(5)	N3-Sr6	2.773(7)	N14-Sr10	2.642(7)	N10-Sr6	2.668(6)
Ta3-N17	1.961(5)	N12-Sr11	2.728(6)	N3-Sr2	2.837(6)	N14-Sr11	2.701(7)	N10-Sr5	2.674(5)
Ta3-N9	1.9651(6)	N12-Sr7	2.751(5)	N3-Sr1	2.936(6)	N14-Sr13	2.856(6)	N10-Sr9	2.686(6)
Ta3-N15	1.968(6)	N12-Sr10	3.221(6)	N3-Sr7	3.118(7)	N4-Sr2	2.533(5)	N10-Sr13	2.785(6)
Ta3-N12	2.006(6)	N15-Sr8	2.616(6)	N6-Sr7	2.560(6)	N4-Sr5	2.583(5)	O1-Sr10	2.456(6)
Ta4-N13	1.906(7)	N15-Sr14	2.668(5)	N6-Sr3	2.611(6)	N4-Sr6	2.591(5)	O1-Sr11	2.471(6)
Ta4-N14	1.922(6)	N15-Sr11	2.675(6)	N6-Sr4	2.690(6)	N4-Sr1	2.679(6)	O1-Sr8	2.545(5)
Ta4-N11	1.958(5)	N15-Sr10	2.764(5)	N6-Sr14	2.714(6)	N4-Sr1	2.976(5)	O1-Sr13	2.559(6)
Ta4-N16	2.073(6)	N15-Sr10	2.775(6)	N6-Sr8	2.798(5)	N5-Sr2	2.630(6)	O1-Sr12	2.731(5)
Ta5-N10	1.898(6)	N17-Sr7	2.549(6)	N11-Sr7	2.570(6)	N5-Sr1	2.698(6)	O1-Sr9	2.741(6)
Ta5-N5	1.903(6)	N17-Sr14	2.586(6)	N11-Sr14	2.611(6)	N5-Sr14	2.744(5)		
Ta5-N7	1.994(5)	N17-Sr2	2.633(5)	N11-Sr6	2.644(5)	N5-Sr6	2.857(6)		
Ta5-N16	2.025(5)	N17-Sr3	2.656(6)	N11-Sr10	2.661(5)	N5-Sr1	3.326(6)		

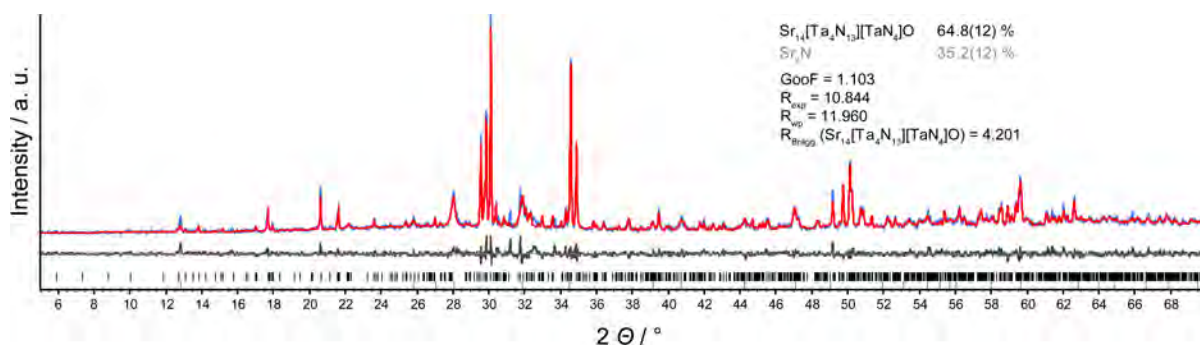


Figure S6.1: Observed (blue) and calculated (red) powder diffraction patterns of $\text{Sr}_{14}[\text{Ta}_4\text{N}_{13}][\text{TaN}_4]\text{O}$ and Sr_2N as well as Bragg reflections (black for $\text{Sr}_{14}[\text{Ta}_4\text{N}_{13}][\text{TaN}_4]\text{O}$ and light grey for Sr_2N) and differential plot (dark grey). Respective weight percentages of the different phases are given in the right upper corner together with selected figures of merit.

Table S6.3: Crystallographic data and specifications to Rietveld refinement of the two-phase sample of $\text{Sr}_{14}[\text{Ta}_4\text{N}_{13}][\text{TaN}_4]\text{O}$ and Sr_2N .

phase	$\text{Sr}_{14}[\text{Ta}_4\text{N}_{13}][\text{TaN}_4]\text{O}$	Sr_2N
formula mass	1436.08	1287.17
crystal system / space group	$P2_1/c$	$R\bar{3}m$
lattice parameters / Å / °	$a = 15.0570(3)$	$a = 3.8570(4)$
	$b = 7.25845(15)$	$c = 20.686(5)$
	$c = 24.2125(5)$	
	$\beta = 97.4204(17)$	
cell volume / Å ³	2624.03(10)	266.51(8)
Z	4	3
X-ray density / gcm ⁻³	6.73(7)	3.5374(11)
linear absorption coefficient / cm ⁻¹	842(9)	374.56(12)
radiation	– Cu-K _{α1} ($\lambda = 154.0596$ pm) –	
monochromator	– Ge(111) –	
diffractometer	– Stoe StadiP –	
detector	– MYTHEN 1K –	
2θ -range / °	– 5–70 –	
temperature / K	– 298 –	
data points	– 4334 –	
number of parameters	– 152 –	
constraints	– 0 –	
software	– TOPAS Academic 4.1 –	
structure refinement	– Rietveld method –	
profile function	– fundamental parameters model –	
background function	– shifted Chebychev –	
R_p	– 9.206 –	
R_{wp}	– 11.947 –	
R_{exp}	– 10.844 –	
R_{Bragg}	4.201	3.199
χ^2	– 1.103 –	

Table S6.4: Selected interatomic angles for $\text{Sr}_{14}[\text{Ta}_4\text{N}_{13}][\text{TaN}_4]\text{O}$ as a result of a single crystal structure refinement. Standard deviations of the last digits are given in parentheses.

Atoms	Angle /°	Atome	Angle /°
Sr10–O–Sr11	96.55(18)	N6–Ta1–N3	110.1(2)
Sr10–O–Sr8	93.62(19)	N6–Ta1–N2	109.9(2)
Sr10–O–Sr13	93.63(18)	N3–Ta1–N2	120.3(2)
Sr10–O–Sr12	92.23(16)	N8–Ta2–N4	109.1(2)
Sr10–O–Sr9	178.0(2)	N8–Ta2–N7	114.4(2)
Sr11–O–Sr8	92.36(19)	N8–Ta2–N2	110.0(2)
Sr11–O–Sr13	169.7(2)	N4–Ta2–N7	102.1(2)
Sr11–O–Sr12	96.40(16)	N4–Ta2–N2	104.0(2)
Sr11–O–Sr9	82.92(16)	N7–Ta2–N2	116.2(2)
Sr8–O–Sr13	85.73(15)	N13–Ta4–N14	113.9(3)
Sr8–O–Sr12	168.8(2)	N13–Ta4–N11	109.3(3)
Sr8–O–Sr9	84.50(15)	N13–Ta4–N16	114.3(3)
Sr13–O–Sr12	84.43(17)	N14–Ta4–N11	101.9(2)
Sr13–O–Sr9	86.86(15)	N14–Ta4–N16	111.1(2)
Sr12–O–Sr9	89.74(17)	N11–Ta4–N16	105.1(2)
N17–Ta3–N9	99.7(2)	N10–Ta5–N5	105.5(2)
N17–Ta3–N15	105.2(2)	N10–Ta5–N7	100.9(2)
N17–Ta3–N12	104.8(2)	N10–Ta5–N1	106.1(2)
N9–Ta3–N15	112.6(2)	N5–Ta5–N7	108.8(2)
N9–Ta3–N12	127.2(2)	N5–Ta5–N16	109.8(2)
N15–Ta3–N12	105.0(2)	N7–Ta5–N16	124.0(2)
N1–Ta1–N6	104.8(2)		
N1–Ta1–N3	106.8(2)		
N1–Ta1–N2	103.5(2)		

Table S6.5: Results of various EDX analyses on different crystallites of a bulk sample of the reaction product. Simultaneous presence of O and N becomes clear (although not reliably quantifiable), no Na can be found and the Sr/Ta ratio is close to the theoretical value (calculated for $\text{Sr}_{14}[\text{Ta}_4\text{N}_{13}][\text{TaN}_4]\text{O}$: $\text{Sr}/\text{Ta} = 14/5 = 2.8$). Sr_2N is observed as the only byproduct (crystallite at position 4). One spectrum is shown exemplary, together with an electron micrograph of the sample.

Position	Element	Atom-%	molar ratio Sr/Ta
1	Sr	25.40	
	Ta	8.82	2.88
2	Sr	43.28	
	Ta	14.43	3.00
3	Sr	29.97	
	Ta	10.13	2.96
∅ 1-3			2.95
4	Sr	31.89	
	Ta	15.65	2.03

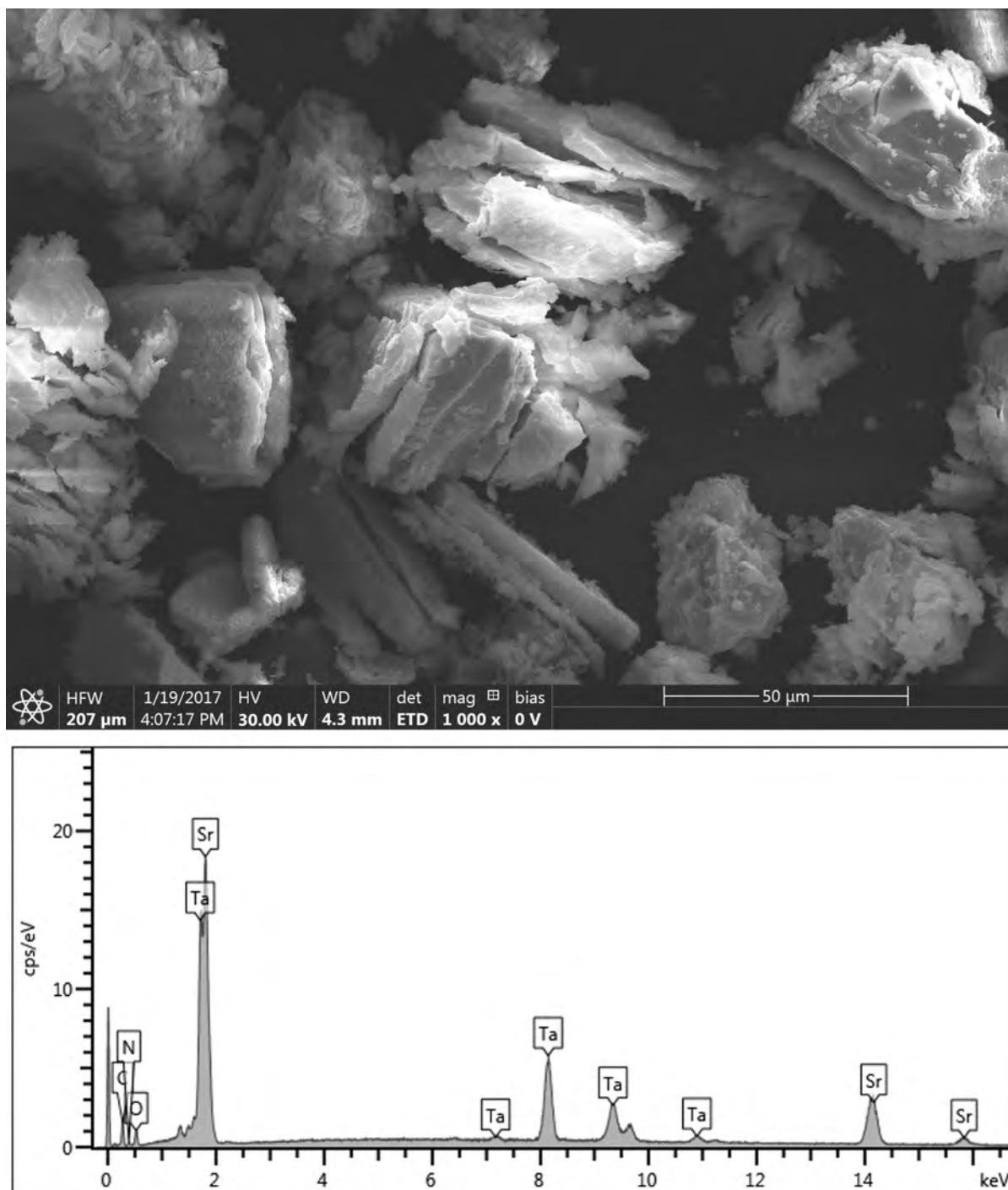


Figure S6.2: Electron micrograph of the sample region for EDX measurements and one exemplary EDX scan (position 2 in Table S6.5).

7 Additional Results

7.1 The Barium Nitridoborate 'Ba₂₃(BN₂)₁₁(BN₃)₃(N)₃'

Experimental

506.9 mg Ba₂N (synthesised according to DiSalvo *et al.*^[1]) were reacted in a *h*-BN crucible at a reaction temperature of 1000 °C for 5 h. The crucible was sealed in a silica ampoule and reaction took place under Ar atmosphere. Prior to use, the crucible was cleaned with boiling ethanol (dried over molecular sieve, pore size: 4 Å) for 1 day to remove boric acid and subsequently dried in vacuo at 300 °C. The product was sensitive to air and moisture, black, very hard and brittle, and was strongly jointed with the crucible.

Crystal Structure

The analysis of the crystal structure of 'Ba₂₃(BN₂)₁₁(BN₃)₃(N)₃' has to be considered as work in progress. The following description of the crystal structure is one possibility, representing the best model so far in terms of existing X-ray diffraction data. However, alternative interpretation possibilities will be discussed.

A black crystal was isolated under dry paraffin oil and centred on a D8-Quest diffraction system with Mo-K_α radiation ($\lambda = 0.71073$ Å). For additional details on data collection and treatments see Table 7.1. Absorption correction was performed with the multiscan method (SADABS).^[2] Indexing, systematic absence conditions and Wilson statistics indicated a trigonal crystal system including centrosymmetry leading to space group $P\bar{3}1c$. First investigations of the data suggested a higher, hexagonal Laue class due to a rotational drilling. The crystal was refined as a twin with the twin matrix (1 1 0, 0 -1 0, 0 0 1). One individuum of the drilling was neglected as it did not contribute significantly to the data (volume fraction: 0.08(5) %). All Ba, B and N atoms – except N4, N51 and N52 due to their site occupation factors smaller than 1 – were refined with anisotropic displacement parameters. From structure refinement the sum formula 'Ba₂₃(BN₂)₁₁(BN₃)₃(N)₃' is obtained. B origins from reaction with the crucible material. Standardised atomic coordinates, anisotropic displacement parameters, selected interatomic distances and angles are listed in Tables 7.2, S7.2, S7.3 and S7.4 of the Supporting Information.

Table 7.1: Crystallographic data and selected details of data collection, structure solution and refinement of 'Ba₂₃(BN₂)₁₁(BN₃)₃(N)₃'. Standard deviations in units of the last digit are given in parentheses.

Crystal system	trigonal
Space group	$P\bar{3}1c$ (no. 163)
Lattice parameters / Å / °	a 11.4087(16) c 23.045(5)
Volume / Å ³	2597.6(8)
Z	2
Calculated density / g · cm ⁻³	4.883
Diffractometer	D8-Quest, MoK α radiation
	Goebel mirror
Data collection temperature /K	295(2)
Absorption coefficient /mm ⁻¹	17.16
Data range θ /°	2.24–30.00
Index range	$-16 \leq h \leq 16$, $-16 \leq k \leq 16$, $-32 \leq l \leq 32$
No. of observed reflections	92629
No. of independent reflections	2540
No. of independent reflections with ($I \geq 2\sigma(I)$)	2513
$F(000)$	3228
Corrections	Lorentz, polarisation ^[2]
Absorption correction	Multi-scan ^[2]
Structure solution	direct methods ^[3]
Structure refinement	full-matrix least squares on F^2 ^[3]
No. of l. s. parameters	113
Goof on F^2	1.089
$R_{\text{int}} / R_{\sigma}$	0.0457 / 0.0129
R values (for reflections with $I \geq 2\sigma(I)$)	$R_1 = 0.0302$, $wR_2 = 0.0744$
R values (all data)	$R_1 = 0.0304$, $wR_2 = 0.0745$
Residual electron density / e ⁻ · Å ⁻³	2.313 / -1.668

Table 7.2: Fractional atomic coordinates, isotropic thermal displacement parameters and site occupation factors for 'Ba₂₃(BN₂)₁₁(BN₃)₃(N)₃'. Standard deviations in units of the last digit are given in parentheses.

Atom	Wyckoff Number	x	y	z	$U_{\text{eq}} / \text{Å}^2$	Site occupation factor
Ba1	6h	0.21477(3)	0.78523(3)	1/4	0.02993(13)	1
Ba2	2d	2/3	1/3	1/4	0.02321(17)	1
Ba3	12i	0.42778(5)	0.21144(6)	0.01108(2)	0.03620(13)	1
Ba4	12i	0.27809(5)	0.14732(5)	0.17150(2)	0.03029(11)	1
Ba5	12i	0.03739(5)	0.50591(5)	0.11603(2)	0.03064(11)	1
Ba6	2b	0	0	0	0.0376(2)	1
B1	4f	1/3	2/3	0.1180(5)	0.026(2)	1
N11	4f	1/3	2/3	0.0599(4)	0.0262(18)	1
N12	4f	1/3	2/3	0.1754(4)	0.039(3)	1
B2	6h	0.5218(4)	0.4782(4)	1/4	0.0222(17)	1
N21	12i	0.4125(8)	0.0488(8)	0.2363(4)	0.047(2)	1
B3	12i	0.1197(12)	0.2757(10)	0.0961(4)	0.040(2)	1
N31	12i	0.2386(19)	0.3306(16)	0.1185(12)	0.217(17)	1
N32	12i	0.0081(9)	0.2292(12)	0.0693(4)	0.055(3)	1
N4	6g	1/2	0	0	0.067(4)	1
B4	2a	0	0	1/4	0.045(5)	1
N41	12i	0.0365(17)	0.1331(19)	0.2500(14)	0.029(5)	0.300(18)
B5	4f	1/3	2/3	0.6148(5)	0.040(3)	1
N511	12i	0.529(4)	0.241(4)	0.1229(15)	0.133(9)	0.53(2)
N512	12i	0.547(4)	0.339(5)	0.1077(16)	0.133(9)	0.47(2)

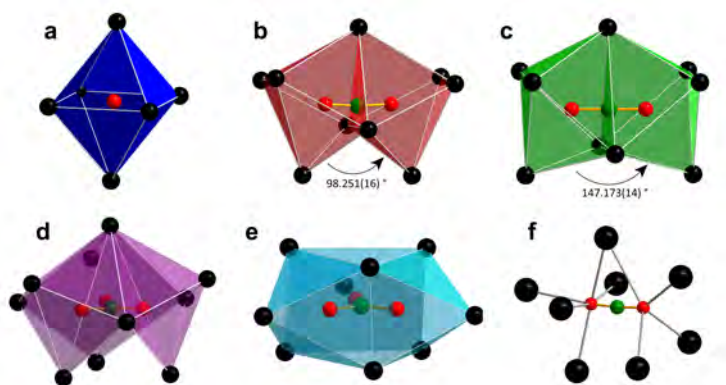


Figure 7.1: Coordination polyhedra around N atoms and BN_x with Ba atoms on vertices in ' $\text{Ba}_{23}(\text{BN}_2)_{11}(\text{BN}_3)_3(\text{N})_3$ '. Ba atoms: black spheres, B atoms: green spheres, N atoms: red spheres. For N41 (d) only one of two possible conformations is shown. In (e) only N511 is shown. N512 accords to a 44° rotation of the $[\text{BN}_3]^{6-}$ around the threefold axis. In (f) no reasonable polyhedra were found.

' $\text{Ba}_{23}(\text{BN}_2)_{11}(\text{BN}_3)_3(\text{N})_3$ ' crystallises in the trigonal crystal system with space group $P\bar{3}1c$, $a = 11.4087(16)$ Å, $c = 23.045(5)$ Å and $Z = 2$. The crystal structure of ' $\text{Ba}_{23}(\text{BN}_2)_{11}(\text{BN}_3)_3(\text{N})_3$ ' consists of 23 crystallographically independent Ba^{2+} cations coordinating three different anionic species: N^{3-} , $[\text{BN}_2]^{3-}$ (three different crystallographically independent units) and $[\text{BN}_3]^{6-}$ (two different crystallographically independent units). The isolated nitride anion, atom N4 in Table 7.2, is coordinated by a slightly distorted octahedron of Ba atoms (see Figure 7.1 a). Interatomic distances range from 2.7032(7) to 2.9783(6) Å and are in accordance with literature data (2.7675(7) Å in Ba_2N).^[1] Ba–N4–Ba angles range from 87.680(17) to 92.899(15) $^\circ$ and corroborate the slight distortion of the $[\text{Ba}_6\text{N}]$ octahedron.

Figures 7.1 b and c show the coordination of N atoms constituting two of the three $[\text{BN}_2]^{3-}$ units around B1 and B2 (see Table 7.2) by Ba atoms. B–N bonding distances range from 1.317(7) to 1.337(15) Å, which corresponds to literature data (1.326(10) to 1.348(10) Å for $\text{Ba}_3(\text{BN}_2)_2$).^[4] The N21–B2–N21 angle is 175.6(5) $^\circ$, whereas the N11–B1–N12 angle amounts to exactly 180 $^\circ$ due to site symmetry. $[\text{Ba}_6\text{N}]$ octahedra are formed, and in both cases they connect via sharing faces with B occupying approximately the centres of connecting faces. Ba–N distances range from 2.873(5) to 3.785(10) Å. Such differentiations in Ba–N distances are commonly reported in literature.^[4] The distortion of the $[\text{Ba}_6\text{N}]$ octahedron is stronger in the case shown in Figure 7.1 c. The shared face of the two octahedra is elongated and thus the angle between the two non-connected octahedra faces is enlarged (98.251(16) $^\circ$ vs. 147.173(14) $^\circ$). For a detailed list of bonding angles see Table S7.4 in the Supporting Information.

A third crystallographically independent $[\text{BN}_2]^{3-}$ unit around B3 (see Table 7.2) exist showing unusually short B–N contacts of 1.271(15) and 1.28(2) Å and a N31–B3–N32 bonding angle of 174.6(15) $^\circ$. Coordination of N atoms by Ba atoms is highly irregular (see Figure 7.1 f) and the respective polyhedra are omitted in Figure 7.2 for clarity. Anisotropic displacement parameters of N31 and N32 are very large (see Table S7.2 of the Supporting Information) and can – as well as the short bonding contacts – not be explained from structural reasons.

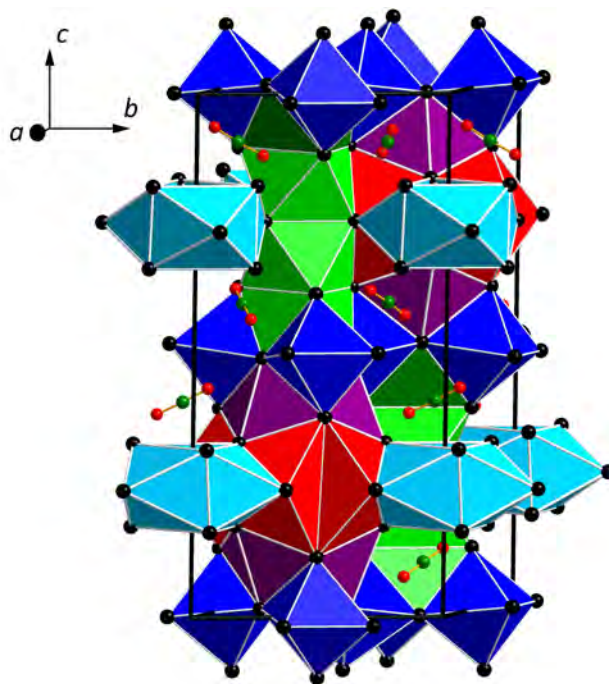


Figure 7.2: Unit cell of 'Ba₂₃(BN₂)₁₁(BN₃)₃(N)₃'. Ba atoms: black spheres, B atoms: green spheres, N atoms: red spheres.

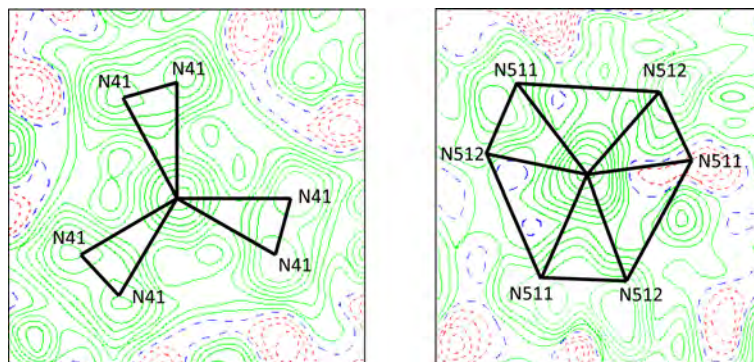


Figure 7.3: Observed electron density around the two crystallographically independent [BN₃]⁶⁻ anions.

The third anionic species are slightly distorted trigonal planar [BN₃]⁶⁻ units around B4 and B5 (see Table 7.2), which are only scarcely documented in literature.^[5-7] The B–N distances range from 1.320(17) to 1.333(9) Å. These values are significantly shorter than those documented in literature (1.44(4) to 1.50(2) Å)^[5] and will be discussed further below. N–B–N angles add up to 119(2)° (for N41–B4–N41) and 120.0(11)° (for N511–B5–N511 and N512–B5–N512, respectively). The N41 atoms are rotationally disordered with mutually exclusive site occupation factors and can be transformed into each other by a rotation of 29.1(13)° around the threefold axis of the [BN₃]⁶⁻ unit. The site occupation factor of N41 was refined to 0.300(18) for one of the two possible conformations, thus in total N41 has a site occupation factor of 0.600. Furthermore, the [BN₃]⁶⁻ unit around B5 can adopt two possible orientations, by rotation of the [BN₃]⁶⁻ unit by 44(2)° around the

threefold axis, which transforms N511 into N512. Thus N511 and N512 have mutually exclusive site occupation factors adding up to 0.47(2) for N512 and 0.53(2) for N511 (see Figure 7.3 and Table 7.2).

The coordination of N atoms by Ba is given by distorted square pyramids and addition of respective B atoms as coordinating atoms leads to distorted octahedra. However, connection between the three square pyramids of the $[\text{BN}_3]^{6-}$ units differs for the two crystallographically independent anions. For N41 the resulting pyramids connect via sharing faces as shown in Figure 7.1 d. The square pyramids coordinating N511/N512 connect via sharing edges resulting in a triaugmented triangular prism (Johnson solid J_{51}).^[8] Ba–N distances range from 2.60(5) to 3.53(3) Å compared to 2.905(2) to 3.549(7) Å in $\text{Ba}_4\text{Pr}_7[\text{Si}_{12}\text{N}_{23}\text{O}][\text{BN}_3]$.^[5] Detailed information about interatomic distances and angles are found in Tables S7.3 and S7.4 of the Supporting Information.

Figure 7.2 exhibits the unit cell of ' $\text{Ba}_{23}(\text{BN}_2)_{11}(\text{BN}_3)_3(\text{N})_3$ ' with all of the described ionic entities and shows the space-filling character of the structure.

Elemental analysis (ICP and CHNS)

ICP analysis was performed to determine the B/Ba ratio in the product. Measurements delivered a molar B/Ba ratio of 1/1.8 deviating only slightly from the theoretical value 1/1.6 in ' $\text{Ba}_{23}(\text{BN}_2)_{11}(\text{BN}_3)_3(\text{N})_3$ '. Determination of O, N and C are not possible with ICP analysis.

To determine the content of N and possible impurities of C and H, CHNS analysis was performed. C was not detected. Traces of H (0.34 wt%) were detected in one measurement cycle, which corresponds to about 12.9 H atoms per formula unit. However, in all further CHNS analyses no H could be detected. N content varied between 9 and 16 wt%, correlating to the theoretical values of 12.6 wt% in ' $\text{Ba}_{23}(\text{BN}_2)_{11}(\text{BN}_3)_3(\text{N})_3$ '.

Raman Spectroscopy

To get direct evidence for the presence of B–N bondings, Raman spectroscopy was performed. Figure 7.4 shows the Raman spectra of a single crystal of ' $\text{Ba}_{23}(\text{BN}_2)_{11}(\text{BN}_3)_3(\text{N})_3$ ' (red line) and the bulk sample (black line), from which the single crystal was isolated. The single crystal was sealed in a capillary filled with dry paraffin oil. The bulk sample was sealed under Argon atmosphere in a capillary. The four broad signals marked with blue arrows can be attributed to vibration modes from paraffin oil (known from reference measurements). The most prominent signal is at 1034 cm^{-1} (marked with a grey arrow) and is attributed to the symmetric stretching vibration of the $[\text{BN}_2]^{3-}$ unit.^[4] The maximum of the corresponding signal in the bulk sample is located at a similar wave number ($\sim 1029\text{ cm}^{-1}$). Signals at very low wave numbers between 560 and 710 cm^{-1} (see Figure 7.4, green circles) could not be assigned in both measurements. However, signals in this regions also occurred in literature and are suspected to be an unknown B–N species.^[4] It is possible that those signals originate from the $[\text{BN}_3]^{6-}$ units described in the crystal structure. The signal at 1362 cm^{-1} in the bulk measurement (marked with a black arrow) can be attributed to residual *h*-BN from crucible material.^[9]

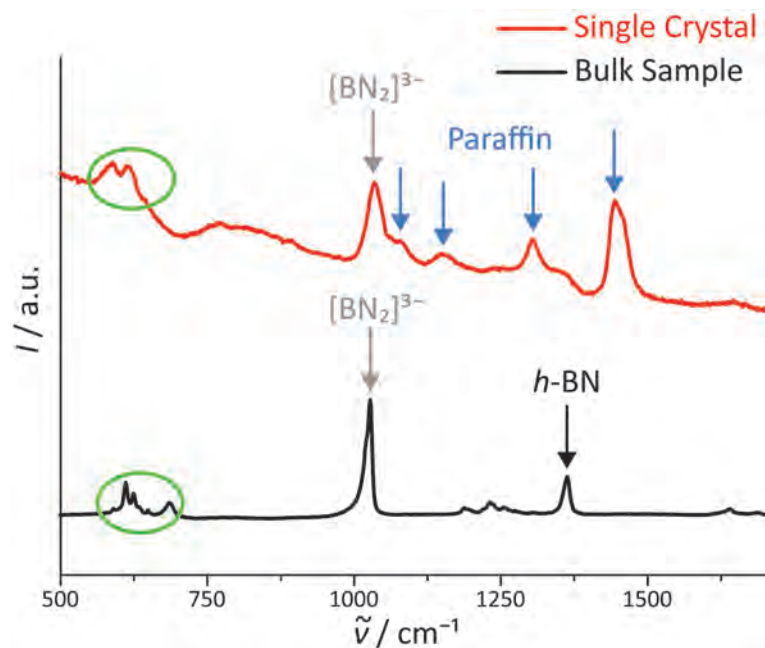


Figure 7.4: Raman spectra of bulk (black line) and single crystal sample (red line) of $\text{Ba}_{23}(\text{BN}_2)_{11}(\text{BN}_3)_3(\text{N})_3$. Signals known from literature are marked with arrows.

Discussion and Conclusion

The refined sum formula deduced from the crystal structure analysis can not be correct. Calculation of charges in $\text{Ba}_{23}(\text{BN}_2)_{11}(\text{BN}_3)_3(\text{N})_3$ shows a surplus of $14 e^-$ (see Table 7.3).

Table 7.3: Charge count in $\text{Ba}_{23}(\text{BN}_2)_{11}(\text{BN}_3)_3(\text{N})_3$.

Atom/Molecular entity	Charge	Number per asymmetric unit	Σ
Ba	2+	23	46+
BN_2	3-	11	33-
BN_3	6-	3	18-
N	3-	3	9-
			14-

For the two $[\text{BN}_2]^{3-}$ units with reasonable Ba coordination polyhedra, structure analysis is very well in agreement with literature data.^[4] Thus, error analysis must mainly focus on the two $[\text{BN}_3]^{6-}$ units as they show significantly shorter B–N distances than documented in literature. Figure 7.5 summarises most likely approaches for the sum formula to achieve charge balance.

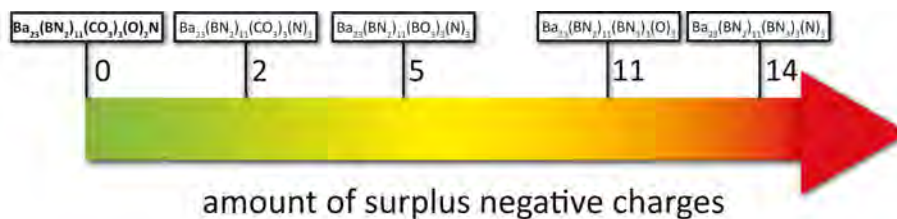


Figure 7.5: Graphical representation of possible variation of the sum formula to achieve charge balance.

Contamination with oxide anions is always a possible source of error leading to a transformation of three $[\text{BN}_3]^{6-}$ anions per unit cell to three $[\text{BO}_3]^{3-}$ anions. By this replacement nine e^- could be removed from the structure. According to literature, B–O distances for $[\text{BO}_3]^{3-}$ anions range from 1.344(12) to 1.451(13) Å in $\text{NaBa}_4(\text{BO}_3)_3$,^[10] which are slightly larger values than reported in this work. However, for *ortho*-borate anions Raman spectroscopic data is known and signals would be expected at $\sim 900 \text{ cm}^{-1}$,^[11] which has not been observed in this work (see Figure 7.4). Furthermore, this would only lead to a partial charge compensation and a surplus of five negative charges would remain. The presence of $[\text{BO}_3]^{3-}$ anions must be excluded because of spectroscopic evidence.

A second possibility would be the contamination with $[\text{CO}_3]^{2-}$ anions originating from residual ethanol. C–O distances in the carbonate anion range from 1.283(13) to 1.289(8) Å in BaCO_3 ,^[12] hence slightly shorter compared to the experimental data in this work. Also even by substituting all $[\text{BN}_3]^{6-}$ anions with $[\text{CO}_3]^{2-}$ anions two negative charges still remain to achieve charge balance. A partial occupation of N^{3-} with O^{2-} in combination with complete substitution of $[\text{BN}_3]^{6-}$ with $[\text{CO}_3]^{2-}$ anions would be a solution to balance charges (see Figure 7.5). However, elemental analysis undermines this theory as no C was detected in the CHNS analysis. Furthermore, Raman spectroscopy disagrees with this theory. For $[\text{CO}_3]^{2-}$ anions strong signals would be expected at 688 cm^{-1} , 1058 cm^{-1} and 1418 cm^{-1} .^[13] Further theories to accomplish charge balance also seem unlikely considering the high synthesis temperatures (e.g. $[\text{OBN}_2]^{5-}$, NCO^-).^[14, 15]

An additional problem arises considering the $[\text{BN}_2]^{3-}$ unit with significantly shorter bonding distances and no reasonable coordination polyhedra (see Figure 7.1 f). In 2014 the acetonitrilide anion $[\text{CCN}]^{3-}$ was postulated in the compound $\text{Ba}_5(\text{TaN}_4)\text{CCN}$.^[16] Documented bonding distances in $\text{Ba}_5(\text{TaN}_4)\text{CCN}$ correlate to data reported in this work. However, elemental analysis again disproves this theory. Furthermore, a substitution of $[\text{BN}_2]^{3-}$ with $[\text{CCN}]^{3-}$ would not contribute to charge balance.

Existing data is not sufficient to give a final statement about ' $\text{Ba}_{23}(\text{BN}_2)_{11}(\text{BN}_3)_3(\text{N})_3$ ' despite excellent single-crystal diffraction data, as can be deduced from very reasonable R values and criteria of quality. Further analysis, crystallographic (e.g. Synchrotron diffraction experiments) as well as spectroscopic (^{11}B and ^{15}N NMR experiments), must be carried out in combination with sophisticated elemental analysis (Paschen analysis to determine the exact O content).

Supporting Information

Table S7.2: Anisotropic displacement parameters for 'Ba₂₃(BN₂)₁₁(BN₃)₃(N)₃'. Standard deviations in units of the last digit are given in parentheses. U_{ij} is defined as $U_{ij} = \exp\{-2\pi^2[U_{11}(ha^*)^2 + \dots + 2U_{21}hka^*b^*]\}$, and U_{eq} is 1/3 of the trace of the anisotropic tensor.

Atom	$U_{11} / \text{\AA}^2$	$U_{22} / \text{\AA}^2$	$U_{33} / \text{\AA}^2$	$U_{23} / \text{\AA}^2$	$U_{13} / \text{\AA}^2$	$U_{12} / \text{\AA}^2$
Ba1	0.02421(19)	0.02421(19)	0.0393(3)	0.0106(2)	0.0034(2)	0.0034(2)
Ba2	0.0215(2)	0.0215(2)	0.0267(4)	0.01073(12)	0	0
Ba3	0.0310(2)	0.0402(3)	0.0297(2)	0.0121(2)	0.00378(15)	0.0119(2)
Ba4	0.0443(2)	0.0377(2)	0.01843(16)	0.0276(2)	-0.00101(14)	-0.00222(16)
Ba5	0.0331(2)	0.0324(2)	0.02284(18)	0.01366(19)	0.00087(14)	0.00190(17)
Ba6	0.0437(4)	0.0437(4)	0.0254(4)	0.02187(19)	0	0
B1	0.026(3)	0.026(3)	0.026(5)	0.0128(17)	0	0
N11	0.028(3)	0.028(3)	0.022(4)	0.0141(14)	0	0
N12	0.050(4)	0.050(4)	0.018(4)	0.025(2)	0	0
B2	0.031(4)	0.031(4)	0.016(3)	0.025(4)	0.001(4)	0.001(4)
N21	0.031(4)	0.031(4)	0.075(7)	0.013(3)	-0.007(3)	-0.003(3)
B3	0.052(6)	0.028(4)	0.040(4)	0.020(4)	-0.014(4)	0.006(3)
N31	0.143(16)	0.065(9)	0.33(3)	-0.031(9)	-0.17(2)	0.087(15)
N32	0.032(4)	0.087(7)	0.039(4)	0.026(5)	0.007(3)	0.027(5)
N4	0.106(14)	0.063(8)	0.036(5)	0.047(11)	0.010(8)	0.012(6)
B4	0.058(9)	0.058(9)	0.018(8)	0.029(4)	0	0
B5	0.055(6)	0.055(6)	0.010(4)	0.028(3)	0	0

Table S7.3: Selected interatomic distances / \AA for 'Ba₂₃(BN₂)₁₁(BN₃)₃(N)₃'. Standard deviations in units of the last digit are given in parentheses.

Atom 1	Atom 2	Distance	Atom 1	Atom 2	Distance
B1-	N12	1.323(15)		N4	2.9240(8)
	N11	1.337(15)		N32	2.972(11)
B2-	N21	1.317(7)		N4	2.9783(8)
B3-	N32	1.271(15)		N31	3.25(3)
	N31	1.28(2)		N512	3.49(4)
B4-	N41	1.36(2)	Ba4-	N31	2.65(2)
B5-	N512	1.36(4)		N41	2.67(3)
	N512	1.36(3)		N511	2.75(3)
	N512	1.36(5)		N21	2.751(10)
	N511	1.39(4)		N41	2.76(2)
	N511	1.40(3)		N32	2.821(10)
	N511	1.40(3)		N21	3.029(8)
Ba1-	N21	2.728(6)		N512	3.116(3)
	N12	2.905(6)		N41	3.226(3)
	N41	2.95(3)		N41	3.31(2)
	N31	3.28(3)	Ba5-	N512	2.60(4)
Ba2-	N21	3.104(9)		N31	2.666(19)
	N21	3.105(6)		N4	2.7032(7)
	N21	3.105(10)		N511	2.91(3)
	N511	3.25(3)		N21	3.112(9)
	N511	3.25(3)		N32	3.193(13)
Ba3-	N512	2.65(3)		N11	3.120(4)
	N511	2.76(3)		N12	3.231(4)
	N32	2.781(8)	Ba6-	N32	3.024(8)
	N11	2.873(5)			

Table S7.4: Selected bond angles / ° for 'Ba₂₃(BN₂)₁₁(BN₃)₃(N)₃'. Standard deviations in units of the last digit are given in parentheses.

Atoms	Angles	Atoms	Angles
N11–B1–N12	180	N41–B4–N41	120.0(11)
N21–B2–N21	175.6(5)	N41–B4–N41	120.0(13)
N31–B3–N32	174.6(15)	N41–B4–N41	120.0(12)
N41–B4–N41	120.0(13)	N512–B5–N512	119(2)
N41–B4–N41	120.0(12)	N512–B5–N512	119(2)
N41–B4–N41	91.0(12)	N511–B5–N512	162(2)
N41–B4–N41	149.0(13)	N512–B5–N512	119(2)
N41–B4–N41	120.0(11)	N511–B5–N512	162(2)
N41–B4–N41	91.0(12)	N511–B5–N512	162(2)
N41–B4–N41	149.0(12)	N511–B5–N511	118.5(18)
N41–B4–N41	149.1(12)	N511–B5–N511	119(2)
N41–B4–N41	90.9(12)	N511–B5–N511	118.4(19)

7.2 The Barium Nitridomolybdate/-tantalate 'Ba₆[Mo_xTa_{1-x}N₄]N_x'

Experimental

32.1 mg Na (distilled, AK Simon, MPI Stuttgart), 63.0 mg Ba (distilled, 99.5 %, SMT Metalle Wimmer, Weinburg, Austria), 17.6 mg Mo (purified by Dr. O. Janka, University of Oldenburg, Germany) and 211.9 mg Ba₂N (synthesised according to DiSalvo *et al.*^[1]) were mixed in a Ta crucible and heated to 600 °C for 5 h under Ar atmosphere. Ta crucibles were cleaned with a mixture of concentrated H₂SO₄, concentrated HNO₃ and HF (40 %) in the ratio 3/1/1 and subsequently dried at 100 °C. The product was dark and showed metallic luster.

Crystal Structure

A metallic, slightly reddish, but metallic, crystal was isolated under dry paraffin oil and centred on an IPDS-1 diffraction system with Mo-K_α radiation ($\lambda = 0.71073 \text{ \AA}$). For additional details on data collection and treatments see Table 7.8. Absorption correction was performed numerically (ABSTompa).^[17] Indexing, systematic absence conditions and Wilson statistics indicated an orthorhombic crystal system including centrosymmetry leading to space group *Cmcm* (see Table 7.7). All Ba, Ta and Mo atoms as well as N2 and N3 were refined with anisotropic displacement parameters. N1 was treated isotropically due to its occupation factor less than 1. From structure refinement the sum formula 'Ba₆[Mo_{0.78}Ta_{0.22}N₄]N_{0.76}' is obtained. Introduced Ta origins from reaction with the crucible material. Standardised atomic coordinates, anisotropic displacement parameters, selected interatomic distances and angles are listed in Tables 7.9, S7.6, S7.7 and S7.8 in the Supporting Information. 'Ba₆[Mo_{0.78}Ta_{0.22}N₄]N_{0.76}' crystallises in the orthorhombic crystal system with space group *Cmcm*, $a = 11.672(3) \text{ \AA}$, $b = 10.177(2) \text{ \AA}$, $c = 10.8729(19) \text{ \AA}$ and $Z = 4$. 'Ba₆[Mo_{0.78}Ta_{0.22}N₄]N_{0.76}' exhibits isolated [Mo/TaN₄] tetrahedra, formed by two crystallographically independent N atoms, N2 and N3. Anisotropic displacement parameters of N have common shape and do not show any abnormalities (see Figure 7.6 a).

Table 7.7: Reflection conditions and Wilson statistics for 'Ba₆[Mo_xTa_{1-x}N₄]N_x'.

Reflection class	Observed for	Wilson statistics (centric: 0.968 acentric: 0.736)
<i>hkl</i>	$h + k = 2n$	–
<i>0kl</i>	$k = 2n$	1.162
<i>h0l</i>	$h, l = 2n$	0.994
<i>hk0</i>	$h + k = 2n$	0.988
<i>h00</i>	$h = 2n$	–
<i>0k0</i>	$k = 2n$	–
<i>00l</i>	$l = 2n$	–

Table 7.8: Crystallographic data and selected details of data collection, structure solution and refinement of 'Ba₆[Mo_xTa_{1-x}N₄]N_x'. Standard deviations in units of the last digit are given in parentheses.

Crystal system	orthorhombic
Space group	<i>Cmcm</i> (no. 63)
Lattice parameters /Å	<i>a</i> 11.672(3)
	<i>b</i> 10.177(2)
	<i>c</i> 10.8729(19)
Volume /Å ³	1291.6(5)
<i>Z</i>	4
Calculated density /g · cm ⁻³	5.170
Diffractometer	IPDS-1, MoK _α radiation
	Graphite monochromator
Data collection temperature /K	295(2)
Absorption coefficient /mm ⁻¹	20.539
Data range ϑ /°	2.66–30.39
Index range	-16 ≤ <i>h</i> ≤ 16, -14 ≤ <i>k</i> ≤ 14, -13 ≤ <i>l</i> ≤ 13
No. of observed reflections	8153
No. of independent reflections	992
No. of independent reflections with (<i>I</i> ≥ 2σ(<i>I</i>))	766
<i>F</i> (000)	1672
Corrections	Lorentz, polarisation ^[3]
Absorption corrections	ABSTompa ^[17]
Structure solution	direct methods ^[3]
Structure refinement	full-matrix least squares on <i>F</i> ² ^[3]
No. of l. s. parameters	37
Goof on <i>F</i> ²	0.931
<i>R</i> _{int} / <i>R</i> _σ	0.0778 / 0.0445
<i>R</i> values (for reflections with <i>I</i> ≥ 2σ(<i>I</i>))	<i>R</i> ₁ = 0.0272, w <i>R</i> ₂ = 0.0553
<i>R</i> values (all data)	<i>R</i> ₁ = 0.0418, w <i>R</i> ₂ = 0.0573
Residual electron density /e ⁻ · Å ⁻³	2.217 / -1.717

Table 7.9: Fractional atomic coordinates, isotropic thermal displacement parameters and site occupation factors for 'Ba₆[Mo_xTa_{1-x}N₄]N_x'. Standard deviations in units of the last digit are given in parentheses.

Atom	Wyckoff Symbol	<i>x</i>	<i>y</i>	<i>z</i>	<i>U</i> _{eq} / Å ²	Site occupation factor
Ta1	4c	0	0.01283(6)	1/4	0.0094(3)	0.221(14)
Mo1	4c	0	0.01283(6)	1/4	0.0094(3)	0.779(14)
Ba1	8g	0.16604(6)	0.29317(6)	1/4	0.03439(18)	1
Ba2	8f	0	0.29190(4)	0.58412(5)	0.02421(15)	1
Ba3	8e	0.18661(4)	0	0	0.01399(12)	1
N1	8g	0.3740(7)	0.4010(8)	1/4	0.0309(19)	1
N2	8f	0	0.1250(6)	0.1102(7)	0.0171(15)	1
N3	8d	1/4	1/4	0	-	0.38(17)

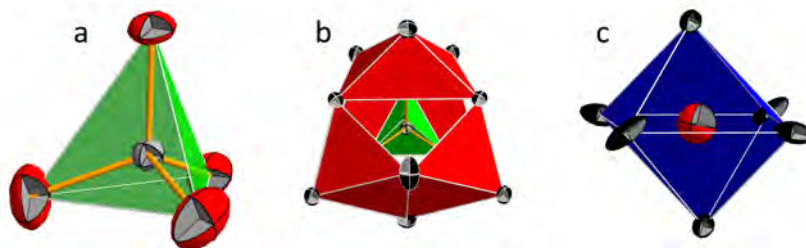


Figure 7.6: Coordination polyhedra in ' $\text{Ba}_6[\text{Mo}_x\text{Ta}_{1-x}\text{N}_4]\text{N}_x$ '. a: tetrahedral nitridometalate anion; b: cuboctahedral coordination of the nitridometalate anion by Ba; c: octahedral coordination of the nitride anion by Ba. Ba atoms: black ellipsoids, Mo/Ta atoms: grey ellipsoids, N atoms: red ellipsoids. Ellipsoids are drawn with 90 % probability level.

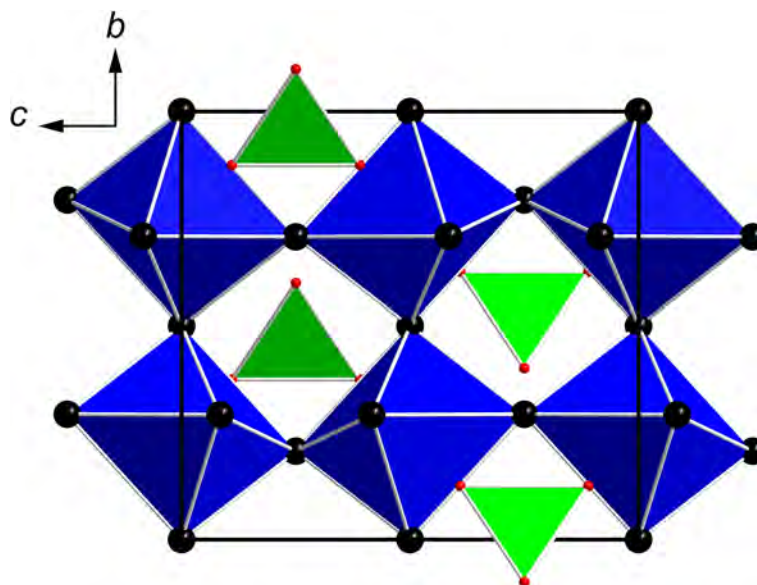


Figure 7.7: Unit cell of ' $\text{Ba}_6[\text{Mo}_x\text{Ta}_{1-x}\text{N}_4]\text{N}_x$ ' projected along a. Ba atoms: black spheres, Mo/Ta atoms: grey spheres, N atoms: red spheres.

Interatomic distances between Mo/Ta and N atoms range from 1.860 to 1.885 Å (see Table S7.7), which is in accordance to literature data for Ba_3MoN_4 (1.848 to 1.885 Å)^[18] and $\text{Ba}_{23}\text{Na}_{11}(\text{Ta}_4\text{N}_4)_4$ (1.926 to 1.950 Å),^[19] corroborating the mixed occupation on the Mo/Ta site. $[\text{Mo}/\text{Ta}_4\text{N}_4]$ tetrahedra are slightly distorted, as bond angles within the *ortho*-nitridomolybdate/-tantalate anions range from 104.5(4) to 111.563(11)° (see Table S7.8). The coordination sphere of the *ortho*-nitridomolybdate/-tantalate anion is a strongly distorted cuboctahedron of 12 Ba atoms (see Figure 7.6 b). Such a cuboctahedral coordination of large, complex anions has already been observed for the suboxometalates (Chapter 3).^[20] Isolated N^{3-} anions (N1, see Table 7.9) fill up the structure with a statistic occupation factor of 0.377(17). They are coordinated octahedrally by 6 Ba atoms (see Figure 7.6 c). Ba–N3 distances range from 2.650 to 3.088 Å (see Table S7.7) and are in accordance to data reported for Ba_2N and Ba_3MoN_4 (2.654 to 3.200 Å).^[1, 18]

The complete structure can be described as a hierarchical variant of a distorted cubic de-

fect anti-perovskite (see Figure 7.8). Ba^{2+} cations and the large *ortho*-nitridomolybdate/-tantalate anions build an *fcc* packing. N^{3-} anions occupy one quarter of the octahedral voids of the *fcc* packing. The $[\text{Ba}_6\text{N}]$ octahedra are connected via sharing corners, and every octahedron is tilted with respect to its neighbour (see Figure 7.7). ' $\text{Ba}_6[\text{Mo}_{0.78}\text{Ta}_{0.22}\text{N}_4]\text{N}_{0.76}$ ' crystallises in the orthorhombic and not in the cubic crystal system as one might expect. This can be attributed to the large difference in size of the individual ions – very large metalate ions ($\sim 4 \text{ \AA}$) versus rather small Ba^{2+} (1.35 \AA) and very small N^{3-} ions (1.46 \AA),^[21] similarly to the orthorhombic distortion in the perovskite structure of CaTiO_3 .^[22] Additionally the tilt effect of the octahedra contributes to the minor distortion from cubic symmetry (lattice parameters only deviate slightly from forming a cubic unit cell).

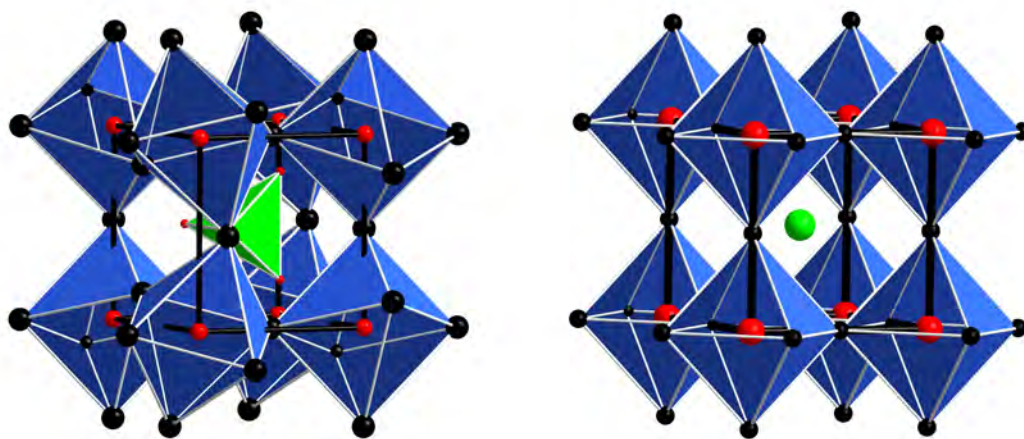


Figure 7.8: Comparison of the distorted perovskite ' $\text{Ba}_6[\text{Mo}_x\text{Ta}_{1-x}\text{N}_4]\text{N}_x$ ' with the structure of CaTiO_3 . The nitridometalate anions correspond to the Ca^{2+} atoms (green), the Ba^{2+} cations correspond to the O^{2-} anions (black), N^{3-} corresponds to the Ti^{4+} cations (red).

Discussion and Conclusion

Although the X-ray analysis of the crystal structure of ' $\text{Ba}_6[\text{Mo}_{0.78}\text{Ta}_{0.22}\text{N}_4]\text{N}_{0.76}$ ' is straightforward and yields excellent R values and only very small residual electron density some unresolved issues remain. Assuming the oxidation states $\text{Mo}^{+\text{VI}}$ and $\text{Ta}^{+\text{V}}$, ' $\text{Ba}_6[\text{Mo}_{0.78}\text{Ta}_{0.22}\text{N}_4]\text{N}_{0.76}$ ' formally has 3.5 free e^- per unit cell within standard deviations of the refined model. As Mo/Ta–N bond lengths correspond very well with literature data for $\text{Mo}^{+\text{VI}}$ and $\text{Ta}^{+\text{V}}$ compounds^[18,19] and neither Mo nor Ta are known in lower oxidation states coexisting with tetrahedral coordination of light elements, a 'compensation' of the free e^- by lower oxidation states of the transition metals is unlikely.

Subvalent compounds containing a mixed occupation of transition metal with such high oxidation states have been documented in literature.^[19] Also a phase width of subvalent compounds given by the partially occupied N1 site has been observed.^[23]

Table 7.10: Charge count in 'Ba₆[Mo_{0.78}Ta_{0.22}N₄]N_{0.76}'.

Atom	Charge	Number per asymmetric unit	Σ
Mo	6+	0.78	4.68+
Ta	5+	0.22	1.1+
Ba	2+	6	12+
N	3-	4.76	14.28-
			3.5+

Partial occupation of the N1 site by H⁻ anions must be considered, as the incorporation of H⁻ anions is a common preparative problem involving syntheses with metallic Ba. According to the amount of electron density (F_{obs}) and arithmetic calculations to fully occupy the octahedral void 90 % H⁻ and 10 % N³⁻ anions would be required, as can be shown by refining mixed but in sum full occupation of the N³⁻ site by H⁻ and N³⁻ instead of refining under-occupied N³⁻ anions. This would not make 'Ba₆[Mo_{0.78}Ta_{0.22}N₄]N_{0.76}' an ionic compound. The compound would still be subvalent. To disprove the existence of H⁻ anions, we attempted to detect hydrogen with solid-state NMR. However, due to the metallic character of the sample, MAS was not possible.

Subvalency in 'Ba₆[Mo_{0.78}Ta_{0.22}N₄]N_{0.76}' seems likely. However, to finally verify subvalency, some additional experimental as well as analytical work (e.g. NMR spectroscopic studies with strongly diluted samples, DFT calculations, EXAFS, EELS and conductivity measurements) are necessary.

Supporting Information

Table S7.6: Anisotropic displacement parameters for 'Ba₆[Mo_xTa_{1-x}N₄]N_x'. Standard deviations in units of the last digit are given in parentheses. U_{ij} is defined as $U_{ij} = \exp\{-2\pi^2[U_{11}(ha^*)^2 + \dots + 2U_{21}hka^*b^*]\}$, and U_{eq} is 1/3 of the trace of the anisotropic tensor.

Atom	$U_{11} / \text{\AA}^2$	$U_{22} / \text{\AA}^2$	$U_{33} / \text{\AA}^2$	$U_{23} / \text{\AA}^2$	$U_{13} / \text{\AA}^2$	$U_{12} / \text{\AA}^2$
Ta1	0.0099(4)	0.0105(3)	0.0080(5)	0	0	0
Mo1	0.0099(4)	0.0105(3)	0.0080(5)	0	0	0
Ba1	0.0360(4)	0.0447(3)	0.0225(4)	-0.0287(3)	0	0
Ba2	0.0456(4)	0.0131(2)	0.0139(3)	0	0	-0.00080(17)
Ba3	0.0121(2)	0.01551(18)	0.0143(3)	0	0	0.00138(17)
N1	0.018(4)	0.044(4)	0.031(6)	-0.011(3)	0	0
N2	0.021(4)	0.020(3)	0.010(4)	0	0	0.004(2)

Table S7.7: Selected interatomic distances / \AA for 'Ba₆[Mo_xTa_{1-x}N₄]N_x'. Standard deviations in units of the last digit are given in parentheses.

Atoms	Atoms	Distances	Atoms	Atoms	Distances
Mo1/Ta1-	N1	1.860(8)	Ba1-	Ba3	3.7955(7)
	N2	1.901(7)		N1	2.664(8)
	Ba1	3.4490(9)		N2	3.000(5)
	Ba2	3.5876(9)		N3	2.9227(5)
	Ba3	3.4857(6)		Ba1	3.8761(17)
Ba2-	N1	3.044(7)	Ba3-	Ba3	3.8441(6)
	N2	2.711(7)		Ba3	4.0433(7)
	N3	3.0876(7)		N1	2.984(4)
	Ba1	4.1175(9)		N2	2.792(4)
	Ba2	3.6072(13)		N3	2.6496(5)

Table S7.8: Selected bond angles / $^\circ$ for 'Ba₆[Mo_xTa_{1-x}N₄]N_x'. Standard deviations in units of the last digit are given in parentheses.

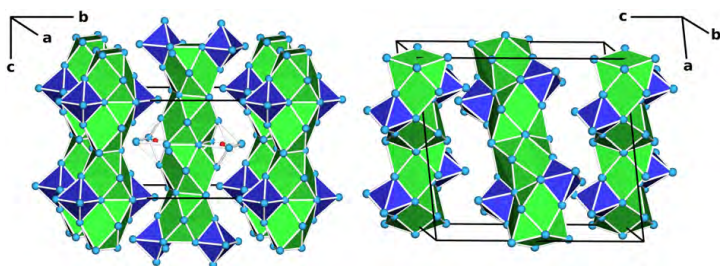
Atoms	Angles	Atoms	Angles
N1-Mo1/Ta1-N1	104.5(4)	Ba3-N3-Ba2	97.544(9)
N1-Mo1/Ta1-N2	11.56(11)	Ba3-N3-Ba2	82.456(8)
N2-Mo1/Ta1-N2	106.2(3)	Ba1-N3-Ba2	93.563(10)
Ba3-N3-Ba1	92.907(12)	Ba1-N3-Ba2	86.437(9)
Ba3-N3-Ba1	87.093(12)		

7.3 References

- [1] O. Reckeweg, F. J. DiSalvo, *Solid State Sci.* **2002**, *4*, 575–884.
- [2] Bruker, Apex2 Version 11, Billerica, Madison (US), **2014**.
- [3] G. M. Sheldrick, *Acta Crystallogr.* **2008**, *A64*, 112–122.
- [4] O. Reckeweg, F. J. DiSalvo, M. Somer, *J. Alloy. Compd.* **2003**, *361*, 102–107.
- [5] M. Orth, R. D. Hoffmann, R. Poettgen, W. Schnick, *Chem. – Eur. J.* **2001**, *7*, 2791–2797.
- [6] J. Gaude, P. L. Haridon, J. Guyader, J. Lang, *J. Solid State Chem.* **1985**, *59*, 143–148.
- [7] O. Reckeweg, H. J. Meyer, *Z. Anorg. Allg. Chem.* **1999**, *625*, 866–874.
- [8] N. W. Johnson, *Can. J. Math.* **1966**, *18*, 169.
- [9] S. Reich, A. C. Ferrari, *Phys. Rev. B* **2005**, *71*, 1–12.
- [10] L. Wu, X.-L. Chen, H. Li, M. He, Y.-P. Xu, X.-Z. Li, *Inorg. Chem.* **2005**, *44*, 6409–6414.
- [11] G. D. Chryssikos, *J. Raman Spectrosc.* **1991**, *22*, 645–650.
- [12] H. P. R. de Villiers, *Am. Miner.* **1971**, *56*, 758–766.
- [13] R. A. Nyquist, C. L. Putzig, M. A. Leugers, *Handbook of Infrared and Raman Spectra of Inorganic Compounds and Organic Salts*, Elsevier, Amsterdam, Netherlands, **1996**, *1*, 20.
- [14] T. Dierkes, M. Stroebele, H. J. Meyer, *Z. Anorg. Allg. Chem.* **2014**, *640*, 1275–1279.
- [15] S. Pagano, G. Montana, C. Wickleder, W. Schnick, *Chem. – Eur. J.* **2009**, *15*, 6186–6193.
- [16] F. Jach, M. Groh, P. Höhn, M. Ruck, *Z. Anorg. Allg. Chem.* **2014**, *640*, 2359.
- [17] A. L. Spek, *Acta Cryst.* **2009**, *D65*, 148–155.
- [18] A. Gudat, P. Hoehn, R. Kniep, A. Rabenau, *Z. Naturforsch.* **1991**, *B46*, 566–572.
- [19] M. Wörsching, F. Tambornino, S. Datz, C. Hoch, *Angew. Chem. Int. Ed.* **2016**, *55*, 10868–10871; *Angew. Chem.* **2016**, *128*, 11026–11030.
- [20] C. Hoch, J. Bender, A. Simon, *Angew. Chem. Int. Ed.* **2009**, *48*, 2415–2417; *Angew. Chem.* **2009**, *121*, 2451–2453.
- [21] R. D. Shannon, *Acta Crystallogr.* **1976**, *A32*, 751–767.
- [22] S. Sasaki, C. T. Prewitt, J. D. Bass, *Acta Crystallogr.* **1987**, *C43*, 1668–1674.
- [23] K. R. Tsai, P. M. Harris, E. N. Lassettre, *J. Phys. Chem.* **1956**, *60*, 345–347.

8 Summary

8.1 Alkali metal suboxometalates – structural chemistry between salts and metals



Via reaction of Cs, Cs₂O and M₂O₃ ($M^{+III} = \text{Al, Ga, Fe}$) the new alkali metal suboxometalates Cs₁₀MO₅ were synthesised. Cs₁₀MO₅ shows both metallic and ionic bonding following the formal description $(\text{Cs}^+)_{10}(\text{MO}_4^{5-})(\text{O}^{2-}) \cdot 3e^-$. Comparable to the Cs-rich suboxometalates Cs₉MO₄ ($M = \text{Al, Ga, In, Fe, Sc}$) with ionic subdivision

$(\text{Cs}^+)_{9}(\text{MO}_4^{5-}) \cdot 4e^-$, they contain an oxometalate anion $[\text{M}^{+III}\text{O}_4]^{5-}$ embedded in a metallic matrix of Cs atoms and can thus be described as a chemical twin. The main structural motifs in Cs₁₀MO₅ are column-like building units, $[\text{Cs}_8\text{MO}_4]$, comparable to those in Cs₉MO₄. However, in Cs₁₀MO₅ those columns are extended by face-sharing $[\text{Cs}_6\text{O}]$ octahedra leading to the overall composition of Cs₁₀MO₅. The columns show ionic behaviour on the inside and metallic behaviour on the surface. No isolated Cs atom is present as in Cs₉MO₄. Cs₁₀MO₅ crystallises in two modifications with new structure types. The orthorhombic modification adopts a structure in space group *Pnmm* with $a = 11.158(3)$, $b = 23.693(15)$, $c = 12.229(3)$ Å and $Z = 4$ (values for Cs₁₀AlO₅). The monoclinic modification crystallises in the space group *C2/c* with $a = 21.195(3)$, $b = 12.480(1)$, $c = 24.120(4)$ Å, $\beta = 98.06(1)^\circ$ and $Z = 8$ (values for Cs₁₀AlO₅). Limits to phase formation are given by trivalency of *M* atoms and by geometric size restrictions for the insertion of $[\text{Cs}_6\text{O}]$ octahedra. Similar to Cs₉MO₄ mixed crystals with the pattern Cs₁₀(M_x^IM_{1-x}^{II})O₅ were obtained. The formation of the two modifications Cs₁₀MO₅ was corroborated by theoretical calculations and thermoanalytical measurements.

8.2 Chemical Twinning of Salt and Metal in the Subnitridometalates

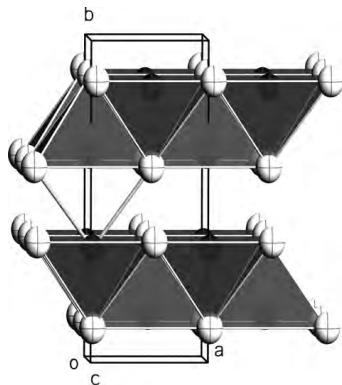
$\text{Ba}_{23}\text{Na}_{11}(\text{MN}_4)_4$ with $M = \text{V}, \text{Nb}, \text{Ta}$



The subnitridometalates $\text{Ba}_{23}\text{Na}_{11}(\text{MN}_4)_4$ were obtained via reaction of Ba_2N , Ba, Na and M ($M^{+V} = \text{V}, \text{Nb}, \text{Ta}$) in Nb or Ta crucibles. $\text{Ba}_{23}\text{Na}_{11}(\text{MN}_4)_4$ crystallise isotypically in a new structure type in the tetragonal space group $P4_2/n$ (no. 86) with $a = 14.131(17) \text{ \AA}$, $c = 18.537(2) \text{ \AA}$ for $M = \text{Ta}$ and $Z = 2$. The crystal structures

show three different motifs: ionic *ortho*-nitridometalate anions, distorted Na-centered $[\text{Na}_8]$ cubes (as cut-out of the bcc structure of elemental Na), and distorted Na-centered $[\text{Ba}_{10}\text{Na}_2]$ icosahedra (similar to the ones found in the Laves phase BaNa_2). Single crystal and powder X-ray diffraction was supplemented by band structure calculations and Raman spectroscopy emphasising the character of a 'chemical twin' with compartments of either ionic or metallic bonding in an overall metallic compound.

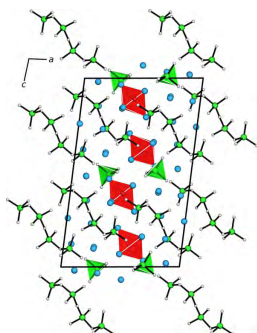
8.3 CsOH and its lighter homologues – a comparison



Single crystals of Caesium hydroxide, CsOH, were grown through slow diffusion of moist air to elemental Caesium stored under dry paraffin oil, and were characterised on the basis of single crystal diffraction data for the first time. CsOH crystallises isotypically to the room temperature modification of NaOH (CrB-type) in the orthorhombic space group $Cmcm$ (no. 63) with $a = 4.3414(15) \text{ \AA}$, $b = 11.959(6) \text{ \AA}$, $c = 4.5036(14) \text{ \AA}$ and $Z = 4$. The structure was compared extensively to all other alkali metal hydroxides with means of group-subgroup relations, and the single crystal structure of CsOH completes the compound class of alkali metal hydroxides. H atom positions could be suggested from the difference Fourier map calculated

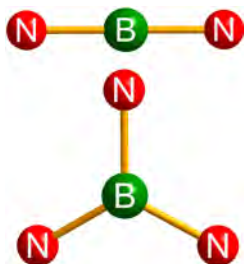
from X-ray diffraction data. Raman spectroscopic investigations on single crystal samples were performed and showed an almost free-ion behaviour of the hydroxide anion.

8.4 The triple salt $\text{Sr}_{14}[\text{Ta}_4\text{N}_{13}][\text{TaN}_4]\text{O}$ – a nitridotantalate oxide with 19-fold rocksalt superstructure



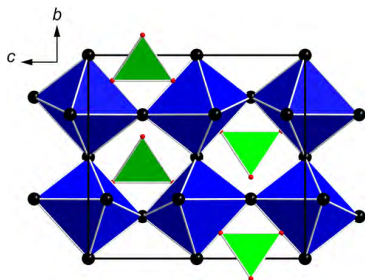
The new compound $\text{Sr}_{14}[\text{Ta}_4\text{N}_{13}][\text{TaN}_4]\text{O}$ was synthesised. It crystallises in a new crystal structure in the monoclinic space group $P2_1/c$ with $a = 15.062(2)$ Å, $b = 7.2484(6)$ Å, $c = 24.266(3)$ Å and $\beta = 97.280(10)^\circ$. The triple salt contains previously unknown $[\text{Ta}_4\text{N}_{13}]^{19-}$ anions together with *ortho*-tantalate and isolated oxide anions. Synthesis approaches included the employment of Sr surplus. The new structure type was established on the basis of single crystal X-ray diffraction data and supported by Rietveld refinement and EDX measurements. It is a complex superstructure of the rocksalt structure type with Ta and Sr atoms forming the fcc packing and N and O atoms occupying 18/19 of the octahedral voids. Structure and stability of the triple salt with respect to other known nitridometalates were considered.

8.5 The Barium Nitridoborate ' $\text{Ba}_{23}(\text{BN}_2)_{11}(\text{BN}_3)_3(\text{N})_3$ '



' $\text{Ba}_{23}(\text{BN}_2)_{11}(\text{BN}_3)_3(\text{N})_3$ ' was synthesised by reaction of Ba_2N with *h*-BN at high temperatures. It crystallises in the trigonal space group $P\bar{3}1/c$ (no. 163) with $a = 11.4087(16)$, $c = 23.045(5)$ and $Z = 2$. Ba^{2+} cations are surrounded by linear $[\text{BN}_2]^{3-}$, trigonal planar $[\text{BN}_3]^{6-}$ and isolated N^{3-} anions. Crystallographic data is supported by elemental analysis and Raman spectroscopy. For the obtained sum formula charge balance is not possible, thus further analysis is necessary to evaluate the nature of this compound.

8.6 The Barium Nitridomolybdate/-tantalate ' $\text{Ba}_6[\text{Mo}_x\text{Ta}_{1-x}\text{N}_4]\text{N}_x$ '



' $\text{Ba}_6[\text{Mo}_x\text{Ta}_{1-x}\text{N}_4]\text{N}_x$ ' was obtained from reaction of Ba_2N with Ba, Na and Mo in Ta crucibles. The compounds crystallises in the orthorhombic space group $Cmcm$ (no. 63) with $a = 11.672(3)$ Å, $b = 10.177(2)$ Å, $c = 10.8729(19)$ Å and $Z = 4$. The structure consists of tetrahedral *ortho*-molybdate/-tantalate anions with mixed Ta/Mo occupation, Ba^{2+} cations and isolated N^{3-} anions with partial occupation. Altogether the structure can be described as a distorted anti-perovskite. The meta- late anions and the Ba^{2+} cations together build an

fcc packing with N^{3-} anions occupying one quarter of the octahedral voids. Charge balancing accounts for a subvalent compound with 3.5 free e^- per unit cell. Further analytical work is necessary to corroborate this statement.

8.7 Concluding Words

In summary this work gave evidence that the research for new subvalent compounds is by no means at its end and should be pursued in the following years. The results presented in Chapters 3 added a new representative to the young class of suboxometalates, and new compounds with unusual structural building units will surely be discovered in the future. Even greater prospects seem to be deducible from the results presented in Chapter 4, wherein the first subnitridometalate is reported. It proves that even highly charged species (metals with oxidation state +V in combination with N atoms with oxidation state -III) can be embedded in a metallic matrix to form a chemical twin. The perspectives to further increase this compound class are almost unlimited considering the vast choice of elements that might be applicable to synthesise new structures. Besides the syntheses of subvalent compounds, single crystal structures of different ionic compounds could be characterised. They range from simple crystal structures, as in the case of CsOH or the perovskite ' $Ba_6[Mo_xTa_{1-x}N_4]N_x$ ', to structures containing highly complicated structural motifs with complex anions, as in ' $Ba_{23}(BN_2)_{11}(BN_3)_3(N)_3$ ' or $Sr_{14}[Ta_4N_{13}][Ta_4N_4]O$.

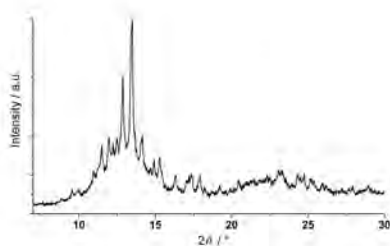
9 Outlook

9.1 Suboxometalates

The results in Chapter 3 expand the structure family of the alkali metal suboxometalates and raise expectations to its further enlargement.^[1] Mixing ionic and metallic building blocks in a chemical twin might lead to interesting materials combining ionic (ferromagnetism, non-Pauli paramagnetism etc.) with metallic properties (conductivity, band magnetism, ductility etc.). Enlarging the ionic structural sublattice could lead to air-stable compounds, incorporating metallic subunits as atom-sized quantum dots in a crystalline arrangement.

To realise new subvalent structures, various synthetic pathways should be considered. For the alkali metal suboxides it has been shown that the basic clusters ($[\text{Cs}_{11}\text{O}_3]$ and $[\text{Rb}_9\text{O}_2]$) already exist in the liquid phase.^[2] The amount of Cs atoms composing the metallic matrix can be varied widely.^[3-10] For suboxometalates we expect similar behaviour with the $[\text{Cs}_8\text{MO}_4]$ columns in Cs_9MO_4 and the $[\text{Cs}_{10}\text{MO}_5]$ columns in $\text{Cs}_{10}\text{MO}_5$ acting as preformed building blocks. This leads to two potential synthetic strategies to obtain new structures. First, it should be possible to increase the amount of Cs atoms in between the columns. First experiments showed that this is not attainable by simply increasing the amount of elemental Cs in the reaction mixture. A feasible synthetic route might be the use of Cs_9MO_4 or $\text{Cs}_{10}\text{MO}_5$ as a precursor in reaction with Cs at low temperatures ($< 200\text{ }^\circ\text{C}$). Synthesis optimisation to obtain phase-pure samples of Cs_9MO_4 and $\text{Cs}_{10}\text{MO}_5$ will be required, which is still difficult in the case of $\text{Cs}_{10}\text{MO}_5$.

Figure 9.1: PXRD pattern after thermal treatment of Cs_9InO_4 at 154°C .



A second approach to obtain new suboxometalates is to reduce the amount of Cs incorporated in the structures. Again, the use of Cs_9MO_4 as a precursor is essential. $\text{Cs}_{10}\text{MO}_5$ cannot be used as precursor as it has no metallic Cs atom which can be removed. Thus, the target compound would be a theoretical ' Cs_8MO_4 ' (in analogy to e.g. the suboxide Cs_{11}O_3). Two different routes should be considered. Removal of the additional Cs atom via careful thermal treatment – comparable to a distillation – is one alternative already documented for subnitrides,^[11] and first experimental work showed promising results. However, the lack of formation of single crystals is a preparative problem using this route and needs to be tackled, as data from powder X-ray diffraction (see Figure 9.1) did not deliver a satisfying structural model, in combination with other analytical methods.

A second route is an 'extraction' of metallic Cs with adequate solvents at very low temperatures ($< 25\text{ }^{\circ}\text{C}$), wherein all solvents need to be completely free of H_2O . Similar experimental procedures have been conducted for various electrides.^[12-14] First experiments showed that the selection of solvent is not straightforward and its acidity is essential. Reaction of liquid NH_3 with Cs_9InO_4 leads to formation of a blue solution (see Figure 9.2) decomposing into the products CsNH_2 , CsOH and elemental In . The following reaction equations suggest a reaction mechanism:

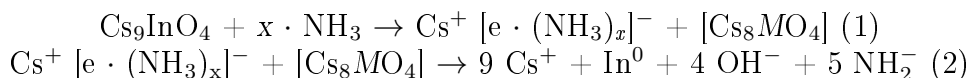
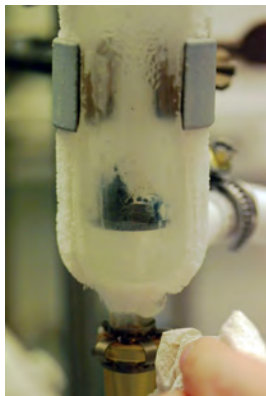


Figure 9.2: Cs_9InO_4 after extraction using NH_3 at -40°C .



NH_3 is too acidic and donates its proton to a free O^{2-} anion. The strong reducing environment of the blue electride solution leads to the reduction of In^{3+} to In^0 . Probably the use of less reactive, organic solvents in combination with complexing agents, e.g. crown ethers or cryptands, is more advisable. However, this requires a lot of experimental work, as many parameters need to be considered (e.g. choice of solvent, temperature, choice of reactants).

A hitherto not understood issue is the limitation of alkali metal suboxometalates to oxometalate anions containing M^{+III} species only.^[1,15,16] As suboxometalates are metallic, there is no obvious reason why other transition metals with oxidation states different than three and similar ionic radii should not be viable. The suboxometalates known so far contain transition metals with d^0 -, d^5 - and d^{10} -configuration. If the electron configuration plays a decisive role on the formation of suboxometalates, thinkable candidates would be Ti^{+IV} , V^{+V} , Cr^{+VI} , Zn^{+II} and Mn^{+VII} .

A further expansion of the anionic substructure by the employment of polyoxometalates (e.g. Keggin anions) as counter ions is imaginable to obtain poly-suboxometalates.^[17] Synthetic approaches aiming in this direction have not been conducted so far, and it is difficult to decide which electronic or geometric parameters will have to be considered. In principle the existence of compounds with oxometalate anions with highly oxidised transition metals which are kinetically inhibited towards an internal redox reaction has been proven and gives hope to achieve comparable results for suboxometalates.^[18] Aside from larger 0-dimensional anionic building blocks, one can imagine similar structures containing 1-, 2- or even 3-dimensional anions.

9.2 Subnitridometalates

With the synthesis of the first subnitridometalates reported in Chapter 4 a new compound class could be established.^[19] The combination of the anionic species $[\text{MN}_4]^{7-}$ with high negative charge with a metallic substructure of Ba and Na, which contains structural features of known elemental or intermetallic structures, is eminent. Structural modifications of $\text{Ba}_{23}\text{Na}_{11}(\text{MN}_4)_4$ should be a first step to further expand the family of subnitridometalates. Similar to the suboxometalates, various synthetic approaches

should be considered, however, the structure of $\text{Ba}_{23}\text{Na}_{11}(\text{MN}_4)_4$ offers even more room for chemical modifications: 1. Modifications of the anionic species; 2. Variation of the Na content; 3. Modifications of the icosahedral subunit. A removal of the metallicly bound Na with similar methods as proposed for the suboxometalates (thermal treatment or extraction of Na) is thinkable for $\text{Ba}_{23}\text{Na}_{11}(\text{MN}_4)_4$.

Also the introduction of higher Na contents and an expansion of the metallic matrix in $\text{Ba}_{23}\text{Na}_{11}(\text{MN}_4)_4$ might be achievable. Using higher amounts of Na compared to Ba/Ba₂N bears the advantage of further lowering the melting point of the reaction mixture, and thus probably increasing the reactivity at low reaction temperatures.^[20] Modifications of the icosahedral $[\text{Ba}_{10}\text{Na}_2]\text{Na}$ subunit in the structure of $\text{Ba}_{23}\text{Na}_{11}(\text{MN}_4)_4$ should be achieved. The icosahedral void occupied by Na is large, and synthesis approaches should aim to substitute Na with the heavier alkali metals K, Rb and Cs. So far the immiscibility of those elements with elemental Ba prevented the incorporation of the heavier alkali metals. This issue needs to be overcome by using alkali metal salts as reactants or a binary flux (e.g. Na/K mixtures).^[20] Finally it has to be evaluated if V^{+V} , Nb^{+V} and Ta^{+V} are the only candidates constituting the metallic centres of nitridometalate anions. Similar to the suboxometalates a prediction which elements are suitable aspirants is not easy and mainly two parameters will probably be decisive. Firstly, geometric restrictions are likely to be essential, so cations with similar ionic radii such as Cr^{+VI} , Mo^{+VI} or W^{+VI} should be in focus of future work.^[21] Secondly, for suboxometalates the oxidation states of the tetrahedrally coordinated metal are suspected to play a potential role in the formation process. Thus, for subnitridometalates experiments involving elements commonly showing oxidation state +V, e.g. P^{+V} , As^{+V} , Sb^{+V} or Bi^{+V} , should be investigated in future work, but not exclusively.

The phase diagrams of Sr–Na is very similar to the one of Ba–Na, so synthesis strategies using Na flux towards Sr subnitridometalates are not hindered in any way.^[20] However, the use of Sr so far led to ionic compounds only, as the results in Chapter 6 show.^[22] It is unknown if subvalent compounds containing Sr cations can be achieved. First synthetic approaches should aim to partly substitute Ba with Sr in the structure of $\text{Ba}_{23}\text{Na}_{11}(\text{MN}_4)_4$, as Sr might prefer the occupation of particular crystallographic sites in this structure. In the suboxides and suboxometalates the lighter Rb can only substitute Cs on a metallic position. Similar behaviour would be expected for Sr with respect to substitution of Ba. If such partial substitutions are successful, a higher Na/Sr ratio in the reaction mixture should further decrease reaction temperatures and might encourage the formation of subvalent compounds containing Sr as the only earth alkaline metal species.

Synthesis of new subnitridometalates does not have to be limited to the structural principles of $\text{Ba}_{23}\text{Na}_{11}(\text{MN}_4)_4$. In Chapter 7 the synthesis of the most likely subvalent compound $\text{Ba}_6[\text{Mo}_x\text{Ta}_{1-x}\text{N}_4]\text{N}_x$ was reported. The commonly known perovskite-like structure indicates that subvalent compounds with complex anions do not have to be arranged in a complicated manner, but can also exhibit simple structural motifs derivable from basic ionic structure types.

Together with the optimisation of synthesis of new subvalent compounds, investigations of structure-property relations should be in the spotlight. Alongside with spectroscopic examinations and theoretical calculations, conductivity and magnetic measurements on phase-pure samples should be performed, and it will be of great interest, how the con-

cept of a chemical twin is correlated to the macroscopic properties of the respective compounds.

9.3 Metal-rich ionic compounds via decomposition

It has already been shown that metal-rich ionic oxometalates can be achieved by using suboxometalates as starting materials.^[24] Further investigations in this direction should especially aim for the synthesis of new Cs oxoscandates and oxogallates, as for oxometalate anions of the other three transition metals ($\text{Fe}^{+\text{III}}$, $\text{Al}^{+\text{III}}$, $\text{In}^{+\text{III}}$) various ionic compounds are already documented in literature.^[23,24] Synthesis strategies should be performed similarly to the synthetic approaches conducted for oxometalates described in literature.^[24] Slow decomposition of Cs_9ScO_4 and Cs_9GaO_4 at mild temperatures should lead to the formation of oxometalates, e.g. ' Cs_5ScO_4 ', ' Cs_5GaO_4 ', ' $\text{Cs}_8\text{Sc}_2\text{O}_7$ ' or ' $\text{Cs}_8\text{Ga}_2\text{O}_7$ '. To estimate appropriate reaction temperatures thermoanalytic methods (DTA or DSC) should be applied in combination with temperature-dependent powder X-ray analysis.

For the synthesis of metal-rich nitridometalates similar strategies should be feasible. However, decomposition of the only known subnitridometalate $\text{Ba}_{23}\text{Na}_{11}(\text{MN}_4)_4$ is only one possible approach leading to ionic compounds that could range from the simple *ortho*- to more complex *catena*- or even *tecto*-nitridometalates. Especially the new compound $\text{Sr}_{14}[\text{Ta}_4\text{N}_{13}][\text{TaN}_4]\text{O}$ presented in Chapter 6 can cross-link to potential new structures. A thermal decomposition of $\text{Sr}_{14}[\text{Ta}_4\text{N}_{13}][\text{TaN}_4]\text{O}$ could lead to nitridometalates containing only one of the two complex anions of $\text{Sr}_{14}[\text{Ta}_4\text{N}_{13}][\text{TaN}_4]\text{O}$, leading to the *catena*-nitridotantalate $\text{Sr}_{19}(\text{Ta}_4\text{N}_{13})_2$ or the simple *ortho*-nitridotantalate $\text{Sr}_7(\text{Ta}_4\text{N}_4)_2$.

These new metal-rich ionic compounds would further increase the number of structures containing complex anions, but they can also be used as reference materials in comparison to subvalent compounds, when conducting spectroscopic measurements or methods considering their macroscopic properties (e.g. conductivity, magnetism).

9.4 References

- [1] M. Wörsching, C. Hoch, *Inorg. Chem.* **2015**, *54*, 7058–7064.
- [2] A. Simon, *Coord. Chem. Rev.* **1997**, *163*, 253–270.
- [3] A. Simon, *Z. Anorg. Allg. Chem.* **1977**, *11*, 5–16.
- [4] A. Simon, E. Westerbeck, *Z. Anorg. Allg. Chem.* **1977**, *428*, 187–198.
- [5] A. Simon, H. J. Deiseroth, *Rev. Chim. Miner.* **1976**, *13*, 98–112.
- [6] A. Simon, H. J. Deiseroth, E. Westerbeck, B. Hillenkötter, *Z. Anorg. Allg. Chem.* **1976**, *423*, 203–211.
- [7] A. Simon, *Z. Anorg. Allg. Chem.* **1976**, *422*, 208–218.
- [8] A. Simon, H. J. Deiseroth, *Z. Anorg. Allg. Chem.* **1980**, *463*, 14–26.
- [9] H. J. Deiseroth, A. Simon, *Rev. Chim. Miner.* **1983**, *20*, 475–487.
- [10] H. J. Deiseroth, A. Simon, *Inorg. Chem.* **1978**, *17*, 875–879.
- [11] U. Steinbrenner, A. Simon, *Z. Anorg. Allg. Chem.* **1997**, *624*, 228–232.
- [12] J. L. Dye, *J. Phys. Chem.* **1984**, *88*, 3842–3846.
- [13] S. B. Dawes, D. L. Ward, R. H. Huang, J. L. Dye, *J. Am. Chem. Soc.* **1986**, *108*, 3534–3535.
- [14] S. B. Dawes, J. L. Eglin, K. J. Moeggenborg, J. Kim, J. L. Dye, *J. Am. Chem. Soc.* **1991**, *113*, 1605–1608.
- [15] C. Hoch, J. Bender, A. Simon, *Angew. Chem. Int. Ed.* **2009**, *48*, 2415–2417; *Angew. Chem.* **2009**, *121*, 2451–2453.
- [16] C. Hoch, J. Bender, A. Wohlfarth, A. Simon, *Z. Anorg. Allg. Chem.* **2010**, *635*, 1777–1782.
- [17] J. F. Keggin, *Proc. R. Soc.* **1934**, *A144*, 75–100.
- [18] V. Hlukhyy, T. F. Fässler, *Angew. Chem. Int. Ed.* **2012**, *51*, 742–747; *Angew. Chem.* **2012**, *124*, 766–771.
- [19] M. Wörsching, F. Tambornino, S. Datz, C. Hoch, *Angew. Chem. Int. Ed.* **2016**, *55*, 10868–10871; *Angew. Chem.* **2016**, *128*, 11026–11030.
- [20] B. Predel, *Landolt-Börnstein, Zahlenwerte und Funktionen aus Naturwissenschaften und Technik, Neue Serie, Bd. Vb – Phasengleichgewichte, kristallographische und thermodynamische Daten binärer Legierungen, B–Ba ... C–Zr*, Springer Verlag GmbH, Heidelberg, Germany, **2005**.
- [21] R. D. Shannon, *Acta Crystallogr.* **1976**, *A32*, 751–767.
- [22] M. Wörsching, M. Daiger, C. Hoch, *Inorg. Chem.* **2017**, DOI:

10.1021/acs.inorgchem.6b03053

- [23] J. Bender, A. Wohlfarth, C. Hoch, *Z. Naturforsch.* **2010**, *65b*, 1416–1426.
- [24] C. Hoch, *Z. Naturforsch.* **2011**, *66b*, 1248–1254.

10 Miscellaneous

10.1 List of Publications

The results compiled in this thesis were published in scientific journals as detailed in the following list.

CsOH and its lighter homologues – a comparison

Matthias Wörsching, Constantin Hoch

published in: *Z. Naturforsch.* **2014**, *69b*, 1229–1236. DOI: 10.5560/ZNB.2014-4163

Sample preparation, literature and database research, structure elucidation and writing the manuscript was done by Matthias Wörsching. Constantin Hoch created graphical material and supervised the work.

Alkali metal suboxometalates – structural chemistry between salts and metals

Matthias Wörsching, Constantin Hoch

published in: *Inorg. Chem.* **2015**, *54*, 7058–7064. DOI:10.1021/acs.inorgchem.5b01060

Writing the manuscript, creation of graphical material, synthesis of the samples, literature research, structure elucidation and evaluation of analytical data were performed by Matthias Wörsching. Constantin Hoch directed and supervised the work.

Chemical Twinning of Salt and Metal in the Subnitridometalates $\text{Ba}_{23}\text{Na}_{11}(\text{MN}_4)_4$ with $\text{M} = \text{V}, \text{Nb}, \text{Ta}$

Matthias Wörsching, Frank Tambornino, Stefan Datz, Constantin Hoch

published in: *Angew. Chem. Int. Ed.* **2016**, *55*, 10868–10871. DOI: 10.1002/anie.201605113

published in: *Angew. Chem.* **2016**, *128*, 11026–11030. DOI: 10.1002/anie.201605113

Writing the manuscript, creation of graphical material, synthesis of the samples, literature research, structure elucidation and evaluation of analytical data were performed by Matthias Wörsching. Theoretical calculations were conducted by Frank Tambornino. Evaluation thereof were performed by Matthias Wörsching and Frank Tambornino in close collaboration. Raman spectroscopic measurements were performed by Stefan Datz. Constantin Hoch directed and supervised the work.

The triple salt $\text{Sr}_{14}[\text{Ta}_4\text{N}_{13}][\text{TaN}_4]\text{O}$ – a nitridotantalate oxide with 19-fold rocksalt superstructure

Matthias Wörsching, Martin Daiger, Constantin Hoch

published in: *Inorg. Chem.* **2017**, DOI: 10.1021/acs.inorgchem.6b03053

Writing the manuscript, creation of graphical material, literature research, structure elucidation and evaluation of analytical data were performed by Matthias Wörsching. Martin Daiger conducted synthesis of the samples. Constantin Hoch directed and supervised the work.

10.2 Contributions to conferences

Caesiumsuboxometallate (oral presentation)

Matthias Wörsching, Constantin Hoch

Hirschegg-Seminar on Solid State Chemistry 2014, Hirschegg, Austria

Auf dem Weg zu Subnitridometallaten (oral presentation)

Matthias Wörsching, Stefan Datz, Constantin Hoch

Hirschegg-Seminar on Solid State Chemistry 2015, Hirschegg, Austria

Towards new subvalent compounds – a new Bariumnitridoborate (poster presentation)

Matthias Wörsching, Stefan Datz, Constantin Hoch

European conference on solid state chemistry 2015, Wien, Austria

Subnitridotiegelate (oral presentation)

Matthias Wörsching, Constantin Hoch

Hemdsärmelkolloquium 2016, Karlsruhe, Germany

The first Barium/Sodium Subnitridometalates $\text{Ba}_{23}\text{Na}_{11}(\text{MN}_4)_4$ ($M = \text{V}, \text{Nb}, \text{Ta}$) (poster presentation)

Matthias Wörsching, Frank Tambornino, Stefan Datz, Constantin Hoch

EuCheMS Chemistry Congress 2016, Seville, Spain

10.3 Deposited crystallographic data

Table 10.1: Deposited crystallographic data

Compound	CSD-Number
CsOH	426540
Cs ₁₀ AlO ₅ (monoclinic)	429344
Cs ₁₀ AlO ₅ (orthorhombic)	429345
Cs ₁₀ GaO ₅ (monoclinic)	429355
Cs ₁₀ (Al/Ga)O ₅ (orthorhombic)	429356
Cs ₁₀ (Al/Fe)O ₅ (orthorhombic)	429358
Ba ₂₃ Na ₁₁ (VN ₄) ₄	431345
Ba ₂₃ Na ₁₁ (NbN ₄) ₄	431343
Ba ₂₃ Na ₁₁ (Ta ₄ N ₄) ₄	431344
Sr ₁₄ [Ta ₄ N ₁₃][Ta ₄ N ₄]O	432368